

**TECHNICAL  
TRANSACTIONS**

**MECHANICS**

**CZASOPISMO  
TECHNICZNE**

**MECHANIKA**

**ISSUE  
2-M (7)**

**ZESZYT  
2-M (7)**

**YEAR  
2015 (112)**

**ROK  
2015 (112)**



**WYDAWNICTWO  
POLITECHNIKI  
KRAKOWSKIEJ**

# TECHNICAL TRANSACTIONS

## MECHANICS

ISSUE 2-M (7)  
YEAR 2015 (112)

# CZASOPISMO TECHNICZNE

## MECHANIKA

ZESZYT 2-M (7)  
ROK 2015 (112)

Chairman of the Cracow  
University of Technology Press  
Editorial Board

**Jan Kazior**

Przewodniczący Kolegium  
Redakcyjnego Wydawnictwa  
Politechniki Krakowskiej

Przewodniczący Kolegium  
Redakcyjnego Wydawnictw  
Naukowych

Chairman of the Editorial Board

**Józef Gawlik**

Scientific Council

**Jan Błachut  
Tadeusz Burczyński  
Leszek Demkowicz  
Joseph El Hayek  
Zbigniew Florjańczyk  
Józef Gawlik  
Marian Giżejowski  
Sławomir Gzell  
Allan N. Hayhurst  
Maria Kušnierova  
Krzysztof Magnucki  
Herbert Mang  
Arthur E. McGarity  
Antonio Monestiroli  
Günter Wozny  
Roman Zarzycki**

Rada Naukowa

Mechanics Series Editor

**Andrzej Sobczyk**

Redaktor Serii Mechanika

Section Editor  
Editorial Compilation

**Dorota Sapek  
Aleksandra Urzędowska**

Sekretarz Sekcji  
Opracowanie redakcyjne

Language correction

**Aleksandra Broniek**  
([www.profenglish.com](http://www.profenglish.com))

Weryfikacja językowa

Typesetting  
Cover Design

**Krystyna Gawlik  
Michał Graffstein**

Skład i łamanie  
Projekt okładki

Basic version of each Technical Transactions magazine is its online version  
Pierwotną wersją każdego zeszytu Czasopisma Technicznego jest jego wersja online  
[www.ejournals.eu/Czasopismo-Techniczne](http://www.ejournals.eu/Czasopismo-Techniczne) [www.technicaltransactions.com](http://www.technicaltransactions.com) [www.czasopismotechniczne.pl](http://www.czasopismotechniczne.pl)

© Cracow University of technology/Politechnika Krakowska, 2015

# Editorial Board Mechanics

## 2-M/2015

### **Editor-in-Chief:**

Andrzej Sobczyk, Cracow University of Technology, Poland

### **Editorial Board:**

Ali Cemal Benim, Duesseldorf University of Applied Sciences, Germany  
Finn Conrad, Technical University of Denmark, Denmark  
Jan Czerwiński, Fachhochschule Biel-Bienne, Switzerland  
Heikki Handroos, Lappeenranta University of Technology, Finland  
Richard Hetnarski, Rochester Institute of Technology, USA  
Monika Ivantysynova, Purdue University, USA  
Daniel Kalinčák, University of Žilina, Slovakia  
Rajesh Kanna, Velammal College of Engineering and Technology, India  
Janusz Kowal, AGH University of Science and Technology, Poland  
Janoš Kundrak, University of Miskolc, Hungary  
Rathin Maiti, Indian Institute of Technology, India  
Massimo Milani, University of Modena & Reggio Emilia, Italy  
Moghtada Mobedi, Izmir Institute of Technology, Turkey  
Abdulmajeed A. Mohamad, University of Calgary, Canada  
Takao Nishiumi, National Defence Academy, Japan  
Petr Noskievic, VSB - Technical University of Ostrava, Czech Republic  
Leszek Osiecki, Gdańsk University of Technology, Poland  
Zygmunt Paszota, Gdańsk University of Technology, Poland  
Zbigniew Pawelski, Lodz University of Technology  
Pieter Rousseau, University of Cape Town, South Africa  
Kazimierz Rup, Cracow University of Technology, Poland  
Rudolf Scheidl, Johannes Kepler University, Austria  
Serhii V. Sokhan, National Academy of Science, Ukraine  
Mirosław Skibniewski, University of Maryland, USA  
Jacek Stecki, Monash University, Australia  
Kim A. Stelson, University of Minnesota, USA  
Jarosław Stryczek, Wrocław University of Technology, Poland  
Edward Tomasiak, Silesian University of Technology, Poland  
Andrzej Typiak, Military University of Technology, Poland  
Edward Walicki, University of Zielona Góra, Poland  
Shen Yu, Chinese Academy of Sciences, China  
Maciej Zgorzelski, Kettering University, USA  
Tadeusz Złoto, Czestochowa University of Technology, Poland

### **Executive Editors:**

Renata Dwornicka, Cracow University of Technology, Poland  
Renata Filipowska, Cracow University of Technology, Poland  
Grzegorz Filo, Cracow University of Technology, Poland

PIOTR CYKLIS, ROMAN DUDA\*

## COMPUTER DRIVEN AUTOMATIC CONTROL OF THE HYBRID TWO STAGE REFRIGERATION CYCLE

### WSPIERANE KOMPUTEROWO AUTOMATYCZNE STEROWANIE HYBRYDOWEGO DWUSTOPNIOWEGO UKŁADU CHŁODNICZEGO

#### Abstract

In the paper the method of automatic control of the two stage hybrid sorption-compression refrigeration system for different ambient conditions is presented. The main advantages of the system are its environmental friendly working fluids and waste or renewable low temperature heat source utilization. The control algorithm is designed for operation in four seasons' conditions. During cold seasons the heat from the second stage condenser, as waste heat, may be used to increase the temperature of the heat pump source. The system is composed of dependent subsystems with individual controls, however it is controlled by the computer program as master control. The issues related to the optimization of operation of the refrigeration system, taking into account the maximum usage of available renewable or waste heat sources, are discussed in the paper.

*Keywords: hybrid, refrigeration cycle, computerised control*

#### Streszczenie

W artykule przedstawiono metodykę automatycznego sterowania dwustopniowej adsorpcyjno-sprężarkowej kaskady chłodniczej w zależności od różnych warunków otoczenia. Główna zaleta prezentowanego systemu wynika z wykorzystania przyjaznych dla środowiska czynników chłodniczych. System wykorzystuje do pracy energię cieplną z niskotemperaturowych źródeł odnawialnych. Algorytm sterujący został przygotowany tak, aby utrzymać pracę systemu przez cały rok. Podczas okresu zimowego ciepło ze skraplacza, jako ciepło odpadowe, może zostać wykorzystane do podwyższenia temperatury źródła pompy ciepła. System zbudowany jest z zależnych od siebie podsystemów, dlatego ich praca zarządzana jest przez program komputerowy. Zostaną omówione zagadnienia związane z optymalizacją pracy systemu chłodniczego biorące pod uwagę maksymalne wykorzystanie dostępnych źródeł ciepła.

*Słowa kluczowe: hybrydowy system chłodniczy, sterowanie komputerowe*

\* Prof. Ph.D. D.Sc. Eng. Piotr Cyklis, M.Sc. Eng. Roman Duda, Faculty of Mechanical Engineering, Cracow University of Technology.

## 1. Introduction

In the Laboratory of Thermodynamics and Thermal Machines Measurements at the Cracow University of Technology the refrigerating laboratory stand has been designed and constructed [1–3]. The system is hybrid and unique since it combines the attitudes of adsorption cycle driven by a low temperature heat source, with compression low temperature stage working with CO<sub>2</sub> [4]. To achieve the best possible results and assure safe plant operation a specially designed control system has been designed [5].

The control system is composed of several parts for each thermodynamic subsystem. However, a master control system with programmed setups for different ambient conditions as well as refrigeration chamber requirements has been also been made.

## 2. Composition of the control system

A schematic diagram of the control system designed for hybrid refrigeration stand TSD [6, 7] is shown in Fig 1. ST0–PC class computer with two displays M0 and M1, communication with measurement cards is provided through RS485, for data gathering from IPC cards the modbus protocol has been used, communication with PLC controller and expansion valve controller, further calculations on the gathered data, data storage, supervising and online graph generation [8, 9].

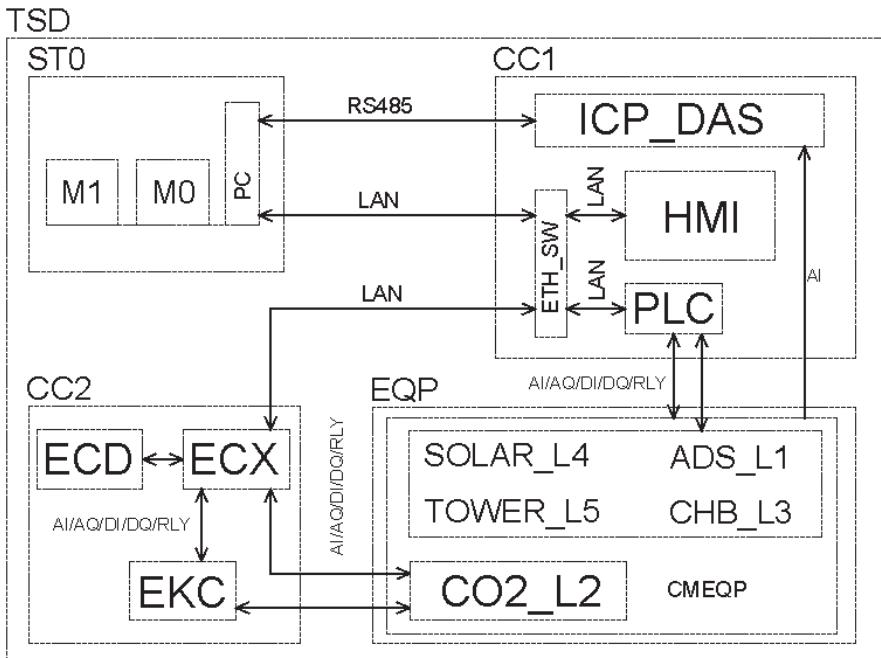


Fig. 1. Block schematics of the system

Professional software has been used, as well as software tools for PLC and HMI programming such as: SIEMENS TIA Portal V.13 STEP 7.

The software "kaskada" for readings of the data from the IPC cards and recalculating them has been written using Visual Studio 2013 Professional. Kaskada\_vi is the part written in Lab View, where the NIST REFPROP for refrigerant properties has been used. Also other software such as CoolPack, Mathcad for calculations have been used.

CC1 MAIN CASE – measurements of: temperature and pressure, mass and volume flow rates, electric power for electric devices. Also a PLC controller for the whole system is included. The main parts are:

- ICP\_DAS 8 pcs. M-7017RC cards, for data acquisition, this as a whole measuring system which gives 64 analog input signals of which 52 are used at this development stage.
- PLC SIEMENS S7 CPU 1217C controller with Ethernet/PROFINET interface and CM 1241 RS485 for communication ports. The PLC is equipped with 14 x DI digital input, 10 x DQ digital output signals, 2 x AI analog input, 2 x AQ analog output signals, to PLC are connected eight expansion modules with sum of: 40 x AI analog inputs, 8 x AQ analog outputs, 16 x RLY relay switched outputs.
- HMI KTP700 Basic PN operator panel with Ethernet/PROFINET interface for communication.

EQP subsystems of the refrigeration stand:

- SOLAR\_L4 solar subsystem presented in Fig. 2: Temperature measurements,  $t_{IN1}$ ,  $t_{IN2}$ ,  $t_{IN3}$ ,  $t_{IN4}$ ,  $t_{OUT1}$ ,  $t_{OUT2}$ ,  $t_{OUT3}$ ,  $t_{OUT4}$ , Pressure measurements  $p_{IN}$ ,  $p_{OUT}$ . Mass flow measurements  $m_1$ . Liquid pump – PCS2 with the electric power measurement.

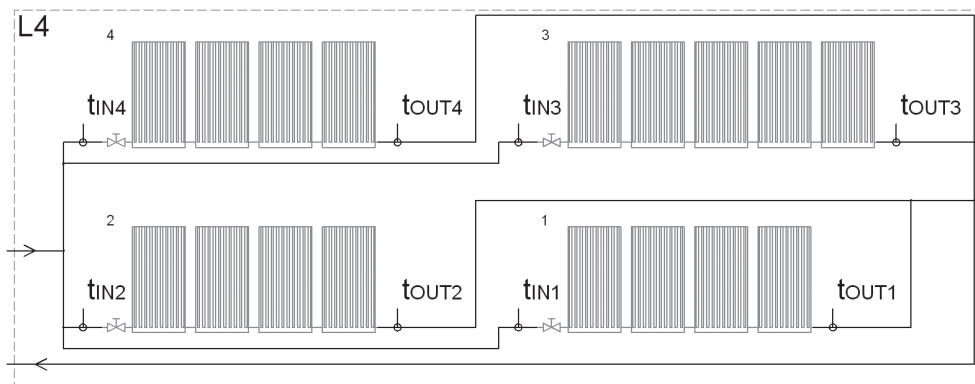


Fig. 2. SOLAR\_L4 solar subsystem

- CHB\_L3 heat container presented in Fig. 3: Temperature measurements,  $t_{z1}$ ,  $t_{z2}$ ,  $t_{AKU}$  in a liquid container. Circulating pumps, P1, P2. Electronic valves,  $ZV_1$ ,  $ZV_6$ .
- ADS\_L1 adsorber presented in Fig. 4: Temperature measurements,  $t_1$ ,  $t_2$ ,  $t_3$ ,  $t_4$ ,  $t_{4SP}$ ,  $t_{5SP}$ ,  $t_5$ ,  $t_6$ . Mass flow measurements,  $m_{1AD}$ ,  $m_2$ ,  $m_3$ . Circulating pumps: PCS1, PCS2, PCS3, PCS4. Adsorber with electric power measurement.

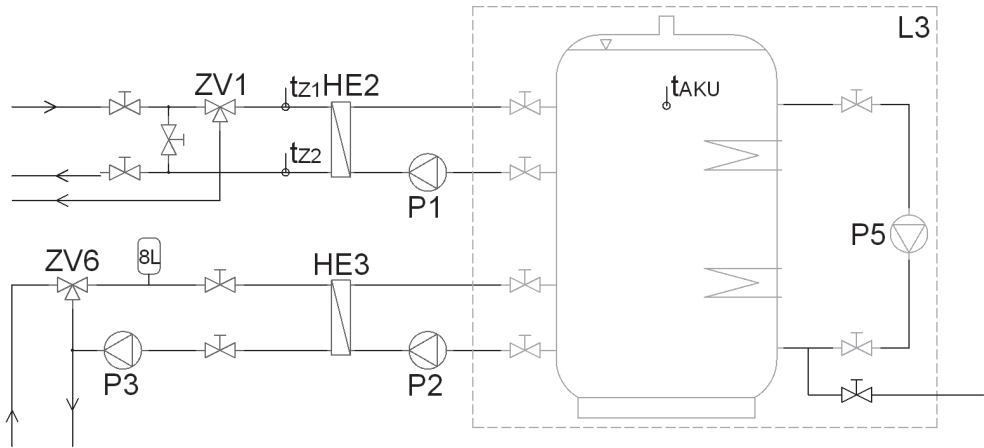


Fig. 3. CHB\_L3 heat storage subsystem

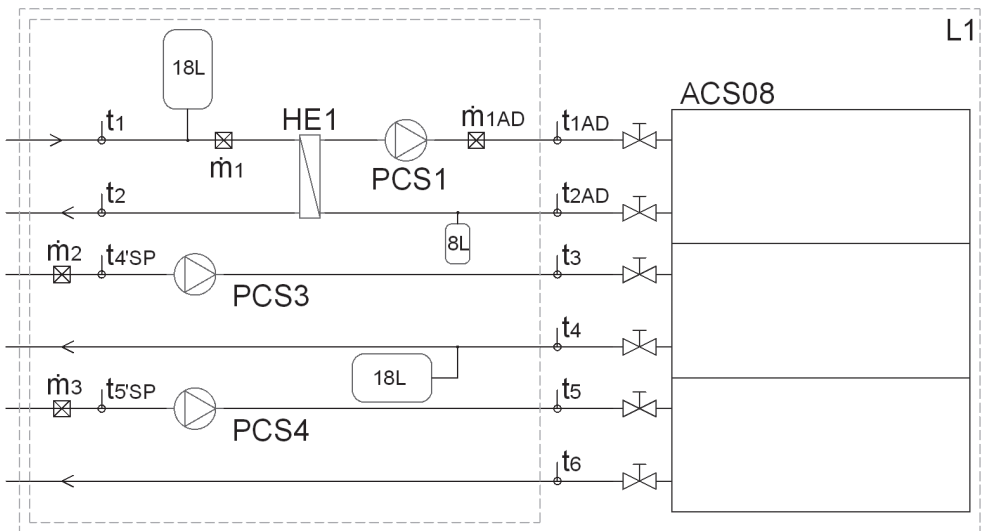


Fig. 4. ADS\_L1 adsorber subsystem

- TOWER\_L5 water sprayed cooling tower: Temperature measurements,  $t_3$ ,  $t_4$ . Mass flow measurements. Fan supply and a water spraying pump with the electric power measurement.
- CMEQP common part of the acting elements: servomotors for valves, circulating pumps.
- ETH\_SW network switch LAN 1000/100/10 Mbit/s.

CC<sub>2</sub> subsystem case CO<sub>2</sub> consists of an independent controller EKC with an independent safety subsystem, an overheating controller for expansion valve ECX. This controller has

been built into awepage where work parameters can be changed using a web page browser, ECD controller parameters display.

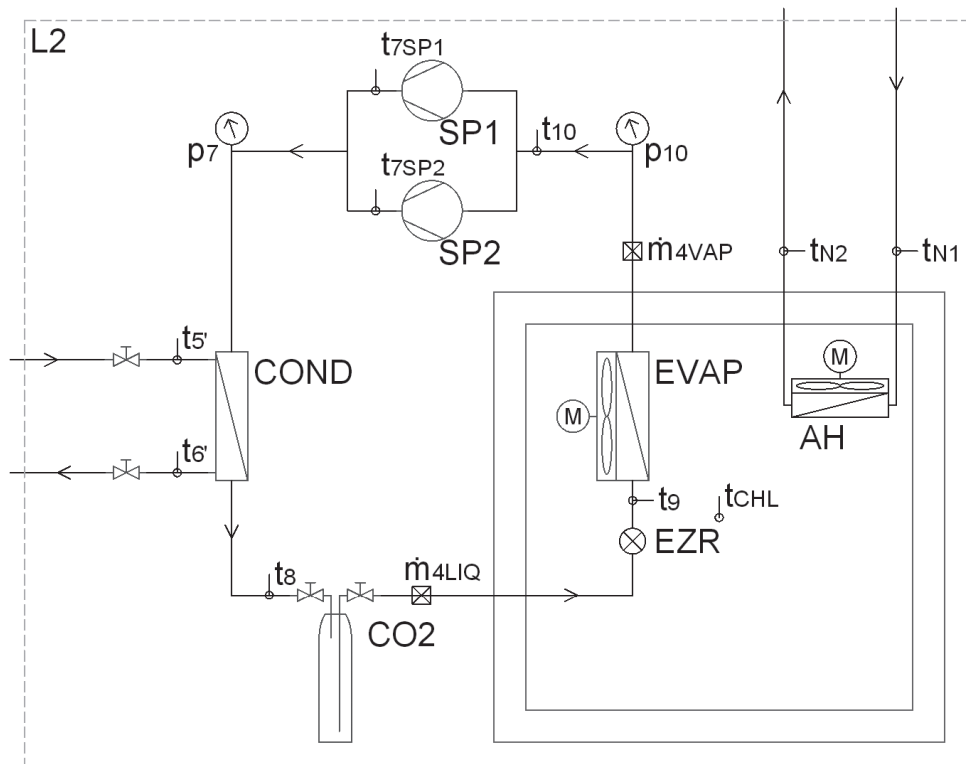


Fig. 5. CO<sub>2</sub>\_L2 compression CO<sub>2</sub> subsystem

CO<sub>2</sub>\_L2 compression system CO<sub>2</sub> presented in Fig. 5: Temperature measurements,  $t_5$ ,  $t_6$ ,  $t_{7SP1}$ ,  $t_{7SP2}$ ,  $t_8$ ,  $t_9$ ,  $t_{10}$ ,  $t_{CHL}$ ,  $t_{N1}$ ,  $t_{N2}$ . Pressure measurements,  $p_7$ ,  $p_{10}$ . Mass flow measurements:  $m_{4LIQ}$ ,  $m_{4VAP}$ . Compressors: SP1, SP2 with the electric power measurement. Frequency inverter. Flow through heater used for simulation of the heat load in the refrigeration chamber.

### 3. Algorithms and optimization

The system has several operation setups for each subsystem.

Subsystem ADS\_L1 – the adsorber operation has four main regimes:

1. Summer day operation (SDW) regime when the input temperature from the heat source exceeds 65[°C], and the ambient air temperature is higher than 13[°C]. Then the adsorption subsystem works in the cooling mode. Since the outlet cooling temperature from the



adsorber is a function of cooling load, it is sufficient to leave the cycle for the lowest possible cooling temperature. This self-adjustment function of the adsorption unit allows to achieve the lowest possible condensing temperature, reducing total energy consumption. This regime works until two above mentioned temperatures used as control functions are exceeded;

2. Summer night operation (SNW), the adsorber work is no longer possible when heat source temperature decreases below 65[°C], then the adsorption system has to be stopped, and only then the cooling tower is used to cool down the CO<sub>2</sub> condenser;
3. Heat pump operation (HPW): this option is used when the ambient air temperature is lower than 13[°C]. Then the adsorber may be used separately as a heat pump for waste and ambient heat and use the heat collector as HT source, while the MT (medium temperature heat) is used for domestic/company heating. In this case CO<sub>2</sub> cycle condenser is cooled down directly from the cooling tower;
4. Additional heater operation (AHW). The temperature of the heat source is below 65[°C] and the requirements for condenser cooling are higher than the cooling tower can give. This may be the case only in special ambient conditions with very high relative air humidity and high temperature when no waste or solar heat source is available.

Subsystem CO<sub>2</sub>\_L2 – compression cycle CO<sub>2</sub>:

1. The cooling requirements for CO<sub>2</sub> condenser may in some cases be limited, and additional cooling power will be required. In this case there are two possibilities: the control signal is released to run the AHW program in the L1 subsystem, in the meanwhile reducing the compressor power;
2. The frequency inverter mounted on one of the cascade controlled compressors, allows to control the refrigeration power with the relationship to current chamber load. The compression cycle works using variable load control which is more efficient than a standard on/off system.

Subsystem CHB\_L3, SOLAR\_L4, TOWER\_L5. The heat container subsystem is simple in operation. It has electric heater with an on/off system only for the L1 AHW mode. Also the valves ZV and pumps have to work in harmony with other subsystem modes.

1. Mode SAC – the solar heat accumulation is controlled using temperature readings. Once the temperature reading is higher than the set point, the PCS2 pump starts and works until the outlet temperature from solar collectors exceeds the temperature in heat container for 15[K]. Then the P1 pump starts and the heat container load starts. This accumulation goes on until the glycol temperature in the solar circuit lowers below the container's temperature plus 2–3[K]. In the case of fast solar collectors temperature decreases the PCS2 pump is off. In the case of full heat container load (95[°C] achieved) the mode SAC changes to the mode SWS. The pump's efficiency is also changed based on temperature readings and heat flux;
2. Mode SW solar work– the heat accumulator is fully loaded (95[°C]), then P1 pump goes off, if the L1 subsystem is on the SDW mode the glycol directly heats the adsorber. In the case when the solar temperature is too high or the subsystem L1 is off, the mode SW changes into the SWS mode. Registered work in this mode is presented in Fig. 6;
3. SWS mode – solar waste mode. This is the case when no heat source is needed (L1 is not operating, accumulator is full) and there is a considerable amount of solar radiation and the temperature readings in the solar subsystem exceed the points set (about 100[°C]), then the pump PCS2 has to be put into operation and all the heat goes to the cooling tower.

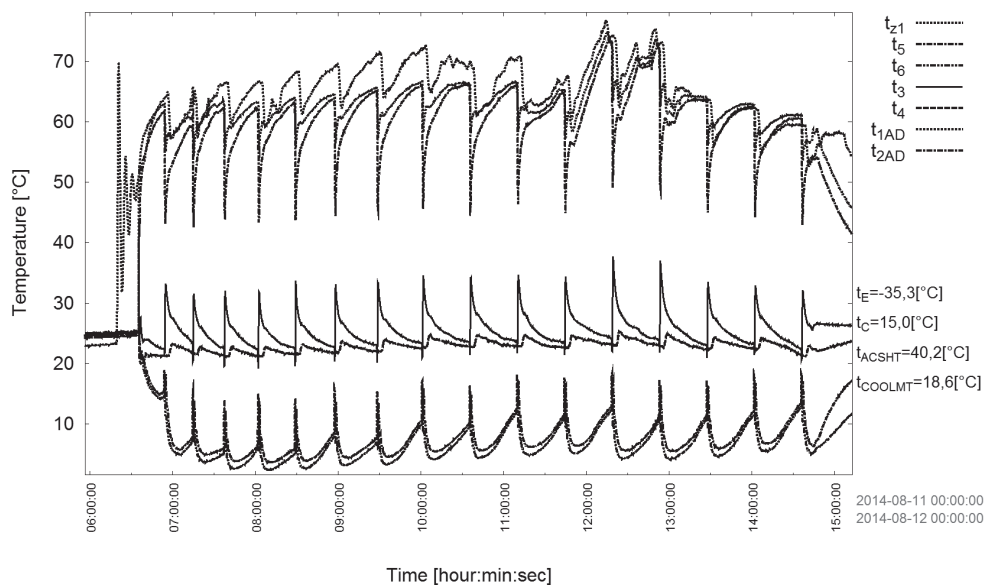


Fig. 6. Graph of temperatures for ADS\_L1 with CO2\_L2 for SW regime

In Fig. 6. A graph of temperatures measured during the system operation in the SW mode is shown. The oscillation of the values is the result of the adsorber's cyclic work. However, this does not influence the LT stage condenser operation. The main optimization criteria of working algorithms of the presented system are the minimum of electric power needed and the maximum possible usage of waste or renewable heat sources. Algorithms presented above are still under development and modification. Also self-adjustment of temperatures and heat fluxes levels for switching between regimes are tested. The first level of algorithms is based on temperatures, the second level on heat fluxes and cooling demand in a steady state, the third level on heat fluxes in unsteady state, the fourth level on prediction of availability of heat sources based on the actual state of the system and the day of year (calendar, season) as well as the actual time and previously recorded data. This has to be done to ensure high quality of operation without frequent unnecessary switching between the modes.

## 5. Conclusions

In this paper the new compression-adsorption hybrid cycle computer driven control system has been shown. The system has been designed, constructed and investigated in the Laboratory of Thermodynamics and Thermal Machines Measurements at the Cracow University of Technology (Politechnika Krakowska).

The system needs to run for different ambient weather conditions, so all setups need to be tested for more than one year. Besides, the control system is very complex so the optimization of its operation is still under development.

## References

- [1] Cyklis P., Kantor R., Górski B., Ryncarz T., *Hybrydowe sorpcyjno-sprężarkowe systemy ziębnicze. Część I – Koncepcja systemu hybrydowego*, Technika Chłodnicza i Klimatyzacyjna, nr 7–8, 2012, 196-197.
- [2] Cyklis P., Kantor R., Górski B., Ryncarz T., *Hybrydowe sorpcyjno-sprężarkowe systemy ziębnicze. Część II – Realizacja systemu hybrydowego*, Technika Chłodnicza i Klimatyzacyjna, nr 8, 2012, 198.
- [3] Cyklis P., Kantor R., Górski B., Ryncarz T., *Hybrydowe sorpcyjno-sprężarkowe systemy ziębnicze. Część III – Wyniki badań systemu*, Technika Chłodnicza i Klimatyzacyjna, nr 1, 2013, 203.
- [4] Cyklis P., Kantor R., *Concept of hybrid adsorption-compression refrigeration system*, Zeszyty Naukowe Politechniki Poznańskiej, 2011.
- [5] Cyklis P., Kantor R., Ryncarz T., Górski B., Duda R., *Experimental investigation of the ecological hybrid refrigeration cycle*, tom 35, nr 3, 2014, 145-154.
- [6] Cyklis P., Kantor R., Górski B., *A New Hybrid Compression-Adsorption Refrigerating System Powered by Solar Collectors*, Heat Transfer and Renewable Sources of Energy, 2012, 195-200.
- [7] Cyklis P., Kantor R., *Thermodynamic analysis of hybrid sorption-compression two stage refrigerating systems*, IIR CONGRESS 2011 Proceedings, 2011.
- [8] Cyklis P., Kantor R., Górski B., Ryncarz T., *The Hybrid Compression-Sorption System for Thermal Energy Transformation*, Proceedings of the 3rd International Conference Low Temperature and Waste Heat Use in Communal and Industrial Energy Supply Systems, Bremen 2012.
- [9] Cyklis P., Duda R., *Metodyka sterowania hybrydowym sprężarko-sorpcyjnym obiegiem chłodniczym*, tom 31, nr 86, 2014, 165-174.

PIOTR CYKLIS, PRZEMYSŁAW MŁYNARCZYK\*

## THE ROLE OF THE CFD MODELLING IN THE SHAPE OPTIMIZATION OF THE PRESSURE PULSATIONS DAMPERS

### ROLA MODELOWANIA CFD W OPTYMALIZACJI KSZTAŁTU TŁUMIKÓW PULSACJI CIŚNIENIA

#### Abstract

Pressure pulsations in volumetric compressors systems have an important influence on the compression power and reliability. This problem occurs not only in huge compressor systems, as in the natural gas piping, in gas mines or national transport systems, but also in a small refrigeration compressors in domestic applications. Nowadays, it is necessary to develop pressure pulsation damping elements which will be effective for different mass flow rate values. One of the solutions are passive damping elements in the form of various types of nozzles. In addition to the decrease of pressure pulsations value, the result is also an increase in power consumption of the compression. Therefore, shape optimization is necessary. In the article the possibility of optimizing the shape of such elements using computational simulations is discussed.

*Keywords: CFD simulations, Pressure pulsations damping, nozzle gas flow*

#### Streszczenie

Pulsacje ciśnienia w instalacjach sprężarek wyporowych mają duży wpływ na ich moce sprężania oraz niezawodność. Problem ten pojawia się nie tylko w dużych systemach sprężarkowych, jak na przykład w sprężarkach gazu ziemnego w kopalniach i rurociągach transportowych, ale również w małych sprężarkach chłodniczych w zastosowaniach domowych. Aktualnie konieczne jest opracowanie elementów tłumiących pulsacje ciśnienia dla różnych wartości strumienia przepływającego czynnika. Jednym z rozwiązań są pasywne elementy tłumiące w postaci różnego rodzaju zwężek. Poza spadkiem wartości pulsacji ciśnienia efektem jest również wzrost poboru mocy sprężania. Wymagana jest więc optymalizacja kształtu takich elementów. Niniejszy artykuł rozważa możliwość przeprowadzenia optymalizacji kształtu pasywnych tłumików pulsacji ciśnienia przy pomocy symulacji komputerowych.

*Słowa kluczowe: Symulacje CFD, Pulsacje ciśnienia, przepływ gazu w dyszy*

\* Prof. Ph.D. D.Sc. Eng Piotr Cyklis, M.Sc. Eng. Przemysław Młynarczyk, Faculty of Mechanical Engineering, Cracow University of Technology.

## Nomenclature

$f_D$	–	dimensionless Darcy’s friction factor from Moody’s diagram or Colebrook’s equations
$L$	–	pipe length
$D$	–	pipe internal diameter
$\rho$	–	fluid density
$v$	–	average flow velocity
$\varepsilon r$	–	relative roughness of the wall
$e$	–	roughness height
Re	–	Reynolds number
$\dot{M}$	–	mass flow rate
$\alpha$	–	flow number
$\varepsilon$	–	expansion number
$A_d$	–	area of the nozzle cross-section
$\Delta p$	–	pressure difference (pressure drop)
$v_1$	–	specific volume before the nozzle

## 1. Introduction

Periodic working machines like volumetric compressors are among the most popular machines in industry. Pressure pulsations attenuation in volumetric compressor systems are constantly one of the most important problems in a compressed gas manifold. Most of the phenomena caused by pressure pulsation, like vibrations, acoustic noise, energy loss, and valves wear are harmful to the installation and its components. A wide range of compressors, from large, low-speed natural gas compressors to small, compact refrigeration compressors with variable speed makes it difficult to find a universal solution. In all cases pressure pulsation reduction is an important engineering task. The standard way to attenuate pressure pulsation is to apply the Helmholtz theory for the muffler design as it is described in [1, 2]. There is still no practical solution to suppress different values of pressure pulsation with variable mass flow rate over time using one compact damping element. The CFD application for simulation of constant and impulse flows through the nozzle can give an answer how the nozzle affects the pulsating flow. Investigations on flow pulsations damping are also shown in literature nowadays [3–5]. Especially simulations of a nozzle flow are widely presented in the publications [6, 7]. The CFD simulation has been used by [8] for the simulation of a single pipe internal flow excited with a single disturbance. It has been shown that the response which is periodic with a constant frequency is characterized by a certain degree of damping.

The core of this article is the answer to the question whether the CFD simulations can be used to optimize the shape of pressure pulsations dampers.

## 2. Nozzle designs

For simulation and experimental investigation several nozzle designs have been prepared. The passive pressure pulsations damping was analysed with specially shaped hyperboloidal nozzles and normalized shaped nozzles like Venturi orifice and Venturi nozzle as it is shown in the Figure 1. Three different internal diameters were chosen:  $\phi 10$ ,  $\phi 15$  and  $\phi 20$ . After preliminary experimental investigations and CFD simulations the most promising shapes were tested in both directions flow and as a configuration of two coupled elements. The key element of this investigation is the assessment of the nozzle's influence on the pulsation attenuation and pressure drop on the basis of a computer simulation and the results compared with the outcomes of the experimental investigations. With normalized shapes computational results may be checked by standard, known analytical equations.

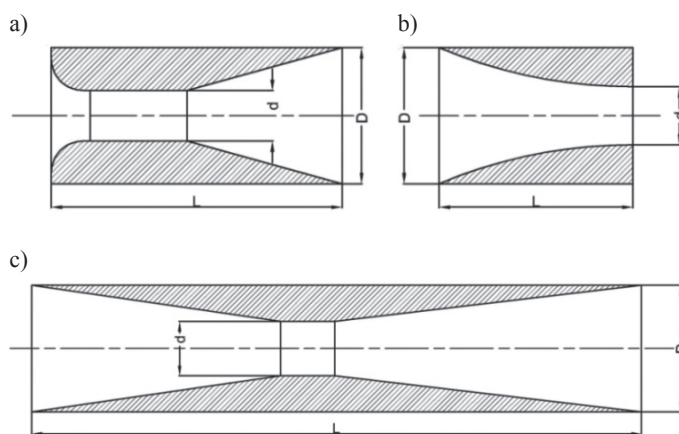


Fig. 1. Shape and main dimensions of the a) Venturi nozzle, b) Hiperboloidal nozzle, c) Venturi orifice

## 3. CFD results verification methods

The desired effects of the designed nozzle impact on pressure pulsations is a reduction in pressure pulsation to at least 20% with insignificant influence on the compressor's power with the same volumetric flow rate.

For this task the CFD simulation method could be selected as a tool for finding the best possible solution. To achieve this goal two different simulation results have to be computed: the unsteady simulation which shows the influence on the pressure pulsation and the steady state simulation which corresponds with the flow restriction affecting the compressor's power.

### 3.1. Experimental investigations

In the experimental investigations of pressure pulsations damping the nozzles were placed at the discharge of screw compressor DS-40 CompAir. The screw compressor was powered by a diesel engine with a variable speed control. The laboratory test stand is shown in Fig. 2.

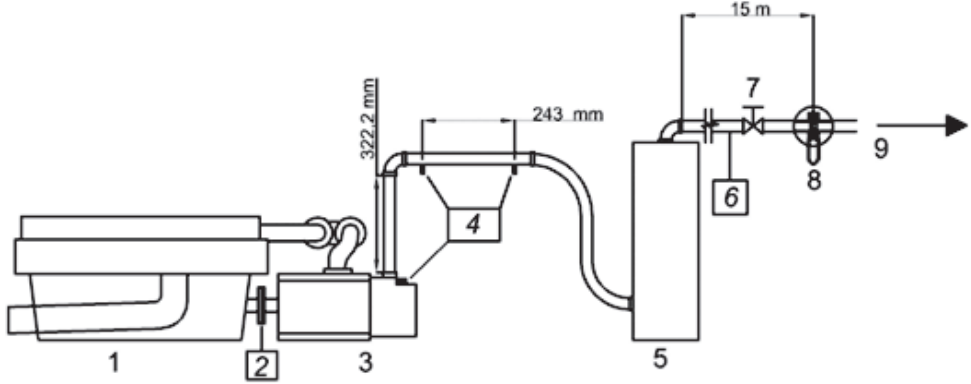


Fig. 2. Measuring system, where: 1 – engine, 2 – torque meter on the propeller shaft, 3 – screw compressor, 4 – pressure pulsations sensors, 5 – oil separator, 6 – static pressure transducer, 7 – throttle valve, 8 – metering orifice, 9 – outflow

The nozzle is located 17mm above the compressor discharge chamber. The ICP Dynamic Pressure Sensors made by PCB Piezotronics were used. The signal from sensors goes through the 4-channel ICP Sensor Line Power unit to the NI USB-6251 data acquisition module. The LabView data acquisition software was used to acquire the pressure pulsation data.

### 3.2. Analytic equations

The results of the steady state CFD flow simulation have been compared for validation with the standard known formulas for normalised shapes. The normalised, known methods for pressure loss in a pipe or a standard nozzle are shown below:

– the Darcy-Weisbach method for tube pressure loss under steady flow conditions [9]:

$$\Delta p = f_D \cdot \frac{L}{D} \cdot \frac{\rho V^2}{2} \quad (1)$$

Where the Darcy's friction factor could be taken from the Moody's diagram or calculated, for example, using the Haaland formula:

$$f_D = -1.8 \log_{10} \left[ \left( \frac{\varepsilon r}{3.7} \right)^{1.11} + \frac{6.9}{Re} \right] \quad (2)$$

or the Swamee-Jain equation:

$$f_D = 0.25 \left[ \log_{10} \left( \frac{e}{3.7D} + \frac{6.9}{Re} \right) \right]^{-2} \quad (3)$$

- For Venturi orifice and nozzle ISO5167 a standard formula may be applied for pressure drop on the element:

$$\Delta p = \frac{\dot{M}^2 v_1}{2\alpha^2 \varepsilon^2 A_d^2} \quad (4)$$

#### 4. CFD Procedures

For the CFD simulations the ANSYS/FLUENT software was used. For all cases a 2D axisymmetric, ideal gas isentropic flow model was used with the Reynolds-Stress turbulence model. Three to six boundary layers at the wall and two areas with a different element size were modelled. The same geometry was used for a steady and unsteady (impulse flow) simulation.

Boundary conditions for an unsteady impulse flow:

- At the inlet mass flow impulse excitation 0.1 [kg/s]. The impulse excitation means that its duration is equal to one time step ( $2e^{-06}$  s),
- Pressure outlet where the pressure at the outlet was defined as the arithmetical average between the pressure outside the domain and the last cell inside the domain,
- Wall (also for closed end elements) where tangential stresses were included in the momentum conservation equation.

Next, the results were spatially averaged at the inlet and outlet to obtain one dimensional flow and pressure pulsations functions, which are the result of the impulse flow excitation. Damping coefficient  $\xi$ , free frequency  $\omega$ , delay time  $\Delta\tau$ , and amplification coefficient K were estimated for each free frequency. The oscillation response has the form shown in Fig. 3.

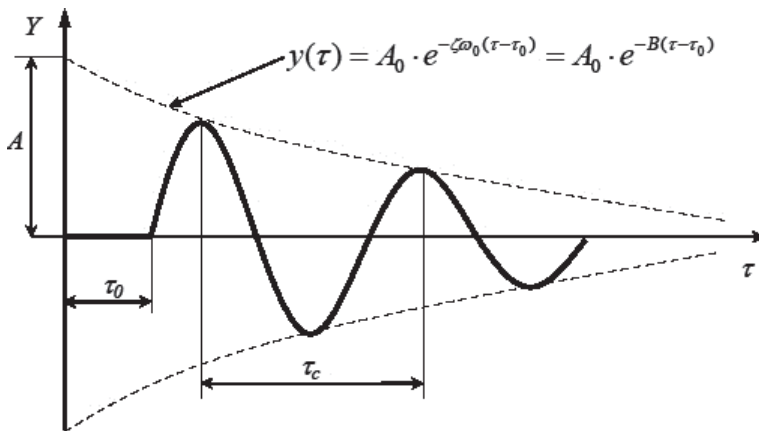


Fig. 3. Damped oscillating function and graphic presentation of its parameters



The analysis of the steady-state flow through the nozzle gives the pressure drop on the element which could be compared to the experimentally received mass flow to the power  $(V/N)$  coefficient's value. The pressure loss on the element has been related to the average pressure in the discharge compressor manifold and the pressure loss on a straight empty pipe (pipe0) using the following formula:

$$\beta = \frac{\Delta p_{nozzle} + p_{discharge}}{\Delta p_{pipe0} + p_{discharge}} \tag{5}$$

Convergent results were obtained for dense Cartesian mesh, using a very high number of elements with the so-called “metrics” above 0.95 for the orthogonal elements. The averaged value of “metrics” for elements above 0.85. The dense mesh caused no convergent results with lower “metrics”. The mesh fragment for the Venturi nozzle is shown in the 4. The points:  $p_0$  and  $p_1$  are the pressure measuring points and the placement of these points is defined in the ISO 5167 standard formula.

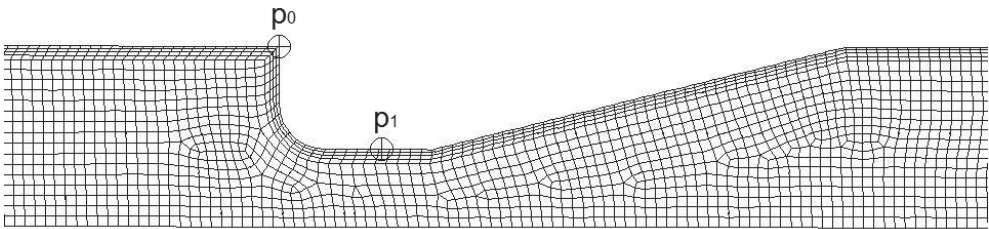


Fig. 4. Venturi nozzle mesh used for simulation

### 5. Results comparison

Results of pressure drop obtained in the steady-state flow for normalised shapes are compared to analytical calculations and are shown in Fig. 5.

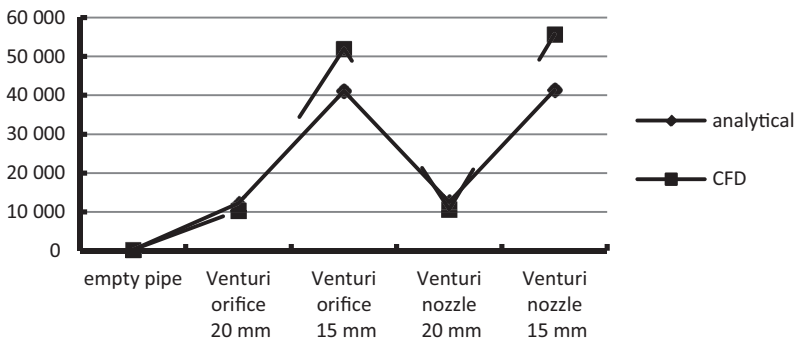


Fig. 5. Comparison of the CFD results with the analytical and standard flow measurement method results for standard shapes

The experimental investigations described in section 3.1 were performed for two different revolution speeds: 1615 rev/min and 2100 rev/min. In the article the results for the higher speed are described. It has been assumed that  $V/N$  is related to the steady flow pressure loss on the element, therefore the steady flow through the element was simulated and the pressure loss was compared with an empty pipe pressure loss during steady flow.

The presented results show that, especially for the elements of one shape group, results from the experiment and from the CFD simulations agree qualitatively. The results are shown in Fig. 6 – experiment and Fig. 7 – CFD.

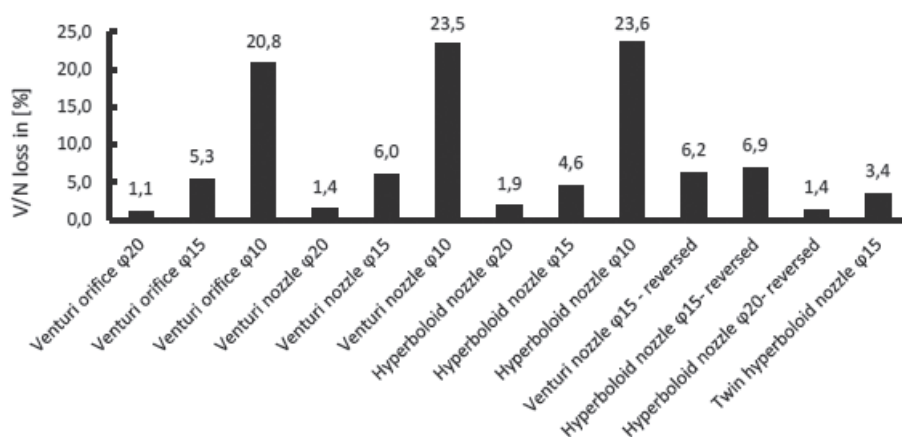


Fig. 6.  $V/N$  power loss in [%] compared to empty pipe for 2100 rev/min

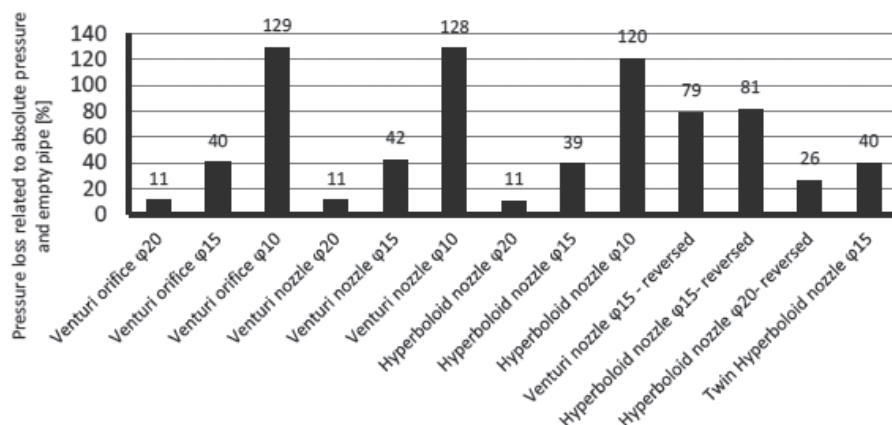


Fig. 7. Relative pressure loss  $\beta$  on damping element in comparison with the pressure loss on an empty straight pipe in [%]

## 6. Conclusions

The possibility to simulate pressure pulsations damping by passive elements is shown in the paper. The CFD simulation results were compared with experimental data and with results obtained in calculations of standard formulas. Due to the limited amount of space the article shows only the relationship between  $V/N$  and  $\beta$  loss. CFD results are not directly the same as experimentally determined parameters, because of the compressor system complex and the simplified CFD model. Referring to the growing number of compressors with a variable revolution speed, it is necessary to find the right shape of the damping element for a certain range of the mass flow rate, therefore the shape optimization is necessary. Experimental investigations provide accurate results but impose serious limitations. Standard formulas are limited to use only for typical shapes. It has been shown that the CFD simulation can be used as a tool to optimise the shape or dimension of the nozzle. According to the results, the conclusion is that the CFD's role in pressure pulsations dampers shape optimization is possible and necessary.

## References

- [1] Cyklis P., *Identyfikacja termodynamiczna elementów instalacji sprężarek wyporowych. Uogólnienie modelu Helmholtza*, Monography, nr 254, Wydawnictwo Politechniki Krakowskiej, Kraków 1999.
- [2] Ma Y.-C., Min O.-K., *Pressure calculation in a compressor cylinder by a modified new Helmholtz modeling*, Journal of Sound and Vibration 243, 2001, 775-796.
- [3] Lee, S.-H., Ih, J.-G., *Effect of non-uniform perforation in the long concentric resonator on transmission loss and back pressure*, Journal of Sound and Vibration 311, 2008, 280-296.
- [4] Hermann J., Koreck J., Maess M., Gaul L., von Estroff O., *Frequency-dependent damping model for the hydroacoustic finite element analysis of fluid-filled pipes with diameter changes*, Mechanical Systems and Signal Processing 25, 2011, 981-990.
- [5] Sadamoto A., Tsubakishita Y., Murakami Y., *Sound attenuation in circular duct using slit-like short expansion of eccentric and/or serialized configuration*, Journal of Sound and Vibration 277, 2004, 987-1003.
- [6] Shademan Y., Barron M., Balachandar R., *CFD Study of effects of geometry variations on flow in a nozzle*, Engineering Applications of Computational Fluid Mechanics, Vol. 6, No. 3, 2012, 412-425.
- [7] Torregosa A., Fajardo P., Gil A., Navarro R., *Development of non-reflecting boundary condition for application in 3D computational fluid dynamics*, Engineering Applications of Computational Fluid Mechanics, Vol. 6, No. 3, 2005, 447-460.
- [8] Sekavcnik M., Ogorevc T., Skerget L., *CFD analysis of the dynamic behaviour of a pipe system*, Forsh Ingenieurwes 70, 2012, 139-144.
- [9] *Engineering toolbox*, [http://www.engineeringtoolbox.com/darcy-weisbach-equation-d\\_646.html](http://www.engineeringtoolbox.com/darcy-weisbach-equation-d_646.html) (date of access: 2014-11-21).

TADEUSZ CZYŻEWSKI\*

## QUATERNIONS – ALTERNATIVE FOR EULER ANGLES IN KINEMATIC ANALYSIS OF MACHINE MECHANISMS

---

### KWATERNIONY – ALTERNATYWA DLA KĄTÓW EULERA W ANALIZIE KINEMATYCZNEJ MECHANIZMÓW MASZYN

#### Abstract

The article presents some types of problems that can occur during solving the inverse kinematics and the steps to prevent them. These problems concern the numerical singularities which occur when Euler angles are used to describe the orientation of the mechanism links in space. This paper proposes to eliminate the mentioned numerical singularities by replacing Euler angles with quaternions. The discussed issues were shown on the example of a backhoe excavator equipment system.

*Keywords: quaternions, Euler angles, inverse kinematics*

#### Streszczenie

W artykule przedstawiono pewien typ problemów, jakie mogą wystąpić podczas rozwiązywania zadania odwrotnego kinematyki oraz kroki pozwalające na ich zapobieganie. Problemy te dotyczą osobliwości numerycznych powstałych w wyniku stosowania kątów Eulera do opisu orientacji członów mechanizmu w przestrzeni. Poniższa praca proponuje wyeliminowanie wspomnianych osobliwości numerycznych poprzez zastąpienie kątów Eulera kwaternionami. Poruszane zagadnienia przedstawiono na przykładzie osprzętu roboczego koparki podsiębiernej.

*Słowa kluczowe: kwaterniony, kąty Eulera, zadanie odwrotne kinematyki*

---

\* M.Sc. Eng. Tadeusz Czyżewski, Institute of Applied Informatics, Faculty of Mechanical Engineering, Cracow University of Technology.

## 1. Introduction

The main task of the kinematic analysis of machines mechanisms is the study of motion of these mechanisms without taking into account the forces and moments that act upon them. In the case of serial mechanisms, an analysis can be divided into two general tasks. The first one is the simple kinematics problem, which is used to obtain the position and orientation of the last element in the kinematic chain. The second one, which is the inverse kinematics problem, is used to determine the values of all joint variables when the position and orientation of the last element of the kinematic chain is known. In serial mechanisms the inverse kinematics problem is much more difficult to solve than the simple kinematics problem [1]. This is due to the fact that the equations describing the relationships between joint variables and the position and orientation of the links are highly nonlinear [2].

The article discusses some types of problems that can occur during solving the inverse kinematics problem and also the steps to prevent them. These problems concern the numerical singularities which occur when Euler angles are used to describe the orientation of the mechanism links in space. This paper proposes to eliminate the mentioned numerical singularities by replacing Euler angles with quaternions. The discussed issues were shown on the example of a backhoe excavator equipment system.

## 2. Kinematic analysis based on the multibody system formalism

Kinematic analysis, which is a part of the theory of mechanisms and machines, is the subject of a lot of research work and publications [1–7]. As a result of these studies several procedures have been developed that allow to automatically perform the kinematic analysis. One such procedure is the multibody system method. A solution of the inverse kinematics problem in the multibody system method is equivalent to solving the following system of equations:

$$\Phi(q, t) = \begin{bmatrix} \Phi^K(q) \\ \Phi^D(q, t) \end{bmatrix} = 0 \quad (1)$$

$$\dot{\Phi}(\dot{q}, q, t) = \Phi_q \dot{q} - \Phi_t = \begin{bmatrix} 0 \\ -\Phi_t^D \end{bmatrix} \quad (2)$$

$$\ddot{\Phi}(\ddot{q}, \dot{q}, q, t) = -(\Phi_q \ddot{q})_q - 2\Phi_{qt} \dot{q} - \Phi_{tt} = \begin{bmatrix} -(\Phi_q^K \ddot{q})_q \dot{q} \\ -(\Phi_q^D \ddot{q})_q \dot{q} - 2\Phi_{qt}^D \dot{q} - \Phi_{tt}^D \end{bmatrix} \quad (3)$$

The formula identified by number (1) is a non-linear system of algebraic equations whose solution is the vector of generalized coordinates. The formulas identified by number (2) and (3) are a linear systems of algebraic equations whose solution is the vector of generalized velocities and generalized accelerations. A detailed description of the above equations is

given in reference [3]. The vector of generalized coordinates describing the position and orientation of all mechanism links can be expressed as follows:

$$\mathbf{q} = [\mathbf{q}_1^T, \mathbf{q}_2^T, \mathbf{q}_3^T, \mathbf{q}_4^T, \mathbf{q}_5^T, \mathbf{q}_6^T, \mathbf{q}_7^T, \mathbf{q}_8^T, \mathbf{q}_9^T, \mathbf{q}_{10}^T, \mathbf{q}_{11}^T, \mathbf{q}_{12}^T, \mathbf{q}_{13}^T, \mathbf{q}_{14}^T]^T \quad (4)$$

The presented above vector (4) describes the position and orientation of the links of the backhoe excavator equipment system, which is shown in Fig. 1. The position and orientation of a single link is determined by the vector and take the following form:

$$\mathbf{q}_i = [\mathbf{r}_i^T, \alpha_i, \beta_i, \gamma_i]^T \quad (5)$$

where:

- $\mathbf{r}_i^T$  – specifies the position of the origin of the local reference system  $\pi_i$  of the link in global reference system  $\pi_0$ ,
- $\alpha_i, \beta_i, \gamma_i$  – three Euler angles  $\alpha, \beta, \gamma$  which describe orientation of the local reference system  $\pi_i$  of the link relative to global reference system  $\pi_0$ .

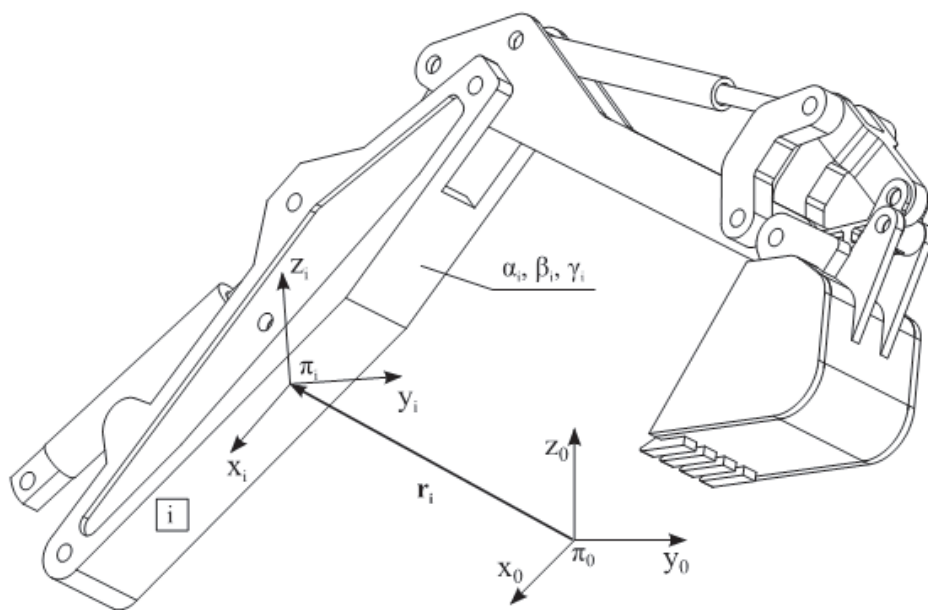


Fig. 1. Backhoe excavator equipment system scheme

The most time consuming step in the kinematic analysis is the calculation of generalized coordinates' vector (4). For this purpose an iterative Newton-Raphson algorithm is most widely used. It allows to determine the approximated values of the roots satisfying the system of equations (1). The Newton-Raphson algorithm was graphically shown in Fig. 2. Vector

function  $\Phi$  (which is the left side of the equation system (1)) could be expanded in Taylor series in the vicinity of point  $q^i$  with an assumption that the norm of vector  $\Delta q_i$  becomes small and the higher-order terms in vector  $\Delta q$  can be neglected:

$$\Phi(q^i + \Delta q) \approx \Phi(q^i) + \frac{\partial \Phi(q^i)}{\partial q_1} \Delta q_1 + \dots + \frac{\partial \Phi(q^i)}{\partial q_N} \Delta q_N = \Phi(q^i) + \Phi_q(q^i) \Delta q \quad (6)$$

Assuming that function  $\Phi$  must satisfy the system of equations (1) at point  $q^{i+1}$  ( $q^i$  is an initial approximation), equation (6) can be compared to zero, under the condition that  $\Delta q = q^{i+1} - q^i$ . Then the equation (6) takes the following form:

$$\Phi(q^i) = \Phi(q^i) + \Phi_q(q^i)(q^{i+1} - q^i) = 0 \quad (7)$$

Which can also be written as:

$$q^{i+1} = q^i + \Phi_q^{-1}(q^i) \Phi(q^i) = 0 \quad (8)$$

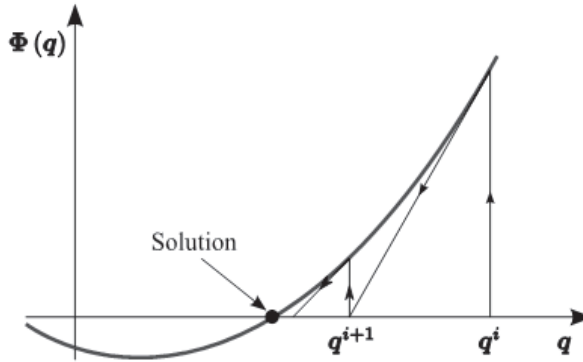


Fig. 2. Graphic presentation of the Newton-Raphson algorithm (only two first steps were shown)

The Newton-Raphson algorithm presented in Fig. 2 is an iterative algorithm, in which a single iteration consists of the following steps:

- Calculation of approximation  $q^{i+1}$  from the formula (8).
- Checking whether the approximation  $q^{i+1}$  satisfies the system of equations (1) with an accuracy of  $\varepsilon$ , i.e. if the condition  $\|\Phi(q^{i+1})\| \leq \varepsilon$  is true.
- If the algorithm in the previous step did not get a solution at a defined number of iterations, then the emergency termination of solution process occurs [4–5].

### 3. Euler angles singularities

In the classical approach to the kinematic analysis of spatial mechanisms, orientation of the particular mechanism links is described by Euler angles. This description, however, has a disadvantage, which is important from the kinematic analysis' point of view [3]. When considering kinematic analysis of the boom separated from the equipment system shown in Fig. 1 boom orientation in space is described by Euler angles in the convention  $z$ - $x$ - $z$ . The global reference system  $\pi_0$  and local reference system  $\pi_1$ , which is connected with boom was defined as shown in Fig. 3. For boom kinematic analysis purposes the following assumptions was made:

- boom is connected to a global reference system  $\pi_0$  with rotational joint in such a way, that it can only perform a rotational movement about an axis  $z_0$ ,
- vector of generalized coordinates of the boom at initialization time has the following coordinates  $\mathbf{q}_1 = [0, 1.78, 0, 0, 0, \pi/2]^T$ ,
- boom relative rotation angle is described by the following relation  $\varphi_1 = t^2 - \frac{\pi}{2}$ ,
- analysis is focused only on obtaining a vector of generalized coordinates of the boom in a defined time span.

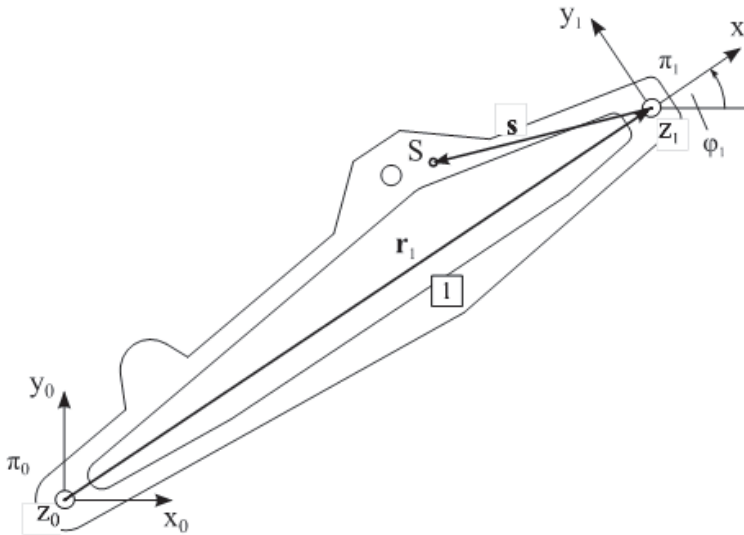


Fig. 3. Boom extracted for kinematic analysis purposes

For calculating the vector of generalized coordinates of a boom the Newton-Raphson algorithm was used. At the first iteration, for the time  $t = 0$  Jacobian matrix is as follows:



$$\Phi_q(q^1) = \begin{bmatrix} -1 & 0 & 0 & -1.78 & 0 & -1.78 \\ 0 & -1 & 0 & 0 & 0 & 0 \\ 0 & 0 & -1 & 0 & 1.78 & 0 \\ 0 & 0 & 0 & 0 & 1 & 0 \\ 0 & 0 & 0 & 0 & 0 & 0 \\ 0 & 0 & 0 & -1 & 0 & -1 \end{bmatrix} \quad (9)$$

Unfortunately, this is a singular matrix because its determinant is equal to 0, and therefore, it cannot be reversed. As a result, an attempt to solve the system of equations (1) finishes with a failure.

The appearance of singularities in the Jacobian matrix is caused by unfavorable adoption of orientation of the reference systems  $\pi_0$  and  $\pi_1$  (in practice it is often required that the  $z$  axes of the local reference systems of links have to be parallel to the  $z$  axis of the global reference system). It is, therefore, apparent that the system of Euler angles in  $z$ - $x$ - $z$  convention is not clearly specified in a situation where the axes of the global and the local reference system are parallel. In this position, the  $xy$  planes of the local and the global reference system are parallel, which means that the positioning of the line of nodes is not clearly defined and, therefore, the precession angle  $\alpha$  is also not uniquely defined. For the same reason it is impossible to uniquely specify intrinsic rotation angle  $\gamma$  [3].

#### 4. Quaternions

One of the solutions of the Jacobian matrix degeneration problem is to replace Euler angles with quaternions. Quaternions are an algebraic structure that extends complex numbers. Quaternions were defined by Hamilton in 1853 in the following form [8]:

$$q_{\mathbb{H}} = s + ia + jb + kc \quad s, a, b, c \in \mathbb{R} \quad (10)$$

where:

$$i^2 = j^2 = k^2 = ijk = -1 \quad (11)$$

$$ij = k, \quad jk = i, \quad ki = j, \quad ji = -k, \quad kj = -i, \quad ik = -j \quad (12)$$

From the kinematic analysis' point of view their algebraic form is more useful, which can be written as follows:

$$q_{\mathbb{H}} = [s, \mathbf{v}] \quad s \in \mathbb{R}, \mathbf{v} \in \mathbb{R}^3 \quad (13)$$

$$q_{\mathbb{H}} = [s, x\mathbf{i}, y\mathbf{j}, z\mathbf{k}] \quad s, x, y, z \in \mathbb{R} \quad (14)$$

Elements of a quaternion which describe rotation of angle  $\theta$  of the mechanism link around vector  $\mathbf{a}$  can be expressed as follows:

$$q_{\text{H}} = \begin{bmatrix} \cos\left(\frac{\theta}{2}\right) \\ \sin\left(\frac{\theta}{2}\right) \cdot a_x \\ \sin\left(\frac{\theta}{2}\right) \cdot a_y \\ \sin\left(\frac{\theta}{2}\right) \cdot a_z \end{bmatrix} \quad (15)$$

As we know, changing the orientation of the mechanism link is the same as changing of orientation of any point which is connected to the link. Thus, if for boom shown in Fig. 3 we determine point  $S$ , whose position in reference system  $\pi_1$  is defined by vector  $\mathbf{s}$ , then describing orientation of vector  $\mathbf{s}$  will be inconsistent with describing the orientation of a boom. For example, rotation of angle  $\varphi_1$  of boom from Fig. 3 around vector  $\mathbf{a}_0$ , which was defined in global reference system  $\pi_0$ , could be written as:

$$\mathbf{s}' = q_{\text{H},1} \mathbf{s} q_{\text{H},1}^{-1} \quad (16)$$

where:

$$q_{\text{H}} = \begin{bmatrix} \cos\left(\frac{\varphi_1}{2}\right) \\ \sin\left(\frac{\varphi_1}{2}\right) \cdot \mathbf{a}_0 \end{bmatrix}, \quad \mathbf{a}_0 = \begin{bmatrix} 0 \\ 0 \\ 1 \end{bmatrix} \quad (17)$$

Like shown previously the kinematic analysis of boom shown in Fig. 3 requires determining Jacobian Matrix for time  $t = 0$ , but orientation of boom will be described with quaternions. Elements of the Jacobian matrix after changing the description of boom orientation will have the following values:

$$\Phi_q(q^1) = \begin{bmatrix} -1 & 0 & 0 & 0 & 0 & -1.78 \\ 0 & -1 & 0 & 0 & 0 & 0 \\ 0 & 0 & -1 & 1.78 & 0 & 0 \\ 0 & 0 & 0 & 1 & 0 & 0 \\ 0 & 0 & 0 & 0 & 1 & 0 \\ 0 & 0 & 0 & 0 & 0 & -1 \end{bmatrix} \quad (19)$$

Values of the above matrix determinant equal 1, therefore it is not a singular matrix and, as a consequence, the Newton-Raphson converges. The use of quaternions in this example

allowed to avoid the singularities from the Jacobian matrix and also to determine a generalized coordinates vector in each time step.

## 5. Conclusions

The use of the Euler angles to describe the orientation of the mechanism links in space, can give rise to singularities in the Jacobian matrix. It is often caused by the fact that the requirements for orientation of links' local reference systems in the global reference system are in conflict with the requirements which have to be fulfilled when Euler angles are used. The use of quaternions for orientation description eliminates the risk that the mentioned singularities will appear and thus increases numerical stability of the Newton-Raphson algorithm. For better consistency of inverse kinematics the algorithm it is good to encapsulate translations and rotations of mechanism links into a unified representation. This can be achieved by using dual quaternions and Clifford algebra to solve the inverse kinematics problem.

## References

- [1] Sariyildiz E., Temeltas H., *Solution of inverse kinematic problem for serial robot using quaternions*, Proceedings of the 2009 IEEE International Conference on Mechatronics and Automation, 26-31.
- [2] Aydin Y., Kucuk S., *Quaternion based inverse kinematics for industrial robot manipulators with Euler wrist*, Proceedings of the 2003 IEEE 3<sup>rd</sup> International Conference on Mechatronics, 581-583.
- [3] Wojtyra M., Frączek J., *Kinematyka układów wieloczłonowych*, Wydawnictwa Naukowo-Techniczne, Warszawa 2008.
- [4] Shabana A.A., *Computational Dynamics 3<sup>rd</sup>*, John Wiley & Sons Ltd., United Kingdom 2010.
- [5] Haug E.J., *Computer aided kinematics and dynamics of mechanical systems. Volume I: Basic methods*, Allyn and Bacon, Massachusetts 1989.
- [6] Nikravesh P.E., *Computer aided analysis of mechanical systems*, Prentice-Hall Inc., New Jersey 1988.
- [8] Hamilton W.R., *Lectures on quaternions*, Hodges and Smith, Dublin 1853.

WOJCIECH CZYŻYCKI\*

## MODELING OF HEAT FLOW THROUGH MULTILAYER INTERNAL SUPPORTS OF CRYOGENIC VESSELS

---

### MODELOWANIE PRZEPIYU CIEPŁA PRZEZ WIELOWARSTWOWE PODPORY MIĘDZYPLASZCZOWE W ZBIORNIKACH KRIOGENICZNYCH

#### Abstract

The article presents the issue of heat flow through internal supports of double-walled cryogenic vessels. The influence of the thermal resistance at the contact plane between supports and vessel materials is discussed. A simulation of heat flow through the support multilayer made of plastic is presented. The simulation takes into account the influence of temperature and local contact pressure on the thermal resistance.

*Keywords: cryogenic, double-walled vessel, internal support, contact thermal resistance*

#### Streszczenie

W artykule przedstawiono zagadnienie przepływu ciepła przez wewnętrzne podpory dwupłaszczyznowych zbiorników kriogenicznych. Omówiono wpływ oporu cieplnego w miejscu styku materiałów podpór i zbiornika. Przedstawiono symulację przepływu ciepła przez podpory wielowarstwowe wykonane z tworzyw sztucznych. W symulacji uwzględniono wpływ temperatury i lokalnej wartości nacisku powierzchniowego na opór cieplny.

*Słowa kluczowe: kriogenika, zbiornik dwupłaszczyznowy, podpory wewnętrzne, kontaktowy opór cieplny*

---

\* Ph.D. Eng. Wojciech Czyżycki, Institute of Applied Informatics, Faculty of Mechanical Engineering, Cracow University of Technology.

## 1. Introduction

Cryogenic vessels have been widely used in the industry and medicine for a long time. Currently, due to the increased interest in the liquefied natural gas LNG, an interest in modern constructions of both fixed and mobile tanks is growing. In the Institute of Applied Informatics, Faculty of Mechanical Engineering at the Cracow University of Technology in cooperation with Works of Chemical Equipment CHEMET SA a number of studies on double-walled cryogenic vessels with vacuum insulation was conducted. Figure 1 shows one of these structures – a tank container for LNG transportation and storage. As part of this work, series of articles on the analysis of heat flow through the insulation fibre [3, 5], as well as on the inner tank mounting structure in the outer tank [4–7] were published. In the further part of the article internal tank mounting elements are referred to as internal supports. This article focuses on the possibility of improving the thermal insulation of internal supports by the use of a multi-layer structure.

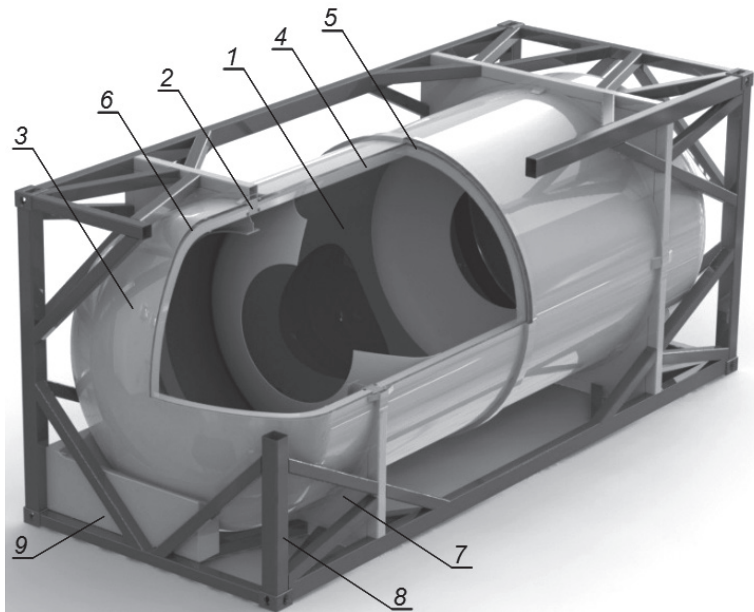


Fig. 1. Model of the LNG tank container for LNG transportation and storage [3]: 1 – inner tank, 2 – inner supports made of plastic materials, 3 – outer tank, 4 – insulation, 5 – radiation shields, 6 – the vacuum, 7 – outer supports, 8 – container frame, 9 – fittings

In general, the amount of heat inflowing the cryogenic tank through internal supports depends on:

- a height and cross-sectional area of the internal supports,
- a thermal conductivity of the internal support material,
- a contact thermal conductivity between internal supports and walls of the tank.

Issues associated with selection of materials for internal supports, their dimensions, and a cross-sectional shape of the supports are widely discussed in the Katarzyna Głowik-Łazarczyk doctoral dissertation [7]. However, issues related to the use of the contact thermal conductivity phenomenon and multi-layer support structures have not been developed in that work.

## 2. Heat flow through supports

If a permanent contact between the internal supports and the walls of the tank and between the individual layers of the multi-layer is assumed, as well as thermal insulation of the side walls with the use of radiation shields and vacuum insulation, some simplifications in the heat flow model can be made. Considering the typical heat transfer mechanisms such as conduction, convection and radiation, in this case convection and radiation are insignificant.

### 2.1. Conductive heat transfer

The basic, essential for the internal support, heat flow method is the conduction described by the Fourier equation. Due to the large temperature differences and an analysis of a three-dimensional model, the full form of the equation [1, 2] is assumed:

$$\mathbf{q} = -\lambda \nabla T \quad (1)$$

where:

- $\mathbf{q}$  – the local heat flux density,
- $\lambda$  – the material's conductivity,
- $\nabla T$  – the temperature gradient.

### 2.2. Contact conductivity

The heat flow through the element consisting of two parts of the same material causes a temperature difference at the contact surface. The difference does not exist if there is no parting plane. This temperature difference is a result of the contact thermal conductivity phenomenon (or its inverse which is the contact thermal resistance). The contact conductance of a single gap decreases with the decrease of pressure forces, and it is also dependent on the hardness of the contact pair materials and the medium which fills the gap in the contact surface. A general relationship presented by Furmański and others [2] has the following form:

$$R_c = \left( \left[ 1.25 \cdot k_s \cdot \frac{m}{\sigma} \left( \frac{P}{H} \right)^{0.95} + \frac{k_g}{Y+M} \right] \cdot A_a \right)^{-1} \quad (2)$$

where:

- $k_s$  – harmonic mean of the thermal conductivity of the two contacting bodies,
- $m$  – total contact area,

- $\sigma$  – effective contact surface of solids,
- $P$  – contact pressure,
- $H$  – hardness of the softer of the materials in contact,
- $k_g$  – thermal conductivity of the medium filling the gap,
- $\bar{Y}$  – the distance between the surface of solids in the cross-section slot,
- $M$  – parameter characterising the gas in the gap in terms of its density.

The equation (2) is difficult in practical use. Part of the parameters set out in equation (2) as  $k_s$ ,  $k_g$ ,  $H$ ,  $M$  varies with temperature changes. Thus, due to large temperature differences which occur in the cryogenic constructions, these changes must also be taken into account. The article considers a case based on the structures of polyamide supports cooperating with shells made of stainless steel and carbon steel. Because of the similarity of the structure to simulation studies of the multi-layer internal supports, contact conductivity coefficients determined in papers [5 and 7] are applied. Figure 2 shows dependence of the contact conductivity on the contact surface average temperature.

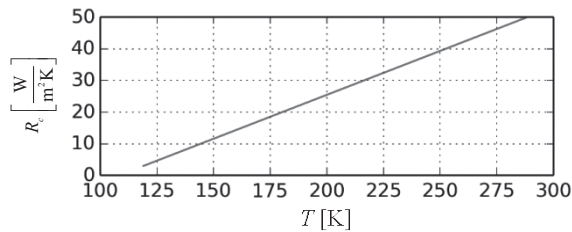


Fig. 2. Dependence of the contact conductivity against the average temperature of the contact surface determined on the basis of [5, 7]

### 3. Geometrical model

Due to the weakening of the structural stability of the support caused by division into multiple layers, it was assumed, that the shape of the support will be simple, with a constant section. As demonstrated in [7], in the case of such supports, the difference between different shapes may reach 4%, and a rectangular cross section with an aspect ratio of 1:4 is the most preferred one. This shape was adopted to study the multilayer supports.

Dimensions of the support (Fig. 3) were set to  $50 \times 200 \times 100$  mm ( $W \times L \times H$ ) as stated in [7]. The minimum thickness of the polyamide layer was set to 4.75 mm, the layers were separated from each other by the stainless steel 0.25 mm thick plates. In the version with a maximum number of layers (15), a monolithic block with a thickness of 25 mm is left. The block is designed to hide the heads of the bolts.

At the beginning of the heat flow analysis the following assumptions were made:

- cryogenic medium: liquid nitrogen,
- the temperature of the cryogenic medium in the container 73 K,
- the ambient temperature of 293 K,
- cryogenic tank material: stainless steel 1.4301,

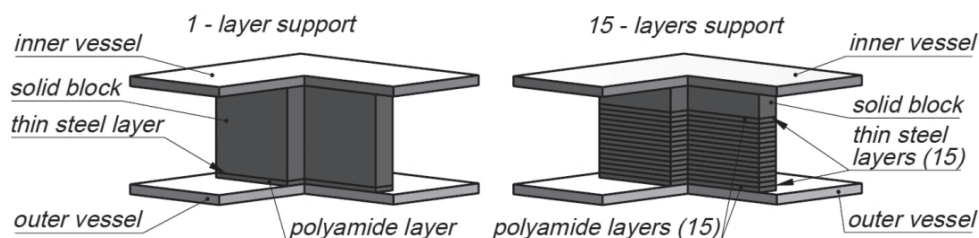


Fig. 3. Simplified simulation model to study the multi-layer support (section without quarter). On the left model with a single layer, on the right model with a maximum number of layers – 15

- shielding container material: constructional steel P355NL1,
- internal support material: PA6,
- omitted details of attachment of the support to the reservoir,
  - omitted thin steel spacers in the FEM model, replaced by the appropriately defined contact surface.

#### 4. FEM model and simulations

FEM model was prepared in the Abaqus CAE system. A fully coupled thermal-stress analysis was chosen. Elements of type C3D8T (*an 8-node thermally coupled-hexadron-brick, trilinear displacement and temperature*) were used.

A simplified model is characterized by the symmetry in two directions, also the load and the boundary conditions are symmetrical in these directions. Therefore, the analysis was carried out using a quarter of an appropriate model. On the section walls were inserted the corresponding symmetry conditions. The outer tank was fixed on the sides and loaded from the outside by the atmospheric pressure. The inner wall of the inner tank was loaded by the internal pressure and the force coming from the weight of the load. These loads correspond to the real load values of the supports under typical operating conditions. Referring to the thermal boundary conditions, the following assumptions were made [7]:

- on the walls in contact with the cryogenic liquid on the natural convection of transmittance values  $337 \text{ W}/(\text{m}^2 \text{ K})$  at a constant fluid temperature  $73 \text{ K}$  is presented,
- on the walls in contact with the air the natural convection of with a transmittance values  $8.98 \text{ W}/(\text{m}^2 \text{ K})$  at a constant ambient temperature of  $293 \text{ K}$  is presented,
- adopted vacuum insulation, heat exchange by radiation and convection is omitted.

Between the layers of the inner support, mechanical and thermal contact was defined. Coefficient of contact conductivity was made dependent on the temperature and contact pressure (Abaqus options: *Surface to surface contact, thermal conductance, Use only pressure-dependency data, temperature-dependent Use date*). The temperature dependence was created using the data shown in Fig. 2. It was also assumed that the full value of the contact conductance is achieved for contact pressure of  $15 \text{ MPa}$ , and it disappears in the absence of contact pressure. Spatial distributions of temperature for 1-layer and 15-layer models are shown in Fig. 4.



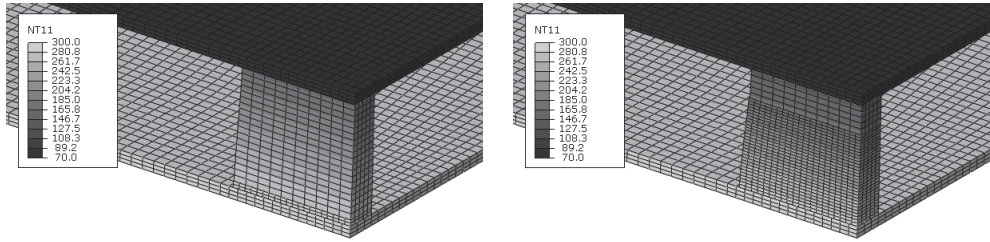


Fig. 4. Spatial distribution of temperature (*NT11* parameter) on 1-layer support (left) and 15-layer support (right)

It was noted that an additional advantage of the multi-layer supports is a more uniform distribution of contact pressures on the support pillars and the max value decreases when the layer number is increasing (Fig. 5a and b). This fact allows to reduce their cross sections. Therefore, a reduced support version was created. The support length was decreased from 200 mm to 160 mm. This version 15 lay min for calculation was named.

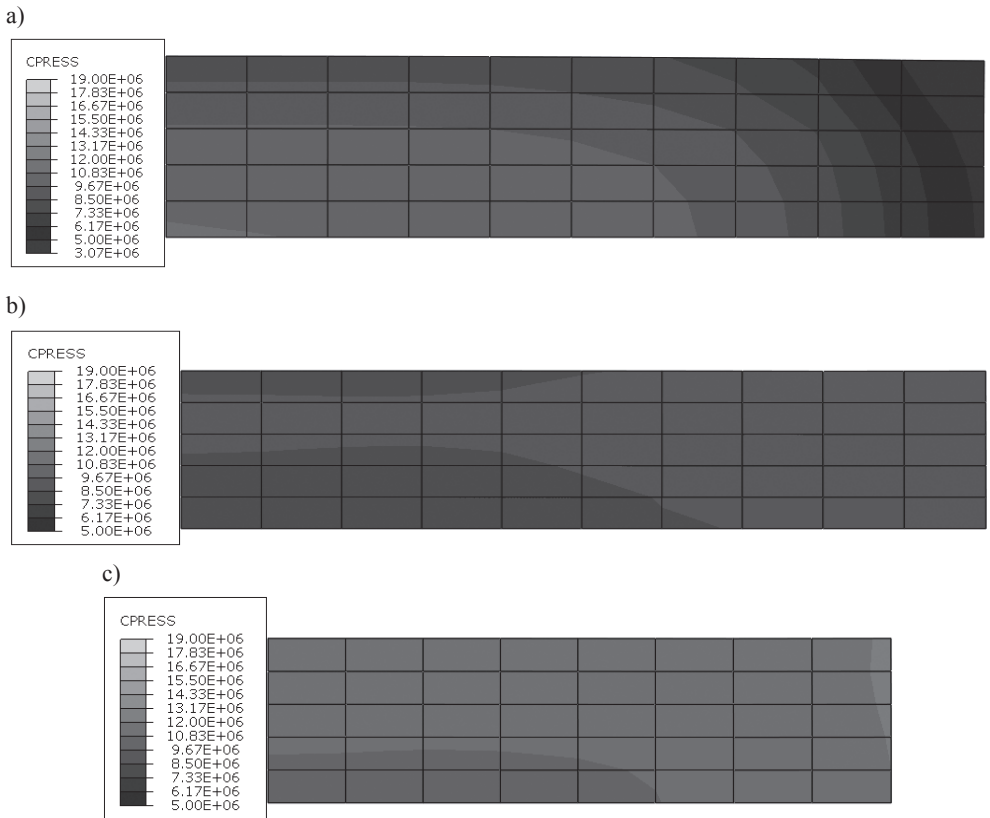


Fig. 5. Contact pressure distribution [Pa]: a) 1 layer version, b) 15-layers – before support reduction, c) 15-layers-min –after support reduction

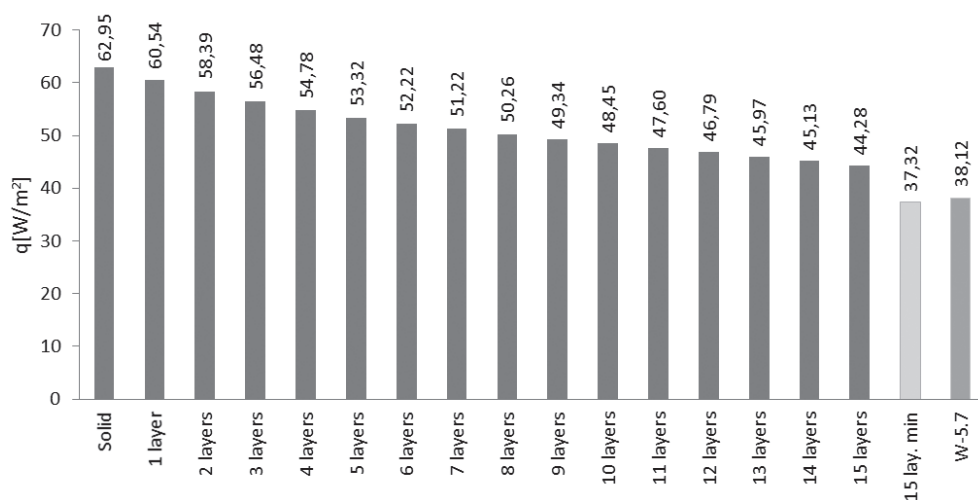


Fig. 6. Heat flux comparison for various number of supports: from *solid* to *15 layers*. Item *15 lay. min* – 15 layer support with reduced length. Item W-5.7 represents a solid support with holes analysed in work [7]

After performing simulations in the Abaqus CAE system, the average values of heat flux on the same parts of the outer wall of the external tank were calculated. The results obtained for both solid and the multi-layered supports are summarized in Fig. 6. Furthermore, the average value of the heat flux obtained on an identical simulation model for the best case presented in [7] (named W-5.7), was added.

The best result was achieved with the largest number of layers, equal to 15. This allows reduction in heat flux of about 30%. It can be seen that the improvement is significant, although it is slightly less than achieved for the best variant in [7], which was 38%. In the case of reduced support, the heat flux decreased to 37.32 W/m<sup>2</sup>, which is almost the same value as for W-5.7, and the maximum contact pressure increased to the value of 16.9 MPa (Fig. 5c), which is still less than the maximum value for the W-5.7 variant (20.5 MPa) [7].

## 5. Conclusion

This paper presents a model of a multi-layer polyamide-metal support designed for supporting an internal tank of a double-walled cryogenic container. These structures are developed by Chemet SA in scientific cooperation with the Institute of Applied Informatics at Cracow University of Technology. As part of the work, strength and thermal calculations of the support were performed. The values of the heat flux between the inner and the outer tank for different support variants were determined. The results were compared to those obtained with monolithic supports with holes as described in [7].

The proposed support is characterized by a similar thermal insulation as a monolithic support with holes. However, the presented solution has several advantages, including a more uniform distribution of contact pressures on the outer surfaces and the possibility of creating a structure comprising different materials in different layers. The latter feature is particularly important because it allows the designer to apply a layer of more expensive material, which has lower thermal conductivity than the polyamide (PVDF, PEEK), without a substantial increase of the total support cost. Also the pressure distribution is more advantageous, which allows reduction of the support cross-section. Thus, it is possible to further improve its insulating properties.

A significant problem in the work carried out on the construction of cryogenic tanks was relatively low availability of material parameters under cryogenic conditions, especially contact thermal conductivity coefficients. Therefore, further studies are needed in order to determine properties of newly constructed structure supports more accurately.

## References

- [1] Flynn T. M., *Cryogenic Engineering*, Marcel Dekker, USA 2005.
- [2] Furmański P., Wiśniewski T., Banaszek J., *Thermal Contact Resistance and other Thermal Phenomena at Solid-Solid Interface*, Institute of Heat Engineering – Warsaw University of Technology, Warsaw 2008.
- [3] Lisowski E., Czyżycki W., *Transport and storage of LNG in container tanks*, Journal of KONES, 18, 3, 2011, 193-201.
- [4] Lisowski E., Czyżycki W., Łazarczyk K., *Simulation and experimental research of internal supports in mobile cryogenic tanks*, Technical Transactions, 8, Wydawnictwo PK, 2010.
- [5] Lisowski E., Filo G., Czyżycki W., *Computer Aided Design in Mechanical Engineering*, [in:] Ch. 4, *Transport of Liquid Natural Gas by mobile tank container*, Bergen University College, 2009.
- [6] Lisowski E., Łazarczyk K., *Badania stanowiskowe nowej konstrukcji kontenera do przewozu płynów kriogenicznych, szczególnie ciekłego azotu i LNG*, Przegląd Mechaniczny, 4, 2010.
- [7] Łazarczyk K., *Poprawa termoizolacyjności zbiorników kriogenicznych*, PhD Thesis, Politechnika Krakowska, Kraków 2012.

TOMASZ DĘBIŃSKI, MARCIN HOJNY, DARIUSZ JĘDRZEJCZYK\*

## STEREOSCOPIC VISUALIZATION FOR MODEL OF DEFORMATION OF STEELS WITH MUSHY ZONE

### WIZUALIZACJA STEREOSKOPOWA MODELU ODKSZTAŁCANIA STALI W STANIE PÓLCIEKŁYM

#### Abstract

The paper deals with visualization of results for simulation of a deformation process of a sample with a mushy zone. The numerical model consists of three basic subsystems: the mechanical, thermal and density changes parts. These describe both solid and semisolid deformation states. Taking into consideration their specific distribution graphical visualization is very helpful for understanding the course of the process. Moreover, a three-dimensional presentation is applied in various fields, ranging from medical imaging systems to technological processes assistance to scientific visualizations and entertainment. The stereoscopic imaging technique is still being developed. It is based on the idea of showing each eye the same scene from a bit different perspective. As an effect the illusion of depth is created due to the way the two images are interpreted by the human brain. Stereoscopy is not a new concept, but in the past few years a significant increase in the interest in this method of visualization could be observed. It is caused by computer and audio-visual technology development. In the paper several techniques of creating stereoscopic images are presented together with their physical bases and devices providing such functionality. The use of projection equipment and possibilities of its application to visualization of semi-solid steel deformation is discussed. Apart from that a description of an implementation of OpenGL specification for stereoscopic presentation of computer simulation results is provided.

*Keywords: computer simulation, graphical user interface, stereoscopic visualization*

#### Streszczenie

W artykule przedstawiono użycie techniki stereoskopowej do wizualizacji wyników symulacji procesu nagrzewania i odkształcania stali ze strefą półciekłą. Model numeryczny składa się z trzech oddzielnych podsystemów: mechanicznego, termicznego i przewidyującego zmiany gęstości opisujących odkształcenie strefy stałej i półciekłej. Biorąc pod uwagę specyficzne rozmieszczenie tych stref, wizualizacja jest bardzo pomocna w zrozumieniu procesu. Obrazowanie trójwymiarowe jest szeroko stosowane, począwszy do medycznych systemów obrazowania, poprzez rozrywkę na wizualizacjach naukowych kończąc. Istnieje wiele technik tworzenia obrazów stereoskopowych, ale wszystkie prowadzą do przedstawienia obrazu z nieco innej perspektywy dla każdego oka. Efekt wywołania złudzenia głębi uzyskuje się dzięki interpretacji przez mózg odpowiednio przygotowanych obrazów. Stereoscopia nie jest techniką nową, jednak w okresie ostatnich kilku lat można zaobserwować kolejny wzrost zainteresowania tą techniką obrazowania dzięki rozwojowi technologii komputerowej i audiowizualnej. W artykule opisano kilka technik tworzenia obrazów stereoskopowych wraz z podstawami fizycznymi oraz przykładowymi urządzeniami umożliwiającymi prezentowanie scen stereoskopowych. Omówiono wykorzystywany sprzęt projekcyjny oraz możliwości zastosowania. Ostatecznie przedstawiono sposób implementacji z wykorzystaniem OpenGL oraz stereoskopową prezentację przykładowych wyników symulacji komputerowej.

*Słowa kluczowe: symulacja komputerowa, interfejs użytkownika, wizualizacja stereoskopowa*

\* Ph.D. Eng. Tomasz Dębiński, Ph.D. Eng. Marcin Hojny, Ph.D. Eng. Dariusz Jędrzejczyk, AGH University of Science and Technology.

## 1. Introduction

Despite a wide usage of computer graphics and a three-dimensional graphics presentation, the three-dimensional approach was used in a flat screen visualization.

In the recent years the techniques of generating and presenting computer graphics have seen an increasing interest in stereoscopic visualization technique.

The solution is not new but modern technology enables its wider use in various areas of life. The general rule in stereoscopic display is to visualize different images for both eyes.

On the market there are many available solutions [1]. Originally simple color filters and contemporary linear or circular polarizers are used.

Recently a technology widely used in projection screens (Wavelength Multiplex Imaging WMI, Dolby 3D Digital Cinema) is based on sending different color spectrum to each eye so that different images are combined into one. Such a composed screen can be seen by using appropriate glasses. Simultaneously a developed autostereoscopic display technology does not require use of special glasses in order to achieve the stereoscopic effect [1].

## 2. Stereo rendering techniques

Stereoscopic technology used active and passive projection. In case of active audience using snapshot LCD glasses synchronized with the alternating, images are displayed to the left and right eye [3].

At the time of display for the left eye the right eye shutter is closed and vice versa.

This solution requires a high refresh rate because of the flickering effect. In case of the passive one, polarized light is used and the flickering effect does not occur. Subscribers use glasses containing two opposite polarized filters. One for the left and one for the right eye. The light in each eye is properly polarized and can only pass through a correct filter.

This principle is used to send different images to the left and right eye. In this way, a depth perception can be created. Because the human eye is not sensitive to the polarization of light, changing the polarization does not affect image visibility.

In practice, the system uses linear and circular polarization. If the light is polarized in one of the mutually perpendicular directions it is referred to as the linear polarization. One disadvantage of this projection type is the loss of information necessary for stereoscopic projection in the case of the observer's head deflection.

This is due to incompatibility of polarization glasses and the projector. However this technology is popular due to its low costs in situations where the possibility of head tilting is limited.

In the case of circular polarization the viewer can bend its head and change the viewing angle relative to the displayed stereoscopic images. This is possible because the light is polarized in one direction. Figure 1 shows that even when the filter wheel is rotated the light passes through.

In the case where a stereoscopic image is obtained by using two flat images the parallax phenomenon is used. If the observed object is outside the plane of the projection image for the left eye it is on the left side and for the right eye it is to the right side. The distance between the left and right is called a positive image of a horizontal parallax. If the object is in

front of the plane the projection for the left eye image is displayed on the right side and the right-eye image to the left. This is known as a horizontal negative parallax. The creation of an image of two points on a flat screen is more complex to commonly used approaches [2, 5, 6].

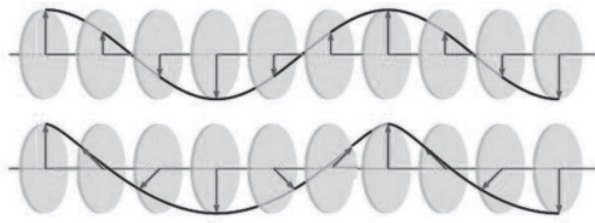


Fig. 1. Comparison between linear and circular filters

**Toe-in** – this approach is used because of the simplicity of the symmetrical projection and there are no special requirements to the used cameras. The cameras are not only shifted relatively to each other, but also rotated and fixed at a common point. That creates a vertical parallax, increasing with distance from the center of the image. This leads to a discomfort for the observer after a long time. Despite the disadvantages of this method it is still used because of an easier use of the cameras in parallel where it is necessary to trim and crop (Fig. 2) [6].

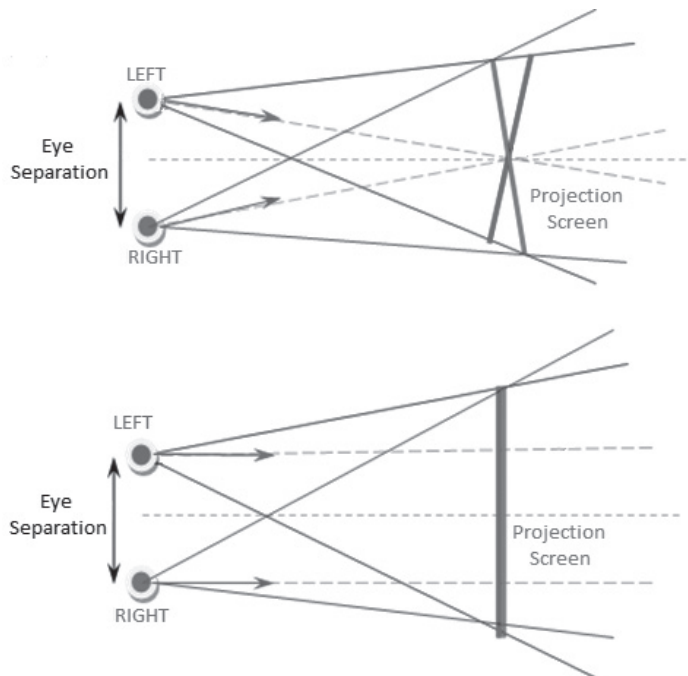


Fig. 2. Diagram of the toe-in and the off-axis (below) methods

**Off-axis** – this is a valid way to obtain stereo images which does not cause a vertical parallax. It is used not only for the horizontal movement but also the camera projection matrix is modified which gives an asymmetric projection result [6].

### 3. Stereoscopic viewing system

The construction of the software to the stereoscopic visualization of results was performed and tested using a system comprising two Gemini Barco IQ R500 LCD projectors. The system provides a modular design enabling the installation of mechanical floor or ceiling cracks first (Fig. 3).



Fig. 3. The modular design of the system based on Barco Gemini

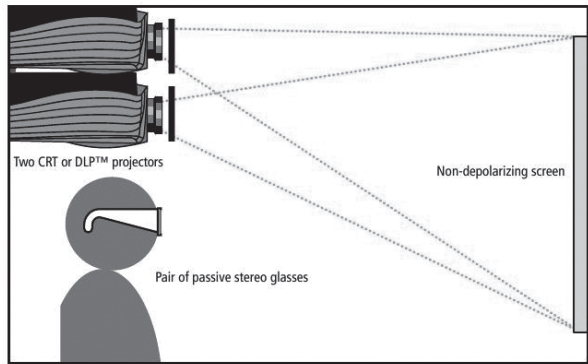


Fig. 4. Chart of the display system

It consists of two projectors with polarizing filters and a screen which does not depolarize light. A schematic of the applied solution was presented on Fig. 4.

### 4. Implementations

Implementations and tests of stereoscopic visualization were performed using OpenGL with nVidia Quad-buffed graphics card (Quadro FX 1500) [7]. Below the perspective projection and projection parameters evaluation are presented (Fig. 5) [8].

For correct setting of perspective parameters, calculation of new left, right, top, bottom parameters is needed.

$$\text{clip}_{\text{near}} = \text{dist} + \text{zero}_{\text{plane}} - \text{near} \quad (1)$$

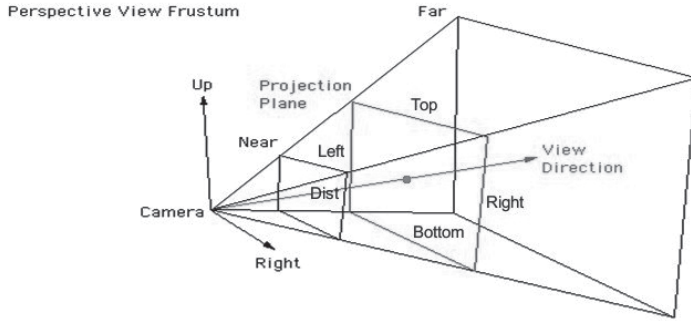


Fig. 5. The perspective projection diagram for one eye's subfield

$$\text{clip}_{\text{far}} = \text{dist} + \text{zero}_{\text{plane}} - \text{far} \quad (2)$$

$$\text{noverd} = \frac{\text{clip}_{\text{near}}}{\text{dist}} \quad (3)$$

$$\text{top}_w = \text{noverd} \cdot \frac{\text{top} - \text{bottom}}{2} \quad (4)$$

$$\text{bottom}_w = -\text{top}_w \quad (5)$$

$$\text{right}_w = \text{noverd} \cdot \left( \left( \frac{\text{right} - \text{left}}{2} \right) - \text{eye} \right) \quad (6)$$

$$\text{left}_w = \text{noverd} \cdot \left( - \left( \frac{\text{right} - \text{left}}{2} \right) - \text{eye} \right) \quad (7)$$

OpenGL function that sets perspective is `glFrustum (...)` [10], the parameters of the view matrix are shown by equation (8).

$$\begin{bmatrix} \frac{2Z_n}{R-L} & 0 & \frac{R+L}{R-L} & 0 \\ 0 & \frac{2Z_n}{T-B} & \frac{T+B}{T-B} & 0 \\ 0 & 0 & -\left( \frac{Z_f + Z_n}{Z_f - Z_n} \right) & -\left( \frac{2Z_f Z_n}{Z_f - Z_n} \right) \\ 0 & 0 & -1 & 0 \end{bmatrix} \quad (8)$$



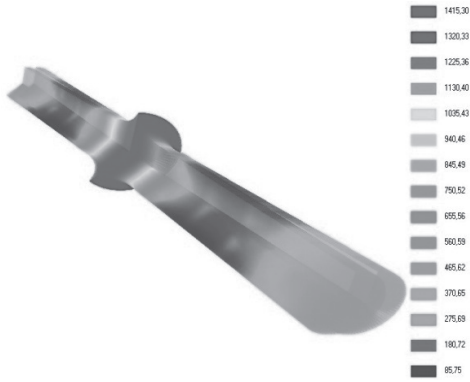


Fig. 6. Temperature (stereo)

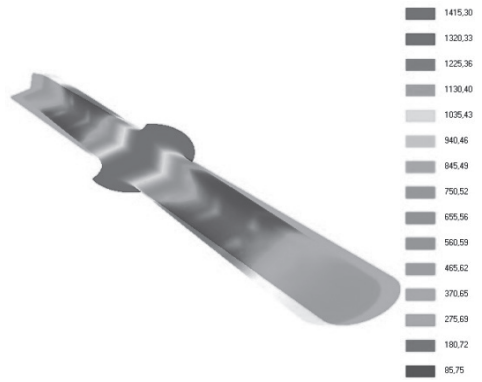


Fig. 7. Temperature (anaglyph)



Fig. 8. Radial velocity (stereo)

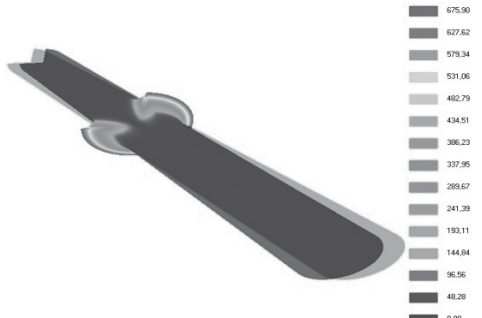


Fig. 9. Radial velocity (anaglyph)

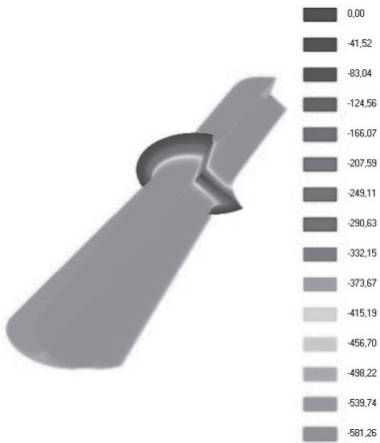


Fig. 10. Axial velocity (stereo)

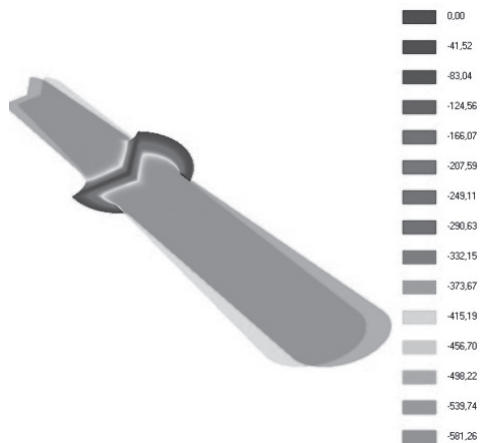


Fig. 11. Axial velocity (anaglyph)

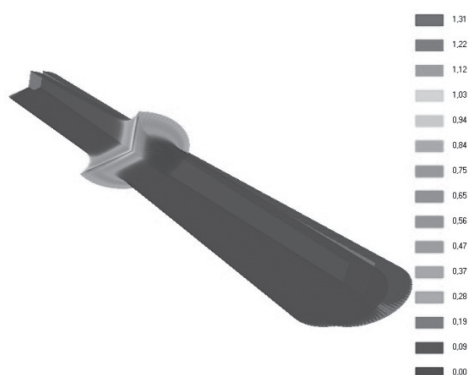


Fig. 12. Intensity of strain (stereo)

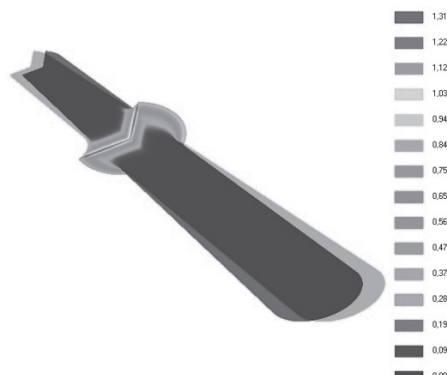


Fig. 13. Intensity of strain (anaglyph)

Where the *right-left* ( $R, L$ ) and the *top-bottom* ( $T, B$ ) variables are the coordinates of the clipping rectangle (projection screen) – the coordinate range, in the plane of zero parallax setting, which will be displayed on the screen. The ratio between (*right-left*) and (*top-bottom*) should equal the aspect ratio of the display. The *near* ( $Z_n$ ) and *far* ( $Z_f$ ) parameters are the z-coordinates values of the clipping planes with *zero plane* parameters as zero plane of zero parallax setting. The next most important parameter is *dist* – the distance from the center of projection to the plane of zero parallax with the *eye* value representing half of the eye separation. The eye obtains a positive value for the right eye subfield and a negative one for the left eye subfield. The projection is in the direction of the negative z-axis.

The discussed algorithms were used in visualization of the calculations results for the heating and deformation process with the semi-zone. Because the process is difficult and complex, both technically and numerically, thus presenting the visualization technique will facilitate the interpretation of the results of calculations. The examples of results on the following pictures from 6 to 13 in both techniques (quad buffer, anaglyph) were presented.

#### 4. Conclusions

In this article the problem of stereoscopic projection is presented with the most frequently used techniques and their advantages and disadvantages. The implementation techniques, modifications in OpenGL projection matrix are also presented. The stereoscopic visualization hardware and its applicability is tested. The best way for stereoscopic visualization is to use a dedicated hardware with a quad buffer, as the anaglyph presentation can cause incorrect display of colors.

Finally, the application for visualization of simulation for the deformation process of a sample in a semi-liquid state was presented. This type of presentation allows a better reception for the observers by making it easy to interpret results.

*The project has been supported by the Polish National Science Centre, Decision number: DEC-2011/03/D/ST8/04041.*

## References

- [1] <http://www.barco.com> (online: 15.12.2014).
- [2] *3D Revolution Productions*, <http://www.the3drevolution.com/3dscreen.html> (online: 15.12.2014).
- [3] Grasberger H.: *Introduction to stereo rendering*, Institute of Computer Graphics Vienna University of Technology, Vienna 2008.
- [4] Holliman S., Dodgson N., Favalora G., Pockett L., *Three-Dimensional Displays: A Review and Applications Analysis*, Ieee Transactions on Broadcasting, Vol. 57, No. 2, June 2011.
- [5] *OpenGL*, <http://www.songho.ca/opengl> (online: 15.12.2014).
- [6] *Information related to stereographics*, <http://paulbourke.net/stereographics> (online: 15.12.2014).
- [7] NVidia documentation manual, [www.nvidia.com](http://www.nvidia.com) (online: 15.12.2014).
- [8] Hawkins K., Astie D., OpenGL. ProgramowanieGier, Helion, 2003.
- [9] *Rendering 3D Anaglyph in OpenGL*, <http://www.animesh.me/2011/05/rendering-3d-anaglyph-in-opengl.html> (online: 15.12.2014).
- [10] *OpenGL*, <http://www.opengl.org> (online: 15.12.2014).

MARIUSZ DOMAGAŁA\*

## MODELLING OF DIRECT ACTING RELIEF VALVE USING CFD-FSI SIMULATION

---

### MODELOWANIE ZAWORÓW PRZELEWOWYCH BEZPOŚREDNIEGO DZIAŁANIA PRZY WYKORZYSTANIU SYMULACJI CFD-FSI

#### Abstract

This paper presents an attempt of using new capabilities of CFD tools in field of fluid-structure interaction simulation, which is called “immersed solids”. This techniques treats solids as objects immersed into fluid domain which moves along with the fluid. This paper presents comparison of selected CFD results of traditional approach and “immersed solids” technique on example of direct acting relief valve.

*Keywords: CFD, FSI, direct acting relief valve*

#### Streszczenie

W artykule przedstawiono wykorzystanie nowych możliwości modelowania CFD w zakresie oddziaływania cieczy na ciała stałe przy wykorzystaniu techniki *immersed solids*. Na przykładzie zaworu przelewowego bezpośredniego działania przedstawiono kilka wybranych wyników symulacji CFD i porównanie z tradycyjnym podejściem w modelowaniu CFD zaworów hydraulicznych.

*Słowa kluczowe: analiza CFD, analiza FSI, zawór przelewowy*

---

\* Ph.D. Eng. Mariusz Domagała, Institute of Applied Informatics, Faculty of Mechanical Engineering, Cracow University of Technology.

## 1. Introduction

Modelling of hydraulic components is not straightforward, even using today's high performance computer CAE systems and associated CFD tools. For example, fluid flow through the channels introduces many nonlinearities and other complicated behaviors. Also, for the case of direct acting relief valves used in some hydraulic systems, there are challenges despite the ostensible simplicity of such problems. The main aim of such valves is to protect the hydraulic system against excessive increase of pressure in the hydraulic system. In the simplest case the direct acting relief valve consists of a lift component and a spring which determines the opening pressure and controls flow through the valve. But even in case of such simple a structure there is a necessity for modeling dynamics of the valve. One of the factors that should be included in the of relief valves is flow forces; and this not an easy task [1]. During last years significant progress occurred in CFD modeling which capabilities were extended with Fluid Structure Interaction simulation [2, 3, 5]. This allows for simulation of dynamic behavior of hydraulic valves and including also flow forces. Despite this advance however, there are still some disadvantageous such as long calculation times and other computer resources demands. Moreover, traditional FSI simulation requires preparing few simulation models to avoid problems with deforming mesh [1]. Recently, a new solution method of FSI appeared. This method allows one to simulate fluid-solids interaction without using deformable mesh. Such approaches are called "Immersed Solids" and are available in CFD code Ansys CFX.

This paper presents an attempt of using "Immersed Solid" technique in modeling of direct acting hydraulic valves.

## 2. Mathematical modeling of "immersed solids" simulation

An immersed solid is a rigid body which moves along with the fluid domain (Fig. 1) The solid object occupies the same volume as a part of the fluid domain which contain the solids.

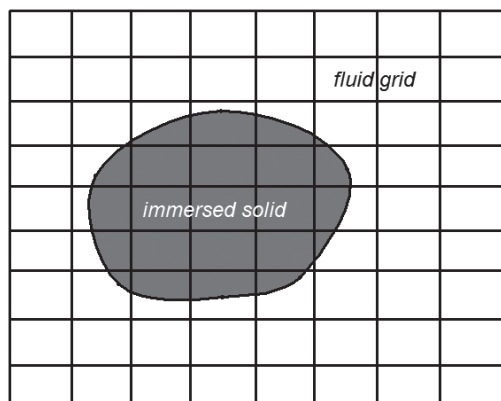


Fig. 1. Immersed solid inside the fluid domain

To model the interaction of fluid and immersed solid the momentum conservation equation needs to be considered as a source term.

For incompressible flows, the momentum conservation equation has the following form:

$$\frac{\partial \mathbf{U}}{\partial t} \rho + \nabla (\mathbf{U} \times \mathbf{U}) \rho = -\nabla p + \nabla \cdot \boldsymbol{\tau} + \mathbf{S} \quad (1)$$

where:

$\mathbf{S}$  – is source term,

$\mathbf{U}$  – is fluid velocity,

$\rho$  – is fluid density,

$p$  – is pressure,

$\boldsymbol{\tau} = \mu \left( \nabla \cdot \mathbf{U} + (\nabla \cdot \mathbf{U})^T - \frac{2}{3} \delta \nabla \cdot \mathbf{U} \right)$  – is a stress tensor,

$\mu$  – is viscosity,

$\delta$  – is Kronecker symbol.

The source term  $\mathbf{S}$  can be expressed as:

$$\mathbf{S} = -\alpha \beta C (\mathbf{U} - \mathbf{U}^s) \quad (2)$$

where:

$\alpha$  – is the momentum scaling factor,

$\beta$  – is the forcing function,

$C$  – is momentum source coefficient,

$\mathbf{U}^s$  – is solid velocity.

## 2. Object of study

The object of study is the direct acting relief valve with a cone shape lift element presented schematically on Fig. 2.

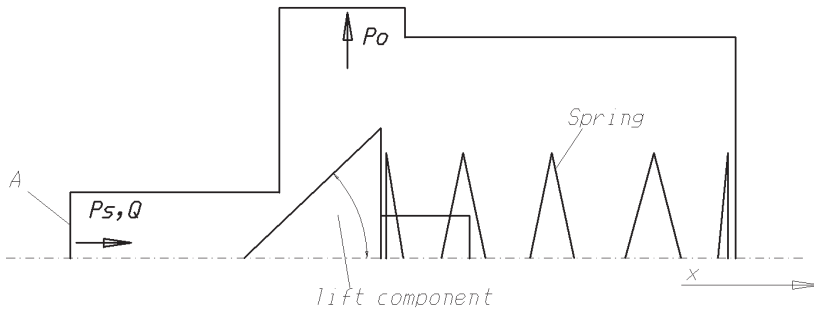


Fig. 2. A scheme of direct acting relief valve

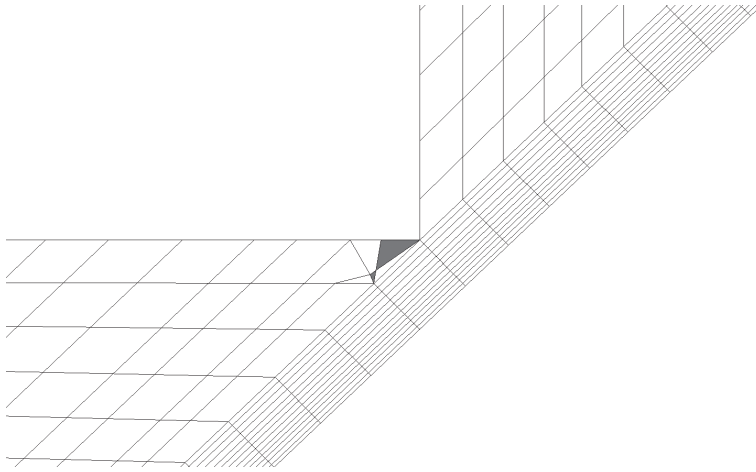


Fig. 3. A distorted cells which may appear during FSI simulation with grid deformation

When the pressure at the hydraulic circuit rise (port A) above the set value ( $p_s$ ) the spring yields and the lift element opens the flow to the tank. A dynamic simulation of this valve requires information about all the forces that act on the lift element. Traditional FSI simulation requires a deformed mesh. However this may lead to relatively long calculation time and introduce other pathologies such as cell distortion. Due to the valve features (no damping element) during operation the lift element may close and open the flow. Therefore, the deformed mesh may cause the distorted cells which may appear during simulation (see Fig. 3). One solution to such a problem may be use few models with grid prepared for simulation of valve in defined opening or re-meshing, when distorted cells appears. However, both approaches are a time consuming process. The problem is solved by using “immersed solids”

### 3. FSI “Immersed Solid” simulation

Immersed solid simulation among many advantages has also some limitations. For example it does not consider viscous forces and the necessity of preparing very fine grid for estimated overlapping solid and fluid domain. For these reasons some preliminary tests were conducted in this work to check the pressure and velocity distribution as well as the value of flow forces for various valve opening. CFD simulations were conducted for steady state conditions for the same flow conditions for two models: in the first the lift element is a wall while in the second it is the immersed solid. Selected fluid velocity distribution is presented on below Figures.

Maximal fluid velocity for both models are very similar, however, the velocity distributions are not similar. This may lead to further consequences. Therefore, the next step is the investigation of flow forces which appear at the lift element during fluid flow. Results for various openings are shown below.

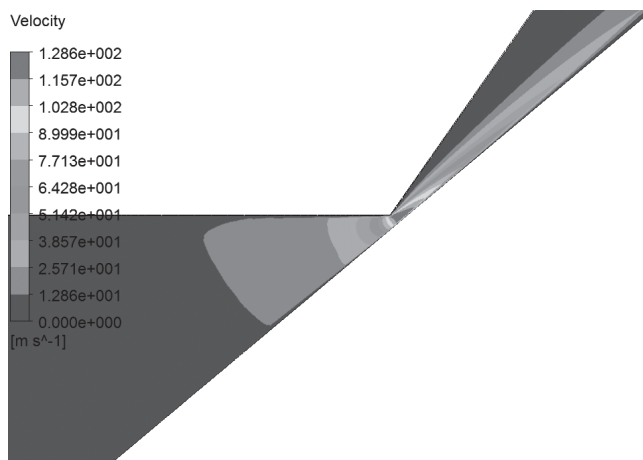


Fig. 4. Fluid velocity: lift element is a wall

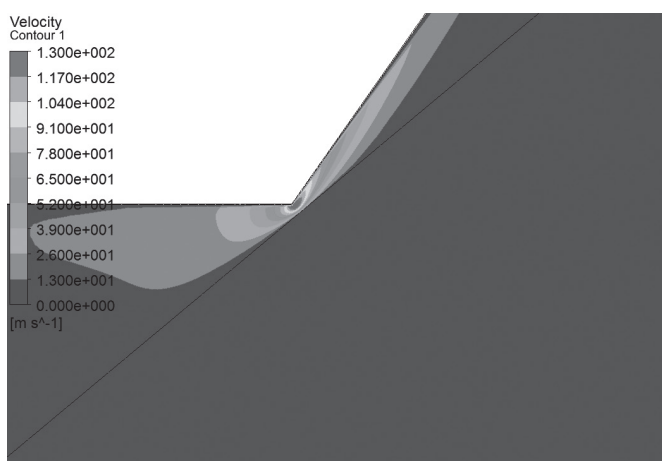


Fig. 5. Fluid velocity: lift element is the “immersed solid”

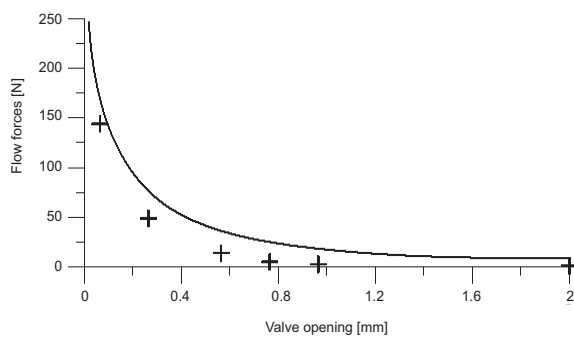


Fig. 6. Flow forces for both models: continuous line: the first models, symbols is the second one



Presented results shown what could be expected, that differences in flow forces even despite the fine grid are significant for both models.

#### 4. Conclusions

This paper presents an attempt at using the “Immersed Solid” FSI technique for the simulation dynamics of direct acting relief valve. Preliminary CFD simulations show that the maximal value of velocity and pressure are very similar for the traditional approach and “Immersed Solid” technique, but velocity distribution for both cases are different. Additionally, CFD simulations provided the values of flow forces, which also confirmed that in case of “Immersed Solid” simulation flow forces have significant differences. Thus, it is concluded that despite the advantages of avoiding problems with deformed mesh, the “Immersed Solid” technique may be used in simulation of dynamics of relief valve in very limited way and rather for preliminary tests but not full value simulation method.

#### References

- [1] Domagała M.J., *Metodyka modelowania zaworów maksymalnych bezpośredniego działania*, praca doktorska, Kraków 2007.
- [2] Domagała M., *CFD analysis of pilot operated relief valve*, Czasopismo Techniczne 3-M/2008, Kraków 2008.
- [3] Beune A., Kuerten J.G.M., Heumen van M.P.C., *CFD analysis with fluid–structure interaction of opening high-pressure safety valves*, Computers & Fluids, Vol. 64, 2012, 108-116.
- [4] Ansys CFX Theory Guide.
- [5] Huguet D., *Dynamic mesh modelling of a direct acting relief valve*, 3<sup>rd</sup> FPNI PhD Symposium, Terrasa, Spain 2004.

PIOTR DUDA, ROMAN DUDA\*

## MODELING OF GAS FLOW THROUGH VALVE (CRV)

---

## MODELOWANIE PRZEPIYU GAZU PRZEZ ZAWÓR (RZR)

### Abstract

The aim of this work is to calculate the effective area of a compressor recirculation valve. Analytical solution and numerical modeling for compressible flow through a valve will be presented. Critical parameters of flow will be determined. Numerical modeling will be performed using ANSYS FLUENT. The results of the numerical solution will be compared with the analytical solutions.

*Keywords: compressible flow, CFD, CRV valve, choking*

### Streszczenie

Celem artykułu jest obliczenie powierzchni efektywnej zaworu recyrkulacji. Przedstawione zostaną rozwiązania analityczne oraz modelowanie numeryczne przepływu czynnika ściśliwego przez zawór. Wyznaczone zostaną parametry krytyczne przepływu. Modelowanie numeryczne przeprowadzone będzie za pomocą programu ANSYS FLUENT. Wyniki z rozwiązania numerycznego porównane zostaną z rozwiązaniami analitycznymi.

*Słowa kluczowe: przepływy ściśliwe, modelowanie numeryczne płynów, zawór recyrkulacyjny, zadławienie*

---

\* Ph.D. D.Sc. Eng. Piotr Duda, prof. CUT; M.Sc. Eng. Roman Duda, Faculty of Mechanical Engineering, Cracow University of Technology.

## 1. Introduction

In many cases turbo charged gasoline engines will have a recirculation valve across the compressor, this type of solution is shown in Fig. 1. The recirculation valve is operated externally and ways of controlling will not be discussed in this paper. The recirculation valve opens especially but not only in two conditions: first when the clutch on the car engine is pressed and the engine is working without a load, and the second one when the gas pedal is pressed and there is a very high load on the engine caused by increasing acceleration. These two cases generate rapid pressure changes. An open recirculation valve prevents the compressor from going into a surge and avoids large pressure spikes that can occur between the compressor and the throttle [8–9].

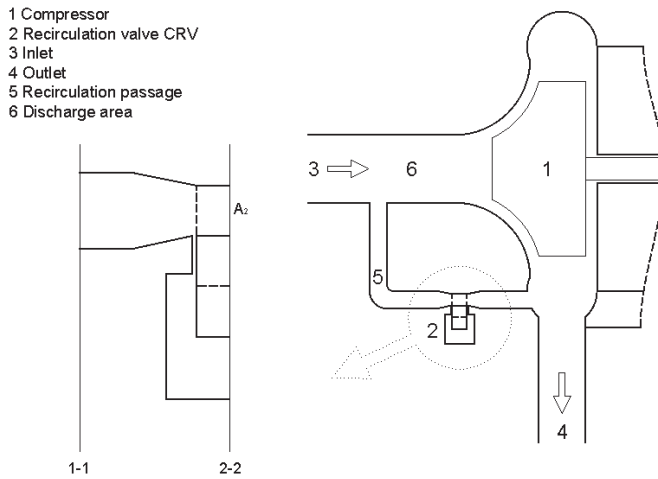


Fig. 1. Compressor with CRV

The compressor operation in the surge region is unstable because the pressure ratio is too large for the small flow rate, causing a reversal flow and pressure drop. The temporary pressure drop allows the flow to reestablish itself but this may lead to compressor longevity issues. Also this causes the turbo speed to drop more rapidly. During the design of CRV its effective area should be calculated.

There are some analytical solutions and one of them will be presented in this article. Simultaneously, CFD modeling will be performed. The aim of this article is to compare these two solutions.

## 2. Isentropic flow

For reversible adiabatic process [1–6]:

$$pp^{-k} = \text{const} \quad (1)$$

the Bernoulli equation of steady flow can be written as:

$$\int \frac{dp}{\rho} + \frac{w^2}{2} = \text{const} \quad (2)$$

The potential energy term is assumed to be negligible. Evaluating the result at two points (1 and 2) presented in Fig. 1 for the isentropic process:

$$\frac{p_2}{\rho_2} \frac{k}{(k-1)} \left[ \left( \frac{p_1}{p_2} \right)^{\frac{k-1}{k}} - 1 \right] + \frac{1}{2} (w_1^2 - w_2^2) = 0 \quad (3)$$

Application of equation (3) to the compressible flow of a body through a fluid. Allow point 1 to be the stagnation point, and take point 2 as an upstream reference point (ahead of the influence region of the body). Because  $w_1 = 0$ , then:

$$p_1 = p_2 \left[ 1 + \frac{(k-1)}{2k} \frac{\rho_2 w_2^2}{p_2} \right]^{\frac{k}{k-1}} \quad (4)$$

where:

- $p$  – pressure of fluid at the inlet,
- $p_2$  – pressure of fluid at the outlet,
- $w_1$  – fluid velocity at the inlet,
- $w_2$  – fluid velocity at the outlet.

Flows through the valve can be taken as isentropic because flow transit time is so small that any friction is ignored. Noting that the  $w_1$  is small reduces equation (3) to the following expression for velocity  $w_2$ :

$$w_2 = \sqrt{\frac{2k}{k-1} \frac{p_1}{\rho_1} \left[ 1 - \left( \frac{p_2}{p_1} \right)^{\frac{k-1}{k}} \right]} \quad (5)$$

The condition of the flow in the valve depends on the value of the pressure after the valve in respect to the critical pressure. The critical pressure can be calculated from the following equation:

$$p_{cr} = p_1 \left( \frac{2}{k+1} \right)^{\frac{k}{k-1}} \quad (6)$$

where  $p_1$  is the absolute pressure at the inlet and it is equal to the sum of static and dynamic pressures:

$$p_1 = p_0 + \frac{1}{2}\rho_1 w_1^2 \quad (7)$$

For  $p_2 \geq p_{cr}$  compressible mass flow rate has the form:

$$\dot{m} = w_2 A_2 \rho_2 \quad (8)$$

By applying equation (5) into equation (8) the following equation can be written:

$$\dot{m} = A_2 \sqrt{\frac{2k}{k-1} \frac{p_1}{\rho_1} \rho_2^2 \left[ 1 - \left( \frac{p_2}{p_1} \right)^{\frac{k-1}{k}} \right]} = A_2 \sqrt{\frac{2k}{k-1} p_1 \rho_1 \left[ \left( \frac{p_2}{p_1} \right)^{\frac{2}{k}} - \left( \frac{p_2}{p_1} \right)^{\frac{k+1}{k}} \right] \left( \frac{p_1}{p_2} \right)^{\frac{2}{k}} \frac{\rho_2^2}{\rho_1^2}} \quad (9)$$

Assuming the equation (1) the relation between pressure at the inlet and outlet takes the form:

$$p_1 \rho_1^{-k} = p_2 \rho_2^{-k} \quad (10)$$

The equation for the mass flow (8) can be written as:

$$\dot{m} = A_2 \sqrt{\frac{2k}{k-1} p_1 \rho_1 \left[ \left( \frac{p_2}{p_1} \right)^{\frac{2}{k}} - \left( \frac{p_2}{p_1} \right)^{\frac{k+1}{k}} \right]} \quad (11)$$

When  $p_2 = p_{cr}$  the mass flow is equal to:

$$\dot{m} = w_{cr} A_2 \rho_{cr} \quad (12)$$

Applying equation (6) mass flow has the form:

$$\dot{m} = A_2 w_{cr} \rho_1 \left( \frac{2}{k+1} \right)^{\frac{1}{k-1}} \quad (13)$$

After simplification equation (13) takes the form:

$$\dot{m} = A_2 \sqrt{k \left( \frac{2}{k+1} \right)^{\frac{k+1}{k-1}} p_1 \rho_1} \quad (14)$$

In the design of the recirculation valve (CRV) it is necessary to calculate the minimum size of the valve area  $A_2$ . The Aabove formulas (9) and (14) depend on the ratio of the pressures  $p_1$  and  $p_2$ . Shapes of valves in case of narrowing the cross-section in the direction of gas flow

does not have a significant importance on the speed and mass flow rate of the gas even if taking into account the friction forces on its walls.

### 3. Calculation of minimum area of valve

The ratio of critical pressure  $p_{cr}$  divided by pressure at the inlet  $p_1$  has the form:

$$r_{cr} = \frac{p_{cr}}{p_1} = \left( \frac{2}{k+1} \right)^{\frac{k}{k-1}} \quad (15)$$

assuming air as fluid  $k = 1.4$  and  $r_{cr} = 0.5283$ .

For  $r > r_{cr}$  the minimum area of the valve can be calculated from:

$$A_2 = \frac{\dot{m}}{\sqrt{\frac{2k}{k-1} p_1 \rho_1 \left[ \left( \frac{p_2}{p_1} \right)^{\frac{2}{k}} - \left( \frac{p_2}{p_1} \right)^{\frac{k+1}{k}} \right]}} \quad (16)$$

For  $r \leq r_{cr}$ :

$$A_2 = \frac{\dot{m}}{\sqrt{k \left( \frac{2}{k+1} \right)^{\frac{k+1}{k-1}} p_1 \rho_1}} \quad (17)$$

Table 1

Calculated minimum area of valve

$\dot{m}$ [kg/s]	T1 = 293 [K]		T1 = 373 [K]		T1 = 473 [K]	
	$p_1/p_0$	$A_2$ [mm <sup>2</sup> ]	$p_1/p_0$	$A_2$ [mm <sup>2</sup> ]	$p_1/p_0$	$A_2$ [mm <sup>2</sup> ]
0.04	1.33	<b>144.465</b>	1.42	<b>144.936</b>	1.52	<b>147.185</b>
0.05	1.45	<b>155.286</b>	1.58	<b>155.012</b>	1.68	<b>161.752</b>
0.06	1.6	<b>162.202</b>	1.75	<b>164.504</b>	1.85	<b>174.572</b>
0.07	1.75	<b>170.099</b>	1.92	<b>174.231</b>	2.05	<b>184.398</b>
0.08	1.9	<b>178.318</b>	2.1	<b>183.119</b>	2.35	<b>187.525</b>
0.09	2.06	<b>185.771</b>	2.35	<b>187.342</b>	2.7	<b>189.848</b>
0.1	2.255	<b>190.815</b>	2.65	<b>189.88</b>	3.17	<b>188.996</b>
0.11	2.53	<b>191.606</b>	3	<b>191.478</b>	3.65	<b>190.297</b>
0.12	2.85	<b>191.746</b>	3.5	<b>189.14</b>	4.3	<b>188.693</b>

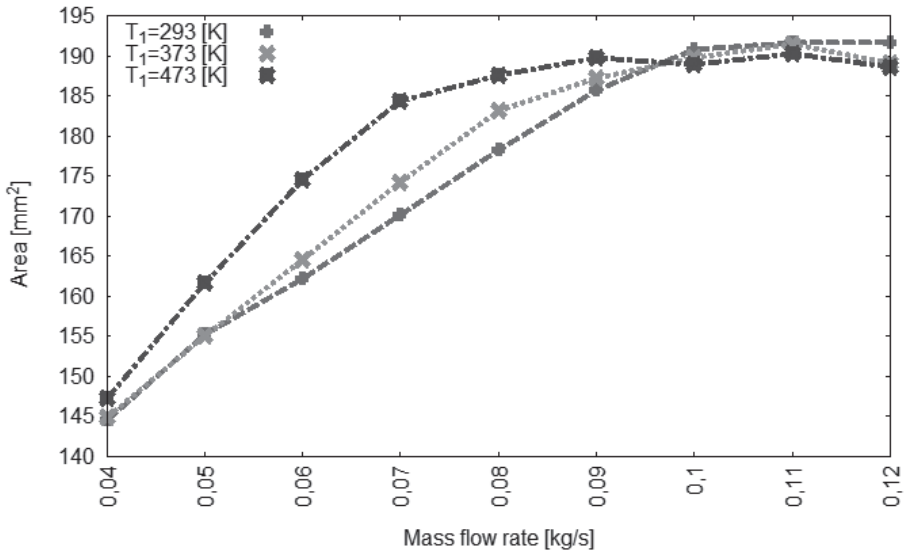


Fig. 2. Minimum area of CRV in the function of mass flow rate

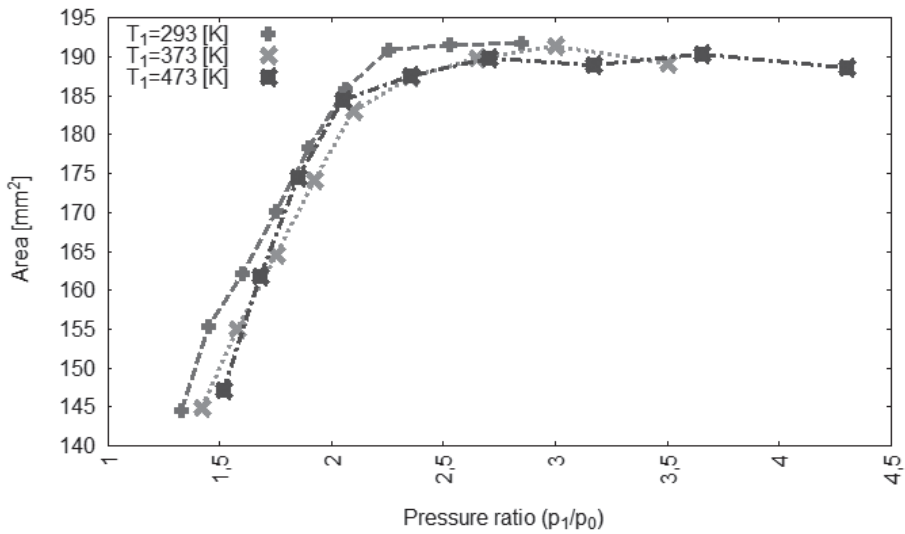


Fig. 3. Minimum area of CRV in the function of pressure ratio

Based on the equation (16) and (17) the minimum area in the function of mass flow rate  $\dot{m}$  is presented in Fig. 2 and the minimum area in the function of pressure ratio  $p_1/p_0$  is shown in Fig. 3, where  $p_0$  is the ambient pressure.

Based on Fig. 2 and Fig. 3 the value of minimal area of the CRV valve was calculated  $A_2 = 195 \text{ [mm}^2\text{]}$ .

#### 4. CFD modeling

Numerical modeling of compressible flow through the CRV valve in a steady state has been conducted [10]. A geometrical model was created from a cylinder which narrows in the length of 20 [mm] in the center. The following dimensions were assumed: the length of 260 [mm] diameter of the cylinder in the center 15.8 [mm]. The minimum cross section area was equal to 195 [mm<sup>2</sup>]. The model is presented in Fig. 4.

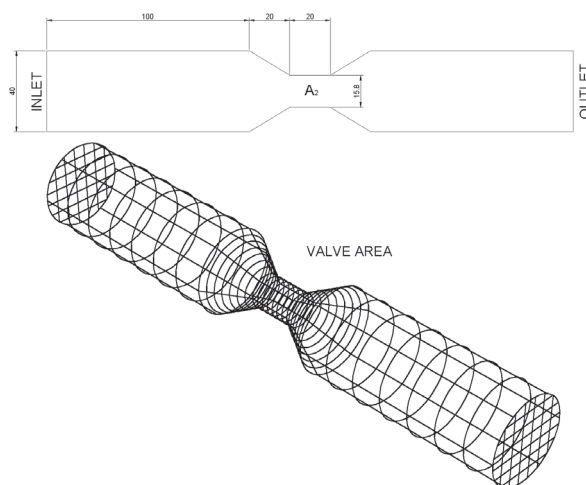


Fig. 4. 2D and 3D model with dimensions and assumed boundary conditions

The model was divided into finite elements tri tetra type of variable size decreasing ten times at the beginning of the narrowing part.

Calculations were carried out based on its density using the equations of mass, momentum and energy conservation. The flow was turbulent and k- $\epsilon$  model with extended walls (enhanced wall fn) was used. For the flowing fluid the air was set at the temperature of 293 [K]; 373 [K]; 473 [K]. The ideal gas law was chosen. Boundary condition for INLET (mass-flow -inlet) was defined by mass flow of 0.04 [kg/s] to 0.12 [kg/s]. At the OUTLET constant operating pressure of 1 [bar] was set. For the adiabatic exponent for air  $k = 1.4$  was defined. The pressure  $p_1$  at inlet area was calculated.

The accuracy of the numerical solution is high. The maximum relative error is about 5%. To simplify the problem a two-dimensional model was created with the same sizes in the  $x$  and  $y$  axis as in the three-dimensional model. The model was divided into finite elements of quad pave type with resizable size decreasing ten times at the beginning of the narrowing area. The computational model and boundary conditions were the same as in the three-dimensional modeling.



Table 2

## Comparison of exact values and calculated by CFD

$\dot{m}$ [kg/s]	T1 = 293 [K]			T1 = 373 [K]			T1 = 473 [K]		
	$p_{\text{exact}}$ [Pa]	$p_{\text{CFD}}$ [Pa]	$\sigma = \frac{p_{\text{exact}} - p_{\text{CFD}}}{p_{\text{exact}}} \cdot 100$ [%]	$p_{\text{exact}}$ [Pa]	$p_{\text{CFD}}$ [Pa]	$\sigma = \frac{p_{\text{exact}} - p_{\text{CFD}}}{p_{\text{exact}}} \cdot 100$ [%]	$p_{\text{exact}}$ [Pa]	$p_{\text{CFD}}$ [Pa]	$\sigma = \frac{p_{\text{exact}} - p_{\text{CFD}}}{p_{\text{exact}}} \cdot 100$ [%]
0.04	133000	136025	<b>2.274436</b>	142000	141200	<b>0.56338</b>	142000	141245	<b>0.53169</b>
0.05	145000	149500	<b>3.103448</b>	158000	155345	<b>1.68038</b>	158000	156690	<b>0.82911</b>
0.06	160000	154905	<b>3.184375</b>	175000	178245	<b>1.85429</b>	175000	174256	<b>0.42514</b>
0.07	175000	171900	<b>1.771429</b>	192000	194234	<b>1.16354</b>	192000	193400	<b>0.72917</b>
0.08	190000	185856	<b>2.181053</b>	210000	208345	<b>0.7881</b>	210000	205789	<b>2.00524</b>
0.09	206000	203436	<b>1.24466</b>	235000	238543	<b>1.50766</b>	235000	228432	<b>2.79489</b>
0.1	225500	227478	<b>0.877162</b>	265000	266703	<b>0.64264</b>	265000	279532	<b>5.48377</b>
0.11	253000	248300	<b>1.857708</b>	300000	304356	<b>1.452</b>	300000	298643	<b>0.45233</b>
0.12	285000	291097	<b>2.139298</b>	350000	348254	<b>0.49886</b>	350000	353575	<b>1.02143</b>

## 5. Conclusions

The method to calculate the effective-minimum area of a compressor recirculation valve (CRV) was presented. Additionally, numerical modeling of compressible flow through the CRV valve in a steady state has been conducted. The created numerical model was presented. The results of the numerical solution were compared with the analytical solutions. The accuracy of the numerical solution is high. The maximum relative error is about 5%.

This type of analysis is applicable in the automotive industry.

## References

- [1] Anderson J.D., *Modern Compressible Flow with Historical Perspective*, 3rd ed., McGraw-Hill, New York 2003.
- [2] Çengel Y.A., Boles M.A., *Thermodynamics: An Engineering Approach*, 4th ed., McGraw-Hill, New York 2002.
- [3] Hodge B.K., Koenig K., *Compressible Fluid Dynamics with Personal Computer Applications*, Prentice Hall, Englewood Cliffs, New York 1995.
- [4] John J.E.A., *Gas Dynamics*, 2nd ed., Prentice Hall, Englewood Cliffs, New York 1984.
- [5] Moran M.J., Shapiro H.N., *Fundamentals of Engineering Thermodynamics*, 4th ed., John Wiley & Sons, New York 2000.
- [6] Oosthuizen P.H., Carscallen W.E., *Compressible Fluid Flow*, McGraw-Hill, New York 1997.
- [7] Zucrow M.J., Hoffman J.D., *Gas Dynamics, Volumes I and II*, John Wiley & Sons, New York 1976.
- [7] Allard A., *Turbocharging and Supercharging*, Cambridge, Patrick Stevens Limited, England 1982.
- [8] Gorla Rama, Khan Aijaz, *Turbomachinery Design and Theory*, Marcel Dekker, New York 2003.
- [9] ANSYS® Fluent, 15.0, *User's manual*, ANSYS, Inc.



PIOTR DUDA, ŁUKASZ FELKOWSKI\*

## MODELING OF STRESS STATE IN THICK WALLED PRESSURE ELEMENT BASED ON EUROPEAN STANDARDS AND PROPOSED CREEP EQUATION

### MODELOWANIE STANU NAPRĘŻENIA W ELEMENCIE CIŚNIENIOWYM ZGODNIE Z EUROPEJSKIMI NORMAMI I ZAPROPONOWANYM RÓWNANIEM PEŁZANIA

#### Abstract

The elements subjected to high temperatures are exposed to phenomena such as the creep, where time-dependent properties of materials should be considered. Many devices of the steam boiler work in creep conditions, what limits the time of their work. The chosen thick-walled superheater header is exposed to a high temperature and pressure and therefore it should be designed according to the European Standards. In this article, the standard requirements for a component operating in creep conditions are presented, and the FEM analysis is performed. In the FEM analysis, the proposed creep equation is used based on the results obtained from experimental tests.

*Keywords: power boilers, creep, lifetime, FEM analysis*

#### Streszczenie

Elementy poddane wysokim temperaturom są narażone na zjawiska, takie jak pełzanie, gdzie czasowo zależne własności materiałowe powinny być uwzględnione. W kotłach parowych duża część urządzeń pracuje w warunkach pełzania, co ogranicza czas pracy tych części ciśnieniowych. Wybrana do analizy grubościenna komora wylotowa przegrzewacza pary jest narażona na działanie wysokiej temperatury oraz ciśnienia, dlatego też projektuje się ją zgodnie z Normami Europejskimi. W artykule zaprezentowano wymagania normowe dla komór pracujących w warunkach pełzania oraz przedstawiono analizę MES. W analizie MES wykorzystano zaproponowane równanie pełzania, bazując na wynikach eksperymentalnych.

*Słowa kluczowe: kotły energetyczne, pełzanie, żywotność, analiza MES*

\* Ph.D. D.Sc. Eng. Piotr Duda, M.Sc. Eng. Łukasz Felkowski, Faculty of Mechanical Engineering, Cracow University of Technology.

## 1. Introduction

A lot of pressure elements of power boilers are subjected to high temperatures, what determines the lifetime of these devices. The creep is the main phenomenon which limits the operation time of these devices.

A lot of failures in power boilers occur in cylindrical elements in stress concentration areas and these parts of components should be monitored.

The pressure parts of boilers are described in the European Directive 97/23/WE (PED) [1] and should be calculated according to the harmonized norms: EN 12952-3 [2] and EN13445-3 [3].

In this article, the European Norms requirements and FEM analysis for the superheater outlet header SH3 is presented. In the FEM analysis the proposed creep equation is used which is based on the results obtained from experimental tests.

## 2. Requirements of European Norms

Water-tube boiler pressure parts must be designed in accordance with the requirements of European Standard EN 12952-3. The wall thickness and other dimensions of pressure parts should be sufficient to withstand the calculation pressure at calculation temperature for the designed lifetime.

The calculations according to EN 12952-3 are based on the design by formulas (DBF). The DBF method may not be enough for complicated shapes of headers with nozzles, and for temperature and time dependent phenomena. This method can be supplemented by calculations based on the design by finite element analysis (DBA) – according to EN 13445-3.

### 2.1. Allowable stress

The stress in pressure elements must not exceed the allowable stress  $f_1$  for elastic conditions [2]. This allowable stress (according to EN 12952) is a function the proof strength or the tensile strength at calculation temperature (equation 1), divided by the safety factor.

$$f_1 = \frac{K}{S_1} \quad (1)$$

where:

- $f_1$  – the allowable stress for elastic condition, MPa,
- $K$  – the material strength value for the design conditions, MPa,
- $S_1$  – the safety factor for the elastic conditions.

The allowable stress  $f_2$  for the creep conditions is based on the temperature and time dependent properties of metals (equation 2). This property according to EN 12952 is the creep rupture strength  $R_{m,t,T_c}$  for the specified lifetime.

$$f_2 = \frac{R_{m t T_c}}{S_2} \quad (2)$$

where:

- $f_2$  – the allowable stress for the creep condition, MPa,
- $R_{m t T_c}$  – creep rupture strength, MPa,
- $S_2$  – the safety factor for the creep conditions,

subscript:

- $t$  – the lifetime [h],
- $T_c$  – the temperature for the creep conditions [°C],

The rupture strength should be defined based on the calculation temperature  $T_c$  and the assumed lifetime  $t$ . The lifetime for the analyzed boiler elements is  $t = 200\,000$  [h]. For this lifetime the safety factor is  $S = 1.25$ , and the allowable stress is  $f_2 = R_{m200\,000 T_c} / 1.25$ . For exceptional cases, when the data of the rupture strength is not available for  $t = 200\,000$  [h], then 100 000 [h] data may be used ( $R_{m t T_c}$  for  $t = 100\,000$  [h]), and the safety factor is then equal to  $S = 1.5$ . For short duration time, the creep rupture strength may be reduced to 10 000 [h], and then the safety factor is  $S = 1.25$ . These safety factors for each time are presented in table 1.

Table 1

**Safety factor as a function of mean creep strength related to time**

Time [h]	Safety factor $S_2$
200 000	1.25
100 000	1.5
10 000	1.25

## 2.2. Creep design check

According to EN 12952-3 the required wall thickness is estimated based on the simple calculation (the DBF method). For pressure and temperature load cases, the stress in the cylindrical header is equal (equation 3):

$$\sigma_1 = p_c \cdot \left( \frac{1}{2} + \frac{d_{is}}{2 \cdot e \cdot v} \right) \quad (3)$$

where:

- $\sigma_1$  – the hoop stress in a cylindrical element, MPa,
- $d_{is}$  – the inside diameter of a header, MPa,
- $e$  – the thickness of a cylindrical header, mm,
- $v$  – the efficiency factor for adjacent branches or isolated openings.

The stress  $\sigma_1$  must be less or equal to the allowable stress  $f$  for the creep load case and elastic load case (equation 4):

$$\sigma_1 \leq f = \min(f_1, f_2) \quad (4)$$

where:

- $f$  – allowable stress for all load cases, MPa,
- $\sigma_1$  – the hoop stress in a cylindrical element, MPa,
- $f_1$  – the design stress for an elastic condition, MPa,
- $f_2$  – the design stress for the creep condition, MPa.

Equation 3 using efficiency factor  $v$  gives conservative results. The factor  $v$  estimation method is described in detail in EN 12952-3. For this reason the FEM analysis (the DBA method) is often used [4]. Requirements and assumptions for this analysis can be found in EN 13445-3. According to EN 13445-3 (for FEM analysis) if the creep checks are required, the two design checks should be considered:

- Creep Rupture Design Check (CR),
- Excessive Creep Strain Design Check (ECS).

The Creep Rupture Design (CR) needs to be checked whether the stress does not exceed design material strength parameters  $R_M$  divided by partial safety factor  $\gamma_R$ . These material parameters depend on the kind of material and monitoring lifetime (table 2). For load cases without monitoring strength parameter  $R_M$  is equal to the creep rupture strength  $R_{m,t,T_c}$  and the safety factor is  $\gamma_R = 1.25$ . For the CR method one should take into account the following conditions:

- linear-elastic ideal-plastic constitutive law (if the design creep constitutive law is not reached),
- von Mises' yield condition and associated flow rule.

Table 2

**RM and  $\gamma_R$  for CR load cases without monitoring**

Material	RM	$\gamma_R$
Steel	$R_{m,t,T_c}$	$1.25$ if $\frac{R_{m,t,T_c}}{R_{p1.0,t,T_c}} > 1.5$ otherwise $\frac{1}{1.2} \cdot \frac{R_{m,t,T_c}}{R_{p1.0,t,T_c}} \leq 1.5$

For Excessive Creep Strain (ECS) in only one condition to meet:

- in each point of the structure, the accumulated equivalent structural creep strain, must not exceed 5%.

This rule can be used, if the design creep's constitutive law is reached.

### 3. Numerical example

For a thick-walled pressure element in the numerical example has been chosen the outlet header of superheater. It is the part of a power boiler. Its geometry is presented in Fig. 1.

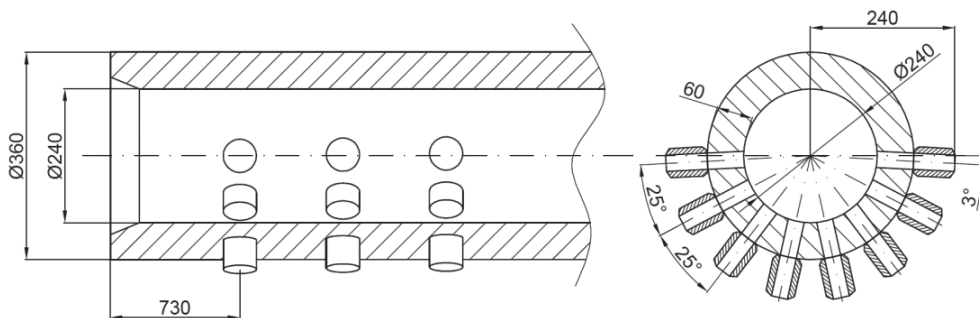


Fig. 1. The outlet header SH3 dimensions

Its outside and inside diameters equal respectively 360 mm and 240 mm. The tubes connected to the header has the diameter of 52 mm and the thickness of 10mm. The outlet header is made of P91 steel. The calculation parameters are: pressure  $P = 284$  [bar], and temperature  $T = 569$  [°C].

#### 3.1. Mechanical properties and creep equation

Steel P91 is often used for components of steam boilers because of high heat resistance and the improved properties in creep conditions. The mechanical and physical properties of P91 steel are presented in the Figure 2 [6].

The creep equation for P91 is built on the base of the uniaxial homogeneous stress states realized in standard material testing [7]. The load and the temperature are kept constant during the test and the axial engineering strain  $\varepsilon$  is plotted versus time  $t$ .

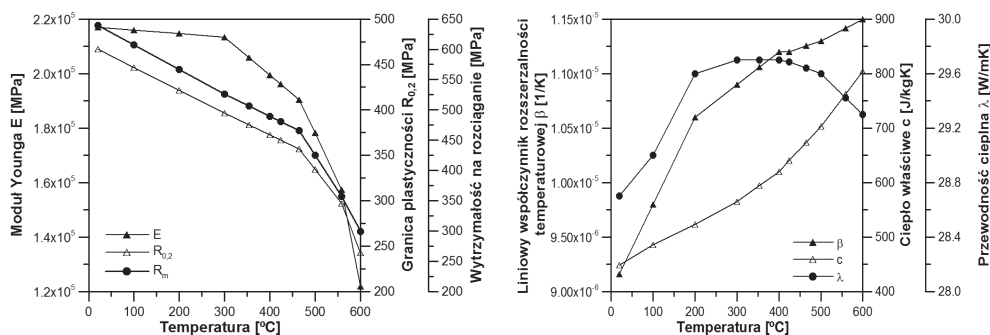


Fig. 2. The mechanical and physical properties of steel P91



Experimental data is interpolated using the modified Garofalo creep equation [8]. Coefficients in this equation describe physical magnitudes. This model describes well the first and the second stage of creep, but also takes the third stage of this phenomenon into account.

### 3.2. Finite Element Model

The numerical model of the header was built in ANSYS [9] and is presented in Fig. 3. The mesh of model consists of 8-node “brick” elements, which are described by linear shape functions.

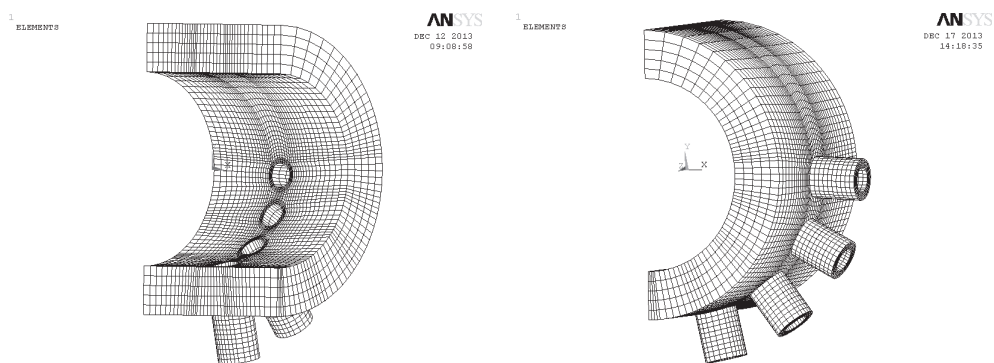


Fig. 3. Discretization of the outlet header SH3

The analyzed model is constrained to provide symmetry conditions and to prevent rigid movement of the body.

### 3.3. Results of FEM analysis

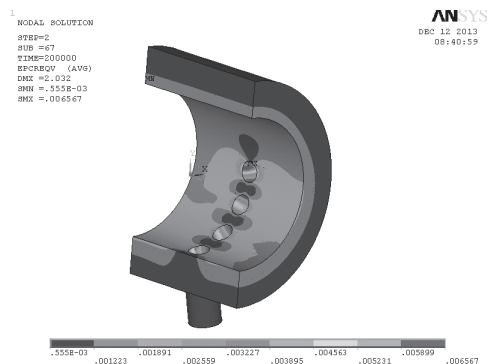
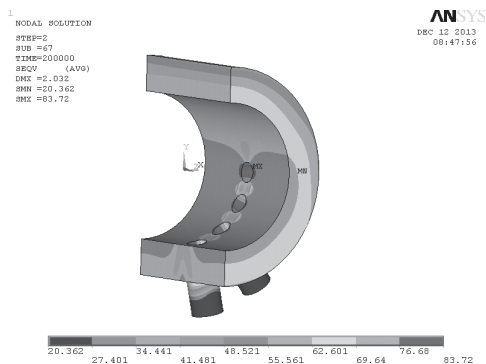
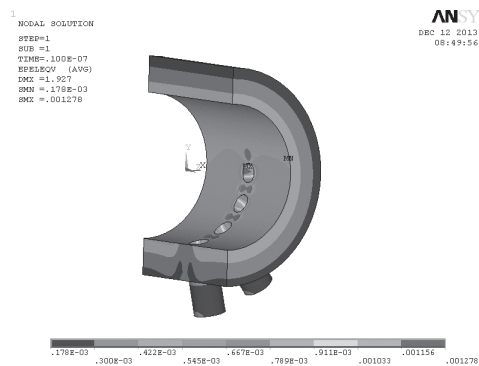
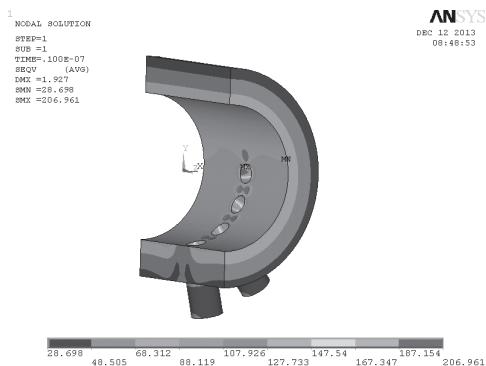
As the result of internal pressure  $P = 284$  [bar] loading and temperature increase from  $20[^\circ\text{C}]$  to  $569[^\circ\text{C}]$  the stress concentration occurs on the inner surface in the opening for the nozzle. Fig. 4 presents the equivalent stress (HMH) distribution at the time  $t = 0$  [h]. The maximum equivalent stress equals  $207$  [MPa]. This stress is lower than yield point, hence the plastic strain doesn't occur.

The distribution of equivalent strain (HMH) for time  $t = 0$  [h] is shown in Fig. 5. The maximum equivalent strain equals  $\varepsilon = 0,13\%$  and is located in the stress concentration point.

Numerical simulation of outlet header's work for  $200\,000$  [h] is possible by using the chosen creep equation. Distribution of the equivalent stress (HMH) in time  $t = 200\,000$  [h] is shown in Fig. 6. The maximum equivalent stress equals  $84$  [MPa] and this stress decline is the result of the creep strain increase.

The maximum equivalent creep strain (HMH) after  $200\,000$  [h] is  $0.66\%$ , and this is the main portion of the equivalent maximum total strain, which reaches about  $0.71\%$  (Fig. 7).

The conducted analysis of all creep strain components at the stress concentration point showed that this concentration is mainly caused by the circumferential strain.



Assuming the value of the safety factor according to EN 13445-3  $\gamma_R = 1.25$  the allowable stress at 200 000 [h] equals  $RM/\gamma_R = 122.5/1.25 = 98$  [MPa]. This means that the first condition for creep analysis according to EN 13445-2 is reached. The maximum equivalent strain calculated in the FEM analysis using the creep equation is less than 5%, which means that the second condition according to EN 13445-3 is obtained.

#### 4. Conclusions

The strength analysis of the outlet header working under the creep conditions was described in this article. The analysis of thick walled element was based on the European standards and the proposed creep equation. Numerical analysis in ANSYS showed that equivalent stress (HMH) for 200 000 [h] is less than allowable stress 98 [MPa]. The maximum equivalent

stress equals 84 [MPa] and this stress decline from 207 [MPa] at the time 0 [h] is the result of the creep strain increase. The results of the presented analysis showed that the main part of the equivalent strain is circumferential strain.

*This research was financed by the Polish Ministry of Science and Higher Education, grant No. NR15-0060-10 /2011, 2010–2013.*

## References

- [1] The Pressure Equipment Directive, 97/23/EC (PED).
- [2] EN 12952-3 Water-tube boilers and auxiliary installations.
- [3] EN 13480-3 Metallic industrial piping. Design and calculation.
- [4] Zeman J.L., *Pressure Vessel Design the Direct Route*, Elsevier, China 2006, 69-82.
- [5] Superheater coils SH3 documentation, Rafako S.A.
- [6] The laboratory results obtained under the Project Development-Behavioral Assessment and forecast long-term operation of new generation steel boiler elements operated above the temperature limit, Instytut Metalurgii Żelaza, Politechnika Krakowska, Rafako S.A.
- [7] Naumenko K., Altenbach H., *Modeling of Creep for Structural Analysis*, Springer-Verlag Heidelberg, Berlin 2007, 1-15.
- [8] Osocha P., *Określenie stopnia uszkodzenia wysokociśnieniowych grubościennych elementów kotłów*, Phd Dissertation, Kraków 2009.
- [9] *ANSYS User's Manual, Revision, 12.0 A.*

JOANNA FABIŚ-DOMAGAŁA\*

## FMEA ANALYSIS OF A HYDRAULIC CYLINDER USING ARTIFICIAL NEURAL NETWORK

---

### ANALIZA FMEA SIŁOWNIKA HYDRAULICZNEGO Z ZASTOSOWANIEM SZTUCZNYCH SIECI NEURONOWYCH

#### Abstract

This paper presents Failure Mode and Effects Analysis (FMEA) on the hydraulic cylinder using matrix analysis and artificial neural network. Functions for each cylinder components were identified. Also relationships between pairs for interacting components and their potential failures were identified. Training and testing of an artificial neural network was conducted in MATLAB software environment.

*Keywords: FMEA, analysis, failure, neural network*

#### Streszczenie

W artykule przedstawiono analizę przyczyn i skutków powstawania potencjalnych wad (FMEA) siłownika hydraulicznego przy wykorzystaniu analizy macierzowej oraz sztucznej sieci neuronowej. Określono funkcje, jakie pełnią poszczególne części siłownika. Zidentyfikowano zależności zachodzące pomiędzy parami współdziałających elementów oraz ich potencjalne wady. Trenowanie i testowanie sztucznej sieci neuronowej przeprowadzono w środowisku programowym MATLAB.

*Słowa kluczowe: FMEA, analiza, wada, sieć neuronowa*

---

\* M.Sc. Joanna Fabiś-Domagała, Institute of Applied Informatics, Faculty of Mechanical Engineering, Cracow University of Technology.

## 1. Introduction

Hydraulic cylinders are one of the most important components of the drive operating mechanisms. These mechanisms and hydraulic cylinders are exposed to external environmental factors such as: dust, variable temperature and dynamic loads. Although the hydraulic cylinders belong to a group of devices with relatively uncomplicated structure they are susceptible to damage and failure. Therefore, the identification of failures in the early stages of its formation allows to undertake an appropriate preventive action, to not allow to extend their influence to other components of the system. According to a study presented in work [1] approx. 75% of all failures is formed during the preparation of manufacturing process but their identification at this stage is very negligible. The moment the failures are identified is the production stage. More than 80% occurring failures are removed during the final inspection and during operation, therefore the cost of its elimination is much higher than elimination of defect on the stage when it arises. It is also important to undertake preventive actions even at the design stage of the product. This allows to reduce the costs due to “poor quality” and such actions are in accordance with “the principle of continuous improvement”, E. Deming. Therefore, the methods which allows to detect potential failures and their causes are still developed. In case of hydraulic components the analysis of available literature [3, 4] and qualitative methods shows that using the matrix analysis (FMEA) may be very effective. Such methods may also be easily integrated with computer systems, particularly with expert systems and allows to identify failures on early stages.

The paper presents a matrix FMEA analysis for hydraulic cylinder using selected artificial neural network.

## 2. The object of analysis

The object of the research is the double action hydraulic cylinder with swivel bearing [1]. The structure of the cylinder is shown in Figure [1], where: 1 – cylinder body, 2 – piston rod, 3 – gland, 4 – piston sleeve, 5 – nut, 6 – self aligned bearing, 7 – cylinder end with self aligned bearing, 8 – piston seal, 9, 11, 12 – sealing ring, 10 – wiper ring, 13 – guide ring.

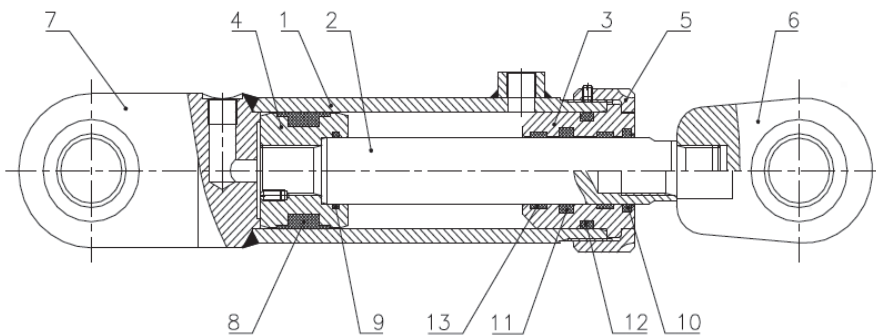


Fig. 1. Scheme of hydraulic cylinder

In order to identify potential failures on a matrix FMEA analysis the hydraulic cylinder structure was decomposed into ten components ( $c$ ) which may cause improper operation. These are: cylinder body ( $c_1$ ), piston sleeve ( $c_2$ ), piston rod ( $c_3$ ), sealing ring ( $c_4$ ), piston seal ( $c_5$ ), wiper ring ( $c_6$ ), ring ( $c_7$ ), gland ( $c_8$ ), nut ( $c_9$ ) and self aligned bearing ( $c_{10}$ ).

### 3. Input data for FMEA analysis

The qualitative analysis of the hydraulic cylinder by matrix FMEA method requires to create two matrix EC (function-component) and CF (component-failure) [3, 4]. Using decomposition of the hydraulic cylinder (defined in Section 2) a seventeen pairs of interacting components have been identified. Pairs ( $p$ ) are shown by the matrix diagram where sign (+) means the relationship between the analyzed elements, sign (–) means no dependence, and sign (x) means the relationship between the same components.

Table 1

Diagram of relations between the interacting components of hydraulic cylinder (p)

	$c_1$	$c_2$	$c_3$	$c_4$	$c_5$	$c_6$	$c_7$	$c_8$	$c_9$	$c_{10}$
$c_1$	x	+	–	+	+	–	–	+	+	–
$c_2$	+	x	+	+	+	–	–	–	–	–
$c_3$	–	+	x	+	–	+	+	+	–	+
$c_4$	–	+	+	x	–	–	–	+	–	–
$c_5$	–	+	–	–	x	–	–	–	–	–
$c_6$	–	–	+	–	–	x	–	+	–	–
$c_7$	–	–	+	–	–	–	x	+	–	–
$c_8$	–	–	+	+	–	+	+	x	+	–
$c_9$	–	–	–	–	–	–	–	+	x	–
$c_{10}$	–	–	+	–	–	–	–	–	–	x

Then, for all the interacting components (Table 1) functions (e) which perform in the hydraulic cylinder have been specified (Table 2).

Based on the identified functions and the analysis of the literature [5] ten failures ( $f$ ) have been identified for interacting pairs of hydraulic cylinder. These are: abrasive wear ( $f_1$ ), crevice corrosion ( $f_2$ ), fretting corrosion ( $f_3$ ), seizure ( $f_4$ ), fatigue friction ( $f_5$ ), pitting ( $f_6$ ), thermal fatigue ( $f_7$ ), adhesive wear ( $f_8$ ), oxidation wear ( $f_9$ ), buckling ( $f_{10}$ ).

Table 2

**Description of functions**

Function	Description
fixing ( $e_1$ )	the correct position of the hydraulic cylinder components, alignment of the hydraulic cylinder
converting ( $e_2$ )	converting fluid pressure energy into mechanical motion straight-back, the main function of hydraulic cylinder
preventing ( $e_3$ )	prevents against of dust, dirt, grains of sand, removes impurities
protecting ( $e_4$ )	preventing oil leakage, seal cylinder, piston and piston rod guided in the cylinder, the lateral loads and vibration resistance

**4. FMEA matrix analysis**

The FMEA analysis includes creating two diagrams of dependence. The first one (Table 3) shows the relationship between the pairs of interacting components ( $p_i$ ) and performed functions ( $e_j$ ). For each element of the matrix  $e_j p_i$  value of 0 or 1 was assigned. If a pair does not perform assigned function than value is 0, if the function is performed than the value is 1. The resulting diagram is size  $[4 \times 17]$  and contains 68 elements.

Table 3

**Diagram of the relationship between functions and pairs (EP)**

	$p_1$	$p_2$	$p_3$	$p_4$	$p_5$	$p_6$	$p_7$	$p_8$	$p_9$	$p_{10}$	$p_{11}$	$p_{12}$	$p_{13}$	$p_{14}$	$p_{15}$	$p_{16}$	$p_{17}$
$e_1$	1	0	0	0	1	0	0	0	0	0	0	0	1	0	0	0	1
$e_2$	0	0	0	0	0	1	0	0	0	0	0	0	0	0	0	0	0
$e_3$	0	0	0	0	0	0	0	0	0	1	0	0	0	0	1	0	0
$e_4$	0	1	1	1	0	0	1	1	1	0	1	1	0	1	1	1	0

The second diagram of dependencies (Table 4) shows the relationships between interacting components ( $p_i$ ) and their potential failures ( $f_j$ ). For each pair of matrix  $p_i f_j$  a value of 0 or 1 have been assigned. A value of 0 is assigned if the defect does not occur for the pair. The value of 1 if the defect occurs. The resulting matrix PF has dimension  $[17 \times 10]$  and has 170 elements. Fragment of PF matrix  $[8 \times 8]$  is shown below.

At the last stage the FMEA matrix analysis use the principle of multiplication of the matrix presented at work [4]:

$$EP \times PF = EF \tag{1}$$

Table 4

**Diagram of the relationship between the pair and their potential failures (PF)**

	$f_1$	$f_2$	$f_3$	$f_4$	$f_5$	$f_6$	$f_7$	$f_8$
$p_1$	1	0	1	1	0	1	1	1
$p_2$	1	0	0	1	0	0	0	0
$p_3$	1	0	0	0	0	0	0	0
$p_4$	1	0	0	1	1	0	0	0
$p_5$	1	1	0	0	0	0	0	0
$p_6$	1	1	0	0	1	1	0	0
$p_7$	1	0	0	1	0	0	0	1
$p_8$	1	0	0	0	0	0	0	0

A diagram showing the probability of failures (f) has been built, for pairs of interacting components (p) due to the function (e) performed by the pair in the hydraulic cylinder. Table 5 shows the probability of occurrence of failures in the range of 0 to 11. Value 11 indicates the highest probability of failure for a given function.

Table 5

**Diagram function – failure (EF)**

	$f_1$	$f_2$	$f_3$	$f_4$	$f_5$	$f_6$	$f_7$	$f_8$
$e_1$	4	3	1	2	0	1	1	1
$e_2$	1	1	0	0	1	1	0	0
$e_3$	2	2	0	1	0	0	0	0
$e_4$	11	3	1	9	2	0	1	1

For analyzed hydraulic cylinder the highest probability is for failure: abrasive wear ( $f_1$ ) for pairs of realizing the protecting function ( $e_4$ ). These are the following pairs:  $p_2, p_3, p_4, p_7, p_8, p_9, p_{11}, p_{12}, p_{14}, p_{15}$  and  $p_{16}$  which includes the seal. These components are more sensitive for failures than others of the hydraulic cylinder because:

- the working liquid is contaminated: present in the liquid particles damage the surfaces of the piston, the piston rod and the O-rings,
- aggressive chemical agents: some working fluids react with seals,
- leaks are caused by high pressure,
- extreme working conditions – when the temperature exceeds the operating limits of the use for sealing materials than seals harden, crack and crumble.



## 5. Analysis of hydraulic cylinder failures using artificial neural network

The artificial neural network is a mathematical relations which imitating the structure and signal processing in the central nervous system of living organisms. Neural networks are the adaptive systems which are capable of pattern recognition due to the learning process. Constant values defining the significance of the inputs (network weights) are determined based on experience (learning examples). By machine learning process we can obtain a situation in which the output data (network response) is close to the actual value. This kind of learning is called supervised learning with the teacher which is most commonly used [7].

Artificial neural networks are characterized by many advantages among which the most important are:

- the ability to learn and generalize the acquired knowledge. Artificial neural networks allow to find regularities in the conditions of a large number of variables of different nature. Such relationships often require the use of complex mathematical operations or are undetectable using mathematical methods,
- the network is resistant to errors in the input data (the noise) and errors appearing in some weights or incorrectly set constant in the model,
- networks enables fast processing of information, often available at the real time.

The most frequently used neural networks are:

- regression or otherwise approximation of unknown functions of several variables (most common), on the basis of experimental observations,
- prediction – predicting the future behavior of the system based on the values of the past within the continuous adjustment of network weights,
- detection of patterns which allows to group signals having similar characteristics (Kohonen networks). This is an unsupervised learning which do not require the training set.

This paper is an attempt to use predictive neural network to identify potential failures at the hydraulic cylinders using the data contained in the FMEA matrix analysis. On the basis of FMEA analysis the three input parameters for the test network and one output parameter were defined. Inputs are the pairs of cooperating components and their functions. The output is a potential failures. The input layer have 24 inputs while the output layer has 9 outputs. The input layer includes 3 cases for learning the network. The first case using 5 neurons, the second case 10 neurons and the third case 20 neurons. The results of the neural network analysis have been developed using the Matlab environment.

I case: 24-5-9: a part of network response of five neurons in the input layer are presented in Table 6.

II case: 24-10-9: a part of network response of ten neurons in the input layer are presented in Table 7.

III case: 24-20-9: a part of network response of twenty neurons in the input layer are presented in Table 8.

The artificial neural networks provide information similar to the information contained in the diagram relationship pair-failure obtained in the FMEA. Therefore, in the next step of the analysis for each considered ANN network the errors of potential failures were identified to select a network with the smallest error. The accuracy of ANN was evaluated by using the of root mean square (RMS). The results are shown in Fig. 2.

Table 6

**Response of ANN for 5 neurons**

	$f_1$	$f_2$	$f_3$	$f_4$	$f_5$	$f_6$	$f_7$	$f_8$
$p_1$	1	6.2e-08	0.9	1	3.7e-05	0.9	1	1
$p_2$	1	4e-05	6.8e-05	0.7	0	2.6e-07	1.5e-06	1.5e-05
$p_3$	1	1e-08	9.5e-04	0	1.4e-09	0	0	1.1e-04
$p_4$	1	8e-06	4.5e-07	0.8	0.83	1.4e-06	4.6e-06	5.5e-05
$p_5$	1	0.9	1e-07	1.3e-08	0	2.4e-07	1.3e-06	1.2e-05
$p_6$	1	0.8	2.4e-06	1.5e-07	1	1	2.7e-06	1.9e-08
$p_7$	1	8.4e-05	1.5e-06	0.9	1.8e-05	9.8e-07	1.3e-06	0.8
$p_8$	1	0	0	0	5e-10	0	2e-04	3.3e-06

Table 7

**Response of ANN for 10 neurons**

	$f_1$	$f_2$	$f_3$	$f_4$	$f_5$	$f_6$	$f_7$	$f_8$
$p_1$	1	0.1	0.1	0.98	1.2e-15	1	0.9	0.9
$p_2$	1	1.1e-04	2.5e-09	0.62	0	0	0.1	0
$p_3$	1	2e-04	0	1.1e-09	0	0	0.2	0
$p_4$	1	0	0	0.2	0	0	0	0
$p_5$	1	0.9	0.4	3.1e-11	0	1e-04	0	0
$p_6$	1	0.8	5.5e-09	1e-10	0	0.4	0	1e-07
$p_7$	1	0	1	0.4	2.2e-16	6.3e-05	0	0.5
$p_8$	1	0	0	1.8e-11	0	3e-04	0	0

Table 8

**Response of ANN for 20 neurons**

	$f_1$	$f_2$	$f_3$	$f_4$	$f_5$	$f_6$	$f_7$	$f_8$
$p_1$	1	1	0,92	0	0	8,5e-12	0	1
$p_2$	1	1	1,3e-05	1	0	8,3e-12	0	0
$p_3$	1	1	1,7e-05	0	0	1,4e-11	0	0
$p_4$	1	1	1,4e-05	0.4	0	8,8e-12	0	0
$p_5$	1	1	1,3e-05	0	0	8,3e-12	0	0
$p_6$	1	1	1,3e-05	0	1	7e-12	0	0
$p_7$	1	1	5,1e-06	0.5	3,9e-05	2,2e-10	0	1
$p_8$	1	1	3,8e-06	0	0	5,1e-11	3,4e-07	0

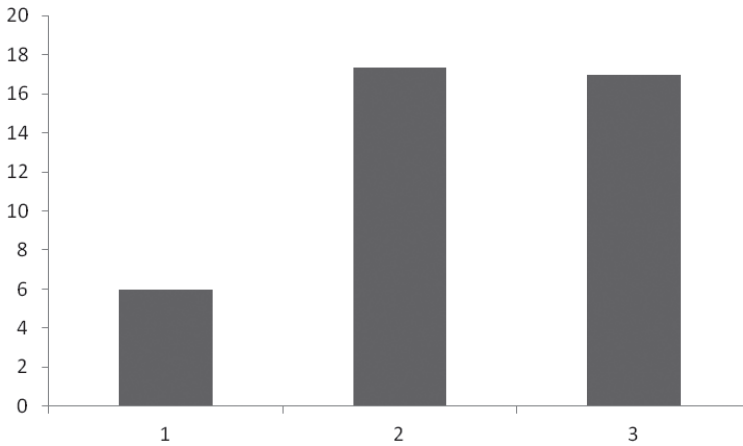


Fig. 2. The RMS value for ANN: 1-network 24-5-9 is 5.97, 2-network 24-10-9 is 17.36, 3-network 24-20-9 is 16.99

As it arises from the graph a network 24-5-9 gives the smallest error so on networks with fewer neurons in the input layer.

## 5. Conclusions

The presented work was an attempt of using neural network in identification of potential failures of hydraulic cylinder. As a learning process of neural network were used data obtained for matrix FMEA analysis. Obtained data shows that the neural network are able properly identify potential failures which may occur in hydraulic cylinder and may be used as an effective tool for FMEA analysis.

## References

- [1] Hamrol A., Mantura W., *Zarządzanie jakością. Teoria i praktyka*, Wydawnictwo Naukowe PWN, Warszawa 2006.
- [2] *Materiały informacyjne*, [www.bipromasz.pl](http://www.bipromasz.pl)
- [3] Roberts R.A., Stone R.B., Tumer Y., *Deriving function-failure similarity information for failure-free rotorcraft component design Method*, In ASME Design for Manufacturing Conference, 2002.
- [4] Arunajadai S.G., Stone R.B., Tumer Y., *Failure mode identification through clustering analysis*, Quality and Reliability Engineering International Journal, Vol. 20, 2004, 511-526.
- [5] Parker Hydraulic, *Hydraulic Cylinder Troubleshooting*, Bulletin 1242/1-GB.

- [6] Tadeusiewicz R., *Elementarne wprowadzenie do techniki sieci neuronowych z przykładowymi programami*, Akademicka Oficyna Wydawnicza PLJ, Warszawa 1998.
- [7] Jakubski J., Dobosz S.M., *Zastosowanie sieci neuronowych do sterowania jakością mas formierskich*, XXXIII konferencja naukowa z okazji Ogólnopolskiego Dnia Odlewnika 2009, Kraków 2009.



GRZEGORZ FILO\*

## ASYNCHRONOUS BUFFER READ METHOD IN DEVELOPMENT OF DAQ APPLICATION FOR SUPPORTING RESEARCH OF HYDRAULIC SYSTEMS

### METODA ASYNCHRONICZNEGO ODCZYTU BUFORA W BUDOWIE APLIKACJI DAQ WSPOMAGAJĄCEJ BADANIA UKŁADÓW HYDRAULICZNYCH

#### Abstract

The paper presents a method of data acquisition from a DAQ card using a direct memory access (DMA) and an asynchronous read of data buffer with the FIFO queue. The method can be used to acquire measurement data in Windows™ system when the required read frequency is higher than the system's clock frequency. The method was used in practice to measure high-speed pressure and position changes in a two cylinder hydraulic system with two-state fast switching valves.

*Keywords: DAQ system, asynchronous data buffer, software development, object oriented programming*

#### Streszczenie

W artykule przedstawiono metodę odczytu danych z karty pomiarowej z wykorzystaniem bezpośredniego dostępu do pamięci (DMA) oraz asynchronicznego odczytu bufora danych i kolejki FIFO. Metoda ta ma zastosowanie do akwizycji danych pomiarowych w systemie Windows, jeżeli wymagana częstotliwość odczytu jest większa od częstotliwości zegara systemowego. Opracowaną metodę zastosowano do pomiaru szybkich zmian ciśnienia i położenia w układzie z dwoma siłownikami i dwustanowymi szybkimi zaworami przełączającymi.

*Słowa kluczowe: system akwizycji danych pomiarowych, asynchroniczny bufor danych, budowa oprogramowania, programowanie obiektowe*

---

\* Ph.D. Grzegorz Filo, Institute of Applied Informatics, Cracow University of Technology.

## 1. Introduction

Most activities related to science and research require the use of data acquisition systems (DAQ) in order to measure many kinds of physical parameters. The fundamental information on the techniques, methods and devices used in the DAQ systems can be found in [1]. Usually, the systems consist of A/D and D/A transducers and their operation is strictly connected with data conversions, which is presented in [2].

Presently, several different types of DAQ systems are used, as stated in [3]. The first option is to use a computer-based system with a DAQ card installed. In this case, the card is responsible for performing the A/D and D/A conversions, acquiring data and storing it in the memory. The computer software communicates with the card via the dedicated driver and performs processing, storage and visualization of the data. The next possibility is to use a system based on autonomous devices, which, however, may be connected to the computer directly using a serial or a parallel communication port. Systems of this kind are usually more expensive, although they are able to achieve higher data reading frequency. On the contrary, the modular data acquisition system consists of functional units connected by a dedicated system bus. The system may be individually assembled and configured to perform a particular task. Usually, the modular DAQ systems are fully self-contained and do not require additional hardware.

In this work a computer-based system is considered, because it is a low cost, universal solution which can be used in various experiments without the need to replace hardware elements. A typical DAQ card for a computer-based system (Fig. 1) contains analog input (AI) and digital input (DI) ports. Some models also have analog output (AO) and digital output (DO) ports. The sampling rate of A/D and D/A converters installed in low-cost cards is usually in the range of 100 kHz to 1 MHz. [4].

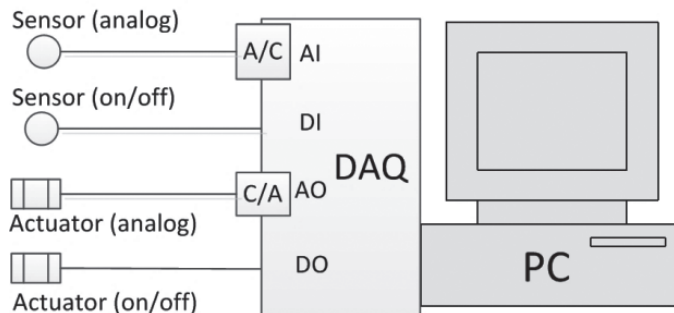


Fig. 1. Typical computer-based DAQ system

## 2. Algorithm and implementation

Application programming interface provided by a DAQ device driver allows a programmer to use two modes of analog input data read by a software-triggered function or an interrupt

function [5, 6]. The software-triggered mode is based on a system timer [6]. Therefore, it does not allow the driver to obtain a high read frequency. Depending on the hardware, the maximum sampling rate in this case is from 20 Hz to 50 Hz. In contrast, data transfer based on interrupts is performed in the background. It, thus, uses less CPU time and speeds the transfer rate. Therefore, this method is recommended for larger amounts of data transfer at higher rates. In general, there are two kinds of interrupt operations for analog input. One generates a hardware interrupt for each conversion, the other one keeps the conversion data in a first-in-first-out (FIFO) queue, then generates a hardware interrupt for half-full of FIFO, or full of FIFO.

The method presented in this work is based on the half-full FIFO hardware interrupt generation. The applied algorithm is presented in Fig. 2.

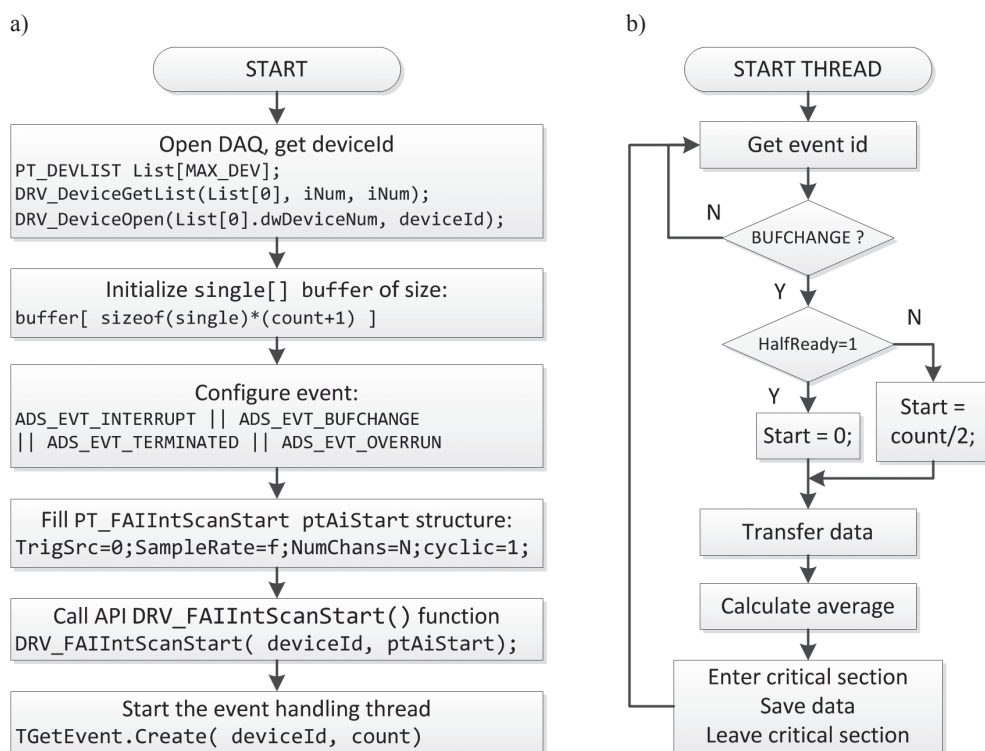


Fig. 2. Algorithm of data acquisition based on half-full FIFO hardware interrupt generation: a) initializing code, b) event handling thread

As can be seen from Fig. 2, the code is divided into two main parts. The first one contains initializing instructions: opening the DAQ device, initializing memory buffer, configuring event id's, filling the proper data structure initializing interrupt data transfer and starting the event handling thread. The second part consists of the thread main loop. At the beginning the event id is read. If the id is `ADS_EVT_BUFCHANGE`, the `HalfReady` flag is checked. On the basis of the value, the first or the second half of the data buffer is transferred into



the data array. Then, the average value is calculated and stored in the global array using the TRTLCriticalSection structure.

### 3. Object of study

A diagram of a hydraulic system used to test the developed DAQ algorithm is presented in Fig. 3.

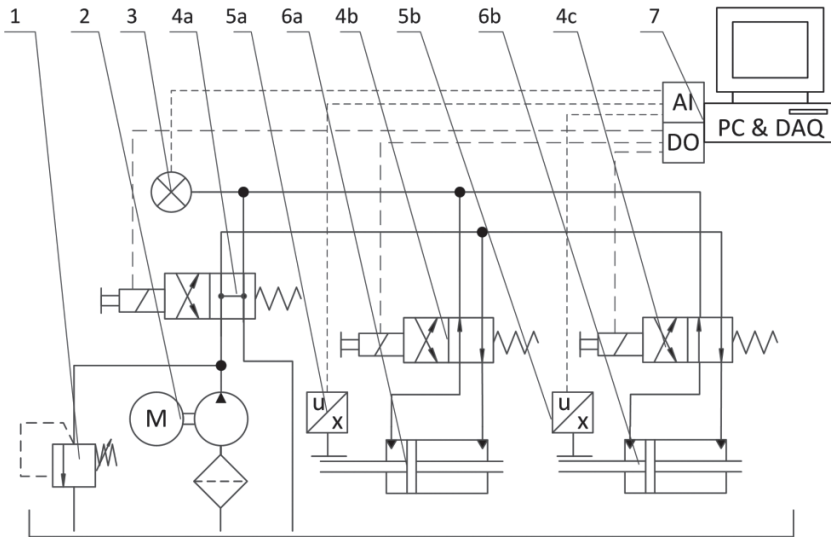


Fig. 3. Hydraulic system: 1 – relief valve, 2 – supply unit, 3 – pressure transducer, 4a, 4b, 4c – control valves, 5a, 5b – displacement transducers, 6a, 6b – hydraulic cylinders, 7 – DAQ system

The hydraulic system contains a supply unit 2 with a proportional relief valve 1, the main control valve 4a and two subsystems (4b, 6a and 4c, 6b), each consisting of a control valve and a hydraulic cylinder. The DAQ system acquires data from a pressure transducer 3 and two displacement transducers 5a, 5b through the AI ports. It also generates binary control signals for control valves using the DO ports. The created test bench is shown in Fig. 4.

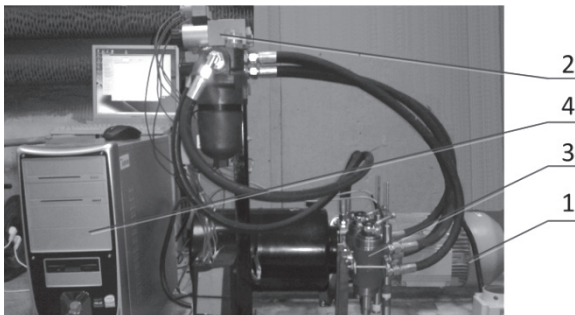


Fig. 4. Test bench: 1 – supply system, 2 – control valves, 3 – hydraulic cylinders, 4 – DAQ system

#### 4. Measurement results

The following values of the DAQ program parameters were set in order to investigate the hydraulic system: the base sampling frequency  $f_{base} = 32$  kHz, number of AI channels to read  $n_c = 4$ , number of samples used to calculate the average value in each step  $n_s = 8$ . Therefore, the resulting sampling frequency  $f_{res}$  was:

$$f_{res} = \frac{f_{base}}{n_c \cdot n_s} = 1 \text{ kHz} \quad (1)$$

The experiments consisted in setting the input signals for each control valve and investigating the system response. The input signal was in the form of a set of rectangular pulses. The response included signals from the displacement transducers and from the pressure transducer. Sample result plots of the pressure and the cylinder displacements are presented in Fig. 5, while in Fig. 6 are shown selected time charts of cylinder 2 displacement in a narrow time interval.

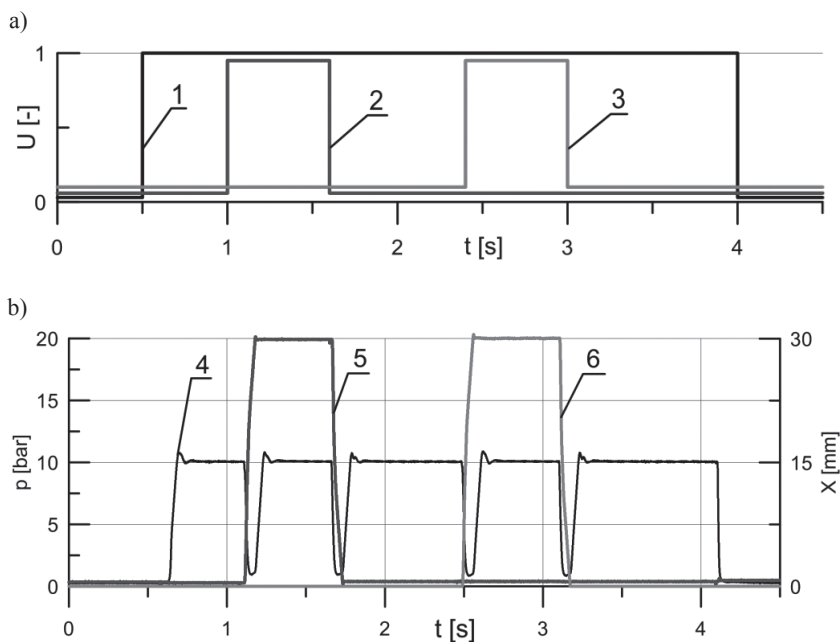


Fig. 5. Time plots: a) input functions, b) time charts; 1 – main control valve, 2, 3 – control valves of cylinders, 4 – pressure, 5 – cylinder 1 displacement, 6 – cylinder 2 displacement

As can be seen from Fig. 5–6, the delay time between setting the input function value and starting the cylinder movement is about 0.09–0.11 s. The movement over a distance of 0.03 m takes about 0.06–0.07 s.

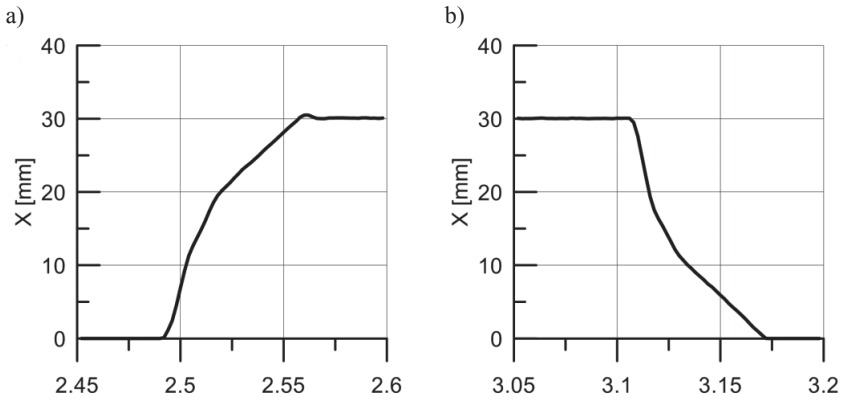


Fig. 6. Section of the cylinder 2 movement chart: a) forward movement, b) backward movement

## 5. Conclusions

This paper concerns the issues of a software development for computer-based DAQ systems. The software was built using the techniques of the object-oriented programming and multi-thread programming. The presented practical application involves using software for acquiring data in the 2-cylinder hydraulic system. The resulting plots of signals indicate that this method allows for reliable and accurate results to be obtained.

The proposed half-buffer read method is universal. Although the sufficient sampling frequency used in the presented experiments was 1 kHz, the tests up to 10 kHz (4 AI ports) or 64 kHz (1 AI port) were also carried out and were successful. The method is limited only by the DAQ card parameters and the computer system's performance.

## References

- [1] Maurizio Di Paolo E., *Data Acquisition Systems*, Springer, 2013.
- [2] Analog Devices Inc., edited by Kester W., *The Data Conversion Handbook*, Newnes 2005.
- [3] Ferrero Martín F.J., Valledor Llopis M. et.al., *Low-cost open-source multifunction data acquisition system for accurate measurements*, Elsevier, Measurement, Vol. 55, 2014, 265-271.
- [4] Advantech, *Advantech Device Driver Manual*, Advantech Industrial Automation, <http://www.advantech.com/industrial-automation>, 2011.
- [5] Włodarczyk P., Pustelny S., Budker D., Lipiński M., *Multi-channel data acquisition system with absolute time synchronization*, Elsevier, Nuclear Instruments and Methods in Physics Research Section A: Accelerators, Spectrometers, Detectors and Associated Equipment, Vol. 763, No. 2014, 150-154.
- [6] Patel J.J., Reddy N. et.al., *Embedded Linux platform for data acquisition systems*, Elsevier, Fusion Engineering and Design, Vol. 89, Issue 5, 2014, 684-688.

GRZEGORZ FILO\*

## THE USE OF LINEAR GUIDES TO MOVE HEAVY LOADS

---

### ZASTOSOWANIE PROWADNIC LINIOWYCH DO PRZEMIESZCZANIA CIĘŻKICH ŁADUNKÓW

#### Abstract

The paper presents results of laboratory tests of linear guides in the application to move heavy loads. The first phase of the work included construction of a test bench in the form of a steel frame running on profiled rails using HIWIN type blocks. Subsequently, investigations involving movement of the frame with various loads were performed. In each case a driving force of an operator was measured. Based on the obtained results, average values of the resistance to motion coefficients were estimated.

*Keywords: linear guides, heavy load movement, resistance to motion coefficient*

#### Streszczenie

W artykule przedstawiono wyniki badań laboratoryjnych prowadnic liniowych w zastosowaniu do przesuwania ciężkich ładunków. Pierwszy etap prac obejmował budowę stanowiska badawczego w postaci stalowej ramy poruszającej się po szynach profilowych z wykorzystaniem wózków typu HIWIN. Następnie przeprowadzono badania polegające na przemieszczaniu ramy z różnymi obciążeniami i pomiarze, w każdym przypadku, niezbędnej siły napędowej. Na podstawie wyników badań oszacowano wartości średnie rzeczywistych współczynników oporów ruchu.

*Słowa kluczowe: prowadnice liniowe, przesuwanie ciężkich ładunków, współczynnik oporu ruchu*

---

\* Ph.D. Grzegorz Filo, Institute of Applied Informatics, Cracow University of Technology.

## 1. Introduction

Linear guides with profiled rails are usually used to provide movement of heavy loads over straight, short distances. The guides can have many practical applications. They can be used in the case of a constant load and low accuracy requirements, as well as when high positioning accuracy, stiffness, resistance to vibration and shock is needed, as stated in [1]. Example applications in the first case, with no special requirements for accuracy, include providing the X-Y movement in devices such as conveyors, packaging machines, welding machines, etc. On the other hand, obtaining the movement of strictly defined parameters, as accelerations, velocities and precise positioning is extremely important in the development of laboratory test benches, high precision measurement technology or numerically controlled devices, as machining centers, EDM machines, lathes, milling machines, cutting machines etc. [2].

A typical linear guide system consists of two rails with an attached even number of movable guide blocks (Fig. 1). Inside of each guide block, a set of rolling elements in the form of metal balls is placed. During the movement, the balls are rolling along a raceway of a rail, which causes a significant reduction of the friction force and allows the operator to perform a precise linear movement. One of the main characteristics of this type system is practically no difference between the static and the dynamic coefficient of friction [2]. This feature means that the load can be moved along the rails using a very small driving force, as well avoid the adhesion effect (slip-stick).

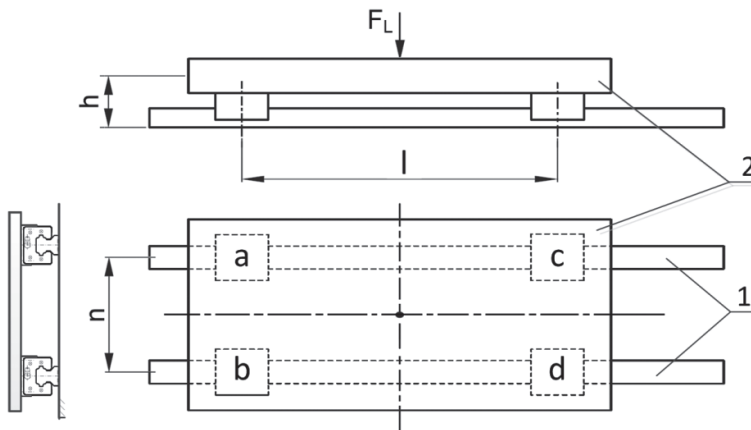


Fig. 1. A diagram of a typical linear guide system: 1 – rails, 2 – frame, a, b, c, d – guide blocks

Modeling and researching linear guide systems is the subject of many projects carried out by the leading research centers. One of the issues undertaken in the research work is to obtain the appropriate characteristics of the motion. For this purpose, M. Rahman et.al. proposed the use of special polymer materials and the proper design of guide blocks [6]. The alternative high-accuracy positioning system based on linear guides was developed by C. Brecher et.al. [5]. In terms of modeling and testing the linear guides' accuracy, the straightness

error measurement methodology has been developed [4]. Furthermore, J.-M. Lai et.al. built a mathematical model and software for the accuracy error diagnosis and measurement using the nonlinear double-ball bar technique (DBB) [7]. Modeling of linear guide geometric errors was the subject of research carried out by P. Majda [3]. The conclusions of this work indicate that the geometric deformations of elements such as rails or guide blocks, which mainly result from the properties of the substrate, may cause additional inaccuracies in the system, what can lead to the increase of the resistance to motion coefficient.

In this work tests of a HIWIN linear guide system were carried out. The system was designed to move large loads on a typical concrete floor. The floor was characterized by the following parameters: maximum undulation  $u < 5.0$  mm/m, roughness  $\mu < 50$   $\mu\text{m}$  and inclination  $i < 1.0\%$ . During the tests, the force required to move the loaded frame was measured. As a result, the actual values of the resistance to motion between the rail and the guide blocks were calculated for various loads. The obtained values were then presented in charts and compared with those which were supplied by the manufacturer of the linear guide system.

## 2. Object of research

Laboratory tests of the linear guide system were carried out on a test bench, which is presented in Fig. 2.

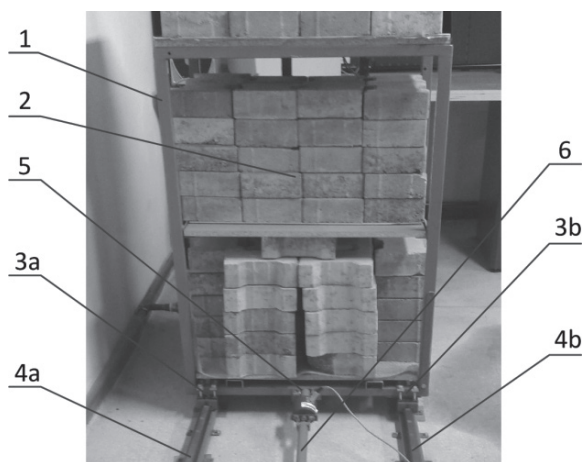


Fig. 2. Object of research: 1 – steel frame, 2 – payload, 3a, 3b – guide blocks, 4a, 4b – rails, 5 – driving force sensor, 6 – handle

The test bench consists of a steel frame 1, which is mounted on four guide blocks (3a, 3b). The guide blocks move on rails 4a, 4b. Cement cubes 2 are applied as a load. The whole system is driven by an operator using a handle 6 with mounted force transducer 5. A CL14U strain gauge force transducer with the symmetric range  $\pm 0.2$  kN is used. The HIWIN guide blocks have the total nominal carrying capacity of  $C_{\max} = 18.8$  kN.

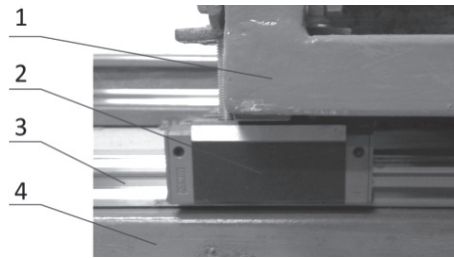


Fig. 3. Attachment of guide block: 1 – frame, 2 – guide block, 3 – rail, 4 – support

Fig. 2 shows the connection between the frame 1 and the guide block 2. As can be seen from the figure, the frame and the guide block are fixed inseparably. On the other side, the block may move on the rail 3, which is attached to the U-shaped section 4 in order to increase the stiffness.

### 3. Results of experiments

Experiments consisted in loading the frame using cement blocks of a certain weight, moving the system over a distance of 3.0 m, then stopping and moving back to the initial position. The experiments were performed with the load from  $F_{L1} = 2.0$  kN to  $F_{L5} = 10.0$  kN with the increment  $\Delta F = 2.0$  kN. The measurement data was acquired using a 14 bit D/A converter with the frequency  $f = 20.0$  Hz. Examples of time plots of the driving force are shown in Fig. 4, while a summary of the results with calculated values of the resistance to motion coefficients are presented in Table 1.

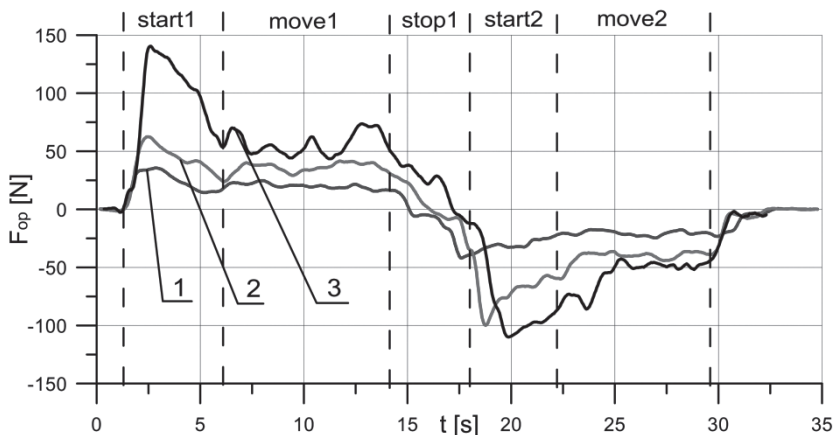


Fig. 4. Time plots of operator force: 1 –  $F_L = 2.0$  kN, 2 –  $F_L = 6.0$  kN, 3 –  $F_L = 10.0$  kN

The presented time plots of the driving force include the following phases of the movement: start of the forward movement **start1**, uniform forward movement **move1**, stop of the movement **stop1**, start of the return movement **start2**, uniform return movement **move2**. Average values of driving forces were calculated on the basis of measurements during both uniform movement phases.

As can be seen from the presented results of the experiments, the value of the summary resistance to motion coefficient decreases as the load increases, from  $\mu = 0.01$  for  $F_{L1} = 2.0$  kN, to  $\mu = 0.0057$  for  $F_{L5} = 10.0$  kN. The values of the coefficient as a function of the load force are presented in Fig. 5 with a second degree polynomial approximating curve. The required driving force as a function of the nominal load percentage and its extrapolation is shown in Fig. 6.

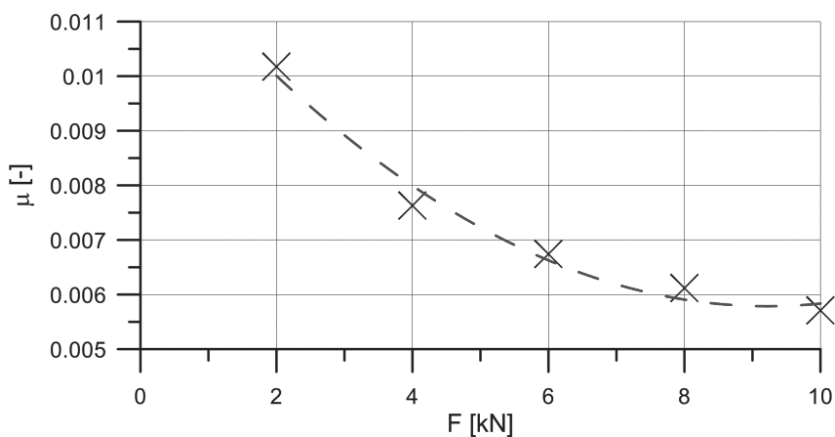


Fig. 5. Resistance to motion coefficient as a function of load force

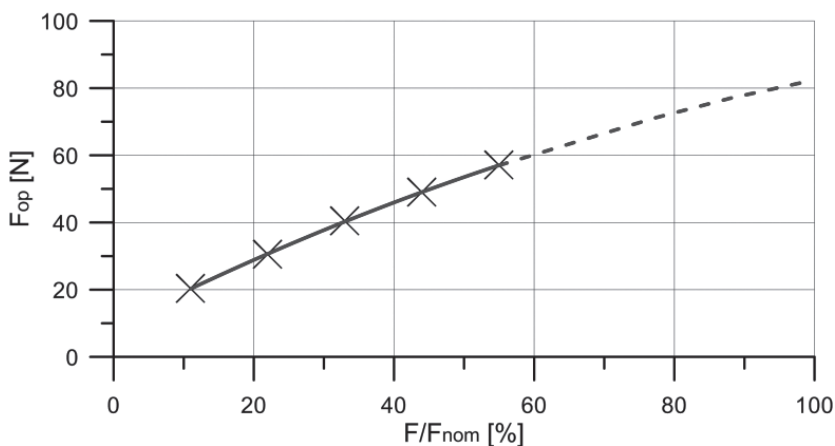


Fig. 6. Required operator force as a function of nominal load percentage



**Summary of driving forces and resistance to motion coefficients**

$F_L$ [kN]	Average operator force [N]		Average operator force [N]	Resistance to motion coefficient
	Forward	Backward		
2.0	19,90	20,77	20,34	0,01017
4.0	30,54	30,48	30,51	0,00763
6.0	39,62	41,27	40,45	0,00674
8.0	47,87	50,11	48,99	0,00612
10.0	56,42	57,68	57,05	0,00571

#### 4. Conclusions

This article concerns the use of a linear guide system to move heavy loads under typical conditions of industrial halls. The test bench was built using typical assembling techniques without any special measuring devices. Neither smoothness nor hardness of the floor was increased. Profiled rails and HIWIN guide blocks were used. Typical cement cubes were used as the load. The experiments were conducted with the load value from 2 kN to 10 kN. It can be seen from the results, that the minimum value of the resistance to motion coefficient  $\mu = 0.0057$  was obtained for the largest load. This result is similar to the catalogue data, which gives the value of the order of 0.004–0.005. The results indicate, that linear guides can be successfully used under the typical conditions of industrial halls or warehouses.

#### References

- [1] HIWIN, *Assembly instructions linear guideways*, Motion Control & Systems Catalogue, HIWIN GmbH, Germany, 2014.
- [2] Bosch Rexroth, *Online Catalog Linear Motion Technology*, Bosch Rexroth AG, Lohr am Main, Germany, 2014.
- [3] Majda P., *Modeling of geometric errors of linear guideway and their influence on joint kinematic error in machine tools*, Precision Engineering, Vol. 36, Issue 3, July 2012, 369-378.
- [4] Zhu L.-J., Li L., Liu J.-H., Zhang Z.-H., *A method for measuring the guideway straightness error based on polarized interference principle*, International Journal of Machine Tools and Manufacture, Vol. 49, Issues 3–4, March 2009, 285-290.
- [5] Brecher C., Utsch P., Klar R., Wenzel C., *Compact design for high precision machine tools*, International Journal of Machine Tools & Manufacture, Vol. 50, Issue 4, April 2010, 328-334.

- [6] Rahman M., Mansur M.A., Lee L.K., Lum J.K., *Development of a polymer impregnated concrete damping carriage for linear guideways for machine tools*, International Journal of Machine Tools and Manufacture, Vol. 41, Issue 3, February 2001, 431-441.
- [7] Lai J.-M., Liao J.-S., Chieng W.-H., *Modeling and analysis of nonlinear guideway for double-ball bar (DBB) measurement and diagnosis*, International Journal of Machine Tools and Manufacture, Vol. 37, Issue 5, May 1997, 687-707.



JACEK HABEL\*

THE IDEA OF DATABASE  
FOR RECORDING INTERMEDIATE STATES  
OF ROTARY PARTS FOR CAPP USE

---

KONCEPCJA BAZY DANYCH  
DO ZAPISU STANÓW POŚREDNICH PRZEDMIOTÓW  
OBROTOWYCH DLA POTRZEB SYSTEMÓW CAPP

Abstract

The paper presents a developed database for recording intermediate states of a workpiece. This solution can be used for automation of the calculation process, intermediate states and blank design generation for wide sets of parts. The calculation formulas, decision parameters and definition of intermediate states are also presented in this paper. The results from the developed SQL queries are attached. The presented idea and implemented database will reduce the time of design of a blank for *rotary and axisymmetric parts* in machining processes.

*Keywords: CAPP, intermediate states of features*

Streszczenie

W artykule przedstawiono bazę danych opracowaną do zapisu stanów pośrednich przedmiotu obrabianego. Prezentowane rozwiązanie pozwala na automatyzację procesu obliczeniowego oraz generowanie stanów pośrednich i półfabrykatu dla szerokiego zbioru części. Stosowne wzory, parametry decyzyjne, definicja stanów pośrednich również zostały przedstawione. Dołączono również przykładowe rezultaty działania opracowanych kwerend SQL. Prezentowany pomysł i zaimplementowana baza danych pozwolą na znaczne skrócenie czasu projektowania półfabrykatów dla przedmiotów obrotowych osiowosymetrycznych, stosowanych w obróbce skrawaniem.

*Słowa kluczowe: CAPP, stany pośrednie cech technologicznych*

---

\* Ph.D. Eng. Jacek Habel, Production Engineering Institute, Faculty of Mechanical Engineering, Cracow University of Technology.

## 1. Introduction

The Computer Aided Process Planning (CAPP) systems are still a promising solution. Other CAx systems, like CAD (Computer Aided Design) or CAM (Computer Aided Manufacturing) are very popular on the market. CAD systems offer e.g. parametric 3D design and facilities to create 2D drawings. CAM systems mostly support the cutting machinetool NC code generation. There are also available integrated CAD/CAM solutions, like Dassault Systemes CATIA. But there is a gap between these systems. The engineers have to create 3D models of a product and then they can use it to create a machining process in CAM. Unfortunately, they need to be a specialist in machining process planning. They have to predict which machinetools will be used, what equipment is necessary, what tools can be applied, how to calculate machining parameters and other similar features. This task could be aided by CAPP systems.

The idea of a CAPP system is not new. The first research studies were published more than 30 years ago. A good example of the CAPP theory can be found in [1]. Chang, in his book [1], defines possible scenarios to create a CAPP system using different techniques. The CAPP system implementation depends on the selected method. The following methods can be distinguished [1]: variant, generative and semi-generative.

The CAPP system is a tool used to create the process plan. It could aim at different manufacturing methods, but a typical application is to aim at machining process planning [3, 5]. In that case, input information is a workpiece data. This data can be entered into the CAPP system manually or can be retrieved from the CAD system (based on e.g. feature recognition procedures) [4, 5]. The machining process plan, recorded and presented in different forms, is an output from CAPP.

## 2. The intermediate states in the machining process

The manufacturing process can be, in general, described as follows. The given *part*, which has to be machined from a selected (or designed) *blank* (semi-finished product or raw material), is passing through successive stages of that process. As a result, the *ready part* (final product), which fulfills quality requirements, is processed. The *workpiece*, passing through the process, is changing its *state* (see Fig. 1), which is referred to as *intermediate state of workpiece features*  $S_f$  where  $f$  is an index of an intermediate state and  $f = 0 \dots F$ , where  $F$  is the highest number of recorded  $S_f$ . There are two special states: *initial state*  $S_0$ , given by a blank design and *final state*  $S_F$ , given by a ready part drawing.

The intermediate states are necessary to create operational drawings, but the creation method depends on their part class (from a technological point of view). To simplify further his considerations, the author made an assumption to consider only *rotary and axisymmetric parts*. This class contains parts like shafts, axles, screws, sleeves, disks etc. It is a very wide class of parts used in mechanical design.

To create a machining process plan, the design of a blank is necessary. The type, geometry, quality of the designed blank has a big influence on the machining process's structure, number of operations, time and cost. That means, the selection and design of a blank is a very significant stage. If the design of a blank is known, then the machining process can be planned.

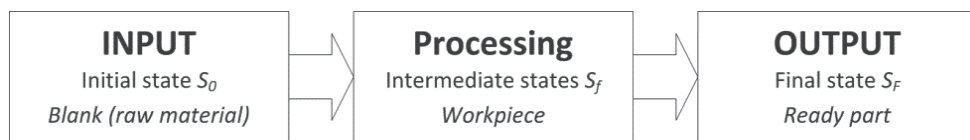


Fig. 1. General model of manufacturing process and intermediate states of workpiece

The design of a blank can be created using a reverse method. By prediction of previous stages, the following intermediate states can be created. Starting from the ready part drawing, the stages like: before finishing (BFN), before medium turning (BMT) and before roughing (BRG) can be calculated. To do this proper values of operational allowances should be applied. Below the process of blank design creation will be presented with intermediate states recording, based on a sampleshaft, presented in Fig. 2.

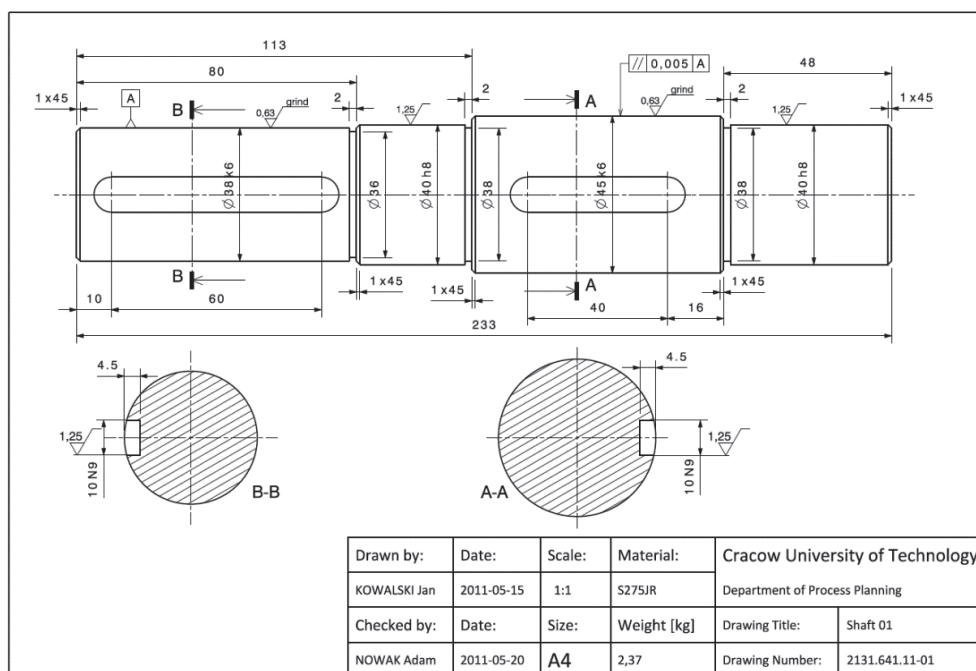


Fig. 2. The example shaft No. 01

The main goal is to design a blank. To do this, it is necessary to find out:

- How to fix the part? It has influence on the predicted cutting allowances.
- How much material will be removed in the form of chips? From the economical point of view, it can be a decisive factor in the blank type selection.

- How many operations have to be applied for each feature (e.g. cylindrical surface)? It has influence on the number of operational allowances.
- The value of operational allowances. It has an influence on the blank's dimensions.

The first decision factor can be  $C_{SR}$ , slenderness of the shaft. It can be calculated using a simplified formula:

$$C_{SR} = \frac{L_T}{D_{\max}} \quad (1)$$

where:

- $L_T$  – total length of the shaft,
- $D_{\max}$  – diameter of the biggest cylindrical surface.

In case of shafts there are three main fixing possibilities:

- In 3-jaw chuck, which is recommended when  $C_{SR} < 3$ ,
- Between centers (or in 3-jaw chuck and supported by live center) is recommended when:  $3 < C_{SR} < 12$ ,
- Between centers with a steady roll it is recommended when:  $C_{SR} > 12$ .

To evaluate how much material will be removed in the form of chips we need to calculate the volume of workpiece  $V_{WP}$  and the volume of the cylinder envelope of workpiece  $V_{CE}$ . It could be calculated using the following formulas:

$$V_{WP} = \sum_{s=1}^n V_s = \sum_{s=1}^n \frac{\pi \cdot l_s \cdot d_s^2}{4} \quad (2)$$

$$V_{CE} = \frac{\pi \cdot L_T \cdot D_{\max}^2}{4} \quad (3)$$

where:

- $s$  – number of step in the analyzed shaft,  $n$  is a total number of steps,
- $l_s$  – length of step of the shaft (cylindrical surface),
- $d_s$  – diameter of step of the shaft,
- $V_s$  – volume of step of the shaft [dm<sup>3</sup>].

Then it is possible to calculate the mass using the following formula:

$$m = \rho \cdot V \quad (4)$$

When volume  $V$  [dm<sup>3</sup>] is calculated, mass  $m$  [kg] results from (4) if material density  $\rho$  is given. For most types of steel  $\rho$  is about 7.85 [kg/dm<sup>3</sup>].

The mass of the removed material  $m_{CP}$  in the form of chips can be expressed as:

$$m_{CP} = m_{CE} - m_{WP} \quad (5)$$

Finally, yield coefficient  $C_Y$  [%], as an absolute rate measured by percentage of the removed material can be calculated from:

$$C_Y = \frac{V_{CE} - V_{WP}}{V_{CE}} \cdot 100\% \quad (6)$$

The value  $C_Y$  can be used for blank type selection. For example, if  $C_Y < 40\%$  we can select the hot-rolled bar, If  $C_Y > 40\%$  we should select the forging type. The limit value (like in this example 40%) should be calculated as a minimum cost balance between the blank's price and the manufacturing cost. This limit is very dependent on the volume of production.

To find out how many operations  $Q_{OP}$  should be applied for each feature, increase accuracy coefficient  $C_A$  can be used. It compares tolerances of applied blanks and each step of the shaft (defined in workshop drawing) [2]:

$$C_A = \frac{T_{BL}}{T_{Fi}} \quad (7)$$

where:

- $T_{BL}$  – tolerance of the selected type of blank [ $\mu\text{m}$ ],
- $T_{Fi}$  – tolerance of a given feature (e.g. cylindrical surface) [ $\mu\text{m}$ ].

Based on  $C_A$  the value can be decided:

- If  $C_A < 10$  then one operation is sufficient,  $Q_{OP} = 1$ ,
- If  $10 < C_A < 50$  then two operations are necessary,  $Q_{OP} = 2$ ,
- If  $C_A > 50$  then three operations will be needed,  $Q_{OP} = 3$ .

The last stage is prediction of cutting allowances. There are a few methods, which can be applied, but the simplest one is to use allowance standards. For example, the IOS Kraków has worked out such standards [2]. The way of finding the right value of allowance is crucial. It is realized in a few steps. Firstly, the class of the part and its material should be recognized. Then the fixing way (workpiece setup), machining type and range should be defined. Finally, having regard to the above criteria, the right data table can be found. This data table contains values of allowances with division into workpiece sizes (length and diameter). It is needed to find out the total length  $L_T$  and average diameter  $D_{AVG}$  (note: this should be equivalent diameter, which gives the same value of the shaft's deflection like the original stepped shaft) of the part. To calculate this equivalent diameter, a simplified formula can be used:

$$D_{AVG} = \frac{A_{WP}}{L_T} = \frac{\sum_{s=1}^n A_s}{L_T} = \frac{\sum_{s=1}^n (l_s \cdot d_s)}{L_T} \quad (8)$$

where:

- $A_{WP}$  – area of longitudinal cross-section of all workpieces [ $\text{mm}^2$ ],
- $A_s$  – area of longitudinal cross-section of a given step of the shaft [ $\text{mm}^2$ ].



Using the presented above formulas, the following results for the sample shaft (see Fig. 1) can be presented for each step of the shaft (Table 1) and for the workpiece (Table 2).

Table 1

**Parameters calculated for each step of Shaft 01**

$s$	$l_s$ [mm]	$d_s$ [mm]	$A_s$ [mm <sup>2</sup> ]	$V_s$ [dm <sup>3</sup> ]	$m_s$ [kg]	$IT$	$T_{BL}$ [μm]	$T_{F1}$ [μm]	$C_A$	$Q_{OP}$
1	80	38	3040	0.0907	0.712	k6	1600	16	100	3
2	33	40	1320	0.0415	0.326	h8	1600	39	41	2
3	72	45	3240	0.1145	0.899	k6	1600	16	100	3
4	48	40	1920	0.0603	0.474	h8	1600	39	41	2

Table 2

**Parameters calculated for workpiece Shaft 01**

$L_F$ [mm]	$D_{max}$ [mm]	$C_{SR}$	$A_{WP}$ [mm <sup>2</sup> ]	$D_{AVG}$ [mm]	$V_{WP}$ [dm <sup>3</sup> ]	$V_{CE}$ [dm <sup>3</sup> ]	$C_Y$ [%]	$m_{WP}$ [kg]	$m_{CE}$ [kg]	$m_{CP}$ [kg]
233	45	5.1	9520	40.8	0.307	0.370	17.1	2.41	2.9	0.49

Table 3

**The calculated intermediate states of Shaft01 (diameters before: BFN, BMT, BRG)**

$s$	$l_s$ [mm]	$d_s$ [mm]	$Q_{OP}$	$d_{BFN}$ [mm]	$d_{BMT}$ [mm]	$d_{BRG}$ [mm]	$d_{BL}$ [mm]
1	80	38	3	38.3	38.9	42.0	50
2	33	40	2	40.0	40.6	43.7	50
3	72	45	3	45.3	45.9	49.0	50
4	48	40	2	40.0	40.6	43.7	50

Moreover, for *Shaft01* the following allowances were selected:

- $Q_{RG} = 3.1$  [mm], allowance on a diameter for rough turning,
- $Q_{MT} = 0.6$  [mm], allowance on a diameter for medium turning,
- $Q_{FN} = 0.3$  [mm], allowance on a diameter for finishing (grinding).

Using these allowance values, the intermediate states of *Shaft01* were calculated. The results are presented in Table 3. Because the yield coefficient is only  $C_Y = 17.1$ [%] and the maximum diameter (including necessary allowances) is  $d_{BRG} = 49$ , it was decided to choose a hot-rolled bar (a blank type) with  $\varnothing 50$  (the bigger one, available on the market) and  $T_{BL} = 1,6$  [mm].

### 3. The idea of a database for recording intermediate states

The most important question is about the process: Can it be automated? (see section 2 above). The answer is yes if the relational database is used.

To realize this idea it is necessary to record the geometry of the ready part, intermediate states and the blank. In the case of *rotary and axisymmetric parts*, the idea of 2.5D representation can be easily applied. Describing it very shortly: there is a closed contour (containing segments, arcs etc.) representing the upper-half of the cross section of the part, which can be rotated to get a 3D object. This method is used in 3D solid modelling and also in CAM to record workpiece geometry. Moreover, one important assumption was made. To simplify the calculation process, only the 1-st level of features will be considered. In case of rotary and axisymmetric parts, the 1-st level of features are machined first, for example their cylindrical (step of shaft), conical or spherical features. Then the 2-nd level features can be machined like: chamfer, rounding, undercut, keyway hole, metric thread etc.

Based on the idea presented above, the ERD diagram of relational database for recording intermediate states was developed and is presented in Fig. 3.

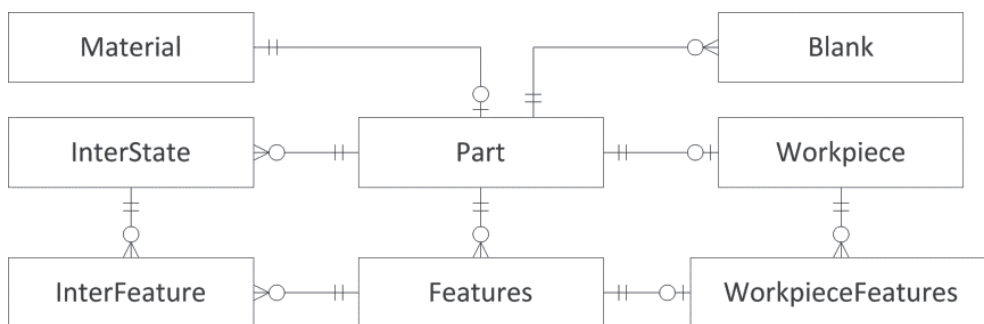


Fig. 3. The developed ERD diagram of relational database for recording intermediate states

To record a set of parts it is necessary to divide the data into two entities. The first table *Part* will contain a set of parts. The second table *Features* will contain the data describing each 1-st level feature of the part. The part can contain many features. Moreover, one material can be assigned to one part. The necessary calculations can be recorded in table *Workpiece* (data about the part) and in table *WorkpieceFeatures* (results for each feature). Using calculation results the intermediate states of a workpiece can be recorded (in table *InterState*) and intermediate states of all the features (in table *InterFeature*). The final result as a blank design can be recorded in table *Blank*.

Moreover, what is not presented on the ERD diagram, other necessary tables were added, which contain: the dimensions and tolerances of hot-rolled bars and forgings, the upper-lower deviations of fits, the cutting allowances for rough, medium and finish turning etc.

#### 4. The implementation of the database and its testing

Based on the developed ERD diagram, the database in MS Access 2010 was created. It contains tables, a user interface (window forms), queries and modules written in the VBA language. For testing purposes, the data about more than 30 different parts was entered into the database. The source data is in tables: *Material*, *Part* and *Features*.

The core procedures was based on SQL queries. First decision parameters were calculated (see section 2). The SQL query, presented below, calculates parameters of each feature (as computed columns). The results, for the first shaft, are presented in Table 4.

```
SELECT IDP, FtNo, D, L, IT, Ra, L*D AS A, 3.14159*([L]/100)*
([D]/100)*([D]/100)/4 AS V, 7.85*V AS m FROM Features;
```

Table 4

The results from the SQL query: calculated parameters for each feature of two selected shafts

IDP	FtNo	D	L	IT	Ra	A	V	m
Part001	1	38	80	6	0.63	3 040	0.09	0.71
Part001	2	40	33	8	1.25	1 320	0.04	0.33
Part001	3	45	72	6	0.63	3 240	0.11	0.90
Part001	4	40	48	8	1.25	1 920	0.06	0.47

The next query calculates parameters for each workpiece (includes aggregated functions and computed columns). The results for the first five shafts are presented in Table 5.

```
SELECT IDP, SUM(L) AS LT, MAX(D) AS Dmax, SUM(A) AS AWP,
SUM(V) AS VWP, SUM(m) AS mWP, LT/Dmax AS CSR, AWP/LT AS DAVG,
3.14159*([Lc]/100)*([Dmax]/100)*([Dmax]/100)/4 AS VCE,
7.85*VWP AS mCE, mCE - mWP AS mCP, (VCE-VWP)/VCE AS CY
FROM WorkpieceFeatures GROUP BY IDP;
```

Table 5

The results from the SQL query: calculated parameters for each of the five selected shafts

IDP	LT	Dmax	AWP	VWP	mWP	CSR	DAVG	VCE	mCE	mCP	CY
Part001	233	45	9520	0,307	2,41	5,1	40,8	0,37	2,9	0,49	17,1%
Part002	430	95	36 325	2,427	19,05	4,5	84,4	3,047	23,92	4,86	20,3%
Part003	310	45	10 800	0,307	2,41	6,8	34,8	0,493	3,87	1,45	37,6%
Part004	315	75	16 693	0,729	5,73	4,2	52,9	1,391	10,92	5,19	47,6%
Part005	444	56	18 218	0,594	4,66	7,9	41	1,093	8,58	3,91	45,6%

Next Table 6 presents the intermediate states of *shaft01* generated by the query, which combines the two tables (*InterState* & *InterFeature*). This example shows possibilities of using the developed database.

Table 6

**The results from the SQL query: the intermediate states of shaft01 – final results**

IDISP	InterName	IDIFN	IFSType	L	D	Ra	IT
Part001_FN	Before finishing	P1F1S1	CYL	80	38.3	1.25	9
Part001_FN	Before finishing	P1F2S1	CYL	33	40	1.25	8
Part001_FN	Before finishing	P1F3S1	CYL	72	45.3	1.25	9
Part001_FN	Before finishing	P1F4S1	CYL	48	40	1.25	8
Part001_MT	Before medium turning	P1F1S2	CYL	80	38.9	5	11
Part001_MT	Before medium turning	P1F2S2	CYL	33	40.6	5	11
Part001_MT	Before medium turning	P1F3S2	CYL	72	45.9	5	11
Part001_MT	Before medium turning	P1F4S2	CYL	48	40.6	5	11
Part001_RG	Before rough turning	P1F1S3	CYL	80	42	20	12
Part001_RG	Before rough turning	P1F2S3	CYL	33	43.7	20	12
Part001_RG	Before rough turning	P1F3S3	CYL	72	49	20	12
Part001_RG	Before rough turning	P1F4S3	CYL	48	43.7	20	12
Part001_BL	Hot-rolled bar	P1F1S4	CYL	3000	50	40	16

## 5. Conclusions

A lot of problems, in implementation of the CAPP system, are connected with workpiece data representation and automation of necessary calculations. The presented idea shows a simple solution of this problem. Thanks to the 2.5D representation of the workpiece (to record its features) and presented in section 2 formulas, it is possible to receive the necessary results automatically. It concerns intermediate states of the workpiece, which occur during machining in operations, and the final design of the blank.

This idea was used to build the database and was tested on more than 30 samples. All results confirm the correctness of the developed database. The next step of this work will be to use this module as a part of CAPP in a semi-generative method [3].

## References

- [1] Chang T.Ch., *Expert Process Planning for Manufacturing*, Addison-Wesley Publishing Company, USA 1990.
- [2] Feld M., *Podstawy projektowania procesów technologicznych typowych części maszyn – Wydanie 3*, Wydawnictwa Naukowo-Techniczne, Warszawa 2007.
- [3] Habel J., *The Idea of Integrated Manufacturing Process Planning System*, Proceedings of 16th FAIM International Conference, University of Limerick, Irland, June 2006, 185-192.
- [4] Pobożniak J., *Integration of CAD and Generative CAPP Based on Feature Technology*, Proceedings of the 3rd International Symposium on Intelligent Manufacturing Systems, Turkey 2001.
- [5] Sormaz D.N., Khoshnevis B., *Generation of alternative process plans in integrated manufacturing systems*, Journal of Intelligent Manufacturing, Vol. 14, 2003, 509-526.

MARCIN HOJNY\*, JACEK TARASIUK\*\*, SEBASTIAN WRÓŃSKI\*\*

## DEVELOPMENT OF THE MODELING STRATEGY FOR THE STEEL DEFORMATION IN SEMI-SOLID STATE – TOMOGRAPHIC STUDIES

### OPRACOWANIE KOMPLEKSOWEGO PODEJŚCIA DO MODELOWANIA ODKSZTAŁCANIA STALI W STANIE PÓLCIEKŁYM – BADANIA TOMOGRAFICZNE

#### Abstract

The condition of steel deformation in a semi-solid state should be as isothermal as possible due to the very high sensitivity of material rheology to even small variations of temperature. The basic reason for uneven temperature distribution (melting zone) inside the sample body on the Gleeble thermo-mechanical simulator is the contact with cold/warm copper handles. The semi-solid conditions in central parts of the sample cause even greater temperature gradient due to latent transformation heat. Such non-uniform temperature distribution is the source of significant differences in the microstructure and, hence, in material rheological properties. In the paper example results of tomographic studies were presented for both experimental variants (with warm and cold handles).

*Keywords: physical simulation, computer tomography, extra-high temperatures*

#### Streszczenie

Proces odkształcania stali w stanie półciekłym powinien być realizowany w warunkach izotermicznych, w związku z dużą czułością własności mechanicznych na niewielkie zmiany temperatury. Głównym powodem nierównomiernego rozkładu temperatury (kształtu strefy przetopienia) w objętości próbki jest wpływ użytych podczas eksperymentów uchwytów miedzianych, tzw. ciepłych i zimnych. Kolejnym ważnym czynnikiem wpływającym na kształt strefy przetopienia jest generowane ciepło krzepnięcia wpływające także bezpośrednio na kształt strefy przetopienia i właściwości mikrostrukturalne i reologiczne. W prezentowanej pracy przedstawiono przykładowe wyniki analiz tomograficznych dla dwóch próbek, z których każda była przetapiana w innej konfiguracji narzędzi (uchwyty zimne i ciepłe).

*Słowa kluczowe: symulacja fizyczna, tomografia komputerowa, wysokie temperatury*

\* Ph.D. Marcin Hojny, Faculty of Metals Engineering and Industrial Computer Science, AGH University of Science and Technology.

\*\* Ph.D. D.Sc. Eng. Jacek Tarasiuk, Ph.D. Sebastian Wroński, Faculty of Physics and Applied Computer Science, AGH University of Science and Technology.

## 1. Introduction

The physical simulations of the melting process were done in the Institute for Ferrous Metallurgy in Gliwice, Poland, using a Gleeble 3800 thermo-mechanical simulator. The steel used for the experiments was the C45 grade steel with 0.45% carbon content. During the experiments samples were heated to 1430°C and after being maintained at a constant temperature they were cooled down. More details about physical and computer simulations of steel deformations in a semi-solid state can be found in [6].

The micro tomography measurements presented in this paper were performed using a “nanotom 180N” device produced by GE Sensing & Inspection Technologies phoenix|X-ray GmbH. The machine is equipped with a nanofocus X-ray tube with a maximum of 180kV voltage. The tomograms were registered on a Hamamatsu 2300x2300 pixel detector.

The reconstruction of the measured objects was done with the aid of proprietary GE software datosX ver. 2.1.0 with the use of Feldkamp algorithm for a cone beam X-ray CT [1]. The post reconstruction data treatment was performed using VGStudio Max 2.1 [2] and a free Fiji software [3] with a plugin BoneJ [4] and Voxler®3 – Golden Software [5]. All the examined specimens were scanned at 160 kV of the source voltage and 60  $\mu$ A, with a rotation of the specimen of 360 degrees in 1600 steps. There was used an aluminum filter of 0.5 mm between the source and the sample. The exposure time was 500 ms and a frame averaging of 6 and image skip of 1 was applied, resulting in a scanning time of 93 minutes. The reconstructed images had a voxel size of  $(6,2 \mu\text{m})^3$ .

## 2. Example results

Both samples denoted as 501 (the variant with a cold handle) and 502 (the variant with a warm handle) underwent the same initial preparations before the final analysis. The reconstructions were denoised using a 3D median filter with the kernel size of 3x3x3, followed by the edge smoothing procedure with a 2D median filter with a 3x3 kernel. Then both samples were reoriented in a way that the origin of the referenced system is located in the middle of the vertical axe (Z axe) of the sample. The Y axe has a radial direction and coincides with the porous changes in the sample. The X axe is perpendicular to Y and Z with a direction fulfilling a clockwise reference system orientation (Fig. 1–2).

Figures 1–2 show the reconstructed surface of the samples with a visible melting zone produced during the experimental process. The topography surface shows a meaningful differences between the samples. The significant changes on the surface of sample 501 were observed, the structure formed in the melting zone reminds a porous material. For the second sample (502) similar changes were observed, although they were smaller and more rough on the surface of this area. The changes on the surface have an impact on the defected area inside the samples. In Figures 3–4 both samples were presented with a transparent surface, enabling to observe not only the outer surfaces of the sample but also its interior.



Fig. 1. Reconstructed surface of sample 501  
(cold handle)



Fig. 2. Reconstructed surface of sample 502  
(warm handle)

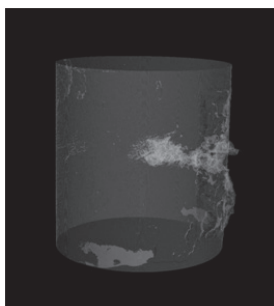


Fig. 3. Visualization of sample 501 in three  
spatial dimensions with transparency

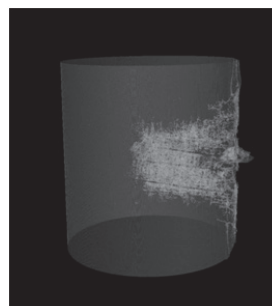


Fig. 4. Visualization of sample 502 in three  
spatial dimensions with transparency

The character of the pores obtained for both samples was different. In both cases, behind the melted area visible on the surface a considerable defected area occurred. Despite a much more complex surface structure of the melt in sample 501, the porous area formed behind that area is much smaller in the sense of the total volume than in the 502 sample. The specific damage visible as bright spots on the material's surface at the bottom of the sample are observable. These are the areas of the material stratification. In a 502 sample, despite a much more extensive area with visible pores and some observable regularities in their spatial arrangement, no damage close to the surface is observed. In both cases, the pore area ends near the sample's symmetry axis.

In the next step, a threshold value within the tomography images was selected, to separate areas filled with the material from the voids (empty areas). For this purpose, analyses of the signal intensity changes on the reconstruction images were conducted. Figure 5 presents changes for voids spaced apart from each other (solid curve) and closely located (point curve). On the basis of the curves' analysis, we decided to take the threshold value equal to 70. The reconstructed object areas with values below the threshold will be treated as voids, whereas the areas above the threshold as a solid metal.



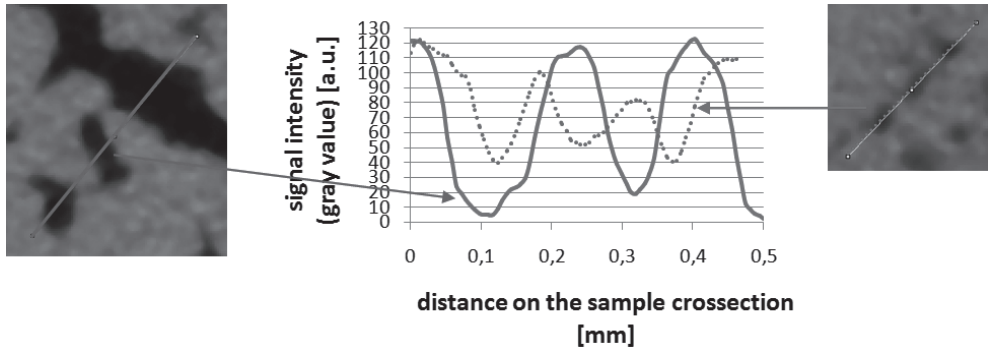


Fig. 5. Signal intensity on a sample reconstruction cross-section measured along the lines marked in a solid and points. Dark parts of the images correspond to the holes, light parts to the metal

After binarization a complex internal structure of the voids in both samples was obtained (Fig. 6a and Fig. 7a). Further analyses were based on the description of the voids within the material. For this purpose fragments belonging to the surface were removed from the

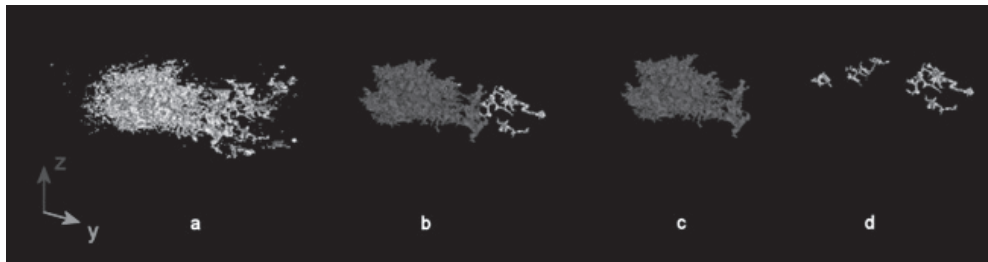


Fig. 6. Spatial structure of all voids in sample 501 (a), a large structure of the connected voids – red color, small non-interconnected voids – yellow color (b, c, d)

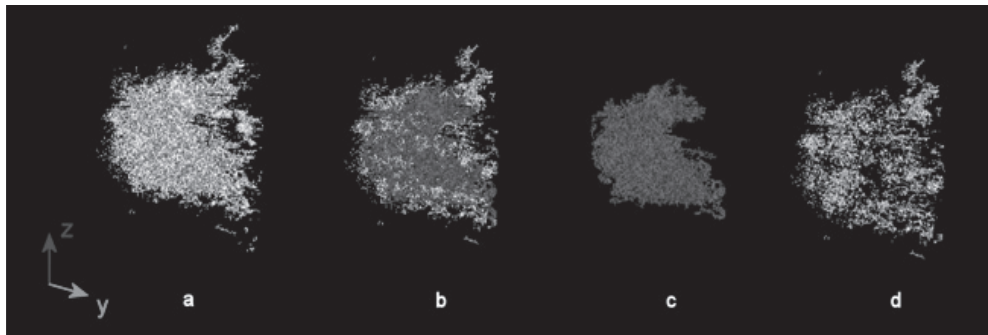


Fig. 7. Spatial structure of all voids in sample 502 (a), large structure of connected voids – red color, small non-interconnected voids – yellow color (b, c, d)

data analyzed. The analysis of the voids' continuity shows that in each sample there is only one large structure of interconnected voids and a big number of small separated voids. Visualization of the internal structures is shown in Figures 6–7. Figure 6a and Figure 7a present the spatial structure of all voids, whereas subsequent figures 6b, c, d and 7b, c, d represent a large structure of connected voids – the red color, and small separated voids – the yellow color.

To evaluate the structure's topology in both samples several parameters were calculated (detailed definitions of all parameters are given in [4] and [5]). Short descriptions of the calculated parameters are listed below. All parameters were calculated using ImageJ with Plugin BoneJ. The results were presented in Table 1:

- Volume, TV: total volume in the selected volume of interest (VOI), mm<sup>3</sup>.
- Surface: surface area of the structure. Iso-surface constructs a triangular surface mesh by marching cubes algorithm and calculates the surface area as the sum of the areas of the triangles making up the mesh. The triangulation uses smoothing algorithms, so the sum of the surface calculated for the structure and for the holes does not have to equal the surface calculated together for the structure and holes.
- Roughness: the area of the particle divided by the volume of the particle. Low value of roughness means smoother surface. A high value of this ratio means more rugged surface.
- Mean diameter: an average diameter [mm].
- St. dev of mean diameter: standard deviation of the mean diameter of a particle.
- Maximal diameter: the diameter of the largest particle [mm].
- DA: degree of anisotropy ( $DA = 1 - 1/tDA$ ), DA is 0 for isotropy and 1 for extremal anisotropy.

Table 1

#### Morphological parameters calculated for the examined samples

Parameter	Units	Sample 501			Sample 502		
		total	structure	holes	total	structure	holes
volume	[mm <sup>3</sup> ]	1.27	1.10	0.05	4.69	3.76	0.93
surface	[mm <sup>2</sup> ]	77	58	4	300	304	80
roughness	–	60.8	53.0	75.5	64.0	80.9	0.20
mean diameter	[mm]	0.069	0.075	0.053	0.053	0.057	0.040
st. dev. of mean diameter	[mm]	0.034	0.033	0.022	0.019	0.019	0.016
maximal diameter	[mm]	0.181	0.181	0.107	0.149	0.149	0.120
degree of anisotropy	–	0.09	0.10	1.0	0.45	0.49	0.42

Distribution of the voids' diameter is presented in Fig. 8.

In both samples a large number of unconnected voids was found. In the 501 sample, there were more than 1500 and in the 502 sample over 4500 holes. The voids, size (volume) distribution for both samples is shown in Fig. 9.

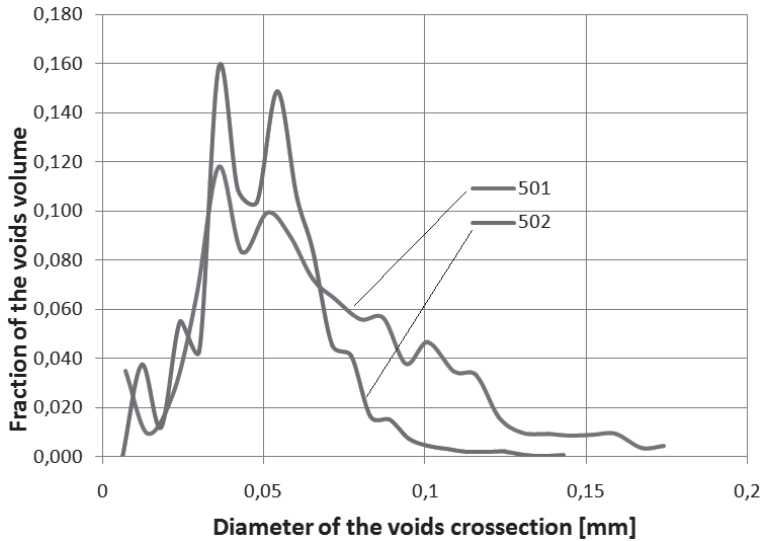


Fig. 8. Distribution of voids' diameters in both samples

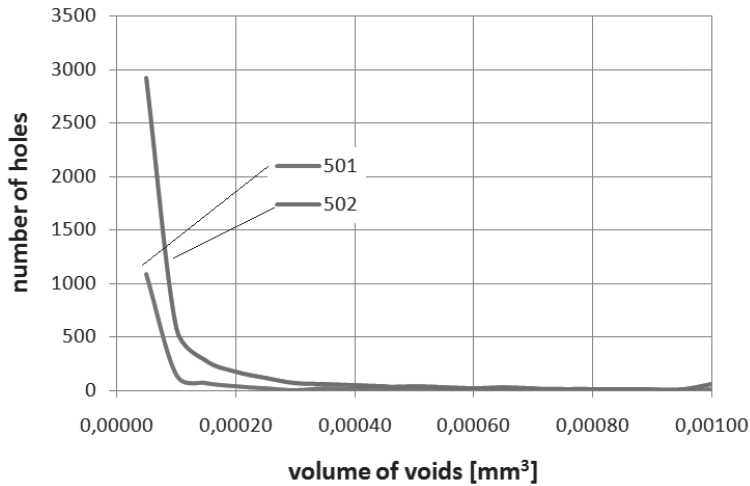


Fig. 9. Distribution of holes' volumes in both samples

For both samples the volume of the voids in each  $6.25 \mu\text{m}$  thick layer, perpendicular to the sample symmetry axis, was determined. The center of the coordinate system was arbitrarily located in the position of the sample's higher porosity (close to the center of the bar). Voids' volume distribution along the sample's symmetry axis was presented in Fig. 10. Both samples have a comparable maximum porosity near the centre, but the width of the porous zone is much larger in the 501 than in the 502 sample.

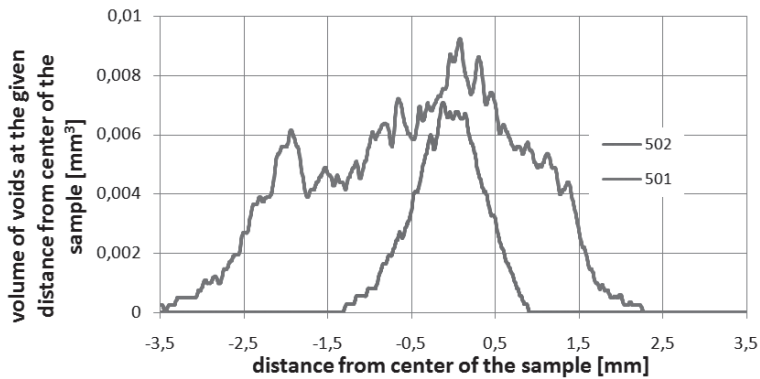


Fig. 10. Volume of the voids in the  $6.25\ \mu\text{m}$  layers perpendicular to the symmetry axis of the samples

In order to present the spatial distribution of coherent structures inside each sample the projections in XY, YZ and XZ planes were calculated. The results were presented in Figures 11–12. From these projections, it appears that the porous areas within the samples have a regular structure. It is especially evident for sample 502. The structure of projections on the plane shows some preferred directions, which are bar axis and the direction along the radius. It is not so clear for sample 501, but some preferred directions of slits were also observed.

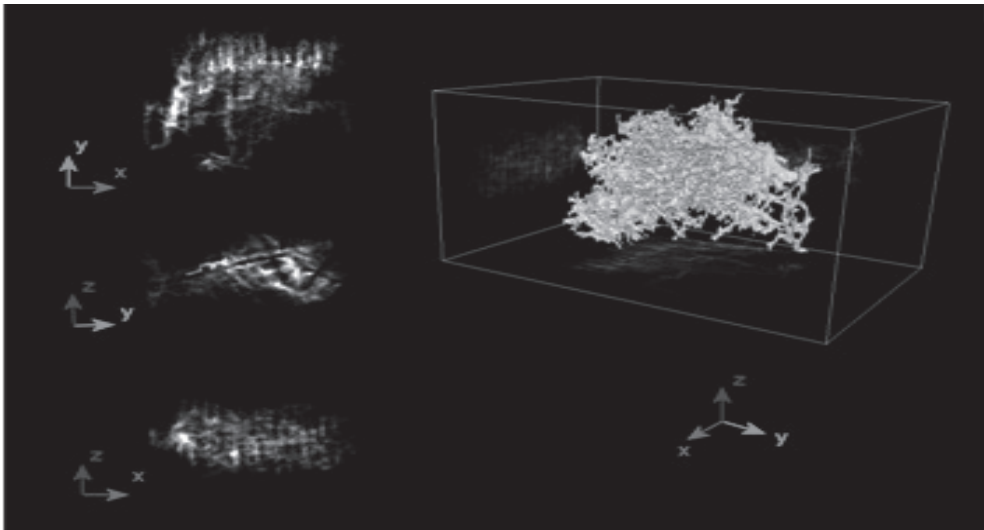


Fig. 11. The spatial distribution of coherent structures for sample 501 with the projections of these structures on the XY, YZ and XZ plane

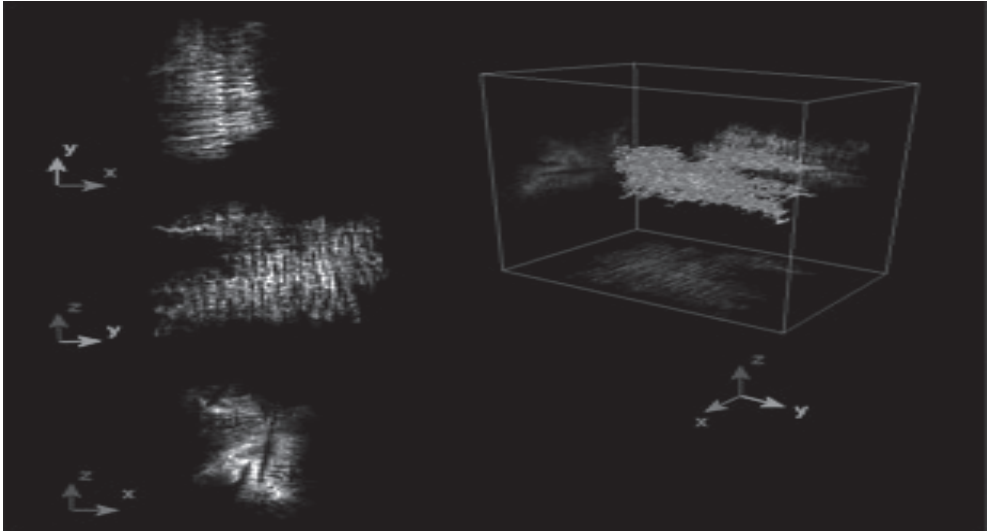


Fig. 12. The spatial distribution of coherent structures for sample 502 with the projections of these structures on the XY, YZ and XZ plane

### 3. Conclusions

In both samples, one coherent area of high volume joining the majority of the voids inside is observed. What is more, in each sample, there is a large number of considerably smaller, irregularly shaped voids not connected with the main structure. Elongation of the voids in both samples is similar. In each of them, about 65% of the voids have a spherical or slightly elongated character. Furthermore, approximately 8% of the voids are very or extremely elongated. The main difference between the two examined samples is the size of the voids. In sample 501 they occupy only  $1.27 \text{ mm}^3$ , and in sample 502 up to  $4.69 \text{ mm}^3$ . In both samples, the unified structure is rougher than the individual holes, which is probably due to its complex shape. The main structure of sample 501, while being smaller in terms of volume, is much larger in a mean diameter (average  $75 \text{ }\mu\text{m}$  compared to  $53 \text{ }\mu\text{m}$  in sample 502). This means that there are fewer slits in sample 501, but they are larger than in 502 sample. On the other hand, the voids within sample 501 are more condensed than in the 502 one.

*The project has been supported by the Polish National Science Centre, Decision number: DEC-2011/03/D/ST8/04041.*

## References

- [1] Feldkamp L.A., Davis L.C., Kress J.W., *Practical cone-beam algorithm*, J. Opt. Soc. Am., 1984, 612-619.
- [2] Reference Manual VGStudio Max Release 2.0 (<http://www.volumegraphics.com/en>).
- [3] <http://fiji.sc/Fiji>.
- [4] Doube M., Kłosowski M.M., Arganda-Carreras I., Cordelières F., Dougherty R.P., Jackson J., Schmid B., Hutchinson J.R., Shefelbine S.J., *BoneJ: free and extensible bone image analysis in ImageJ*, Bone, Vol. 47, 2010, 1076-1079.
- [5] <http://www.goldensoftware.com/products/voxler>
- [6] Hojny M., *Projektowanie dedykowanych systemów symulacji odkształcania stali w stanie półciekłym*, Wyd. Wzorek, 2014 (w druku).



MICHAŁ KLUZIEWICZ\*

## EXPERIMENTAL VERIFICATION OF KINETOSTATIC MODEL OF STRUT SUSPENSION MECHANISM

---

### EKSPERYMENTALNA WERYFIKACJA KINETOSTATYCZNEGO MODELU MECHANIZMU ZAWIESZENIA Z KOLUMNĄ PROWADZĄCĄ

#### Abstract

The process of experimental verification of the MacPherson-strut mechanism model is presented. The mentioned model is used to estimate wheel load components based on measured internal reaction forces. Chosen constructional solutions of sensors mounting are described along with sensors calibration methods. The kinematic characteristics of a model and real suspension mechanism (measured on a test stand) are compared.

*Keywords: vehicle dynamics, MacPherson strut suspension modeling, measuring loads on a rotating wheel*

#### Streszczenie

W artykule przedstawiono przebieg doświadczalnej weryfikacji modelu mechanizmu prowadzenia koła. Model ten służy do estymacji składowych obciążenia koła jeźdnego samochodu na podstawie mierzonych sił wewnętrznych w przegubach. Zaprezentowano rozwiązania konstrukcyjne zabudowy czujników oraz metody ich kalibracji. Porównano charakterystyki kinematyczne modelu i rzeczywistego mechanizmu zmierzone na stanowisku badawczym.

*Słowa kluczowe: dynamika samochodu, modelowanie zawieszenia z kolumną MacPhersona, pomiar sił i momentów działających na koło*

---

\* M.Sc. Michał Kluziewicz (Ph.D. Student), Institute of Automobiles and Combustion Engines, Faculty of Mechanical Engineering, Cracow University of Technology.



## 1. Introduction

The issue of vehicle motion modelling requires implementing the characteristics of examined tires [8]. Among the known methods of tire characteristics estimation the measurement can be conducted either on test benches or in real conditions using a test vehicle and a circuit [4]. The author's main research is focused on a development of a tire-to-gravel surface interaction model. For the use of the mentioned application, in a view of best conditions representation, it is crucial to conduct appropriate road tests.

Having regard to the high purchase cost of direct measuring hubs and tough working conditions, the innovative authorial measuring system enabling indirect tire characteristics estimation has been designed [2]. This system exploits an existing MacPherson strut suspension. One mechanism performs various roles: wheel guiding, shock absorbing and reaction forces measuring in rod joints (Fig. 1). In respect to the known tire-surface case studies, this type of measuring device has not been used for road tests before.

Measuring forces and moments in a point of contact between tire tread and road surface is the main goal of the research. A scientific method of computing longitudinal and transversal tire force characteristics of a vehicle running on a loose surface is presented. The described approach is indirect and based on a measurement of internal forces and suspension mechanism configuration coordinates. The torques and forces relation is described by Jacobian matrices. The computer aided calculations are programmed and executed in the Matlab environment.

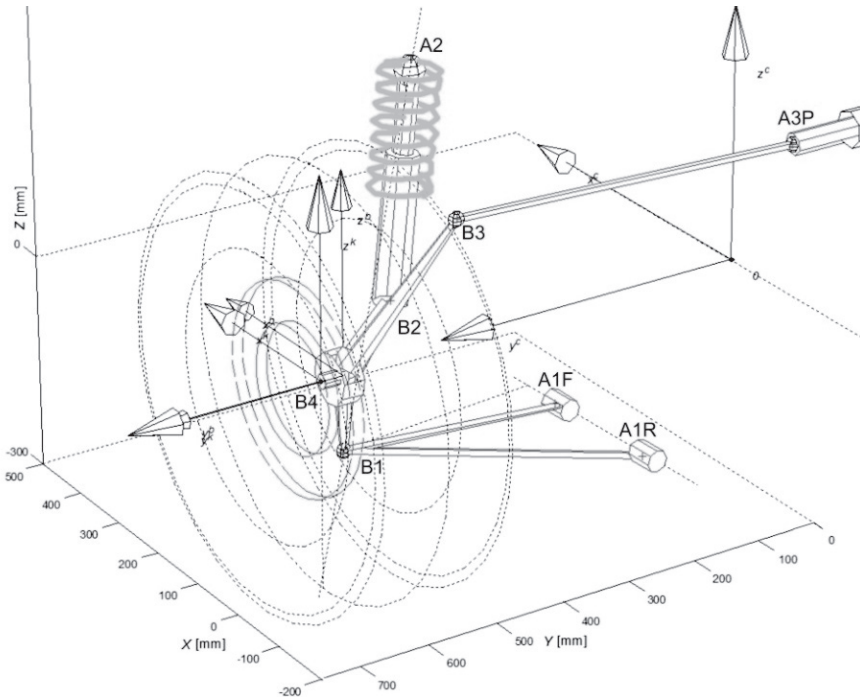


Fig. 1. 3D solid model of Citroen Saxo MacPherson strut suspension

The verification of the formula by a comparison of model and real measured kinematic characteristics is included. The designed and manufactured components of the measuring system are described along with the sensor calibration procedure. Geometric, kinematic and quasi-static (forces and torques estimation) descriptions of the suspension mechanism are presented.

The featured test vehicle is a front wheel drive, fully rally-prepared Citroen Saxo VTS, with a MacPherson strut front suspension.

## 2. Task definition of load estimation

External loads' characteristics ( $F_x, F_y, M_z$ ) in the point of contact between the tire tread and road surface are assumed as in the following equation [2]:

$$F_x, F_y, M_z = f(F_z, \gamma, \alpha, S_x, \beta, T_b, r_d, \text{surface parameters}) \quad (1)$$

where:

- $F_x, F_y, M_z$  – Tire load components estimated by internal loads of suspension mechanism in a specific suspension travel position ( $s$ ) and steering rack setting ( $p$ );
- $F_z$  – Tire vertical load, measured indirectly through suspension travel and force in the top mount;
- $\gamma$  – Wheel camber angle, estimated by: known suspension dimensions, measured suspension travel ( $s$ ), steering rack setting ( $p$ ) and chassis roll angle;
- $\alpha$  – Tire slip angle, estimated via longitudinal and lateral vehicle speed (Correxit QL) and steering wheel rotation angle (cable sensor);
- $S_x$  – Longitudinal tire slip, estimated via vehicle speed, wheel rotation speed, and dynamic wheel radius;
- $\beta$  – Vehicle sideslip angle, calculated from longitudinal and lateral vehicle speed;
- $T_b$  – Tire tread temperature, measurement is conducted with pyrometer gauge;
- $r_d$  – Dynamic wheel radius, estimated via axial force in a damper module.

Surface parameters such as loose layer depth, size distribution, moisture content, soil volume density.

A kinematic model of MacPherson strut suspension (Fig. 1) was formulated according to the following assumptions: quasi-static conditions; internal forces in a suspension are determined by method of joints; direct kinematic task is solved using the vector method [5].

For a specified mechanism setting, defined by suspension travel ( $s$ ) and the steering rack's position ( $p$ ), a static task can be described by the following equation:

$$\mathbf{W} = \mathbf{J}^T \mathbf{R} \quad (2)$$

where:

- $\mathbf{W} = [F_x \ F_y \ F_z \ M_x \ M_y \ M_z]^T$  – complex load vector translated to the wheel's centre of rotation,
- $\mathbf{R} = [R_1 \ R_2 \ R_3 \ R_4 \ R_5 \ R_6]^T$  – internal loads vector:  $R_1$  – reaction in a front wishbone rod joint;  $R_2$  – reaction in a rear wishbone rod joint;  $R_3$  – reaction in a steering rod;  $R_4, R_5, R_6$  – longitudinal, lateral and vertical reactions in a strut top mount,
- $\mathbf{J}$  – jacobian matrix for static analysis of parallel mechanism [5].

Equation (2) describes linear relations between an unknown external load ( $\mathbf{W}$ ) and the measured internal load ( $\mathbf{R}$ ) in the mechanism. Forces and torques in the centre of wheel rotation are related with joints reactions by the jacobian matrix. The jacobian matrix is determined for a specific suspension travel position ( $s$ ) and steering rack setting ( $p$ ).

### 3. Kinematic characteristics of wheel suspension

For the purposes of kinematic analysis, the 3d solid model of MacPherson suspension of a Citroen Saxo test car is implemented into the Matlab software. Subsequently, the mechanism is strictly measured and the gathered data is entered. At this stage, with the aim of verifying kinematic relations, the following values were measured as a function of suspension travel ( $s$ ): camber angle ( $\gamma$ ) [°], toe ( $\delta$ ) [mm], track width change [mm].

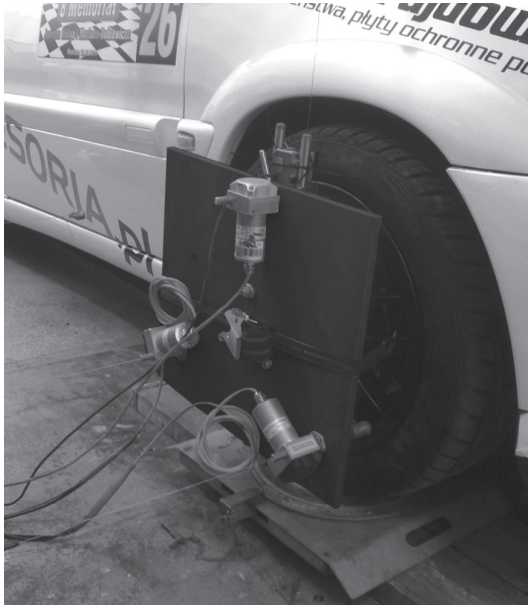


Fig. 2. Measuring adapter with 4 cable sensors attached to the wheel

Front wheels were set on turntables to avoid the influence of tangent forces. The front axle was supported with a jack and loaded with weights of the total of 300 kg. A measuring plate with 4 cable sensors was mounted to the rim (Fig. 2). One of the cables was attached to the car body in order to measure the suspension travel. Other three cables were fixed to the solid pillar. By measuring displacements of equilateral triangle vertices, the aforementioned values change can be obtained [1]. The data was logged with Spider 8 data acquisition system and the Catman module.

The measured real suspension characteristics (green) were compared to the corresponding ones received from a kinematic model (black) (Fig. 3).

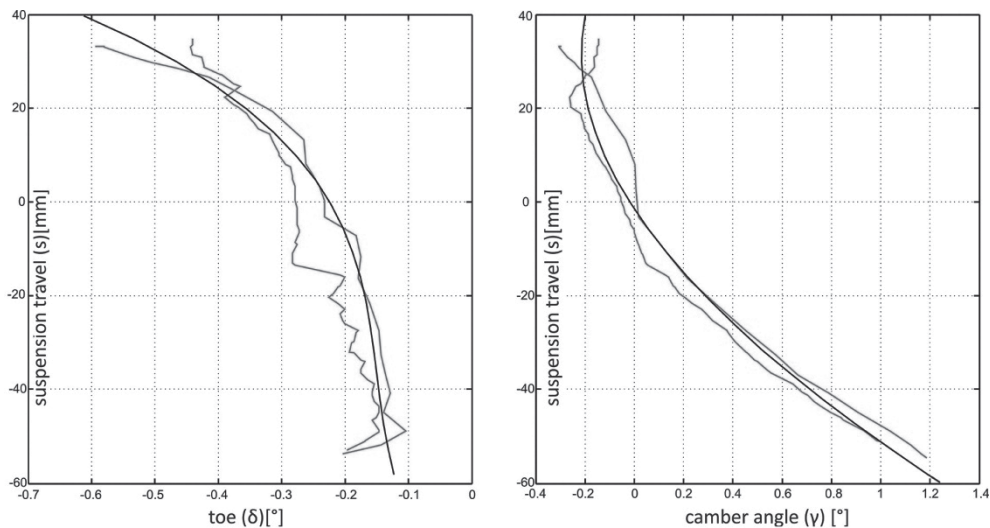


Fig. 3. Plot of a toe change and camber angle change as a function of suspension travel

Both presented characteristics retrieved from the model are fair representations of real traces. On this basis, it can be concluded that the kinematic model is properly specified. To obtain improved results, steering rod length should be precisely measured.

#### 4. Designed solutions of measuring system

Kistler 3-axis force sensor is mounted in a strut top mount (Fig. 1, point A2) and used for longitudinal, vertical and transversal (lateral) force measurement. Rubber bushing is replaced with uniball, thereby pliability and internal friction of joint are negligible (Fig. 4a).

A 3-component force sensor is used for the dynamic and quasistatic measurement of the three orthogonal components of any force acting on the top and bottom plate. It contains three pairs of quartz force measuring elements, one of which is sensitive to pressure in the z direction and two others to shear forces in the x and y directions. Measurement takes place practically without displacement [10]. As the effect of force acting on quartz elements, charges occur at the connections. Charges are converted to a  $0\div 10$  V signal by an industrial charge amplifier. Afterwards, the voltage signal from three separate channels is gathered by the data acquisition system and logged.

#### 5. Calibration procedure of load sensor in top mount

Proper axial tension is crucial for transverse and longitudinal shear forces transmission through static friction from the top and base plate to the surfaces of the force transducer.

Tensile forces are measured as a relief of the preload. Adequate contact surface preparation and preload ensures high rigidity and accuracy (Fig. 4b).

Irrespective of the given calibration certificate, the sensor was tested under various load states to determine the sensitivity of a complete measuring arrangement.

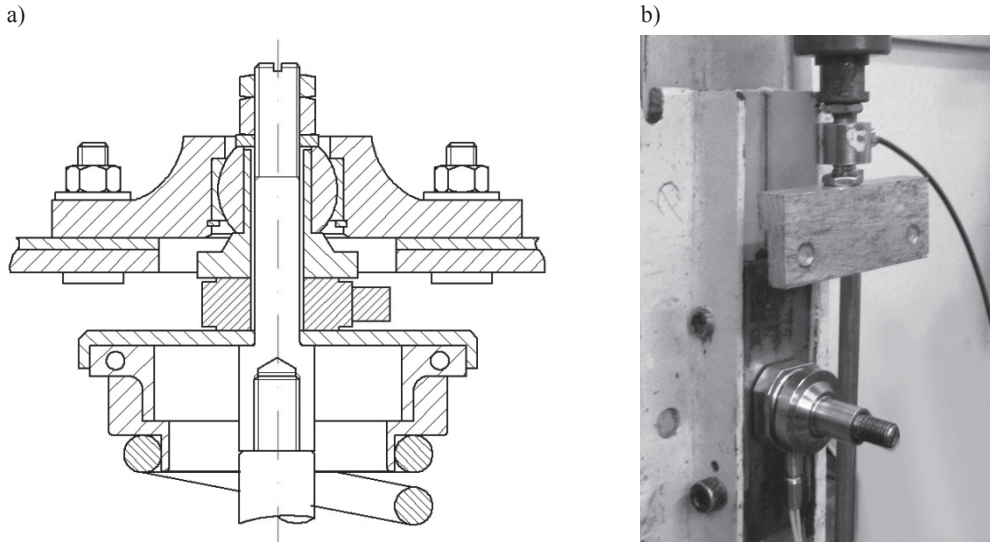


Fig 4. a) Simplified drawing of designed MacPherson strut top mount with 3-axis ( $F_x$ ,  $F_y$ ,  $F_z$ ) force sensor (blue), adapters and preload bolt, b) On-site sensor assembly

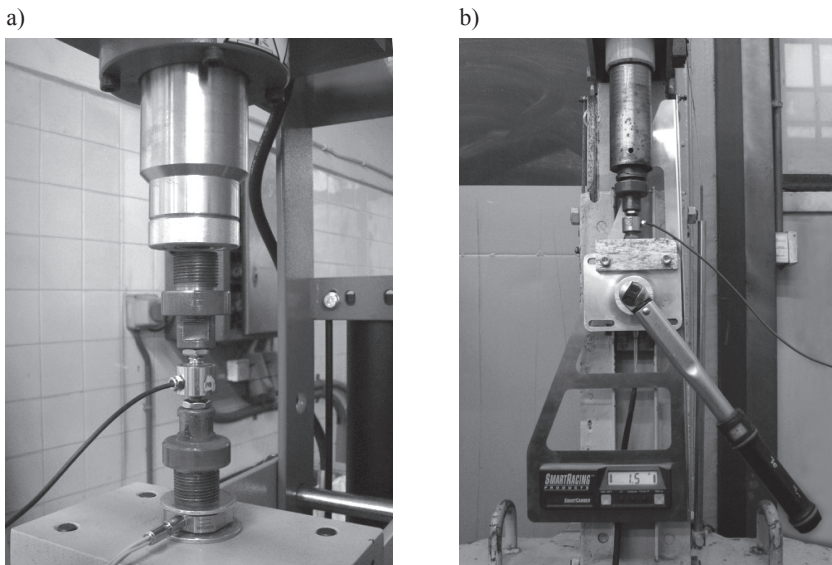


Fig. 5. a) Test stand 1 for calibration of  $F_z$  load component, b) Test stand 2 for a complex load state

The first test was aimed at correlating readings from the mentioned piezoelectric sensor and factory calibrated HBM U9C strain gauge. Both sensors were simultaneously squeezed onto a hydraulic press (Fig. 5a). The Z force values from a HBM sensor were assumed as a reference. The executed benchmark confirmed good linearity of the measured values (Fig 6). The obtained sensitivity insignificantly differs from the one provided by a manufacturer. While measuring miniscule loads (1000 N or less) without a preload, extra caution is recommended because of the sensor nonlinearity.

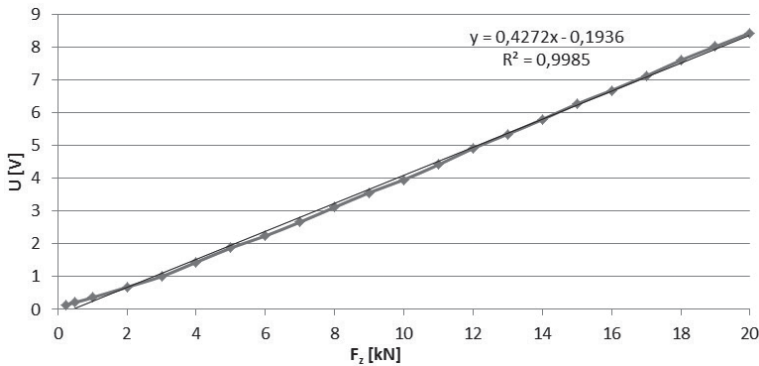


Fig. 6. Output voltage of a 3-axis sensor as a function of vertical load  $F_z$

In order to provide a desirable sensor preload, torque wrench is used for tightening the measuring structure (Fig. 5b). The preload bolt has a M12x1.75 metric thread which is coated with a copper slip. The relation between the tightening torque and compressive force is close to linear and the ratio is around 50 N/Nm.

As the final step, a complete structure of the suspension strut top mount was assembled and tested to prove usability of the sensor in complex load states (Fig. 5b).

The tension bolt was tightened with a torque of a 60 Nm, resulting in a 30 000 N preload force in a Z-axis direction. Subsequently, a screw press was used to exert loads from  $-3$  kN to 5.5 kN in axis  $X$  (Fig. 7).

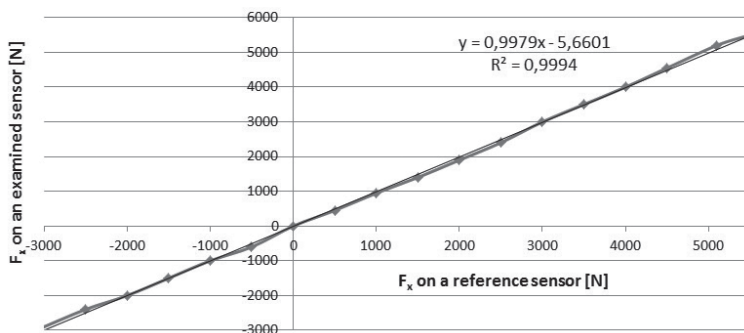


Fig. 7. Relation between  $F_x$  readings on an examined and a reference sensor

Conducted test confirmed the correctness of given sensitivity coefficient and appropriate preload for the desired  $F_x$  and  $F_y$  load range.

## 6. Conclusions

An example of a computer aided estimation of the tire external load state ( $\mathbf{W}$ ) by measured internal suspension reactions ( $\mathbf{R}$ ) is presented. The foregoing linear relations are described with the jacobian matrix.

The measured kinematic characteristics of strut suspension are compared to the modeled ones. Good functions matching confirms the validity of the kinetostatic model.

The designed constructional solution of sensor mounting is described along with the sensor calibration method. A benchmark of the examined and reference sensors has demonstrated satisfactory conformation of the measurement. Usability of the selected sensor has been proved on a test stand in uniaxial and complex load states.

In the context of ongoing research following actions will be completed:

- fitting of the complete measuring system into the test car,
- trials of different wheel load states on a test rig,
- conducting road tests.

## References

- [1] Góra M., Maniowski M., *Verification of 6DOF platform with wire-based sensors for spatial tracking*, The Archive of Mechanical Engineering, LVIII 2011, Number 2.
- [2] Kluziewicz M., Maniowski M., *Estimation of wheel load state by using suspension joints reactions*, *Badania Pojazdów*, praca zbiorowa pod redakcją Władysława Mitiańca, Opracowanie Monograficzne, Kraków 2014, 61-71.
- [3] Kluziewicz M., Maniowski M., *Stany nadsterowności podsterownego samochodu z przednim napędem*, *Zeszyty Naukowe Instytutu Pojazdów Politechniki Warszawskiej*, z. 1 (77), 2010, 169-177.
- [4] Knapczyk J., Gansiniec O., Maniowski M., *Charakterystyki opony samochodowej (175/70R14)*, *Teka Komisji Nauk.-Prol. Motoryzacji PAN O. Kraków*, z. 22, Kraków 2001.
- [5] Knapczyk J., Maniowski M., *Elastokinematic Modeling and Study of Five-Rod Suspension with Subframe. Mechanism and Machine Theory*, Vol. 41, 2006, 1031-1047.
- [6] Knapczyk J., Maniowski M., *Porównanie uproszczonych modeli dynamicznych opony toczącej się ze znośaniem*, *Materiały Autoprogres-Konmot*, Warszawa 2002.
- [7] Luty W., *Nieustalone stany znośnienia boczno-ogumienia kół jezdnych w symulacji ruchu krzywoliniowego pojazdu*, *Prace Naukowe Politechniki Warszawskiej*, Warszawa 2013.
- [8] Pacejka H.B., *Tyre and Vehicle Dynamics*, Butterworth-Heinemann, SAE, 2002/2006.
- [9] Prochowski L., *Mechanika ruchu. Pojazdy samochodowe*, WKŁ, 2008.
- [10] *3-Component Force Sensor Type 9047C, Instruction Manual* ([www.kistler.com](http://www.kistler.com)).

WALDEMAR KWAŚNY, TYMOTEUSZ JUNG\*

## THE INFLUENCE OF DEPOSITION CONDITIONS ON STRUCTURE OF PVD COATINGS OBTAINED IN THE MAGNETRON PROCESS

---

### WPLYW PARAMETRÓW NANOSZENIA NA STRUKTURĘ POWŁOK OTRZYMANÝCH W MAGNETRONOWYM PROCESIE PVD

#### Abstract

This paper presents the influence of deposition conditions on texture and stress results of TiN coatings deposited by using the PVD magnetron process. Modification of parameters was related to the changes of temperature and substrate potential. The article presents the results of an analysis of texture and stress measurement obtained by X-ray methods and the results of microhardness measurement.

*Keywords: PVD coatings, stress analysis, structure and texture, X-ray analysis*

#### Streszczenie

W pracy przedstawiono wpływ parametrów nanoszenia na teksturę i naprężenia powłok TiN uzyskanych w magnetronowym procesie PVD. Modyfikacja parametrów dotyczyła zmiany temperatury procesu oraz polaryzacji podłoża. W artykule przedstawiono wyniki analizy tekstury i pomiaru naprężeń uzyskane metodami rentgenowskimi oraz wyniki pomiaru mikrotwardości.

*Słowa kluczowe: powłoki PVD, analiza naprężeń, struktura i tekstura, analiza rentgenowska*

---

\* Prof. Waldemar Kwaśny, M.Sc. Tymoteusz Jung, Institute of Engineering Materials and Biomaterials, Faculty of Mechanical Engineering, Silesian University of Technology.



## 1. Introduction

In response to the growing requirements for modern engineering materials, one can observe an increased intensity of research that is moving towards developing materials and coatings with the best properties. Nowadays, one of the most popular groups of coating deposition methods is the physical vapor deposition (PVD). This method allows the preparation of many types of coatings, both mono and composed of several elements or phases. With the advancement of science many substitutes of the PVD process were developed, thereby modifying its usability. The aim of this study was to investigate the influence of the deposition condition on the structure of PVD coatings obtained in the magnetron process. [1, 2, 4].

## 2. Material for study and research methodology

Experiments were made on samples from the PM-HS6-5-3-8 sintered high speed steel contained 1.28% C, 4.2% Cr, 5.0% Mo, 6.4% W, 3.1% V and 8.5% Co. The specimens were heat treated in salt bath furnaces with austenitizing at the temperature of 1180°C and triple tempering at the temperature of 540°C. The specimens were loaded into a single vacuum chamber with a magnetron designed for the ion sputtering, then were placed at the distance of 70 mm from magnetron disk. After obtaining the  $6-7 \cdot 10^{-2}$  Pa vacuum the coating deposition process was carried out in 460, 500 i 540°C with the substrate potential equal to 0 V and in 500°C with the substrate potential equal to -100 V and -200 V. The cleaning process was carried out at the pressure of 25 Pa during 5 minutes, with the matrix potential of 900 V in the argon atmosphere. The TiN layer was deposited for 60 minutes under conditions given in Table 1. The magnetron disk was made from titanium alloy containing: 90% Ti, 5,7% Al, 1,4% Cr i 2,0% Mo [1, 2, 4].

Table 1

Coating deposition process parameters

Process temperature [°C]	Substrate potential [V]	Chamber pressure [Pa]	Magnetron voltage, U [V]	Magnetron current, I [A]
460	0	$5,1 \cdot 10^{-1}$	360	7
500	0	$5,1 \cdot 10^{-1}$	360	
	-100	$5,2 \cdot 10^{-1}$	350	
	-200	$5,1 \cdot 10^{-1}$	350	
540	0	$5,1 \cdot 10^{-1}$	360	

Evaluation of phase composition of the obtained coatings was made using PANalytical X'Pert PRO diffraction system, using filtered radiation from the cobalt lamp with a voltage of 40 kV and heater current of 30 mA. The X-ray phase analysis of the investigated coatings was conducted in the Bragg-Brentano geometry and in grazing incidence geometry (primary beam angle - 2°) using appropriately the PIXcel 3D detector and a proportional detector.

Measurements were made within the  $2\theta$  angle range from 40 to  $100^\circ$ . In order to analyse the texture of the created coatings, three pole figures were measured for each analyzed sample using a reflection method employing Euler's circle of diameter 187 mm in a range of samples inclination angle from 0 to  $80^\circ$ . The orientation distribution function (FRO) was conducted by the ADC method using iterative operator in LaboTex 3.0 [3]. Stress analysis was made using the  $\sin^2\psi$  technique in the X'Pert Stress software [1, 2, 5].

### 3. The results

The results of X-ray phase composition analysis confirmed the existence of the expected layer. Figure 1 shows the diffraction pattern of the analyzed coating in Bragg – Brentano and grazing incidence geometry.

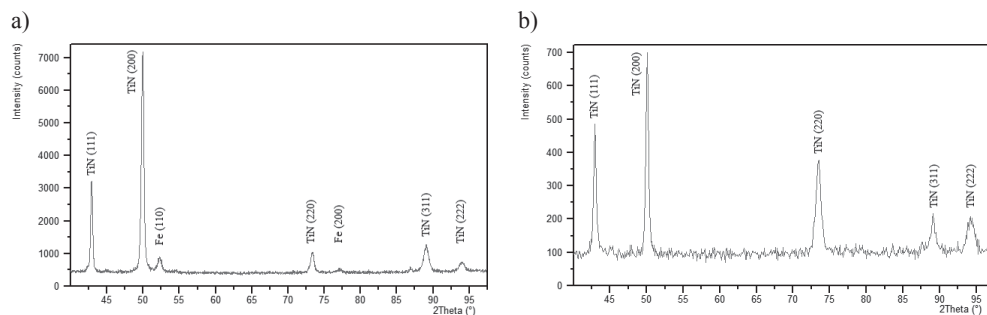


Fig. 1. Diffraction pattern of the sintered high speed steel PM HS-6-5-3-8 with the TiN coating performed in: a) Bragg – Brentano geometry, b) grazing incidence angle geometry (substrate potential 0 V)

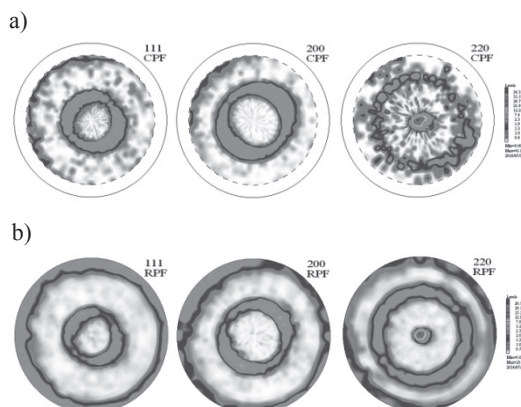


Fig. 2. Pole figures (111), (200) and (220) TiN coating deposited onto the PM HS6-5-3-8 sintered high speed steel obtained by magnetron sputtering: a) experimental, b) calculated by FRO (substrate potential  $-100$  V)

Texture analysis of the examined coatings was conducted based on 3 experimental pole figures (Fig. 2a). FRO of the analyzed materials was shown in figure 3 and pole figures calculated by FRO in Figure 2b. The analysis of pole figures indicates the occurrence of axial component texture <100> for layers made with substrate potential 0V. A negative substrate potential caused change orientation from <100> to <110>. Particular results of texture analysis are shown in Table 2.

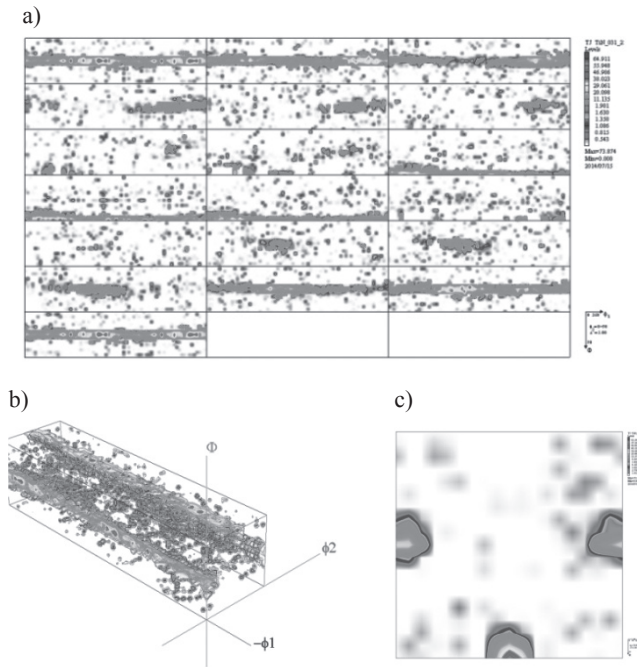


Fig. 3. FRO of TiN coating deposited onto the PM HS6-5-3-8 sintered high speed steel by magnetron sputtering: a) section  $\phi_2$ , b) FRO, 3D view, c) section  $\phi_1$  (substrate potential  $-100$  V)

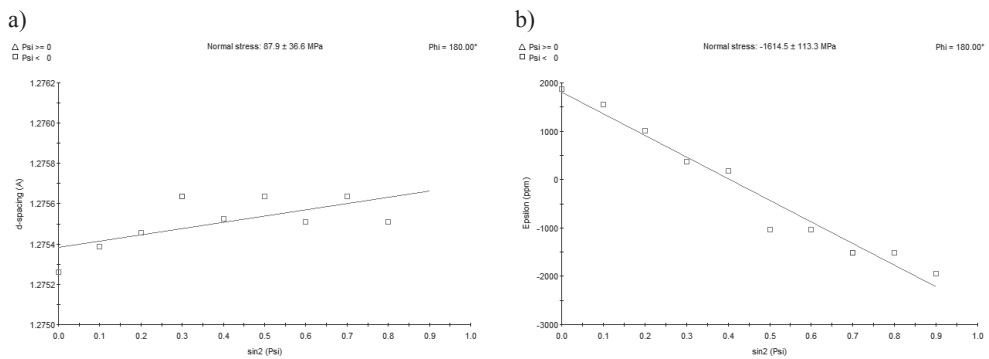


Fig. 4. Stress measurement results of TiN layer deposited in: a) substrate potential 0V, b) substrate potential  $-100$  V

Stress calculated by the  $\sin^2\psi$  method (Fig. 4) has shown that coatings made in the negative substrate potential have severe compressive stress. It was unable to determine the stress results for coatings made in the substrate potential equal  $-200$  V due to presence of a strong texture  $\langle 110 \rangle$ . Particular results of stress analysis and microhardness measurements are shown in Table 2.

Table 2

**Results of the texture and stress analysis and microhardness measurements of TiN layers obtained in the magnetron sputtering**

Process temperature [°C]	Substrate potential [V]	Texture (type / share)	Stress [MPa]	Microhardness [HV <sub>0.1</sub> ]
460	0	$\langle 100 \rangle$ / 37%	411.6±77.8	1817
500	0	$\langle 100 \rangle$ / 35%	87.9±36.6	1785
	-100	$\langle 110 \rangle$ / 31%	-1614.5±113.3	2661
	-200	$\langle 110 \rangle$ / 45%	–	1977
540	0	$\langle 100 \rangle$ / 40%	-592.7±79.6	1983

#### 4. Conclusions

Based on the experimental results the following conclusions were made:

1. Based on the stress measurements, it was found that the negative substrate potential affects the growth of compressive stress of coatings. For the substrate potential of  $-100$  V stress amounted to  $-1614.5 \pm 113.3$  MPa;
2. Based on the texture analysis, it was found that the negative substrate potential causes a change in the orientation of  $\langle 100 \rangle$  to  $\langle 110 \rangle$ ;
3. Among the tested coatings, coatings deposited at  $500^\circ\text{C}$  with substrate potential of  $-100$  V had the biggest microhardness  $2661\text{HV}_{0.1}$  had; these coatings had the highest compressive stress, too.

*Tymoteusz Jung is a holder of a scholarship from the project "DoktoRIS – Scholarship program for innovative Silesia" co-financed by the European Union under the European Social Fund.*

## References

- [1] Kwaśny W., *Predicting properties of PVD and CVD coatings based on fractal quantities describing their surface*, Journal of Achievements in Materials and Manufacturing Engineering, Vol. 37, 2009, Issues 2, 125-192.
- [2] Dobrzański L.A., Kwaśny W., *Effect of the substrate bias on structure and properties of the TiN coatings obtained in the PVD process*, Inżynieria Materiałowa, nr 6 (137), Międzyzdroje 2003, 453-456.
- [3] Pawlik K., *Determination of the Orientation Distribution Function from Pole Figures in Arbitrarily Defined Cells*, Physica Status Solidi (b) 134, 1986, 477-483.
- [4] Lukaszewicz K., Czyżniewski A., Kwaśny W., Pancielejko M., *Structure and mechanical properties of PVD coatings deposited onto the X40CrMoV5-1 hot work tool steel substrate*, Vacuum, nr 86, 2012, 1186-1194.
- [5] Kwaśny W., Nuckowski P., Jung T., Rdzawski Z., Głuchowski W., *Effect of plastic deformation on the structure and texture of CuSn6 alloy*, Technical Transactions, 1-M/2013, Kraków 2013, 213-219.

PAWEŁ LEMPA, EDWARD LISOWSKI\*

## AUTOMATED GENERATION OF 3D MODELS OF HYDRAULIC COMPONENTS

---

## ZAUTOMATYZOWANE GENEROWANIE MODELI 3D ELEMENTÓW HYDRAULICZNYCH

### Abstract

This paper presents methods for automatic generation of 3D models of hydraulic components. For the purposes of generating models the authors' own software and PTC Creo Parametric CAD system was used.

*Keywords: hydraulic component 3D model*

### Streszczenie

W artykule przedstawiono metody automatycznego generowania modeli 3D elementów hydraulicznych. Na potrzeby generowania modeli wykorzystano autorskie oprogramowanie i PTC Creo Parametric CAD system.

*Słowa kluczowe: element hydrauliczny model 3d*

---

\* MSc. Eng. Paweł Lempa, Prof. Ph.D. D.Sc. Eng. Edward Lisowski, Institute of applied Informatics, Faculty of Mechanical Engineering, Cracow University of Technology.

## 1. Introduction

The paper presents the automated generation of 3D models of hydraulic components. The purpose of the generating models is to visualize and test the correctness of the previously prepared geometric parameters of hydraulic elements. The automation of the model generation significantly speeds up the process of evaluating the correctness of these models.

For the purposes of generating models the authors' own software was used which works with the PTC Creo Parametric CAD system. The PTC Creo Parametric CAD system allows for the creation of complex 3D models that can be saved in various formats, which allows them to be opened and tested in various programs. Also the PTC Creo Parametric CAD system allows for testing models for such attributes as lack of collision between the individual elements or their movement. The authors' own software was created in C++ language on the Visual Studio platform, and it works in Windows systems. It uses a graphical interface with predefined types of hydraulic components.

The paper presents the process of generating only one of the predefined hydraulic components that the created software is capable of. The selected element is a gearwheel pump.

## 2. Parametric description of a sample hydraulic component – gearwheel model of the pump

The modelling of involute gearing is necessary to use a curve called the involute of the circle. In the PTC Creo Parametric CAD system also at the geometric modelling gearwheels parametric curves can be used conveniently. To draw an involute tooth's profile equations described in the literature [1, 2, 4–6] are used (more important variables are shown in Fig. 2).

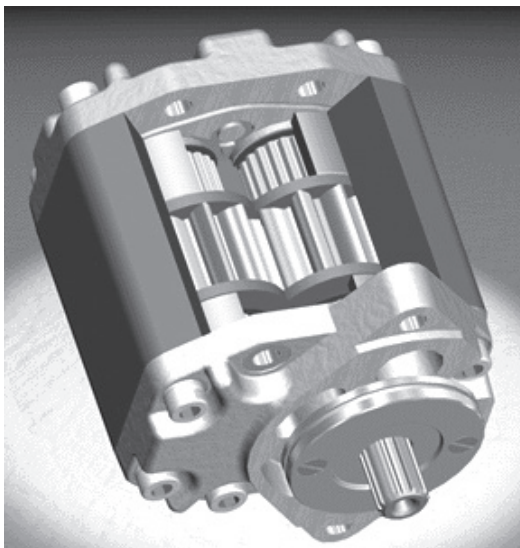


Fig. 1. Parametric 3D model of a gear pump

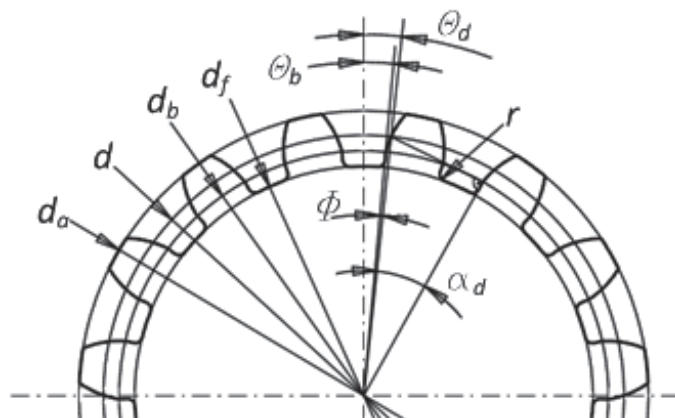


Fig. 2. Parametric 3D model of a gear pump

The main parameters of the gear are as follows:  
reference diameter:

$$d = m \cdot l_z \quad (1)$$

basic circle diameter:

$$d_b = d \cdot \cos(\alpha) \quad (2)$$

tip clearance:

$$c = 0.2 \cdot m \quad (3)$$

height of a tooth head:

$$h_a = (y + x) \cdot m \quad (4)$$

height of a tooth root:

$$h_f = (y - x) \cdot m + c \quad (5)$$

where:

- $m$  – module pitch of a gear,
- $l_z$  – number of teeth,
- $\alpha$  – pressure angle,
- $x$  – addendum modification coefficient,
- $y$  – tooth height coefficient.

At generation of an involute curve in the PTC Creo Parametric it is convenient to use parametric notation in polar coordinates [4]:



$$r = -\left(\frac{d_b}{2} + t \frac{d_a - d_b}{2}\right) \quad (6)$$

$$\Theta = \tan\left(\arccos\left(\frac{d_b}{2r}\right)\right) \frac{180}{\pi} - \arccos\left(\frac{d_b}{2r}\right) - \Theta_b \quad (7)$$

$$z = 0 \quad (8)$$

where:  $\theta_b$  – start of uncoiling the involute from the base circle, which can be calculated using geometrical relations:

$$\theta_b = \theta_d - \Phi \quad (9)$$

$$\Theta_d = \frac{90}{l_z} \quad (10)$$

$$\Phi = \tan(\alpha_d) - \alpha_d \quad (11)$$

$$\alpha_d = \arccos\left(\frac{d_b}{d}\right) \quad (12)$$

where:  $\theta_d$  – position of the angle of the involute point on the dividing wheel.

In the described example the parameters defining the geometry of the gearwheel are as follows: the number of teeth, module, pressure angle, displacement outline coefficient and height tooth coefficient. As additional parameters can be used:  $r_f$  – fillet radius at the base of the tooth and  $b$  – gearwheel width.

Due to the record of equations required by the PTC Creo Parametric appropriate substitutions were made, for example, DB for  $d_b$ , ALFA for  $\alpha$ , etc. Before the introduction of equations for the PTC Creo Parametric it is necessary to put this data into the program. These parameters can be inserted by selecting *Tool/Parameters* or directly as relationships by the command *Tool/Relations* (Fig. 3). Equations and data can be inserted directly or copied from the previously prepared ASCII file. After introducing the parameters and the relations auxiliary curves were prepared. By using the *SKETCH* command, two circles were drawn on the *FRONT* plane to which corresponding parameters DF i DA were assigned. At the plane *FRONT*, when you chose *Datum/Equation*, and after selecting the type of the coordinate system as *Cylindrical*, involute equation was inserted as shown in Fig. 4.

The next step was to generate a cylinder by the command *Extrude*. In the sketchbook an auxiliary circle with a diameter of DA was used as an outline of the base of the cylinder. For this purpose, it was projected by the command *Edge/Use/Single*. The projection of the cylinder was made by entering parameter B as its height (Fig. 4). After generating a cylinder one notch was made, for that purpose *Extrude* command was selected with option *CUT*.

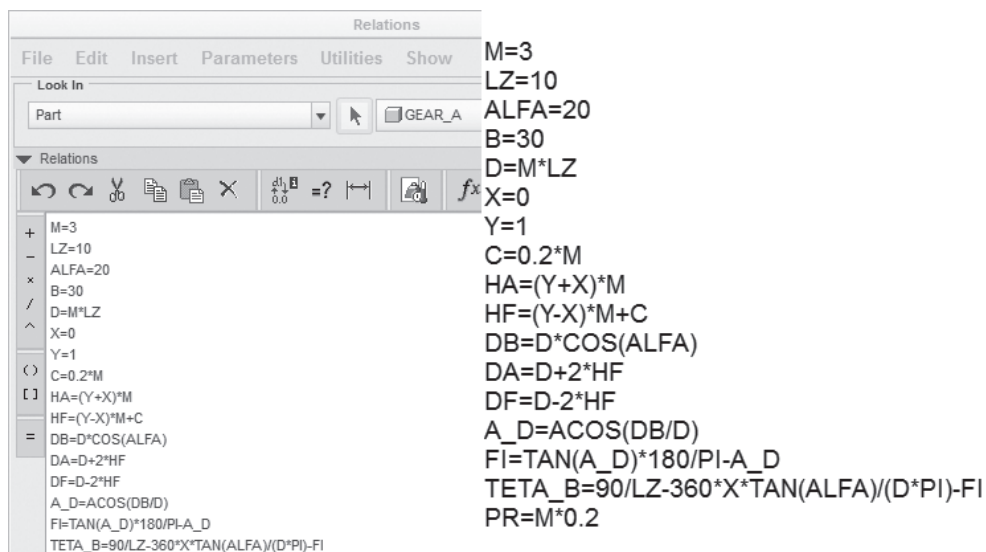


Fig. 3. Window Relations with the inserted equations and relations which describe the modeled gear wheel

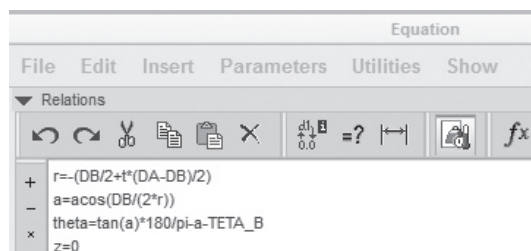
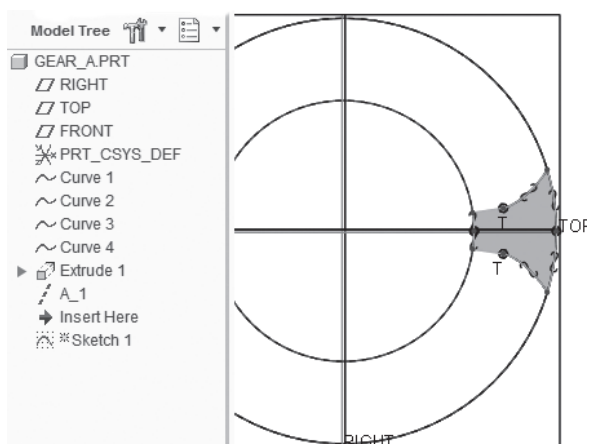


Fig. 4. Window with inserted involute equations in cylindrical coordinates

Fig. 5. Profile of the notch (T – points of contact in the curves describing the outline of the notch)



For sketchbook this operation selected the frontal area of the roller. The profile of the tooth notch is made, using mostly previously prepared curves. Using the options *Edge/Use/Single*, circles with diameters DA and DF and involute are projected on the sketchbook. Subsequently, the involute was extended tangentially by a section to the circle DF and rounded by radius PR to the circle DF (Fig. 5). After sketching half of the outline of the tooth its mirror image was made and then the sketch was used to remove the material and receive a one cut notch (Fig. 6).

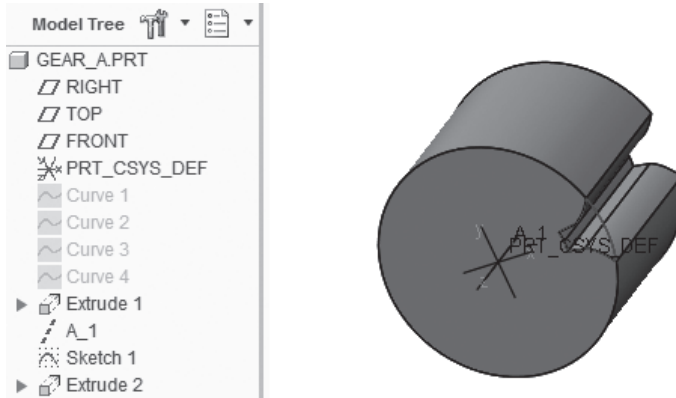


Fig. 6. The model after performing one notch

*Pattern* command and option *Axis* (wheel pattern) were used for the arrangement on the circumference of a wheel other notches. In the relation window you need to add a variable corresponding to the number of the copies and assign it a value, for example  $P16 = LZ$ . After refreshing (*Edit/Regenerate*) notches will be replicated all over the wheel (Fig. 7).

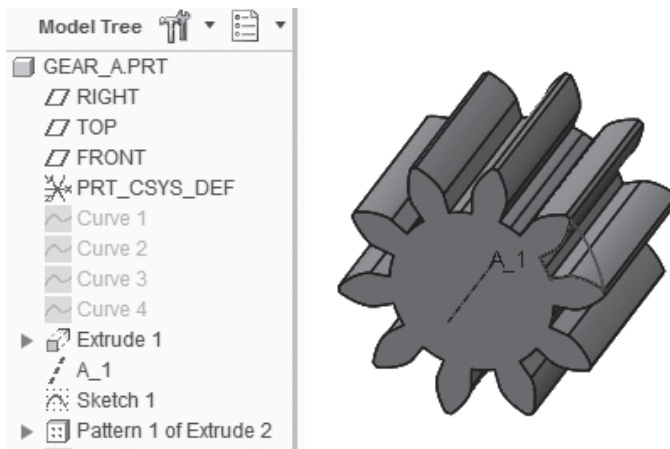


Fig. 7. A parametric model of the gearwheel: 1 – involute, 2 – outline of the tooth, 3 – material in the form of cylinder, 4 – a set of notches

### 3. Models generator

A program for the automated generation of 3D models was created using the C++ language on the Visual Studio 2013 platform. This software can automatically generate selected models in the PTC Creo Parametric CAD system. For connection and generation of models a Creo Parametric TOOLKIT 3.0 [3] was used. Creo Parametric TOOLKIT 3.0 is a set of software customization tools that, inter alia, allows to automate processes of generating models. To use this software several programming languages can be used (e.g. Java or C++). The PTC Creo Parametric CAD system can only work in the Windows systems, therefore the NET platform was used to create this program.

### 4. Conclusions

This paper presents the automated generation of 3D models of hydraulic components. To generate 3D models was used the authors' own software using C++ and Creo Parametric TOOLKIT 3.0 for working with the PTC Creo Parametric CAD system. The generation process works very well and fast. The generated models are always complete and consistent with the objectives of geometry. One hydraulic element generation was presented in this paper, the gearwheel pump. Further possible improvements of the software are: adding more hydraulic elements options to generate, adding automated tests for created models, and add new types of models.

### References

- [1] Ivantysyn J., Ivantysynova M., *Hydrostatic pumps and motors: principles, design, performance, modelling, analysis, control and testing*, TechBooks International, 2003.
- [2] Ionel II. *Pumps and pumping*, Elsevier Science Pub. Co., Inc., New York 1986.
- [3] Parametric Technology Corporation, *PTC Creo® Parametric 3.0 PTC Creo Object TOOLKIT C++ User's Guide*, Release Notes, 2014.
- [4] Lisowski E., *Automatyzacja i integracja zadań projektowania z przykładami dla systemu Pro/Engineer Wildfire*, Wyd. PK, Kraków 2007.
- [5] Kollek W., Palczak E., *Optymalizacja elementów układów hydraulicznych*, Zakład Narodowy im. Ossolińskich, Wrocław 1996.
- [6] Sclater N., Chironis NP., *Mechanisms and mechanical devices sourcebook*, McGraw-Hill, New York 2001.



EDWARD LISOWSKI\*, JANUSZ RAJDA\*\*

## CFD ANALYSIS OF FLOW FORCES ACTING ON THE SPOOL OF DIRECTIONAL CONTROL VALVE TYPE WE10J

### ANALIZA CFD SIŁ HYDRAULICZNYCH DZIAŁAJĄCYCH NA SUWAK ROZDZIELACZA TYPU WE10J

#### Abstract

The paper presents a CFD analysis of flow forces acting on a spool of directional control valve type WE10J. This is a four-port, three-position, solenoid directly operated valve with a nominal diameter of 10 mm and working pressure up to 35 MPa. The aim of the study was to investigate whether hydraulic forces acting on the spool during the flow of working fluid through the valve could be reduced by changing the geometry of that spool. ANSYS/Fluent software was used for the CFD analysis.

*Keywords: CFD analysis, hydraulic directional control valve, flow forces, ANSYS/Fluent*

#### Streszczenie

W artykule przedstawiono analizę CFD sił hydraulicznych działających na suwak rozdzielacza hydraulicznego typu WE10J. Jest to rozdzielacz czterodrogowy, trzypolożeniowy, sterowany bezpośrednio elektromagnetycznie o nominalnej średnicy przełotu 10 mm i ciśnieniu roboczym do 35 MPa. Celem analizy było zbadanie, czy poprzez zmiany geometrii suwaka możliwe jest zmniejszenie wartości sił hydraulicznych działających na ten suwak przy przepływie cieczy roboczej przez rozdzielacz. Do analizy CFD zastosowano program ANSYS/Fluent.

*Słowa kluczowe: analiza CFD, rozdzielacz hydrauliczny, siły hydrauliczne, ANSYS/Fluent*

\* Prof. Ph.D. D.Sc. Eng. Edward Lisowski, Institute of Applied Informatics, Faculty of Mechanical Engineering, Cracow University of Technology.

\*\* Ph.D. Janusz Rajda, Ponar Wadowice S.A.

## 1. Introduction

Directional control valves direct solenoid operated are used in the drive and control of various machines and equipment. They change the direction movement of the working element. Their relatively simple design and low power consumption by the solenoid makes them readily used, especially in hydraulic systems with not a very high fluid flow rate. For large values of the flow rate, pilot operated directional control valves are used where a solenoid directly operated valve is a pilot. The design of pilot operated directional control valves is more complicated, as they have a greater weight and larger dimensions. Hence, the producers of directional control valves try to extend the scope of the flow rate for directional control valves directly operated. This is not a simple task, because on the one hand, it requires optimization of the flow channels to reduce the flow resistance, while on the other hand, we must seek to limit the flow forces associated with the flow. Their growth significantly affects the balance of forces acting on the spool, causing finally inability to control the valve. The valve in question WE10J was initially produced for a flow range of 80 dm<sup>3</sup>/min., and subsequently that range was increased by 50% [5] without changing the external dimensions. Now, the aim is to double the stated initial scope, and even more. In this paper a CFD analysis using ANSYS/Fluent will be presented, which focuses on the study of the impact of the spool geometry for the hydrodynamic reaction.

## 2. The object of the study

Directional control valves WE10 are produced with various configurations of flow paths. This paper refers to one type, marked WE10J [5], which is often used to control the direction of movement of the actuator or hydraulic motor. This valve is built of a body 1 made of casting, spool 2, centering springs 4, and two solenoids 3. The standard design of the valve spool is shown in Table 1, marked as A1. For the study, variations of design solutions have been selected to investigate which one would have the best performance. They are symbolized by A1 to A6.

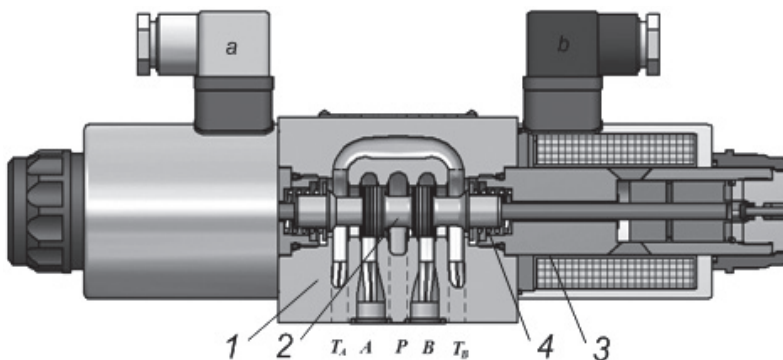


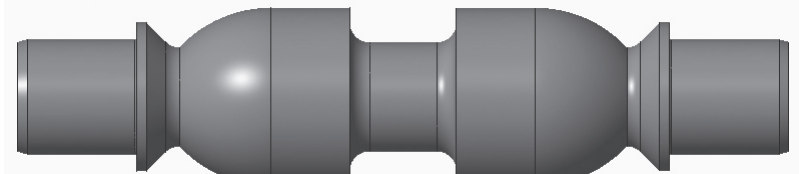

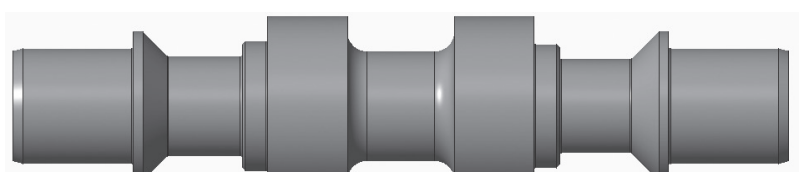
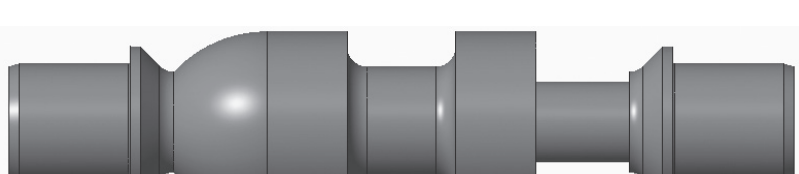


Fig. 1. chematic overview of directional control valve WE10J

**Various spool designs selected for the study**

A1	
A2	
A3	
A4	
A5	
A6	



### 3. Discrete model of flow paths

For the purposes of the CFD analysis, it was necessary to build a geometric model of the fluid filling communication channels of the valve. That was done in the Creo Parametric software using Boolean operations on properly prepared components representing respective volumes of the valve [4]. Geometric models of the flow paths resulting from logic operations are shown in Figure 2. Due to the fact that paths  $PA$  and  $BT$  are identical with paths  $PB$  and  $AT$ , path  $PB$  and  $AT$  were selected to study. Because the individual paths are disjoint geometrically, their analysis may be carried out individually for each flow path. In the paper the analysis process will be shown on the example of  $AT$  flow path. FEM mesh and flow models were performed using ANSYS/Fluent software. Fig. 3 shows a discrete model of the

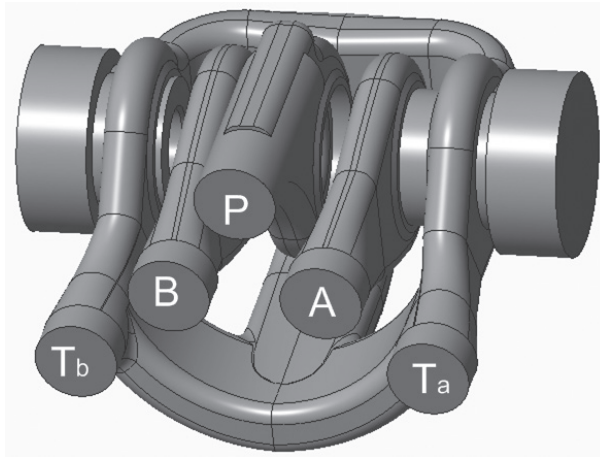


Fig. 2. Fluid geometrical model

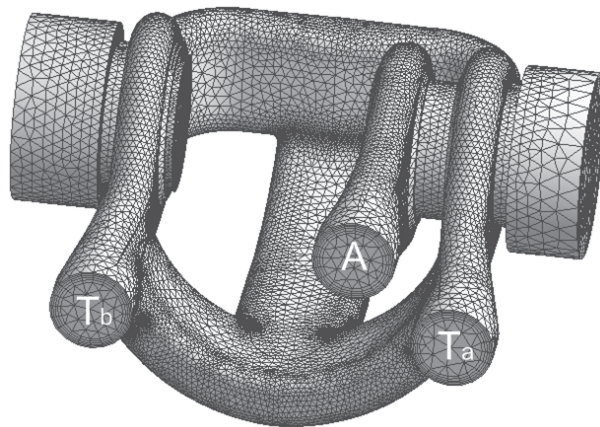


Fig. 3. Mesh of the flow path  $AT$

flow path *AT*. This model was made by means of the advanced features of compaction of the net. Five boundary layers were used for the channel surfaces, and in areas with complex geometry the grid was properly compacted. The path model *AT* includes 2 601 524 cells and 802 625 nodes.

#### 4. CFD model

In order to perform the analysis the kind of flow must be determined. Due to the fact that in the directional control valve there are no conditions for the formation of laminar flow, the turbulent flow pattern was assumed to simulate flow. The ANSYS/Fluent program allows to choose from a variety of models available including: *k-ε*, *k-ω* and *Reynolds*. In the case of flow through the directional control valve *k-ε* model works well enough due to the fact that in the valve there are no conditions for the formation of laminar flow. Thus, for the simulation study the turbulence model was chosen. The kinetic energy of the turbulence and dissipation factor are computed from the following equations [1]:

$$\frac{\partial}{\partial t}(\rho k) + \frac{\partial}{\partial x_i}(\rho k u_i) = \frac{\partial}{\partial x_j} \left( \alpha_k \mu_{eff} \frac{\partial k}{\partial x_j} \right) + G_k + G_b - \rho \varepsilon - Y_M \quad (1)$$

$$\frac{\partial}{\partial t}(\rho \varepsilon) + \frac{\partial}{\partial x_i}(\rho \varepsilon u_i) = \frac{\partial}{\partial x_j} \left( \alpha_\varepsilon \mu_{eff} \frac{\partial \varepsilon}{\partial x_j} \right) + C_{1\varepsilon} \frac{\varepsilon}{k} (G_k + C_{3\varepsilon} G_b) - C_{2\varepsilon} \rho \frac{\varepsilon^2}{k} \quad (2)$$

In these equations  $G_k$  represents the increase in the kinetic energy of turbulence caused by a gradient of average velocities.  $G_b$  is the energy generated by the phenomenon of buoyancy.  $Y_m$  is the energy associated with the compressibility of liquids,  $C_{1\varepsilon}$ ,  $C_{2\varepsilon}$  and  $C_{3\varepsilon}$  are constants of the model,  $s_k$ ,  $s_\varepsilon$  are respectively Prandtl's numbers.

Turbulent viscosity,  $\mu_t$ , is calculated as follows:

$$\mu_t = \rho C_\mu \frac{k^2}{\varepsilon} \quad (3)$$

Model constants  $C_{1\varepsilon} = 1.44$ ,  $C_{2\varepsilon} = 1.92$ ,  $C_m = 0.09$ ,  $s_k = 1.0$ ,  $s_\varepsilon = 1.3$ .

To carry out the calculation in the ANSYS/Fluent program after generating the grid, boundary conditions in the Setup module of the program must be defined. In the option *Boundary Conditions* as inlet velocity magnitude is assumed to be normal to boundary. *Value Velocity* magnitude is introduced as an input parameter to Workbench. As an outlet condition the outlet pressure is taken. Value  $k$  and  $\varepsilon$  are introduced as intensity and length scale. Using model Results of the ANSYS/Fluent program, with the command *Calculators* and *Expressions to Workbench* there are introduced as parameters  $F_x$ ,  $F_y$  and  $F_z$  forces acting on the valve spool.

## 5. Results of calculations

The CFD analysis was performed for the spool in a position allowing the flow from port *P* to *B* and from *A* to *T*. The results of the analysis showed that the greatest force values associated with the fluid flow were on the way from port *A* to *Tb*. Therefore, in the paper test the results for this flow path are shown. As a result of the conducted study, distributions of the fluid flow velocity and pressure on the walls were determined. Fig. 4 shows the velocity distribution along the stream lines, and Fig. 5 in the longitudinal section of the flow path. Calculations were made for the following boundary conditions:

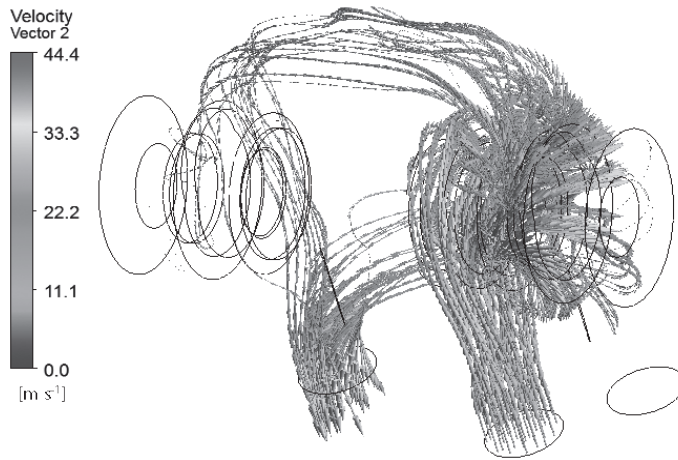


Fig. 4. Fluid velocity vectors along the stream lines for flow path *ATa*

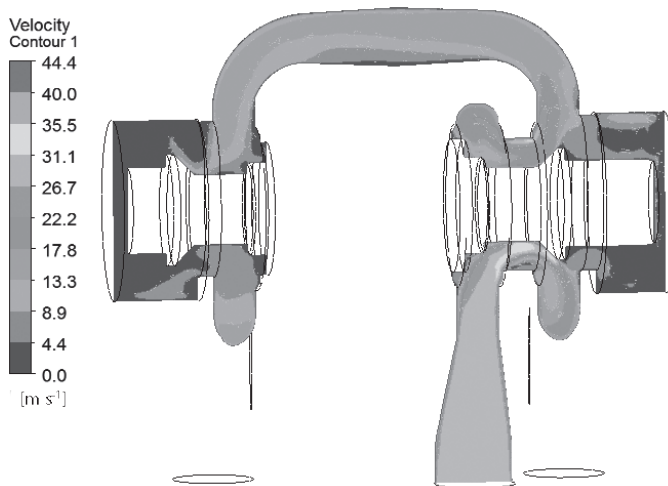


Fig. 5. Fluid velocity vectors in the longitudinal section for flow path *ATa*

- the average velocity of the fluid in the plane of port  $A$ :  $v = 28$  m/s, which corresponds to the flow rate  $Q = 160$  dm<sup>3</sup>/min,
- the outlet pressure in the plane of port  $Ta$ :  $p = 0.1$  MPa.

As it is clear from the results, the maximum value of the local velocity does not exceed 1.6 average value at the inlet to port  $A$ .

Fig. 6 shows the distribution of pressure on the walls of the spool. During the flow from port  $A$  to  $Tb$  the fluid flows in both ends of the spool. As it is evident from the pressure distribution, higher pressure at the spool is from channel  $A$ , what results in the formation of the resultant axial force directed opposite to the direction of the solenoid force. Table 1 shows the pressure loss at fluid flow from port  $A$  to  $Tb$  and the value of hydraulic forces obtained for flow rate  $Q = 160$  dm<sup>3</sup>/min.  $F1$  stands for the value of force acting on the surface of the spool from port  $A$ , while  $F2$  for the value of hydraulic force acting from port  $Tb$ .  $F$  is the value of the resultant of the two forces acting on the valve spool.

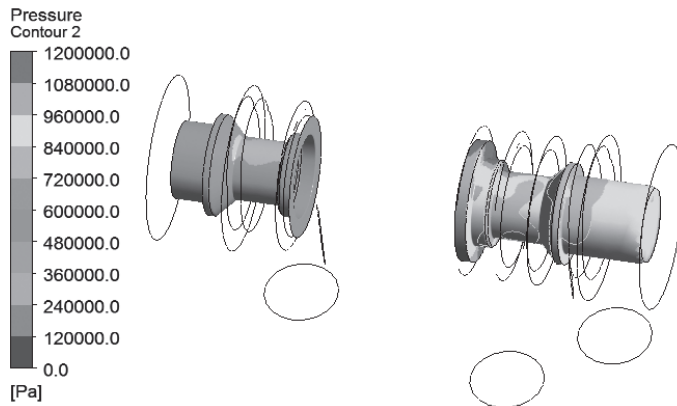


Fig. 6. Pressure distribution on the spool surface

Table 2

**Pressure losses and forces associated with the flow from port a to Tb**

Variant	$\Delta p$ [MPa]	$F1$ [N]	$F2$ [N]	$F$ [N]
A1	0.92	-224.94	165.84	-59.10
A2	1.10	-229.10	167.68	-61.43
A3	2.26	-224.96	164.48	-60.48
A4	0.95	-212.22	145.72	-66.50
A5	0.90	-213.05	149.46	-63.59
A6	0.91	-220.12	149.53	-70.58

As it can be seen from the data presented in Table 2, the resulting hydraulic forces  $F1$  and  $F2$  associated with the fluid flow have opposite directions, what makes their operation

to a large extent mutually compensating. There remains, however, some value of unbalance. Table 1 shows various designs of spools but they do not fully solve the problem. The lowest value of the resultant force was obtained for variant A1, while the lowest flow rate loss for variant A5.

## 6. Conclusions

The paper has presented a CFD analysis of the four port directional control valve WE10J of nominal size 10, intended for the use at flow up to 120 dm<sup>3</sup>/min. The study was conducted for a wider range of up to 160 dm<sup>3</sup>/min. in order to estimate the permissible scope of its work. The CFD analysis has shown a possibility of a much greater range of the flow rate. That is, however, connected with the formation of the fluid forces which act on the valve spool in the direction opposite to the solenoid force. The formation of fluid forces is inevitable for a wide range of flow rate. On the basis of the flow forces defined by the CFD analysis, a solenoid and return spring of respectively sufficient strength can be chosen. Furthermore, the range of parameters for proper performance of the valve can be determined.

## References

- [1] Launder B.E., Spalding D.B., *The Numerical Computation of Turbulent Flows. Computer Methods in Applied Mechanics and Engineering*, 3, 1974, 269-289.
- [2] Lisowski E., Domagala M., *Determination of static characteristic of direct acting relief valve*, Proceedings of the 1st international conference on computational methods in fluid power technology, Melbourne 2003, 211-220.
- [3] Lisowski E., Rajda J., *CFD analysis of pressure loss during flow by hydraulic directional control valve constructed from logic valves*, *Energy Conversion and Management* 65, 2013, 285-291.
- [4] Lisowski E., Czyżycki W., Rajda J., *Three dimensional CFD analysis and experimental test of flow force acting on the spool of solenoid operated directional control valve* *Energy Conversion and Management*, Volume 70, June 2013, 220-229.
- [5] *Directional spool valve type WE10 electrically operated*, Catalogue, Ponar Wadowice, WK 499 780, 2013.

FILIP LISOWSKI\*

## NUMERICAL COMPUTATION OF STRESSES AND DEFORMATIONS IN THE PLANETARY ROLLER SCREW COMPONENTS

### OBLICZENIA NUMERYCZNE NAPRĘŻEŃ I ODKSZTAŁCEŃ W ELEMENTACH PLANETARNEJ PRZEKŁADNI ŚRUBOWEJ ROLKOWEJ

#### Abstract

The paper presents finite element analysis of stresses and deformations of planetary roller screw components. The finite element model takes into account the frictional contact between helical surfaces. The results of numerical calculations for the contact problem were compared with the theoretical solution based on the Hertz theory. The obtained results can be used in the development of design procedures of planetary roller screw.

*Keywords: Planetary roller screw, finite element analysis, contact analysis*

#### Streszczenie

W artykule przedstawiono analizę naprężeń i odkształceń elementów planetarnej przekładni śrubowej rolkowej. W modelu MES uwzględniono kontakt z tarciami pomiędzy powierzchniami śrubowymi. Wyniki z obliczeń numerycznych dla zagadnienia kontaktowego porównano z rozwiązaniem teoretycznym w oparciu o wzory Hertza. Otrzymane wyniki mogą być wykorzystane w rozwoju procedur projektowych.

*Słowa kluczowe: Przekładnia śrubowa rolkowa, analiza MES, analiza kontaktu*

\* M.Sc. Eng. Filip Lisowski, Institute of Machine Design, Faculty of Mechanical Engineering, Cracow University of Technology.

## 1. Introduction

Planetary Roller Screw (PRS) is a mechanical actuator that is characterized mainly by high efficiency, high load capacity, resistance to dynamic loads and resistance to a hostile work environment. In comparison with a more common ball screw, roller screws have larger contact surfaces of rolling elements, higher axial stiffness and lower noise. However, because of manufacturing (fine grinding, surface hardening) and unitary production PRS is much more expensive.

The main elements of a planetary roller screw (Fig. 1), which transfer the load, are: screw (1), nut (3) and rollers (2). The movement of the rollers is synchronized by the planetary toothed conjunction (4, 5). The cores of the rollers are based in the endplates (6).

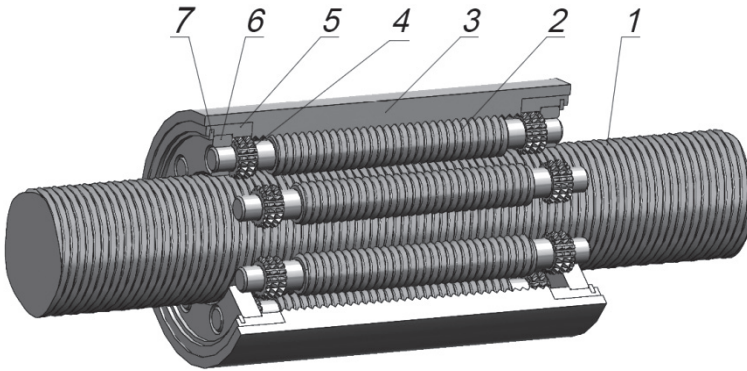


Fig. 1. Planetary roller screw structure; 1 – screw, 2 – roller, 3 – nut, 4 – satellite toothed wheel, 5 – end plate, 6 – sun toothed wheel, 7 – retaining wheel

The previous publication related to the stress analysis and the load distribution in the planetary roller screw components concerned mainly: the analysis of the displacements and the load distribution between cooperating elements and the related determination of the stiffness of the cooperating areas [2], analysis of the load distribution for the preliminary design based on the analytical model and a study on the load cases [5], the procedure of the preliminary design of PRS including also an analysis of the carrying capacity of the threads based on the Hertz theory [3], a mathematical model for contact analysis, where series of equivalent balls are used to replace the rounded profile of the roller's thread [8], an optimal design and contact analysis concerning an attempt to reduce the contact area between the screw, the roller and the nut for trapezoidal threads [4].

The main goal of this paper was to investigate displacements and stresses of the cooperating components of a planetary roller screw including the contact between the screw, the roller and the nut simultaneously. An additional objective was to investigate the shape of the contact regions on the thread's surfaces and to compare numerical results with the theoretical solution based on the Hertz theory.

The presented studies were carried out for the following pitch dimensions of the screw, roller and nut:  $d_s = 30$  mm,  $d_r = 10$  mm,  $d_n = 50$  mm and the thread pitch  $p = 2$  mm.

## 2. Theoretical solution of the contact problem

An approximate method of the solution to the problem of two bodies in contact, using the Hertz theory, was presented in [1, 7] and developed in [6]. The theory relates to the general case of compression of two elastic bodies with the radii of curvature for the first body:  $R_{11}$ ,  $R_{12}$  and for the second body:  $R_{21}$ ,  $R_{22}$  where  $R_{11} < R_{12}$  and  $R_{21} < R_{22}$ . For the cooperation of the roller, screw and nut threads (Fig. 2), the radii of the curvatures were accepted as given in eq. 1–3, where indexes  $r$ ,  $s$ ,  $n$  refer consecutively to the roller, the screw and the nut.

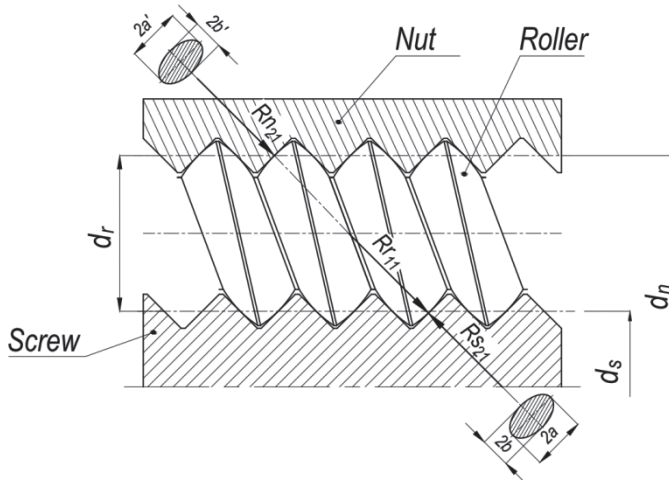


Fig. 2. Pitch diameters of planetary roller screw components and theoretical ellipse of contact

The following radii take into account respectively the curvatures of the threads' profiles and the curvatures of the helix lines.

$$Rr_{11} = \frac{d_r}{2 \sin(\alpha_0)}, \quad Rr_{12} = \frac{(d_r/2)^2 + p^2}{p} \quad (1)$$

$$Rs_{21} = \frac{(d_s/2)^2 + p^2}{p}, \quad Rr_{12} = \infty \quad (2)$$

$$Rn_{21} = \frac{(d_n/2)^2 + p^2}{p}, \quad Rr_{22} = \infty \quad (3)$$

where:

- $d_s, d_n, d_r$  – pitch diameter of the screw, the nut and the roller,
- $\alpha_0$  – thread flank angle,
- $p$  – thread pitch.



Contact pressures can be calculate using the eq. (4).

$$P_o = \frac{3}{2} \frac{F_c}{\pi \cdot a \cdot b} \quad (4)$$

where:

$F_c$  – contact pressure force  
 $a, b$  – semi-axes of the ellipse of contact determined from eq. (5).

$$a = m_H \sqrt[3]{\frac{3\pi F_c}{2} \frac{\kappa}{A+B}}, \quad b = n_H \sqrt[3]{\frac{3\pi F_c}{2} \frac{\kappa}{A+B}}, \quad \kappa = \frac{1-\nu^2}{\pi E} \quad (5)$$

where:

$\nu$  – Poisson's ratio,  
 $E$  – Young's modulus.

Based on the coefficients  $A$  and  $B$ , depending on the radii of curvatures, an auxiliary angle  $\theta$  is determined (eq. 6–7). For this angle, Hertz coefficients  $m_H$  and  $n_H$  appearing in eq. 5 can be determined.

$$\theta = \arccos\left(\frac{B-A}{A+B}\right), \quad A+B = \frac{1}{2} \left( \frac{1}{R_{11}} + \frac{1}{R_{12}} + \frac{1}{R_{21}} + \frac{1}{R_{22}} \right) \quad (6)$$

$$A-B = \frac{1}{2} \sqrt{\left(\frac{1}{R_{11}} - \frac{1}{R_{12}}\right)^2 + \left(\frac{1}{R_{21}} - \frac{1}{R_{22}}\right)^2 + 2\left(\frac{1}{R_{11}} - \frac{1}{R_{12}}\right)\left(\frac{1}{R_{21}} - \frac{1}{R_{22}}\right)\cos(2\varphi)} \quad (7)$$

where:

$\varphi$  – angle determining the relative position of contact planes.

The values of the Hertz coefficients can be taken from the tables in the literature [7] for  $\theta \in \langle 30^\circ \div 90^\circ \rangle$  with an accuracy of  $5^\circ$  or in [1]  $\theta \in \langle 1^\circ \div 90^\circ \rangle$  with an accuracy of  $1^\circ$ . Publication [6] also delivered continuous functions of Hertz coefficients  $m_H$  and  $n_H$  as given in eq. 8 and eq. 9.

$$m_H^{-1} = -0,72576 \cdot \theta^4 + 0,306757 \cdot \theta^3 - 0,425848 \cdot \theta^2 + 0,817353 \cdot \theta + 0,018040 \quad (8)$$

$$n_H = -0,640562 \cdot \theta^6 + 3,471455 \cdot \theta^5 - 7,405219 \cdot \theta^4 + 7,984778 \cdot \theta^3 - 4,592703 \cdot \theta^2 + 1,771294 \cdot \theta + 0,108768 \quad (9)$$

### 3. Finite element analysis

The analysis of stresses and deformation was performed by applying ANSYS software. A finite element model (Fig. 3) included a 1/10 section of a planetary roller screw within a single cooperating pair of threads and was prepared using 20-node solid elements SOLID95 and contact elements TARGE170 and CONTA 174. Contact elements were defined on much larger areas than the surface areas resulting from the Hertz theory (Fig.4). Due to complex geometry of threads an irregular mesh was used. In the regions of contact, the mesh was refined with element size  $h = 0,01$  mm. The coefficient of friction  $\mu = 0.1$ ; Young modulus  $E = 2,11 \cdot 10^5$  MPa and Poisson ratio  $\nu = 0.3$  were accepted. The axial load, which was applied to the core of the nut, was accepted at the low, medium and high level  $F = \{25, 50, 100\}$  N.

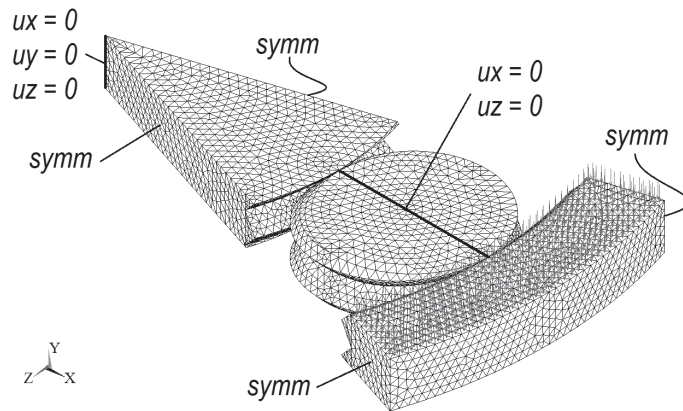


Fig. 3. Finite element model of 1/10 section of PRS with boundary conditions

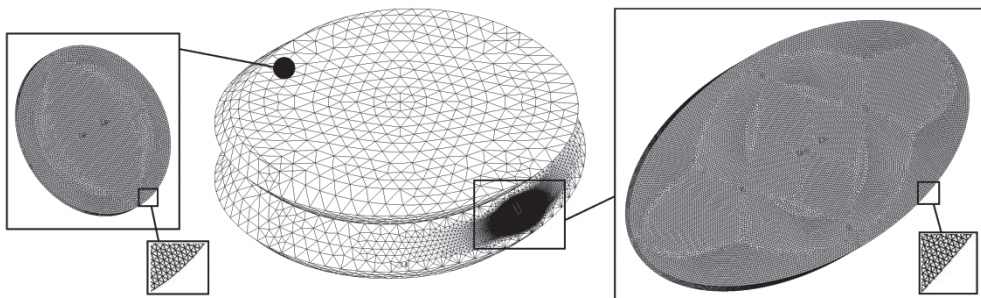


Fig. 4. Mesh refinement in the contact regions in example of the roller (element size  $h = 0.01$  mm)

### 4. Results

The results obtained from the theoretical and finite element analysis are summarized in Tables 1–3. In Fig. 5 to Fig. 10 the results obtained for the axial load  $F = 50$  N are presented.

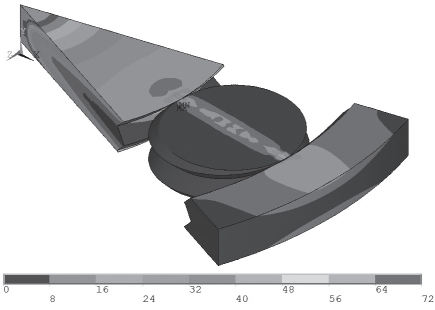


Fig. 5. Huber-Mises-Hencky reduced stress

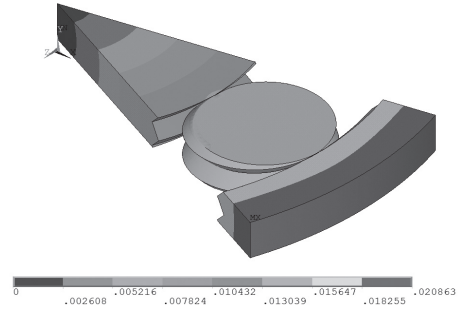


Fig. 6. Displacement vector sum

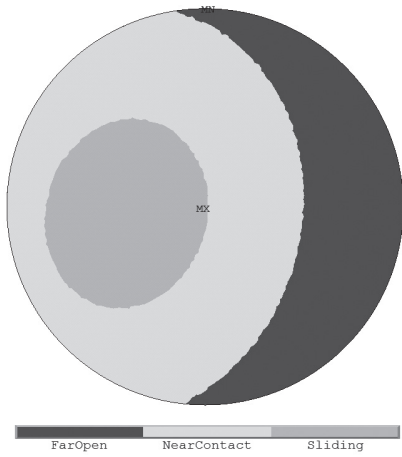


Fig. 7. Contact area between the roller and screw determined with FEA

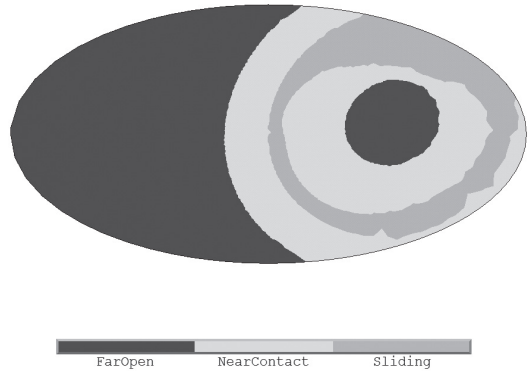


Fig. 8. Contact area between the roller and the nut determined with FEA ( $F = 50\text{ N}$ )

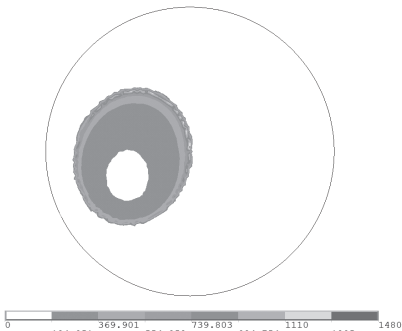


Fig. 9. Contact pressure between the roller and screw determined with FEA

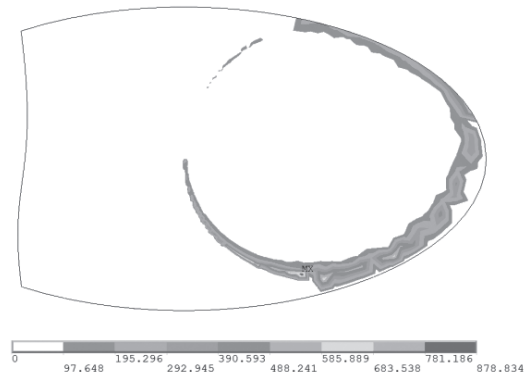


Fig. 10. Contact pressure between the roller and the nut determined with FEA

Fig. 5 and Fig. 6 present Huber-Mises-Hencky the sum of reduced stress and displacement vector. Fig. 7 and Fig. 8 show the contact areas determined based on FEM, with the indication of the sliding zone. The contact area between the screw and the roller is closed, but between the roller and the nut there is an edge zone. Fig. 9 and Fig. 10 present contact pressure between the screw roller and the nut. The difference in the contact pressure for numerical and theoretical solutions is at the level of 0–39% for the contact between the screw and roller and decreases with the increase of the axial load (Tab. 1). A similar result is obtained for the contact between the roller and the nut. For comparison, the pressure around the border of the sliding zone was taken. The difference of local displacements in the contact areas between the screw and roller as well as the roller and nut is about 16% (Tab. 3).

Table 1

**Contact pressure and the contact regions between the roller and screw**

Axial Load [N]	Contact pressure (Hertz) [MPa]	Contact pressure (FEM) [MPa]	Relative error of contact pressure
25	999	608	39.1%
50	1259	1480	17.6%
100	1585	1586	0.1%

Table 2

**Contact pressure and the contact regions between the roller and nut**

Axial Load [N]	Contact pressure (Hertz) [MPa]	Contact pressure (FEM) [MPa]	Relative error of contact pressure
25	969	–	–
50	1221	879	28.0%
100	1585	1531	0.5%

Table 3

**Axial displacement in the contact regions (FEM)**

Axial Load	Axial displacement in contact region of screw (FEM)	Axial displacement in contact region of nut (FEM)	Displacement factor
F [N]	$u_{y(s-r)}$ [mm]	$u_{y(n-r)}$ [mm]	$u_{y(n-r)}/u_{y(s-r)}$
25	0.00654	–	–
50	0.01306	0.01519	1.16
100	0.02616	0.03064	1.17

## 5. Conclusions

The consistency of the theoretical and numerical results for the contact analysis was achieved only after a significant increase in the axial load. Using the finite element analysis gives good results at a medium and high level of the axial load. At low values of the axial load the results of the FEA should be assessed carefully.

In fact, the displacement can be larger due to the roughness of the surfaces, which in the FEM is omitted, and the displacements obtained from the FEM analysis for the low level of the axial load are comparable to roughness of the surfaces. For a high level of the axial load the influence of surface roughness on the accuracy of the cooperation can be omitted. It would be useful to carry out experimental studies verifying the influence of the surface roughness for a low load level.

## References

- [1] Cooper D.H., *Tables of Hertzian contact-stress coefficients*, University of Illinois, Report R-387, 1968.
- [2] Lisowski F., *The Analysis of displacements and the load distribution between elements in a Planetary Roller Screw*, Applied Mechanics and Materials, Vol. 86, 2014, 361-364.
- [3] Lisowski F., *Procedura wstępnego projektowania planetarnej przekładni śrubowej rolkowej z przekładnią zębatą*, Przegląd Mechaniczny, 4/2014, 39-49.
- [4] Ma S., Liu G., Zhou J., Tong R., *Optimal design and contact analysis for Planetary Roller Screw*, Applied Mechanics and Materials, Vol. 86, 2012, 361-364.
- [5] Ryś J., Lisowski F., *The computational model of the load distribution between elements in a planetary roller screw*, Journal of Theoretical and Applied Mechanics, Vol. 52, No. 3, 2014.
- [6] Romanowicz P., Szybiński B., *Analytical and numerical assessment of fatigue properties in rolling bearings*, 4th International Conference on Integrity, Reliability & Failure, 2013.
- [7] Timoshenko S., Goodier J.N., *Teoria sprężystości*, McGraw-Hill Book Company, 1951.
- [8] Zhang X., Liu G., Ma S., Tong R., Luo H., *Study on axial contact deformation of planetary roller screw*, Applied Mechanics and Materials, Vol. 155–156, 2012, 779-783.

FILIP LISOWSKI\*

## OPTIMIZATION OF A CURVILINEAR THREAD PROFILE IN A PLANETARY ROLLER SCREW

---

### OPTIMALIZACJA KRZYWOLINIOWEGO ZARYSU GWINTU W PLANETARNEJ PRZEKŁADNI ŚRUBOWEJ ROLKOWEJ

#### Abstract

The paper presents an application of the Finite Element Method (FEM) in stress analysis and optimization of thread profiles in cooperation of the roller with the screw in the planetary roller screw mechanism. The problem of the roller and the screw threads cooperation as well as related geometrical parameters were described. The optimization problem was formulated with the aim of obtaining a better effort of threads and lower contact pressure depending on the geometry.

*Keywords: Planetary roller screw, thread profile, finite element method, optimization*

#### Streszczenie

W artykule przedstawiono zastosowanie Metody Elementów Skończonych (MES) w analizie naprężeń i optymalizacji zarysu gwintów do współpracy rolki ze śrubą w planetarnej przekładni śrubowej rolkowej. Opisano zagadnienie współpracy gwintów śruby i rolki oraz związane z nim parametry geometryczne zarysu gwintów. Sformułowano zadanie optymalizacyjne, mające na celu poprawę wytrzymałości i zmniejszenie nacisków kontaktowych w zależności od geometrii gwintów.

*Słowa kluczowe: Planetarna przekładnia śrubowa rolkowa, zarys gwintu, metoda elementów skończonych, optymalizacja*

---

\* M.Sc. Eng. Filip Lisowski, Institute of Machine Design, Faculty of Mechanical Engineering, Cracow University of Technology.

## Denotations

$d_s, d_n, d_r$	– pitch diameter of the screw, the nut and the roller [mm]
$n_s, n_n, n_r$	– thread starts of the screw, the nut and the roller [mm]
$a_{rs}$	– distance between the axes of the roller and the screw [mm]
$a_{rn}$	– distance between the axes of the roller and nut [mm]
$x_1, x_2$	– dimensions of the undercut in the thread notch [mm]
$R_r, R_s$	– radii of the screw and the roller thread flank [mm]
$\sigma_{HMH}^{\max}$	– Huber-Mises-Hencky reduced stress in the notch of thread (model without undercut) [MPa]
$\sigma_{HMH}^{\max_u}$	– Huber-Mises-Hencky reduced stress in the notch of thread (model with undercut) [MPa]
$C_{\text{press}}^{\max}$	– maximum contact pressure on thread (model without undercut) [MPa]
$C_{\text{press}}^{\max_u}$	– maximum contact pressure on thread (model with undercut) [MPa]

## 1. Introduction

A Planetary Roller Screw (PRS) is a low friction mechanism quite similar to a ball screw. It is used to convert the rotational motion of the screw into a linear motion of the nut or inversely (inverted planetary roller screw). Providing more contact points than the ball screws, planetary roller screws have higher load capacity with a similar efficiency (70%–90%) [5]. Previous publications on the planetary roller screw related to the thread profile problems concerning: cooperation of threads and the resulting necessity for using a curved thread profile [1], determination of the roller thread profile for a trapezoidal thread due to non-interference of cooperating threads [7], determination of the stiffness of the cooperating areas between the screw, roller and nut in order to determine the load distribution using a simplified model [2]. The values of this stiffness delivered for the specified range of axial forces were essential in [6] to determine load distribution between cooperating elements using the analytical model. In the paper [3], the procedure of a preliminary design of the planetary roller screw, including the limitation due to the carrying capacity of a thread determined based on the Hertz theory was presented.

The aim of this paper was to investigate the influence of the undercut in the notch of the thread on the stress state and contact pressure within a single pair of cooperating threads. The goal of the paper was carried out by the use of optimization.

## 2. Principle of operation and limitations

The PRS consists of a screw, an arbitrary number of rollers and a nut. The rollers, which spin in contact and transfer the load between the screw and the nut are additionally connected with the nut by the planetary toothed conjunction. The role of this connection is to synchro-

nize the planetary movement of the rollers. The screw and the nut have multi-start threads whereas the rollers have a single thread.

To enable cooperation of the rollers with the nut, the axial displacement of the rollers relative to the nut must be equal to zero. This will take place when the helix angles of the nut and the rollers are the same and kinematic conditions are met [4]. Assuming the start of roller thread  $n_r = 1$ , the relation between pitch diameters of the screw and the rollers is obtained (eq. 1).

$$n_n = \frac{d_s + 2d_r}{d_r} = \frac{d_n}{d_r} \quad (1)$$

On the assumptions that rollers cooperate with the screw without slipping it appears that the starts of the screw and nut thread are equal  $n_s = n_n$  [3].

An orbit, which includes the axes of the rollers is concentric with respect to the screw and the nut. The distance between the axes of the rollers and the nut and the distance between the axes of the roller and the nut must be equal (eq. 2)

$$a_{rn} = (d_n - d_r)/2, \quad a_{rs} = (d_s - d_r)/2, \quad a_{rn} = a_{rs} \quad (2)$$

From the above conditions result in the limitation on the screw and the nut thread start given by eq.3.

$$(d_s/d_r) = n_s - 2 = n_n - 2 \quad (3)$$

The smallest thread start of the screw and the nut is  $n_s = n_n = 3$ . The relations between pitch diameters are strictly defined (eq. 4)

$$d_n = n_n d_r = n d_r, \quad d_s = (n_n - 2)d_r = (n - 2)d_r \quad (4)$$

### 3. Profile of the threads

In order to ensure correct operation of the mechanism it is required to maintain constant pitch diameters of cooperating elements [1]. These diameters depend on the location of the contact points on the threads' flanks. To eliminate the fluctuations of pitch diameters, at least one of the cooperating thread's profile should be curvilinear (Fig. 1).

The most advantageous distribution of the contact pressure is obtained when one of the thread profiles is convex, whereas the other one is concave (Fig. 1c). The actual size of the contact area depends on the ratio of the curvatures' radii of the screw and the roller thread's flank. However, an assumption of too small a difference between these radii, may significantly increase the contact area and shift the contact point and worsen the conditions of the threads cooperation. A significant stress concentration appears in the notch of the screw's thread (Fig. 6). The value of this maximum stress can be reduced by a partial relieving of the screw's thread. It can be achieved by introducing an undercut in the notch of a thread (Fig. 8).



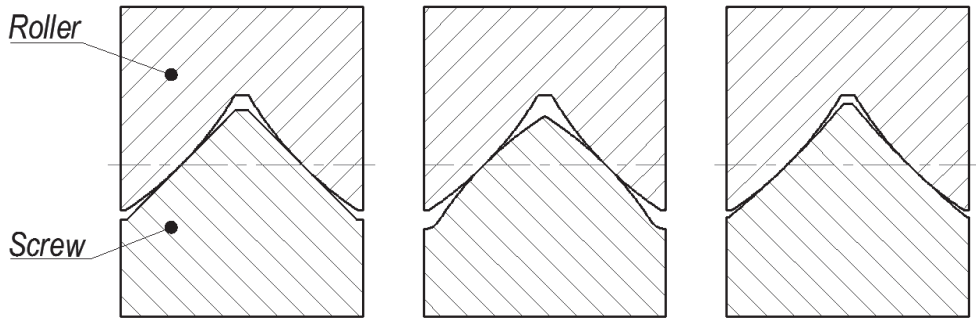


Fig. 1. Curvilinear thread profiles of the screw and the roller: a) screw – flat, roller – convex, b) screw – convex, roller – convex c) screw – concave, roller – convex

The conception of relieving the thread can be applied individually, only for one element (screw or roller).

#### 4. Optimization of the curvilinear thread profiles with an undercut in the notch of the thread

##### 4.1. A finite element model

To solve the optimization problem a 2D finite element model including sections of cooperating threads of the screw and roller was built (Fig. 2). The pitch dimensions of the screw and the roller as well as the thread pitch were accepted as follows:  $d_s = 30$  mm,  $d_r = 10$  mm,  $p = 2$  mm. The 8-node elements PLANE82 available in the ANSYS software were used. The plane's strain was accepted. The contact was defined only for a single pair of cooperating threads. Contact elements CONTA172 and TARGET169 were accepted.

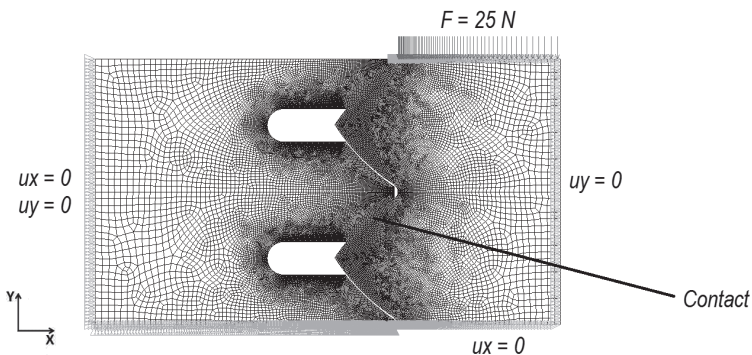


Fig. 2. Finite element model of the screw and the roller threads with boundary conditions

The coefficient of friction in the plane of the model was set to  $\mu = 0.1$ . the axial load  $F = 25$  N was applied to the surface of the roller's core. Young modulus  $E = 2.11 \cdot 10^5$  MPa and Poisson ratio  $\nu = 0.3$  were accepted.

#### 4.2. Design variables, state variables and objective function

The geometry of threads was parameterized as shown in Fig. 3. As the design variables for optimization problem, the dimensions of undercut  $x_1$ ,  $x_2$  and the radius of the roller thread flank's curvature  $R_r$  were assumed. The radius of the screw thread flank's curvature was accepted as  $R_s = k \cdot R_r$ , where  $k = 1.5$ . The coefficient  $k$  has been selected so that the segment of the threads being in contact is not bigger than 20% of the thread flank's length. Contact pressure on the thread flank was accepted as a state variable. Restrictions assumed for design and state variables as well as starting points are summarized in Table 1.

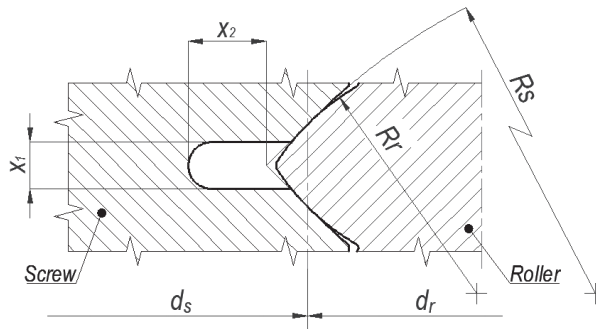


Fig. 3. Design variables and dimensions of the screw and the roller thread

Table 1

#### Design and state variables with restrictions and optimization starting points

Design variables	Sp1	Sp2	Sp3	Sp4	Restrictions
$x_1$	0.1	1	1	0.1	$0.1 < x_1 < 1$
$x_2$	0.5	3	3	0.1	$0.1 < x_2 < 3$
$R_r$	2	2	10	20	$2 < R_r < 20$
State variables					
$R_s$	$1.5 \cdot R_r$	$1.5 \cdot R_r$	$1.5 \cdot R_r$	$1.5 \cdot R_r$	–
$C_{press}^{\max, u}$	–		–		$C_{press}^{\max, u} < 0.6 C_{press}^{\max}$

As an objective function Huber-Mises-Hencky reduced stress in the notch of the screw's thread was accepted. The aim of the optimization was to determine the minimum of the function (eq. 5).

$$Q(x_1, x_2, R_r) = \sigma_{\text{HMH}}^{\text{max}_u} \tag{5}$$

$$Q \rightarrow \min \tag{6}$$

where:

- $Q$  – objective function,
- $\sigma_{\text{HMH}}^{\text{max}_u}$  – Huber-Mises-Hencky reduced stress in the thread undercut,
- $x_1, x_2, R_r$  – design variables.

### 4.3. Results

Table 2 summarized the results obtained for the following starting points. Fig. 4 and Fig. 5 present the values of the maximum Huber-Mises-Hencky reduced stress in the thread’s undercut and the maximum contact pressure on the thread obtained from optimization. The results were compared with two reference geometry without any undercut in the thread notch. First (**Ref 1**) with a radius of  $R_r = 2$  mm, and the second (**Ref 2**) with  $R_r = 20$  mm.

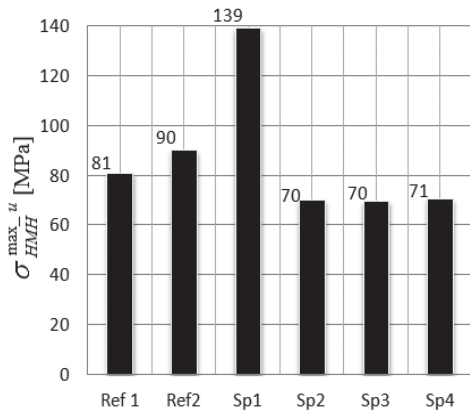


Fig. 4. Maximum Huber-Mises-Hencky reduced stress in the thread undercut

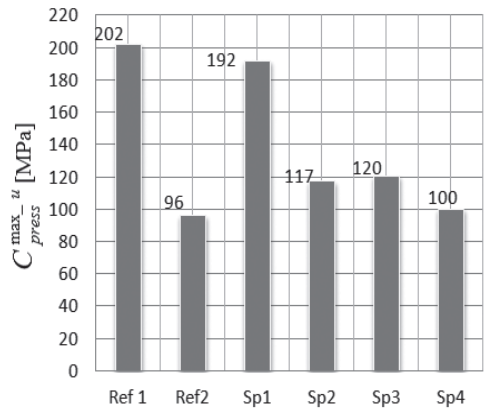


Fig. 5. Maximum contact pressure on thread

Table 2

#### Design and state variables for the best optimization results

Design variables	Sp1	Sp2	Sp3	Sp4
$x_1$	0.11	0.83	0.85	0.78
$x_2$	0.18	0.1	0.1	0.1
$R_r$	2.00	12.77	11.59	19.91
State variables				
$R_s$	3.00	19.16	17.39	29.87
$C_{\text{press}}^{\text{max}_u}$	191.9	117.1	120.4	99.87
$\sigma_{\text{press}}^{\text{max}_u}$	139.2	69.9	69.7	70.58

For the best optimization result (**SP4**), in reference to **Ref 1**, the decrease of the stress concentration in the thread notch was about 12 % and the decrease of the contact pressure was about 50% whereas in comparison with **tRef 2**, about 21% decrease of the stress concentration in the thread notch and a slight increase (about 4%) of the contact pressure was obtained.

Fig. 6 and Fig. 7 present Huber-Mises-Hencky reduced stress and contact pressure on the thread for the reference geometry (Ref 2), whereas Fig. 8 and Fig. 9 for the best result of the optimization (Sp4).

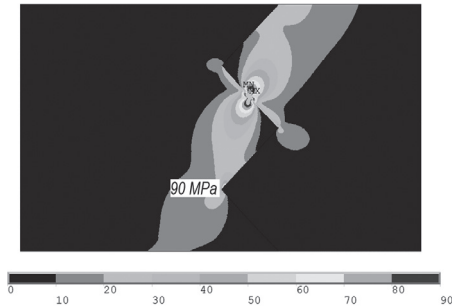


Fig. 6. Huber-Mises-Hencky reduced stress for the reference geometry (Ref 2) ( $\sigma_{\text{press}}^{\text{max}} = 90 \text{ MPa}$ )

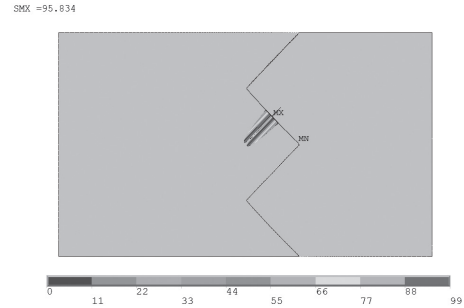


Fig. 7. Contact pressure on the thread for the reference geometry (Ref 2) ( $C_{\text{press}}^{\text{max}} = 96 \text{ MPa}$ )

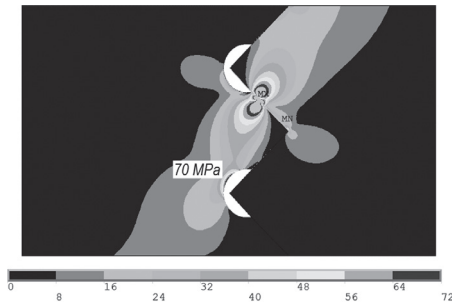


Fig. 8. Huber-Mises-Hencky reduced stress for the best result of the optimization (Sp4) ( $\sigma_{\text{press}}^{\text{max}} = 70 \text{ MPa}$ )

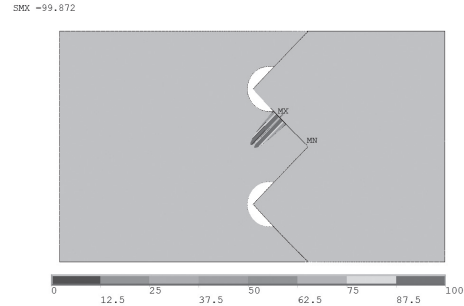


Fig. 9. Contact pressure on the thread for the best optimization result (Sp4) ( $C_{\text{press}}^{\text{max}} = 100 \text{ MPa}$ )

## 5. Conclusions

The result obtained from the finite element analysis with the optimization procedure showed that the use of the undercut in the thread notch has a positive effect on the reduction of stress concentration. Concerning an effect on a single cooperating pair of threads, it can be concluded that it is recommended to use the values of the optimization parameters based on the proportion referred to the thread pitch as follows:

$$x_1/p \approx 0.4; \quad x_2/p \approx 0.05; \quad R/p \approx 10$$

However, it should be taken into account, that too wide an undercut can undermine the contact zone. At the same time, the results obtained for the reference models (without undercut), revealed that the increase in the radii of the roller and the screw thread's flank curvature results in a significant reduction in the contact pressure. However, at the same time it slightly increases stress concentration in the thread notch.

Such an undercut could be also advantageous due to lubrication. It can act as a place for lubricate accumulation. From the manufacturing point of view, it is advantageous to make undercuts in the thread notches of the rollers.

## References

- [1] Hojjat Y., Mahdi A.M., *A comprehensive study on capabilities and limitations of rollers crew with emphasis on slip tendency*, Mechanism and Machine Theory, Vol. 44, No. 10, 2009, 1887-1899.
- [2] Lisowski F., *The Analysis of displacements and the load distribution between elements in a Planetary Roller Screw*, Applied Mechanics and Materials, Vol. 86, 2014, 361-364.
- [3] Lisowski F., *Procedura wstępnego projektowania planetarnej przekładni śrubowej rolkowej z przekładnią zębatą*, Przegląd Mechaniczny, 4/2014, 39-49.
- [4] Ma S., Liu G., Tong R., Zhang X., *A New Study on the Parameter Relationships of Planetary Roller Screws*, Mathematical Problems in Engineering, Volume 2012, Article ID 340437.
- [5] Nale M.J., *The Tribology Handbook (Second Edition)*, Butterworth Heinemann, Oxford 1995.
- [6] Ryś J., Lisowski F., *The computational model of the load distribution between elements in a planetary roller screw*, Journal of Theoretical and Applied Mechanics, Vol. 52, No. 3, 2014.
- [7] Warchoń S., *Wyznaczanie zarysu gwintu rolki dla trapezowego zarysu gwintu śruby w rolkowej przekładni śrubowej*, Czasopismo Techniczne, 1-M/2010, Kraków 2010.

JAROSŁAW MATLAK, DAMIAN SŁOTA\*

## SOLUTION OF THE STEFAN PROBLEM BY INVOLVING MATERIAL SHRINKAGE

---

### ROZWIĄZANIE ZAGADNIENIA STEFANA Z UWZGLĘDNIENIEM SKURCZU MATERIAŁU

#### Abstract

In this paper we describe an algorithm for solving the one-dimensional Stefan problem by involving metal shrinkage. In this algorithm we use the finite element method supplemented by the procedures allowing to define the position of moving interface and the change material size associated with shrinkage. We present also some examples illustrating the precision of the presented method.

*Keywords: solidification; Stefan problem; shrinkage*

#### Streszczenie

W artykule opisano algorytm rozwiązywania jednowymiarowego zagadnienia Stefana z uwzględnieniem skurczu metalu. W algorytmie tym użyto metody elementów skończonych uzupełnionej o procedury pozwalające określić położenie ruchomej granicy między fazami oraz zmianę objętości materiału związaną ze skurczem. Przedstawiono również przykład przedstawiający dokładność prezentowanej metody.

*Słowa kluczowe: krzepnięcie, problem Stefana, skurcz materiału*

---

\* M.Sc. Eng. Jarosław Matlak, Ph.D. D.Sc. Eng. Damian Słota, prof. PŚI, Institute of Mathematics, Silesian University of Technology

## 1. Introduction

Difference between density of the liquid and its solid phase causes shrinkage of metal during its solidification (there exist also substances, such as water, volumes of which expand during solidification). In this process an air-gap forms between the form and the cast, which has an influence on creating an interfacial thermal resistance between the mould and the cast. This thermal resistance determines the mould heat flux and thus affects the billet's quality, such as the cracks and oscillation marks.

Solidification of pure metals is mathematically modeled by means of the Stefan problem [1–3]. This problem consists in determination of the temperature distribution in liquid and solid phases. Simultaneously, the position of the boundary between the phases should be found as well. The Stefan problem is a non-linear problem [3]. Nonlinearity is connected with the Stefan condition resulting from the heat balance on the moving interface. In simple cases it is possible to find an exact solution of the Stefan problem [4, 5], but generally to find a solution to this problem the numerical or numerically-analytical methods must be used [1, 2, 6–8].

A mathematical model for describing processes involving the simultaneous heat and mass transfer with the phase transition in foods undergoing a volume change (shrinkage or expansion) is presented in paper [9]. To approximate the solution of the problem the finite element method and the Arbitrary Lagrangian-Eulerian method were used. Natale et al. in paper [10] determined the temperature distribution in solid and liquid one-dimensional regions and the position of two free boundaries in the solidification process with either shrinkage or expansion. The results were obtained for three different boundary conditions. In all cases, the explicit solution was given by the parametric representation of a similarity type. The one-dimensional problem of pure metal solidification involving metal shrinkage was considered also in paper [11], where the perturbation method for small Stefan numbers was used to find the solution.

In this paper we intend to show an algorithm for solving the one-dimensional Stefan problem involving metal shrinkage. In this algorithm we will use the finite element method supplemented by the procedures allowing to define the position of the freezing front and the change of material size associated with material shrinkage. To determine the boundary position we use an algorithm in which, on the basis of the Stefan condition, the size of the time step is iteratively selected so that the boundary moves to the adjacent node [2]. To determine the change in size we propose a procedure based on the mass balance. We present also some examples illustrating the precision of the presented method.

## 2. Formulation of the problem

Let us consider a domain (ingot domain) occupied by liquid and solid phases. This domain is variable in time. Sizes of the liquid and solid phases will change, whereas the size of the ingot will change as well due to the material shrinkage involved. We consider solidification of pure metal modeled by using the Stefan problem [1, 2]. Thus, inside domain  $\Omega = \{(x, t): 0 \leq x \leq d(t), 0 \leq t \leq t^*\}$  the heat conduction equation is given [11]:

$$c_i \rho_i \frac{\partial u(x, t)}{\partial t} = \lambda_i \frac{\partial^2 u(x, t)}{\partial x^2} + (i-1) \left( 1 - \frac{\rho_1}{\rho_2} \right) \frac{d\xi(t)}{dt} \frac{\partial u(x, t)}{\partial x} \quad (1)$$

$(x, t) \in D_i \times (0, t^*)$  where  $i = 1$  for liquid phase,  $i = 2$  for solid phase, intervals  $D_1 = (0, \xi(t))$  and  $D_2 = (\xi(t), d(t))$  represent the liquid and solid phases, respectively,  $\xi$  is a function describing the position of the moving boundary (the freezing front),  $d$  denotes a function describing the length of the area associated with metal shrinkage,  $c_i$  is the specific heat,  $\lambda_i$  is the thermal conductivity coefficient,  $\rho_i$  denotes density of the corresponding phase and  $\left( 1 - \frac{\rho_1}{\rho_2} \right)$  is the shrinkage factor. There are also the following initial conditions given:

$$u(x, 0) = u_0, \quad \xi(0) = \xi_0, \quad d(0) = d_0 \quad (2)$$

and the boundary conditions:

$$-\lambda_1 \frac{\partial u(0, t)}{\partial x} = q(t), \quad t \in (0, t^*) \quad (3)$$

$$-\lambda_2 \frac{\partial u(d(t), t)}{\partial x} = \alpha (u(d(t), t) - u_\infty), \quad t \in (0, t^*) \quad (4)$$

where  $\alpha$  is the heat transfer coefficient and  $u_\infty$  denotes the ambient temperature.

On the moving interface the condition of temperature continuity and the Stefan condition are defined as follows:

$$u(\xi(t), t)^+ = u(\xi(t), t)^- = u^* \quad (5)$$

$$\kappa \frac{d\xi(t)}{dt} = \lambda_2 \left. \frac{\partial u(x, t)}{\partial x} \right|_{x=\xi(t)}^+ - \lambda_1 \left. \frac{\partial u(x, t)}{\partial x} \right|_{x=\xi(t)}^- \quad (6)$$

where  $u^*$  is the phase change temperature and  $\kappa$  describes the latent heat of solidification per volume unit.

In the considered problem functions  $u$ ,  $\xi$  and  $d$ , describing temperature distribution, the freezing front position and the changes of area size, respectively, are unknown. The other functions ( $u_0$ ,  $q$ ), coefficients and constants ( $c_i$ ,  $\rho_i$ ,  $\lambda_i$ ,  $\alpha$ ,  $\kappa$ ,  $u^*$ ,  $u_\infty$ ,  $\xi_0$ ,  $d_0$ ) are given.

### 3. Method of solution

In this section we describe the procedure for solving the problem formulated above. Supposing that the total weight of the material is equal to  $m_0$  and is constant in time of the modeled process, we are able to write the mass balance equation  $m_0 = m_1 + m_s$ , where  $m_1$  and



$m_s$  represent the mass of the material in the liquid and the solid state, respectively. The one-dimensional problem can be used, among others, to describe the phenomena occurring inside the slab with thickness  $d(t)$ , height  $h$  and width  $l$ , where  $d(t) \ll h$  and  $d(t) \ll l$ . In this case the previous equation can be written as:

$$m_0 = \xi(t)\rho_1hl + (d(t) - \xi(t)\rho_2)hl \quad (10)$$

By transforming the above relation we can determine function  $d$ :

$$d(t) = \frac{m_0 - \xi(t)\rho_1hl}{\rho_2hl} + \xi(t) \quad (11)$$

The initial mass  $m_0$  is equal to  $m_0 = \xi_0\rho_1hl + (d_0 - \xi_0)\rho_2hl$  (equation (10) for  $t = 0$ ), therefore:

$$d(t) = \frac{(\xi_0 - \xi(t))\rho_1}{\rho_2} + (d_0 - \xi_0) + \xi(t) \quad (13)$$

If we additionally assume that in the initial moment the whole bar is in the liquid phase, i.e.  $d_0 = \xi_0$ , the above equation is simplified to the form:

$$d(t) = \frac{\rho_1}{\rho_2}(d_0 - \xi(t)) + \xi(t) \quad (14)$$

To find the approximate solution of presented problem we use the finite element method [2, 12]. For moment  $t_k$  we divide interval  $[0, d(t_k)]$  into  $n$  elements  $0 = x_0^k < x_1^k < \dots < x_{n-1}^k < x_n^k = d(t_k)$ .

To determine the position of the interface we use an algorithm in which, on the basis of the Stefan condition, the size of the time step is iteratively selected so that the boundary moves to the adjacent node [2]. In this method we want the freezing front to move between the successive nodes starting from node  $x_n^0$  in moment  $t_0 = 0$ , i.e. in the  $k$ -th step the boundary should be in node  $x_{n-k}^k$ . It requires a variable size of the time step. Let us suppose that after  $k - 1$  time steps (in moment  $t_{k-1}$  the boundary is in node  $x_{n-k+1}^{k-1}$ . The method assumes that after the  $k$ -th step (in moment  $t_k$ ) of length  $\Delta t$  the boundary will be in node  $x_{n-k}^k$ . From the condition of temperature continuity it follows that in moment  $t_k$  the temperature in node  $x_{n-k}^k$  is equal to the solidification temperature  $u^*$ . In this way we obtain the heat conduction problem in intervals  $[0, x_{n-k}^k]$  and  $[x_{n-k}^k, d(t_k)]$  with the known boundary conditions which should be solved. We know also the temperature distribution in the previous time step. Thereby, by using the finite element method (or some other method) we can determine the temperature distribution in moment  $t_k$  and then the heat flux on the moving interface. Certainly, the determined values depend on the time step size  $\Delta t$  which we determine iteratively by using the Stefan condition. At the beginning of each step of calculations we assume the time step size, for instance, as equal to the final time step size from the previous stage of calculations.

Then we determine the corresponding temperature distribution in moment  $t_k$ , based on which we determine the heat fluxes on the moving interface, i.e. in node  $x_{n-k}^k$  from the side of the liquid and solid phase. By using the Stefan condition we improve the time step size  $\Delta t$  and recalculate the temperature distribution in moment  $t_k$ . The process of improving the time step size is repeated until the desired accuracy  $\varepsilon$  would be reached.

We describe now the procedure of determining time step size  $\Delta t$  in more detail. Let us remember that elements located between the adjacent nodes have the same mass  $m = m_0/n$ . The length of the element for the liquid and solid phase is, respectively, equal to:

$$h_1 = \frac{m}{\rho_1} = \frac{d_0}{n}, \quad h_2 = \frac{m}{\rho_2} = \frac{d_0}{n} \frac{\rho_1}{\rho_2} \quad (17)$$

Thereby, in moment  $t_k$  the coordinates of nodes are the following:

$$x_i^k = \begin{cases} ih_1, & i \leq n-k \\ (n-k)h_1 + (i-n+k)h_2, & i > n-k \end{cases} \quad (19)$$

Let us denote  $u_{i,k} = u(x_i^k, t_k)$  and  $u^k = [u_{0,k}, \dots, u_{n,k}]^T$ .

From the Stefan condition for  $t = 0$  we have:

$$\kappa \frac{\xi(\Delta t) - \xi_0}{\Delta t} = \lambda_2 \frac{\partial u(x, u)}{\partial x} \Big|_{x=d(0)} - \lambda_1 \frac{u_{n,0} - u_{n-1,0}}{h_1} \quad (20)$$

After some transformations and by using the boundary condition we get:

$$\Delta t = \frac{-\kappa h_1}{-\alpha(u^* - u_\infty) - \lambda_1 \frac{u^* - u_{n-1,0}}{h_1}} \quad (21)$$

It will be the initial time step size. After determining the temperature distribution in moment  $t_k$  we make a correction of the time step size, i.e. for  $k < n$  we have:

$$\Delta t = \frac{-\kappa h_1}{\lambda_2 \frac{u_{n-k+1,k} - u^*}{h_2} - \lambda_1 \frac{u^* - u_{n-k-1,k}}{h_1}} \quad (22)$$

and for  $k = n$  we have:

$$\Delta t = \frac{-\kappa h_1}{\lambda_2 \frac{u_{n-k+1,k} - u^*}{h_2} + q(t_n)} \quad (23)$$

In the above equations we applied the boundary conditions (5) and (6) and difference quotients for the left- and right-side derivative of the temperature on the moving interface.

In order to determine the temperature in moment  $t_k$  we use the finite element method by obtaining the matrix equation [2, 12]:

$$C\dot{u} + Ku = f \quad (24)$$

where  $C$  is the heat capacity matrix and  $K$  is the heat conductivity matrix taking into account the component resulting from the convective component in equation (1). Matrices  $C$ ,  $K$  and vector  $f$  are constructed on the grounds of the Galerkin method [2, 12]. Due to the movement of the boundary between the adjacent nodes, these matrices have to be recalculated for every  $k$ . If parameters  $c$ ,  $\rho$ ,  $\lambda$ ,  $q$ ,  $u_\infty$ ,  $\alpha$  are not constant over time, the matrices and vector  $f$  have to be recalculated also for every  $\Delta t$ . We can discretize the above equation by using the implicit scheme:

$$\left( \frac{1}{\Delta t} C + K \right) u^k = \frac{1}{\Delta t} C u^{k-1} + f \quad (26)$$

By solving the above system of linear equations we get the temperature distribution in moment  $t_k$  which allows us to determine the new time step size  $\Delta t$ .

#### 4. Computational example

We start with a theoretical example for which an exact solution is known. In the considered example we assume:  $c_1 = 1$ ,  $c_2 = \frac{9}{5}$ ,  $\rho_1 = 1$ ,  $\rho_2 = \frac{10}{9}$ ,  $\kappa = \frac{11}{10}$ ,  $\lambda_1 = \frac{1}{2}$ ,  $\lambda_2 = \frac{20}{9}$ ,  $u^* = 0$ ,  $u_\infty = -2$ ,  $\xi_0 = d_0 = 1$ ,  $t^* = 1$ ,  $u_0(x) = 1 - e^{2(x-1)}$ ,  $q(t) = e^{2(t-1)}$  and  $\alpha(t) = \frac{21}{10} e^{\frac{1701}{2000}t} \left( 3 - e^{\frac{1701}{2000}t} \right)^{-1}$ .

An exact solution of the above problem is given by functions:

$$d(t) = 1 - \frac{t}{10}, \quad \xi(t) = 1 - t, \quad u(x, t) = \begin{cases} 1 - e^{2(x+t-1)}, & (x, t) \in D_1 \times (0, t^*) \\ 1 - e^{\frac{189}{200}(x+t-1)}, & (x, t) \in D_2 \times (0, t^*) \end{cases}$$

The calculations were performed for the grid dividing area  $\Omega$  into 50, 100, 200 and 500 elements. The time step size was determined iteratively with accuracy 0.001 s. Most often three or four iterations were enough to get this accuracy. Table 1 presents the run time of the algorithm, the maximal and averaged absolute error of the time step size determination and the obtained final time.

Figure 1 displays temperature curves for the grid dividing the area into 200 elements. The dashed lines represent the approximate curves for  $x_p = 0$  (dotted),  $x_p = 0.5$  (dashed) and  $x_p = d(t)$  (dot-dashed), whereas the solid lines represent the exact curves for these points.

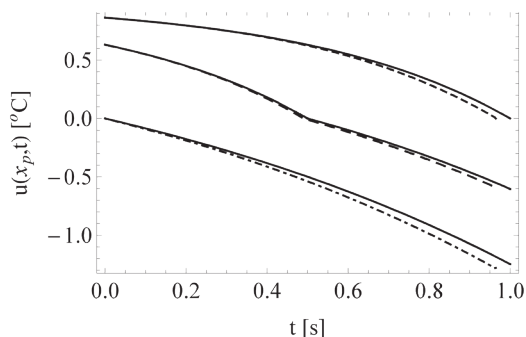


Fig. 1. Temperature curves in points  $x_p = 0$  (dotted),  $x_p = 0.5$  (dashed) and  $x_p = d(t)$  (dot-dashed) for  $n = 200$  (solid lines – exact values, dashed lines – approximate values)

Table 1

**Run time and the errors of approximate solution**  
( $\Delta$  – absolute errors,  $t^*$  – final time)

$n$	Run time [s]	$\Delta_{\max}$	$\Delta_{\text{avg}}$	$T^*$
50	0.345	0.0542	0.0182	0.905
100	1.764	0.0419	0.0140	0.951
200	11.170	0.0357	0.0112	0.957
500	139.406	0.0318	0.0107	0.961

Figure 2 shows the moving interface position  $\xi(t)$  (left figure) and length  $d(t)$  of the area (right figure). The dashed lines represent the approximate values and the solid lines represent the exact values. It can be seen that the error of time step size selection decreases with an increase of the grid density. Thus, by increasing the grid density we may get the more accurate results, although the increase in the accuracy is small with respect to the increase of the algorithm's run time.

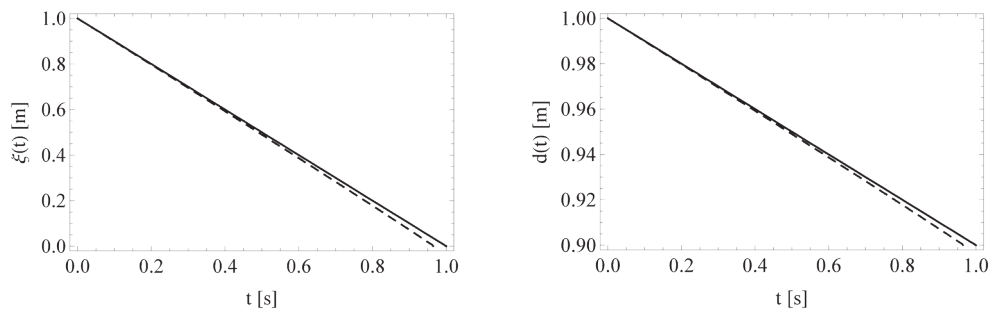


Fig. 2. Position  $\xi(t)$  of the moving interface (left figure) and length  $d(t)$  of the area (right figure) for  $n = 200$  (solid line – exact values, dashed line – approximate values)

## 5. Conclusions

In this paper we have described the algorithm for solving the Stefan problem involving material shrinkage. In this algorithm we used the finite element method supplemented by the procedures allowing to define the moving interface position and the change of the material size associated with material shrinkage. To determine the boundary position we used the algorithm in which, on the basis of the Stefan condition, the time step size was iteratively determined so that the boundary moved to the adjacent node. To determine the change of size we proposed the procedure based on the mass balance.

The presented method allows to obtain more accurate results by increasing the grid density, although the increase in the accuracy is small with respect to the increase of the algorithm run time. We may also increase the accuracy by using in the finite element method the square elements instead of the linear ones or by using some other methods to solve the classical Stefan problem. In the nearest future we plan to examine both of these possibilities.

## References

- [1] Crank J., *Free and Moving Boundary Problems*, Clarendon Press, Oxford 1996.
- [2] Mochnacki B., Suchy J.S., *Methods in Computations of Foundry Processes*, PFTA, Cracow 1995.
- [3] Özişik M.N., *Heat Conduction*, Wiley & Sons, New York 1993.
- [4] Voller V., Falcini F., *Two exact solutions of a Stefan problem with varying diffusivity*, Int. J. Heat Mass Transfer, Vol. 58, 2013, 80-85.
- [5] Zhou Y., Wang Y., Bu W., *Exact solution for a Stefan problem with latent heat a power of position*, Int. J. Heat Mass Transfer, 2014, 69, 451-454.
- [6] Furenes B., Lie B., *Using event location in finite-difference methods for phase-change problems*, Numer. Heat Transfer B, Vol. 50, 2006, 143-155.
- [7] Voller V.R., Swaminathan C.R., *General source-based method for solidification phase change*, Numer. Heat Transfer B, Vol. 19, 1991, 175-189.
- [8] Grzymkowski R., Hetmaniok E., Pleszczyński M., Słota D., *A Certain Analytical Method Used for Solving the Stefan Problem*, Thermal Science, Vol. 17, 2013, 635-642.
- [9] Purlis E., Salvadori V., *A moving boundary problem in a food material undergoing volume change – Simulation of bread baking*, Food Research International, Vol. 43, 2010, 949-958.
- [10] Natale M., Marcusa E., Tarzia, D., *Explicit solutions for one-dimensional two-phase free boundary problems with either shrinkage or expansion*, Nonlinear Anal.: Real World Appl., Vol. 11, 2010, 1946-1952.
- [11] Yang Z., Sen M., Paolucci S., *Solidification of a finite slab with convective cooling and shrinkage*, Appl. Math. Modelling, Vol. 27, 2003, 733-762.
- [12] Grzymkowski R., Kapusta A., Nowak I., Słota D., *Numerical Methods. The Initial-Boundary Value Problems*, WPKJS, Gliwice 2009 (in Polish).

MARCIN MIGUS\*, KAROL OSOWSKI\*\*, ARTUR OLSZAK\*\*\*,  
ANDRZEJ KĘSY\*\*, ZBIGNIEW KĘSY\*\*

## COMPUTER-AIDED MACHINE DESIGN WITH REGARD TO NEW TECHNOLOGIES AND MATERIALS

---

### KOMPUTEROWE WSPOMAGANIE W BUDOWIE MASZYN Z UWZGLĘDNIENIEM NOWYCH TECHNOLOGII I MATERIAŁÓW

#### Abstract

The aim of the paper is to present the issue of using computer-aided methods as well as 3D printing technologies and not typical materials connected with it. Selected problems that can occur while applying computer-aided methods and their solutions have also been described.

*Keywords: computer-aided methods, design, high-speed machining, 3D printing, design problems*

#### Streszczenie

W artykule przedstawiono zagadnienie wykorzystania metod komputerowego wspomaganie konstruowania oraz wytwarzania z użyciem technologii drukowania 3D oraz związanych z tą technologią nietypowych materiałów. Opisano wybrane problemy, jakie występują podczas stosowania metod komputerowego wspomaganie w praktyce inżynierskiej. Przedstawiono sposoby rozwiązania tych problemów.

*Słowa kluczowe: metody komputerowego wspomaganie, konstruowanie, obróbka szybkościowa, drukowanie 3D, problemy konstrukcyjne*

---

\* Ph.D. Eng. Marcin Migus, The State School of Higher Education in Sandomierz.

\*\* M.Sc. Karol Osowski, Prof. Ph.D. Eng. Andrzej Kęsy, Prof. Ph.D. Eng. Zbigniew Kęsy, Institute of Applied Mechanics and Energetics, Faculty of Mechanical Engineering, Kazimierz Pułaski University of Technology and Humanities in Radom.

\*\*\* Ph.D. Eng. Artur Olszak, New Chemical Syntheses Institute in Puławy.

## 1. Introduction

Currently, computer-aided engineering work plays an important role in machine design. The design process as well as the production process may be supported with new methods and technologies.

Computer-aided design can be used in the preliminary stage of the machine design process [1]. The result is the increase in the accuracy and the calculation design time reduction as well as the possibility of construction optimization [2].

Due to the development of computer-aided design, new design technologies appeared. They are: high-speed machining carried out using CNC machine tools and an additive manufacturing method using 3D printers. New technologies for the machine part design caused the application of materials that have not been widely used yet [3].

However, despite a considerable progress in the development of new technologies, including the software for computer-aided design of machine parts in practical applications, there is a number of new problems requiring unusual approach from the constructor.

The article presents selected examples of problems that occur when using computer-aided engineering works concerning calculations, virtual model design and 3D printing technology, including the use of not typical materials. In addition, ways to solve these problems have been suggested.

## 2. Calculation of non-Newtonian fluid flows

In order to meet requirements to design a machine part, as soon as materials with new properties have been produced the constructor looks forward to using them as soon as possible.

The main obstacle in practical applications is the lack of theoretical basis regarding behaviors of these new materials while influenced by different factors. This is due to the fact that basic research is costly and time-consuming. One of the ways to solve this problem is modifying traditional calculation methods, in order to find a way to carry out calculations with sufficient accuracy for the construction process.

In machine design, two kinds of smart fluids are used: magnetorheological fluids, responding to the magnetic field presence and electrorheological fluids, activated when using the electric field [4, 5]. An important feature of these fluids is that their rheological properties can be described by the Newtonian model, but only in the absence of the physical field (magnetic or electric), according to the equation:

$$\tau = \mu \cdot \dot{\gamma} \quad (1)$$

where:

- $\tau$  – shear stress,
- $\mu$  – viscosity,
- $\dot{\gamma}$  – shear rate.

To simulate the behavior of smart fluids in the presence of a suitable physical field, non-Newtonian rheological models have been used (e.g. Herschel-Bukley, Ostwald-de Waele), but the Bingham's model is the most commonly used:

$$\tau = \mu_p \dot{\gamma} + \tau_0 \quad (2)$$

where:

- $\mu_p$  – plastic viscosity,
- $\tau_0$  – yield stress.

During the process of machine design using magnetorheological or electrorheological fluids, it is often necessary to carry out calculations for the right fluid flow, e.g.: calculations of fluid flow rate through the work channels based on the dimensions of these channels and pressure decrease along the channels. In case of channels with the simple structure (rectangular or cylindrical), such calculations can be carried out on the basis of analytical equations [6].

For channels with more complicated shapes, it is necessary to carry out numerical calculations. The Navier-Stokes equation for describing the motion of the Newtonian fluid with constant viscosity  $\mu$  [7] is commonly used for flow calculations. However, this equation cannot be used directly for the magnetorheological or electrorheological fluid flow because these fluids are non-Newtonian.

To enable calculations of non-Newtonian fluid flow, the concept of apparent viscosity  $\mu_a$ , which is treated as viscosity  $\mu$  has been introduced. Small changes in shear rate  $\dot{\gamma}$  have been taken into consideration [8]. A method for determining the apparent viscosity  $\mu_a$  for a selected  $A$  point located on the straight Bingham fluid model is shown in Fig. 1.

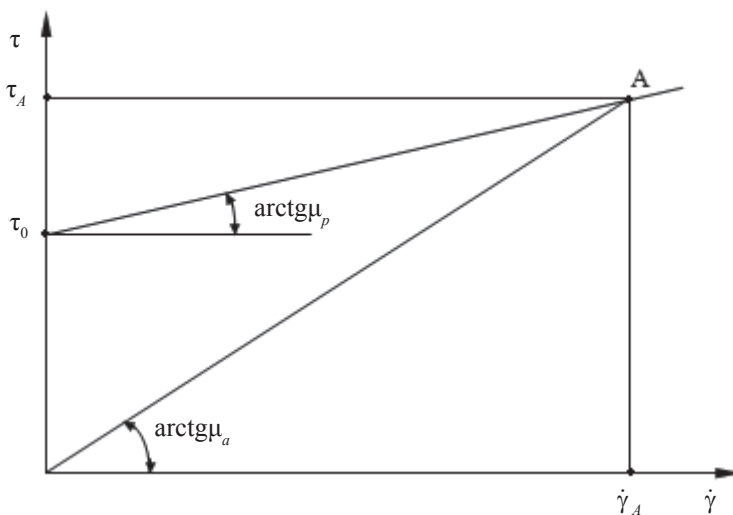


Fig. 1. A method for determining the apparent viscosity  $\mu_a$



Apparent viscosity  $\mu_a$ , described by the equation:

$$\mu_a = \frac{\tau_A}{\dot{\gamma}_A} \quad (3)$$

can also be interpreted as the angle of inclination of arcustangens line joining the origin of the coordinate system to point  $A$ . Fig. 1 shows that for the Bingham mathematical model when  $\dot{\gamma}_A \rightarrow 0$  that  $\mu_a \rightarrow \infty$  and when  $\dot{\gamma}_A \rightarrow \infty$  then  $\mu_a \rightarrow \mu_p$ . In practice, in the case of low shear rate  $\dot{\gamma}$  is a maximum of  $\mu_a = 1000 \cdot \mu$  [9], where  $\mu$  refers to the viscosity of the magnetorheological or electrorheological fluid in the absence of an adequate physical field.

For example, the differences between the flow rates of the magnetorheological fluid in a magnetic field of a rectangular channel, calculated on the basis of the analytical equations and by using the ANSYS FLUENT software (using the Navier-Stokes equation and apparent viscosity) is shown in Fig. 2 [9].

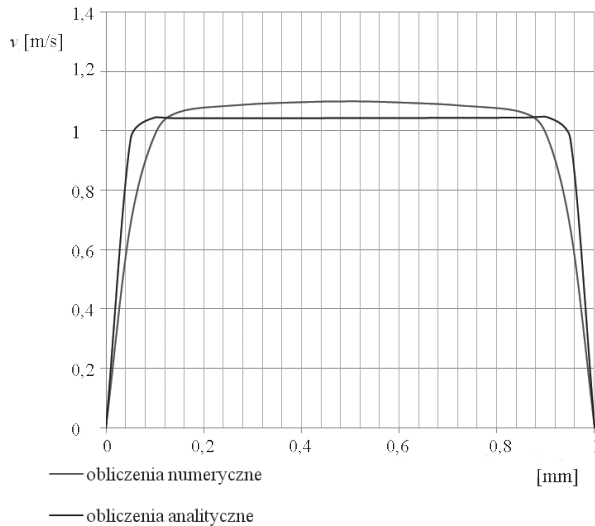


Fig. 2. The results of calculation of velocity flow in the rectangular channel with the height of 1 mm for  $\tau_0 = 10$  kPa, acc. [9]

As it is shown in Fig. 2 these differences, except for the extreme points, do not exceed 10%, which is within the range of permissible errors in engineering calculations. However, for the channel with a more complex shape, the simulation errors are much greater.

The described conduct of simulation allows to omit the problem connected with the lack of accurate computational models and has a practical application in the design of automotive shock absorbers, hydraulic brakes and clutches filled with these fluids.

### 3. The creation of solid models

The basic element of the three-dimensional graphics used in the process of designing and manufacturing machine parts (e.g. High-speed machining, or 3D printing) is the solid model. To create solid models, computer aided design (CAD) programs are used. The most popular ones are programs designed to create technical documentation in 2D and 3D, such as Autodesk Inventor, SolidWorks, ProEngineer. These programs allow the user to introduce changes and improvements, validate the design in terms of assembly and have their own catalogues of standardized structural elements [10, 11]. However, following the practice, in spite of using the right computer program commands, errors preventing its further use, may occur.

During the solid model design, a sketch is created. To create the 2D sketch, 2D graphics or a typical technical documentation is used. Then based on the sketch part, a 3D solid model is generated by using computer program, which is stored in a computer file used by CNC machine tool or a 3D printer.

One of the errors that can occur when creating a solid model of a complex machine part may take place during the surface generating process when the 2D sketch has sharp edges [1, 11], as illustrated in Fig. 3. Another error can occur when there is improper penetration of a solid model's surface with another part's surface [1, 10] (Fig. 4).

A way to eliminate these errors is to simplify the construction by eliminating complex line connections in the sketch [1, 10, 11]. The results should be monitored on a regular basis so other errors can be avoided in the design process.

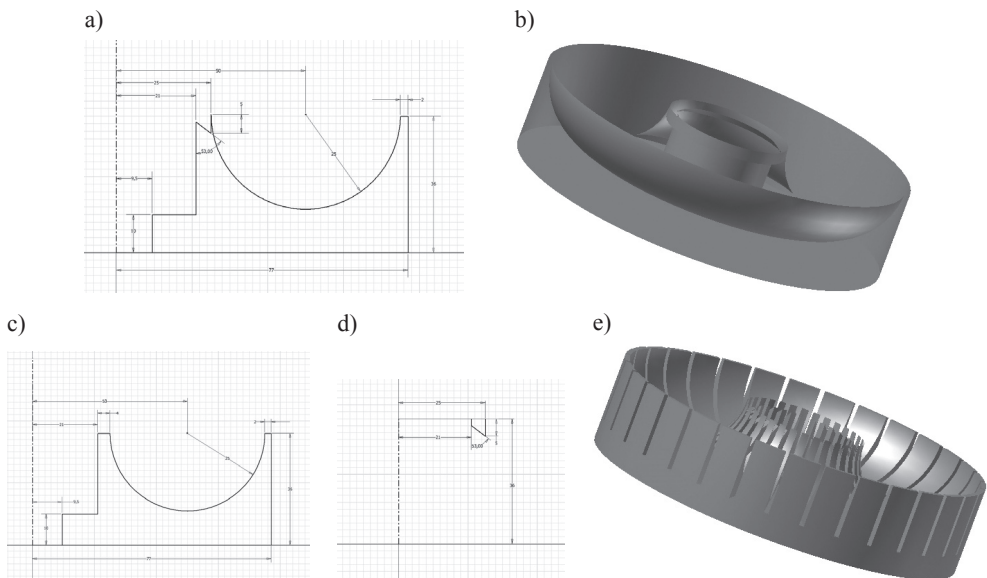


Fig. 3. The incorrect generation of sharp edges after the conversion from a sketch into the solid model: a – an accurate sketch of the structure, b – the wrong model transformations, c – a simplified sketch, d – the element causing the problem as a separate sketch, e – a correctly generated solid model

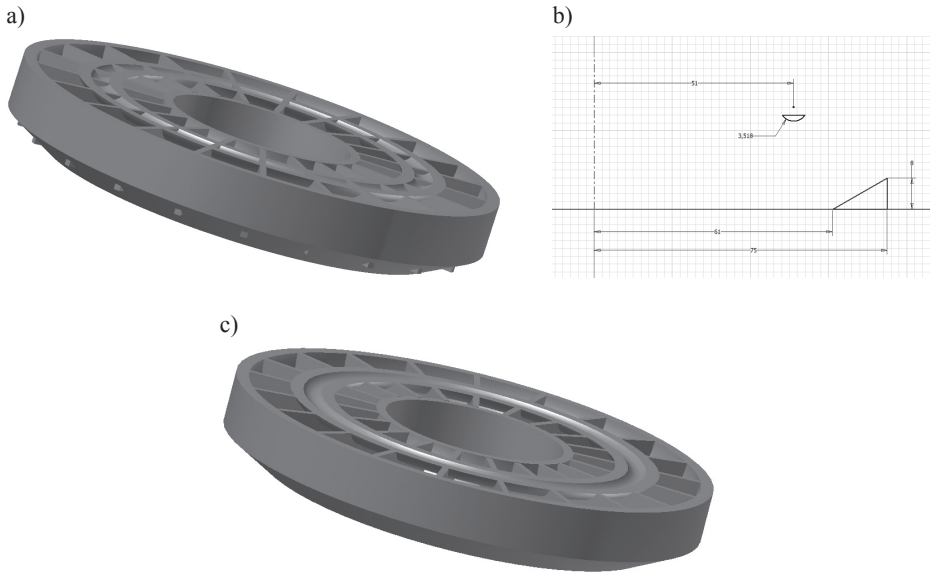


Fig. 4. The incorrect penetration of the surface after replacing the sketch in a solid model by another solid model: a – a solid model with the visible errors penetration surface, b – sketch fragments in which the penetration occurs and which should be removed, c – an improved solid model

#### 4. 3D Printing

3D printing allows for a quick manufacturing of some machinery parts, regardless of the complexity of their shape, so 3D printing is more and more widely used in various branches of the engineering industry, especially in aviation, but also for medical purposes [3]. Parts can be formed from various materials, such as metal powders (iron, aluminum, copper, titanium), plastics (polymers, nylon, polycarbonate resins) and ceramics. Due to the fact that 3D printing is an additive creating method, and its advantage is the optimal use of the material, which reduces the cost of part manufacturing. This technology is particularly useful for the construction of prototypes.

3D printing is an incremental way of forming a three-dimensional object. The shape of each layer is determined on the basis of the solid model of the manufactured parts. First, the solid model is created as a shearer model, stored in the computer memory as a set of coordinates of the vertices of triangles covering the surface of the part and the coordinate vectors perpendicular to these triangles. It has been assumed that the file has the extension “.stl”.

The next step to create a layer model is the use of specialized 3D printer software. Based on this model, a set of points forming lines for layers of the construction is created, which enables the proper control of the 3D printer head.

In the case of manufacturing parts with complex shapes, during changing a solid model into a longwall model, errors can occur as a result of software malfunction. These are generally fragments of a solid model not covered by the so-called “degenerated” triangles

– the triangles whose vertices are collinear or triangles which overlap. Fig. 5a shows the hydrodynamic torque converter impeller made of nylon on a 3D printer, and Fig. 5b shows a magnified part of the rotor including blade connection with the casing, where the most “degenerated” triangles appear while creating a layered model.

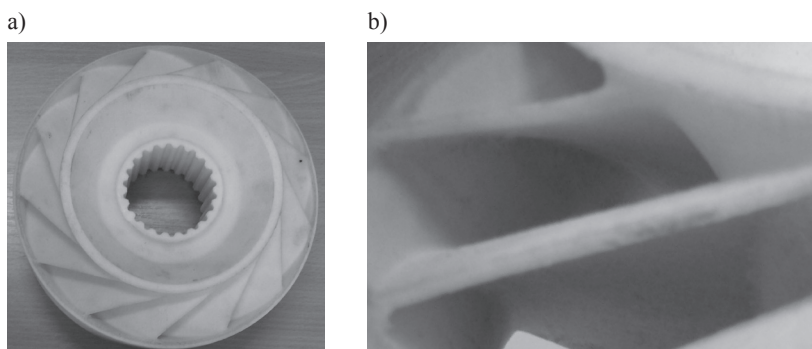


Fig. 5. The rotor of PHM 28 hydrodynamic torque converter made on a 3D printer: a – general view, b – a view of the blades connection with casing

The removal of these errors requires the use of specialized software so the 3D printer manufacturers recommend programs that should be used, or they attach the appropriate software for their products. However, this software guarantees the correct operation of 3D printers only in the case of machine parts with simple shapes. In complicated cases, the software choice is not obvious due to a wide range of computer programs.

Problems relating to manufacturing by means of 3D printing are not limited to software malfunction, but are generally associated with the design features of machine parts such as material or dimensions and tolerances of the manufactured parts [12]. The material used in 3D printers is selected in order to meet the requirements of the printing process [13].

Currently, the most widely used metal to manufacture machine parts, using 3D printing technology is titanium and its alloys. However, titanium is a “difficult” material in the machining process as well as in welding, which significantly makes the process of part manufacturing more difficult. Applying new technologies, where unusual materials are used, makes designers predict the possibilities of the emergence of unusual properties in the manufactured part and consider this fact in the process of quality control.

The small size of 3D printer workspaces, especially those in which the working materials are metal powders, limits the size of machine parts. Parts with dimensions exceeding the workspace dimensions can be created by combining smaller fragments. However, such a solution greatly complicates the design and needs further development of joining component part methods.

During the machine part manufacturing process, using 3D printing, the dimensional accuracy of parts may depend on the machine settings as well as the kind and size of geometric elements of this part. As shown in [14], errors occurring during the manufacturing of a part made of nylon, significantly exceeded the maximum amount of errors declared by the manufacturer of 3D printers in the technical documentation of the printer. In addition,

the distribution of these errors was random and unpredictable. In order to avoid the effect of errors on the correctness of the implementation of the manufactured machine part, dimensional inspection is needed thorough the manufacturing process and, if necessary, additional machining should be used.

## 5. Conclusions

On the basis of considerations referring to the selected problems in the application of computer-aided methods for the design and manufacturing of machine parts, the following conclusions can be made:

1. The combination of computer-aided methods of design with the performance of manufacturing technologies and the usage of unusual materials for the manufacturing of machine parts allow for quick manufacturing of a part at a significantly reduced cost and it is an important contribution to the development of mechanical engineering;
2. The use of computer-aided methods, however helpful it may be, is associated with the occurrence of difficulties and problems that do not exist in the traditional ways of designing and manufacturing machine parts. At the same time, these problems occur during the use of computer-aided methods for the design of specific machine part manufacturing;
3. Due to the diversity and unpredictability of the problems arising in the practical application of computer-aided methods for the machine part design and manufacturing, the use of computers does not relieve engineers from continuous monitoring of the design and the manufacturing process.

## References

- [1] Migus M., Olszak A., Kęsy A., Kęsy Z., *Wybrane problemy komputerowego modelowania i wytwarzania podzespołów hydrokinetycznych*, III Konferencja naukowo-techniczna „Obrabiarki sterowane numerycznie i programowanie operacji w technikach wytwarzania”, Radom–Jedlnia Letnisko 2014.
- [2] Miecielica M., *Techniki szybkiego prototypowania – Rapid Prototyping*, Przegląd Mechaniczny, zeszyt 2/2010, 39-45.
- [3] Osowski K., Kęsy A., Kęsy Z., *Expert system for 3D printing technology*, 15th Annual International Conference Rapid Product Development Association of South Africa “Talent Driver Innovation”, Stias, Stellenbosch 6–7 November, 2014, Proceedings.
- [4] Ławniczak A., Milecki A., *Ciecze elektro- i magneto-reologiczne oraz ich zastosowania w technice*, Wydawnictwo Politechniki Poznańskiej, 1999.
- [5] Kęsy Z., *Modelowanie i badanie elektoreologicznych i magneto-reologicznych cieczy roboczych*, Wydawnictwo Politechniki Radomskiej, 2009.
- [6] Wilczyński K., *Reologia w przetwórstwie tworzyw sztucznych*, Wydawnictwo Naukowo-Techniczne, 2001.
- [7] Kosma Z., *Podstawy mechaniki płynów*, Wydawnictwo Politechniki Radomskiej, 2005.

- [8] Jang Y.J., Suh M.S., Yeo M.S., Choi S.B., *The Numerical Analysis on Channel Flows of ER Fluids*, 5<sup>th</sup> International Conference on Electro-rheological Fluids, Magneto-rheological Suspensions and Associated Technology, Sheffield, UK, 1995, 764-771.
- [9] Gołdasz J., *Magnethoreological Shock absorbers. Automotive context*, Kraków 2012.
- [10] Kęsy A., Migus M., *Komputerowe wspomaganie konstruowania kół lopatkowych podzespołów hydrokinetycznych*, *Mechanik*, 12/2011, na płycie CD, 987.
- [11] Migus M., Kęsy A., *Modelowanie bryłowe kół lopatkowych podzespołów hydrokinetycznych*, *Materiały Międzynarodowej Konferencji Naukowo-Technicznej „Napędy i Sterowania Hydrauliczne i Pneumatyczne”*, Wrocław 2012, 143-152.
- [12] Kęsy A., Kotliński J., *Mechanical Properties of Parts Produced by Using Polymer Jetting Technology*, *Archives of Civil and Mechanical Engineering*, Vol. X, No. 3, 2010, 37-50.
- [13] Kęsy A., Sarnik P., *Przekładnia hydrokinetyczna z kołami lopatkowymi wykonanymi metodą szybkiego prototypowania*, *Napędy i Sterowanie*, nr 2, 2010, 12-15.
- [14] Kotliński J., Kęsy Z., Kęsy A., Jackson M., Parkin R., *Dimensional deviations of machine parts produced in Laser Sintering technology*, *International Journal of Rapid Manufacturing*, Vol. 1, No. 1, 2009, 88-98.



PRZEMYSŁAW MŁYNARCZYK\*, GRZEGORZ DZIATKIEWICZ\*\*

## NUMERICAL MODELLING OF THE OPTICAL DEMULTIPLEXER PHOTONIC STRUCTURES

---

### MODELOWANIE NUMERYCZNE STRUKTUR FOTONICZNYCH OPTYCZNEGO DEMULTIPLESERA

#### Abstract

Photonic structures and their application are one of the most intensively studied areas of modern optics. They are used in devices such as blue lasers, optical fibres or optical add-drop multiplexers. The paper describes the possibility of designing the photonic structure of the optical demultiplexer using the application written by the authors.

*Keywords: photonic crystals, optical demultiplexer, numerical modelling*

#### Streszczenie

Kryształy fotoniczne oraz ich zastosowania są jednymi z najintensywniej badanych obszarów współczesnej optyki. Znajdują zastosowanie w takich urządzeniach jak niebieskie lasery, światłowody fotoniczne czy optyczne multipleksery sumująco-selekcjonujące. Artykuł opisuje możliwość projektowania struktury fotonicznej optycznego demultiplesera przy zastosowaniu napisanej przez autorów aplikacji.

*Słowa kluczowe: kryształy fotoniczne, optyczny demultiplexer, modelowanie numeryczne*

---

\* M.Sc. Eng. Przemysław Młynarczyk, Institute of Thermal and Process Engineering, Faculty of Mechanical Engineering, Cracow University of Technology.

\*\* PhD. Eng. Grzegorz Dziatkiewicz, Institute of Computational Mechanics and Engineering, Faculty of Mechanical Engineering, Silesian University of Technology.



## 1. Introduction

The concept of photonic crystals was formed at the same time in 1987 in two research centres in the USA. One of the first scientists who dealt with photonic structures was Eli Yablonovitch from Bell Communications Research in New Jersey who was working on the materials for photonic transistors. The second one was Sajeev John from Princeton University who was working on increasing the efficiency of lasers used in telecommunication. Both scientists discovered and formulated the concept of photonic band gap which became the basis of these structures' applicability. In 1991 Yablonovitch created the first photonic crystal and in 1997 a method of mass production of these structures was developed [1]. A natural prototype of the photonic crystal is an opal, a mineral derived from the cluster of silicates, found in many places around the world including Poland, mainly in the lower Silesia where the former was located in nickel ore mines, and which is a component of green opals (chrysopras). Nowadays an intensive study of photonic structures are conducted which reveals more and more new applications. The paper shows the application of numerical calculations for designing an optical photonic demultiplexer. The Helmholtz equation of electromagnetic propagation in the one-dimensional heterogeneous photonic structure is solved numerically to obtain the transmittance characteristics. The resultant complex linear system of equations gives complex amplitudes of the incident and reflected waves on each interlayer. The written computer code allows to perform the basic design of the various 1D photonic structures.

## 2. Photonic structures

The photonic crystal is a periodic structure composed of different dielectric materials. By changing the differences between the refractive indices of materials the effect of "trapping" different wavelengths of light can be achieved, this phenomenon is called the photonic band gap. In general, the properties of the photonic crystal depend on the size, number of layers, the geometry and individual properties of the materials forming the crystal. There are three structures of photonic crystals: one-, two-, and three-dimensional. In the modelling of the electromagnetic field in the photonic crystal many methods known in the optics or electrodynamics are used. For example: the plane wave method and the finite difference time domain method, which are used for solving the time-dependent Maxwell equations of both electric and magnetic fields, the moments method and its numerous varieties as well as semi-analytical and analytical methods. So far, the analytical solutions of Maxwell's equations were found only for the simplest one-dimensional photonic crystal [3, 4].

### 2.1. One-dimensional photonic crystals

The simplest example of a one-dimensional photonic structure is the form of periodic multi-layer dielectric stacks called the Bragg mirror as it is shown in Fig 1.

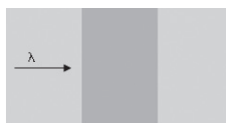


Fig. 1. Simple Bragg mirror

If the electromagnetic wave with a  $\omega$  frequency drops on such a structure, a part of the wave energy is reflected. This property is used in typical signal filters. Bragg mirrors are designed with respect to the reflection spectrum for a selected wavelength range. So designing one-dimensional photonic crystals is a process of an appropriate selection of a number of layers, their thickness and materials with appropriate refractive indices. One-dimensional photonic crystals are used in such systems like optical demultiplexers, optical filters, the so called: “blue lasers”, ultra-white pigments, photonic semiconductors etc.

## 2.2. Two-dimensional photonic crystals

Light propagating in the two-dimensional photonic crystal can be separated into two independent polarized waves, for which there is no longer a common photonic band gap. Trapping or controlling photons is possible by the use of two-dimensional forbidden gaps in the expected direction of wave propagation and by obtaining a high refractive index in the perpendicular direction. Two-dimensional photonic structures may become the most important component of modern optical technology. Integration of these structures with electronic systems is crucial for constructing a new generation of computers based on electro-optical chips.

Nowadays the most popular use of this type of photonic structures are optical add-drop filters which are a combination of two devices: multiplexer and demultiplexer. The main feature of such a filter is to isolate (drop) a band of an electromagnetic wave (EM) or the addition (add) band of the EM wave to the desired light beam. Two dimensional structures are mainly produced by using two-dimensional lithographic [5].

## 2.3. Three-dimensional photonic crystals

Three-dimensional photonic structures have periodicity in all three directions. The main advantage of such a structure is inhibiting and directing the photons resulting from the phenomenon of spontaneous emission. Three-dimensional structures can be produced using techniques known from electronic industry. There is still a lot of unanswered questions about the three-dimensional photonic crystals, and the main aim will be to complete inhibition of spontaneous emission which is theoretically possible by using infinitely thick crystals [5].

## 3. Electromagnetic wave propagation in 1D structure

The relationship between electric and magnetic fields are described by Maxwell’s equations. These four equations are the basis for electromagnetic wave propagation modelling [6].

Considering only the propagation of the electric field in the vacuum, one dimensional wave equation can be obtained:

$$\frac{\partial^2 E}{\partial x^2} - \frac{1}{c^2} \frac{\partial^2 E}{\partial t^2} = 0 \quad (1)$$

where:

- $E$  – the electric field vector,
- $x$  – spatial coordinate,
- $c$  – the speed of light in the vacuum,
- $t$  – time.

Referring to the Helmholtz solution of this equations it is possible to model the harmonic wave in photonic crystals. Assuming the solution in the form of a harmonic wave propagation through the materials with different coefficients of dielectric permittivity, and thus with other factors of wave refraction, according to [1, 7] the following harmonic solution is obtained:

$$E_{pr} = E_p e^{ik_0 r} + E_r e^{-ik_0 r} \quad (2)$$

where:

- $E_{pr}$  – the amplitude of the propagating wave electric field,
- $E^p$  – the amplitude of the incident wave electric field,
- $E^o$  – the amplitude of the reflected wave electric field,
- $r$  – spatial coordinate,
- $i$  – the imaginary unit,
- $k_0$  – the wave vector dependent to medium refractive index.

For the photonic structure consisting of  $m$ -layers, as shown in Fig. 2, the solution of Helmholtz equation for  $m$ -th layer becomes:

$$E_m(x) = A_m e^{im_k x_m} + B_m e^{-im_k x_m} \quad (3)$$

where:

- $n_m$  – a refractive index for the  $m$ -th layer,
- $x_m$  – an coordinate position in the  $m$ -th layer,
- $A_m$  – the amplitude of the wave incident on the  $m$ -th layer,
- $B_m$  – the amplitude of the wave reflected on the  $m$ -th layer,
- $k$  – a wave vector.

Introducing the continuity conditions for every interlayer:

$$E_m(x_m) = E_{m+1}(x_m) \quad (4)$$

$$\frac{\partial}{\partial x} E_m(x_m) = \frac{\partial}{\partial x} E_{m+1}(x_m) \quad (5)$$

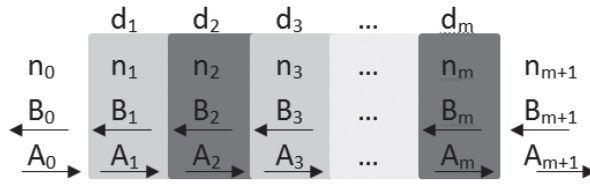


Fig. 2. Photonic structure consisting of  $m$  layers

the system of equations for each surface between the layers is obtained:

$$A_m e^{i n_m k x_m} + B_m e^{-i n_m k x_m} = A_{m+1} e^{i n_{m+1} k x_m} + B_{m+1} e^{-i n_{m+1} k x_m} \quad (6)$$

$$i n_m k A_m e^{i n_m k x_m} - i n_m k B_m e^{-i n_m k x_m} = i n_{m+1} k A_{m+1} e^{i n_{m+1} k x_m} - i n_{m+1} k B_{m+1} e^{-i n_{m+1} k x_m} \quad (7)$$

For the structure with  $N$  layers, the system of  $2N+2$  equations with  $2N+4$  unknowns is built by applying the continuity conditions (4) (5) for each interlayer and for the first and the last surface of the structure. The unknowns are complex amplitudes of the incident and reflected waves on each interlayer. It is a system of complex linear algebraic equations, with respect to  $A_i$  and  $B_i$ .

Such a system of equations can be solved assuming the boundary conditions for  $A_0$ , for example equal to 1, which is the amplitude of wave incident on the crystal, and  $B_{m+1} = 0$  meaning that there is no reflections between the last layer and the surrounding medium. The reflection coefficient, which is the most important parameter of the photonic crystal, is determined by the relation [5]:

$$R = \left( \frac{B_0}{A_0} \right)^2 \quad (8)$$

#### 4. Numerical model of optical demultiplexer

To solve the system of equations the Cramer method was used. This method is most convenient in the present case because it is important to find only one unknown  $B_0$ . The program calculates the reflection coefficient  $R$  in the loop sequence for each wavelength in a given range with a specific, defined difference for the subsequent two wavelength [8].

##### 4.1. Optical demultiplexer

The optical add-drop multiplexer is a device used for separating the appropriate wavelength from the full range of optical wavelength propagating in a single optical fiber. At the same time such a device can add another pre-selected light to obtain expected range of the wavelength. The optical demultiplexer can be a part of the optical add-drop multiplexer

or standalone device with many applications in networks and other optical devices. A key element of this device is a Bragg mirror with a defect. This is a typical 1D photonic crystal with a defect, which means that to the periodically stacked layers one layer with other parameter of refractive index or thickness is introduced. By proper selection of layers and defect parameter can be designed a structure with reflection coefficient equal to 1 for the entire range of the incident wave with the exception of one chosen length.

#### 4.2. Numerical calculation results

The applied numerical method allows to define any photonic structures. Flexibility relates to the number of layers and their refractive indices and thicknesses. For the purpose of this article a simple structure shown in the Fig. 3 is considered. It is a five-layer structure, of a thickness equal to  $1 \mu\text{m}$ , consisting of alternating layers of material with refractive index equal to 3.5 and air ( $n = 1$ ).

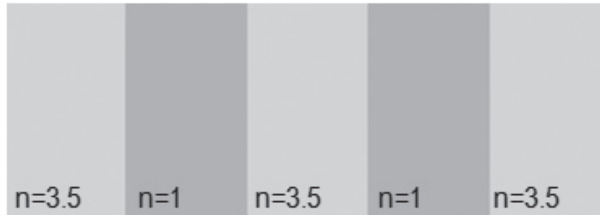


Fig. 3. Five-layer photonic crystal structure which is a part of the optical demultiplexer

For the structure shown in the Fig 3, without embedded defect, a complete wave reflection for the wavelength range from  $1.24$  to  $1.32 \mu\text{m}$  (infrared light) is obtained. Numerical results are shown in the Fig. 4.

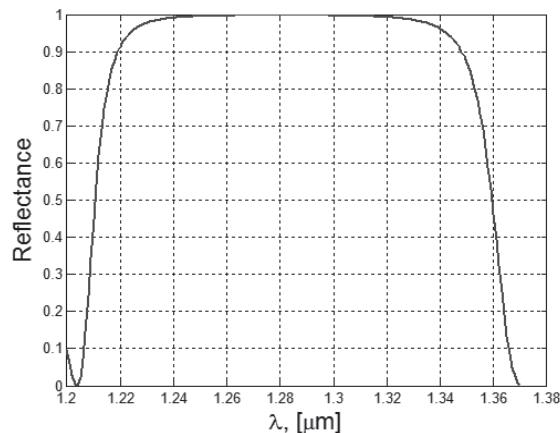


Fig. 4. Reflectance spectrum for the structure without defect

The defect into the central layer is introduced by the change of the thickness. The numerical result for thickness change by  $312 \mu\text{m}$  is shown in the Fig. 5.

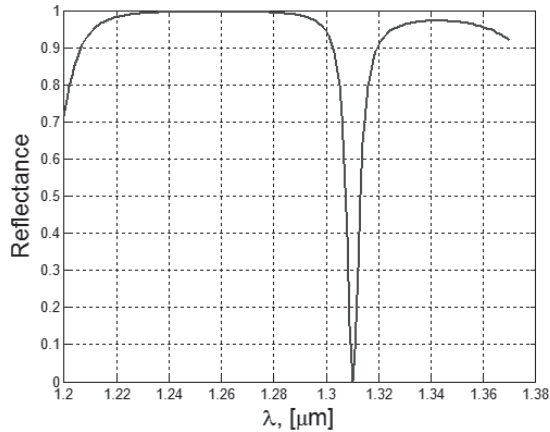


Fig. 5. Reflectance spectrum for the structure with defect

As can be seen in the Fig. 5. for the structure with defect, the complete transmission by the crystal was achieved for the wavelength of  $1.310 \mu\text{m}$ . After several numerical simulations a graph which describes the Bragg defect thickness dependence on the length was plotted. The graph is shown in the Fig. 6.

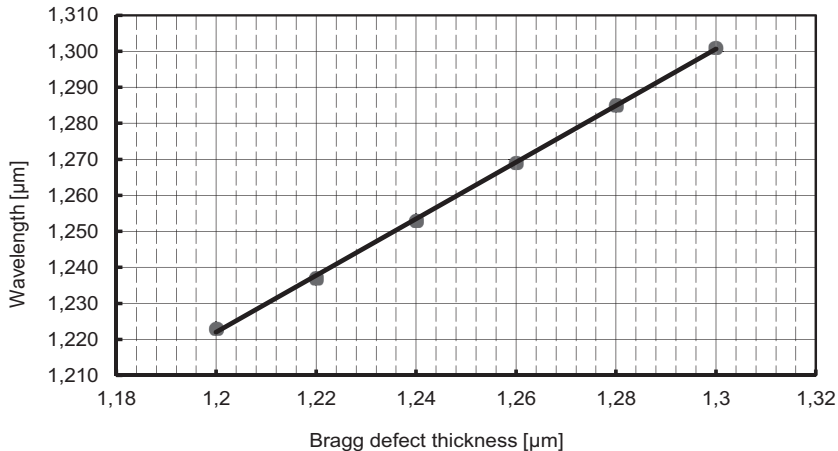


Fig. 6. Wavelength of transmitted wave vs. the Bragg defect thickness

The same calculations can be performed by changing the refractive index of the Bragg defect and the results are shown in the Fig. 7. However, such a design is problematic because each time a material with suitable refractive index should be found.

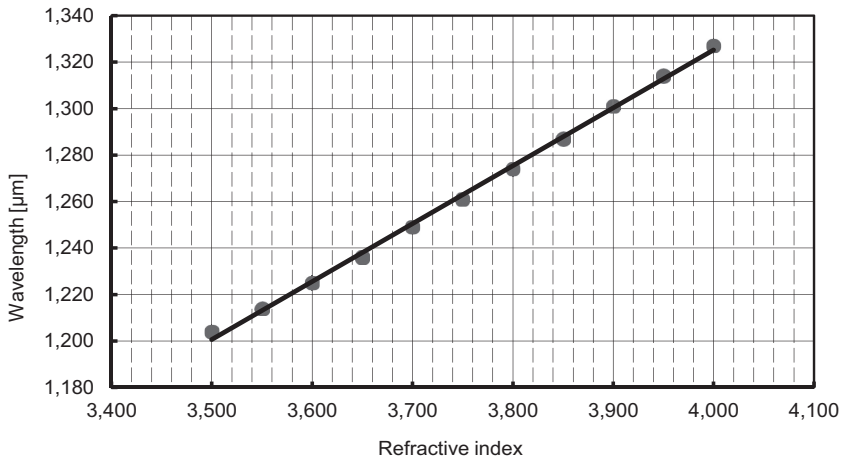


Fig. 7. Wavelength of transmitted wave vs. the refractive index

## 5. Conclusions

Photonic crystals have an increasing role in modern optic technology and every year there is more and more applications of such structures. The article described a possibility of designing the optical demultiplexer photonic structures using the numerical model. The numerical model allows to define all necessary parameters of the photonic crystal structure. The article shows that by such a program one can create tables and graphs serving as a quick and effective tool to design photonic crystal parameters. In the future, the use of photonic crystals will be increasing so the development of this type of applications will be necessary and unavoidable.

## References

- [1] Inonue K., Ohtaka K., *Photonic Crystals. Physics, fabrication and applications*, Springer-Verlag, Berlin 2004.
- [2] Baba T. *Photonic Crystals – an Introduction*, [http://www.jsps.go.jp/j-bilat/fos\\_ja/data/jishi\\_06/abst08.pdf](http://www.jsps.go.jp/j-bilat/fos_ja/data/jishi_06/abst08.pdf), online: 2014-11-26.
- [3] Skorobogatuy M., Yang J., *Fundamentals of photonic crystal guiding*, Cambridge University Press, Cambridge 2008.
- [4] Joannopoulos J.D., Johnson S.G., Winn J.N., Meade R.D. *Photonic Crystals. Modling the flow of light*, Princeton University Press, New Jersey 2008.
- [5] Maldovan M., Thomas E.L., *Periodic materials andinterference lithography for photonics, phononics and mechanics*, WILEY-VCH Verlag GmbH & Co. KGaA, Weinheim 2009.
- [6] Haznadar Z., Stih Z., *Electromagnetic fields, waves and numerical methods.*, Springer-Verlag, Berlin 2004.

- [7] Yasumoto K., *Electromagnetic Theory and Applications for Photonic Crystals*, CRC Press, Boca Raton 2005.
- [8] Młynarczyk P., *Modelowanie numeryczne elementów z kryształów fotonicznych*, Praca dyplomowa inżynierska, Politechnika Śląska, Gliwice 2010.





HASSAN MOMENI\*, MARIUSZ DOMAGAŁA\*\*

## CFD SIMULATION OF TRANSPORT SOLID PARTICLES BY JET PUMPS

---

## SYMULACJA CFD TRANSPORTU CZĄSTEK STAŁYCH W POMPACH STRUMIENICOWYCH

### Abstract

This paper presents CFD simulation of solid particle transport by jet pump. Simulation was conducted using Lagrangian-Eulerian CFD approach. There is presented simulation of transport of mixture of water and solid particles with various density by jet pump with annular motive nozzle. The CFD simulations allowed to obtain trajectory for individual particles as well as their maximal velocity.

*Keywords: jet pump, CFD, particle tracking simulation*

### Streszczenie

W artykule przedstawiono symulację transportu cząstek stałych w pompach strumienicowych przy wykorzystaniu narzędzi CFD. Symulacje przeprowadzono dla pompy z dyszą centralną przy różnych gęstościach ciał stałych. Przeprowadzone symulacje pozwoliły uzyskać trajektorie oraz maksymalne prędkości cząstek stałych podczas pracy pompy.

*Słowa kluczowe: pompa strumienicowa, analiza CFD, transport cząstek stałych*

---

\* Ph.D. Hassan Momeni, Institute of Machine and Maritime Technology, Bergen University College.

\*\* Ph.D. Mariusz Domagała, Institute of Applied Informatics, Faculty of Mechanical Engineering, Cracow University of Technology.

## 1. Introduction

Jet pumps are widely used in many industry branches like chemical, petrochemical, energy and even in food industry. Among many advantageous of jet pumps the most important are: no moving parts, simplicity, reliability and relatively low cost. Such features cause that jet pumps are used for transport of extremely hazardous liquids, slurries or even mixture of liquids and solid particles [1]. There is available a lot of design of jet pumps, but the main group we can distinguish is pump with circumferential or central nozzle. For the transport of solid objects the more convenient is to use jet pump from the first group. Jet pumps can also be distinguish depending on the driving and driven fluid. The jet pump in which both streams are liquids is known as Liquid-Jet-Liquid pump. Such pumps can be used also for transport liquids which contains solid particles. Simulation of jet pump is not an easy task, even in case of LJJ pumps when both streams are homogenous and in the same state conditions. It is even more difficult when we have to simulate transport of liquids which contain solid particles. Such simulations are possible with the use of Computational Fluid Dynamics method and Lagrangian-Eulerian approach [2].

## 2. Mathematical modeling of solid particles in CFD

Flow of fluid through jet pump is governed by well known Navier-Stokes equations, which in CFD methods are solved numerically. In case of mixture with solid particles we have to add additional particle transport model. As the CFD use Eulerian approach for solving fluid flow one of the way to describe particle tracking is the Lagrangian approach. This involves the integration of particle paths through the discretized domain. Individual particle is injected to fluid domain and an additional source term is added to fluid mass, and momentum equations. The equation of motion for individual particle can be written as [3]:

$$m_p \frac{d\mathbf{U}_p}{dt} = \mathbf{F}_D + \mathbf{F}_B + \mathbf{F}_R + \mathbf{F}_{VM} + \mathbf{F}_P \quad (1)$$

where:

- $\mathbf{F}_D$  – drag force at the particle,
- $\mathbf{F}_B$  – buoyancy force,
- $\mathbf{F}_R$  – centripetal and Coriolis force,
- $\mathbf{F}_{VM}$  – virtual mass force, this force is caused by accelerating some of surrounding fluid by the particle,
- $\mathbf{F}_P$  – is the pressure force.

The drag force  $\mathbf{F}_D$  on a particle is proportional to the slip velocity between the particle and fluid velocity:

$$\mathbf{F}_D = \frac{1}{2} C_D \rho_F A_F |\mathbf{U}_F - \mathbf{U}_P| (\mathbf{U}_F - \mathbf{U}_P) \quad (2)$$

The buoyancy force  $\mathbf{F}_B$  is:

$$\mathbf{F}_B = \frac{\pi}{6} d_p^3 (\rho_p - \rho_f) \mathbf{g} \quad (3)$$

The centripetal and Coriolis force force  $\mathbf{F}_R$  is:

$$\mathbf{F}_R = m_p (-\boldsymbol{\Omega} \times \mathbf{U}_p - \boldsymbol{\Omega} \times \boldsymbol{\Omega} \times \mathbf{r}_p) \quad (4)$$

The virtual mass force  $\mathbf{F}_{VM}$  can be expressed as:

$$\mathbf{F}_{VM} = \frac{C_{VM}}{2} m_f \left( \frac{d\mathbf{U}_f}{dt} - \frac{d\mathbf{U}_p}{dt} \right) \quad (5)$$

The pressure force  $\mathbf{F}_p$  is:

$$\mathbf{F}_p = m_p \frac{\rho_f}{\rho_p} (\mathbf{U}_f \nabla \mathbf{U}_f - \mathbf{R}_f) \quad (6)$$

$$\frac{d\mathbf{U}_p}{dt} = \frac{1}{m_p + \frac{C_{VM}}{2} m_f} (\mathbf{F}_D + \mathbf{F}_B + \mathbf{F}_R + \mathbf{F}'_{VM} + \mathbf{F}_p) + \frac{1}{m_p} \mathbf{F}_R \quad (7)$$

For steady state conditions:

$$\mathbf{F}'_{VM} = \frac{C_{VM}}{2} m_f (\mathbf{U}_f \nabla \mathbf{U}_f \mathbf{F}_R - 2\boldsymbol{\Omega} \times \mathbf{U}_f - \boldsymbol{\Omega} \times \boldsymbol{\Omega} \times \mathbf{r}_p) \quad (8)$$

where:

$m_f = \frac{\pi}{6} d_p^3 \rho_f$  – mass of fluid surrounding the particle,  $d_p$  is the particle diameter,

$m_p = \frac{\pi}{6} d_p^3 \rho_p$  – mass of the particle,

$\mathbf{R}_f = -2\boldsymbol{\Omega} \times \mathbf{U}_f - \boldsymbol{\Omega} \times \boldsymbol{\Omega} \times \mathbf{r}_p$ ,

$C_{VM}$  – coefficient,

$\mathbf{U}_f, \mathbf{U}_p$  – fluid and particle velocity, respectively,

$\mathbf{g}$  – gravity vector,

$\boldsymbol{\Omega}$  – computational frame angular velocity.

## 2. Simulation model

Numerical simulation was conducted in ANSYS CFX for model presented on Fig. 1. For simulation purposes only a half model was used, on the symmetry plane an appropriate boundary conditions were applied.

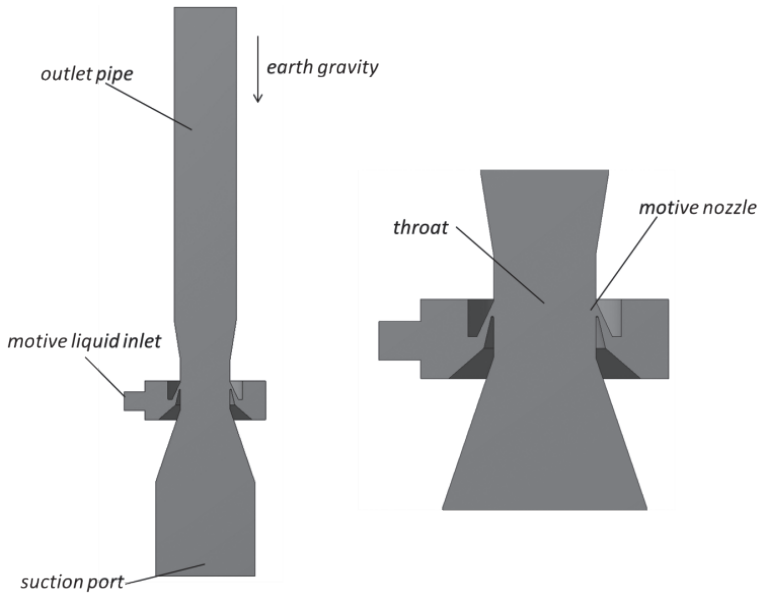


Fig. 1. Model of LJI pump used in CFD simulation

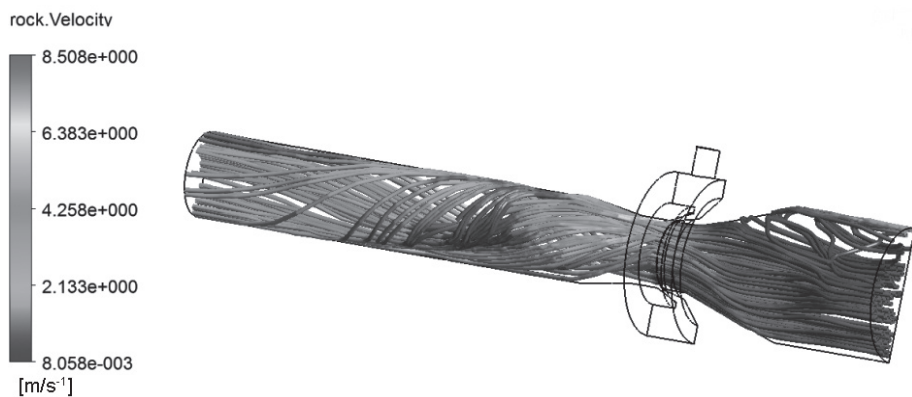
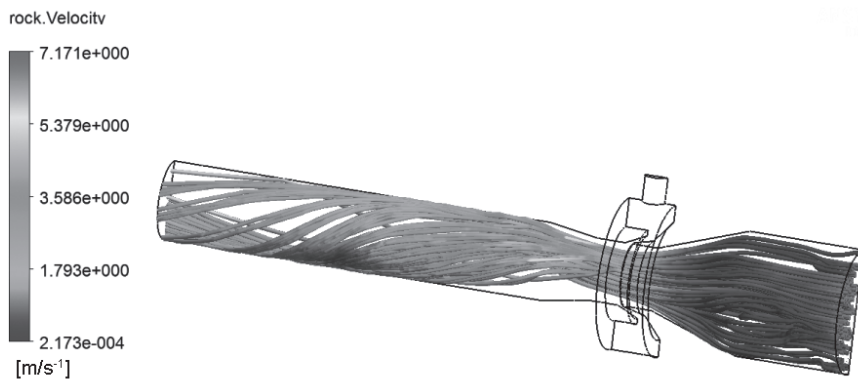
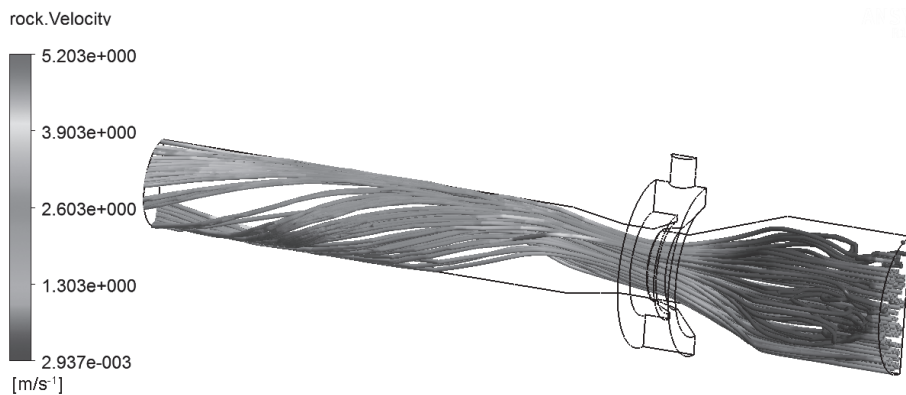
The diameter of suction port is 160 mm, where the solid particles are injected. Solid particles have 5 mm diameters and have possibility of collision of each other and with pump walls. During simulation constant fluid velocity at motive inlet was defined, it was 15 m/s, while density of solid particles were changed from density equal to water (for very light rock particles) to density of 3500 kg/m<sup>3</sup>, what corresponds to heavy rocks. Simulations were conducted for steady state conditions, for turbulent flow at thermal equilibrium state. No erosion or cavitation was included in simulation model.

### 3. CFD results

Results of the CFD simulations are presented on Figs 2–4, which shows particle trajectories for identical flow conditions and diameter of particles but with various density of solid particles. Solid particles varies from ratio  $r = 1$  to  $r = 3.5$ , where  $r = \frac{\rho_p}{\rho_F}$ ,  $\rho_F$  is water density, while  $\rho_p$  is particle density.

Results presented on Fig. 1 shows that the particle velocity is not uniform and some swirls appears after the particles passing the throat what might be caused by non uniform fluid velocity at this region. Furthermore, the maximal velocity of solid particles is almost 1/3 than fluid velocity. Maximal velocity of particles is reached after they went through the throat.

Next figures shows trajectory for particles with higher density. When comparing results presented on Fig. 2, Fig. 3 and Fig. 4 we may noticed that as the particles density rises the

Fig. 2. Solid particles trajectory for density ratio  $r = 1$ Fig. 3. Solid particles trajectory for density ratio  $r = 2$ Fig. 4. Solid particles trajectory for density ratio  $r = 3.5$

amount of particles which is taken away by fluid decrease. It can be also found that the trajectory of particles changes as the density of particle increase. And also maximal particle velocity drops from 8.5 m/s to 5.2 m/s.

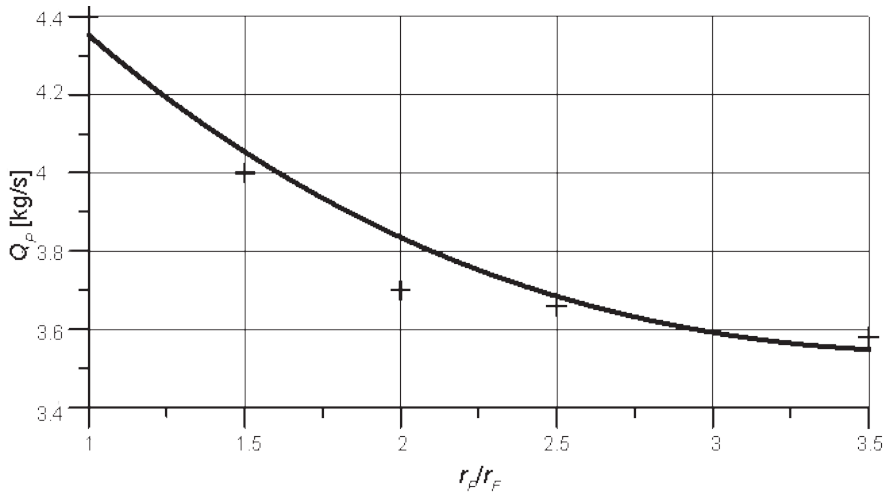


Fig. 5. Mass flow rate of solid particles depending on particle diameter

Figure 5 shows the mass flow rate at the pump outlet for various particles density and reach values of 4.4 kg/s for particle density equal to water ( $r = 1$ ) to value 3.58 kg/s for density ratio  $r = 3.5$ .

#### 4. Conclusions

This article presents CFD simulation of transport solid particles by jet pump using Lagrangian-Eulerian approach. Simulations were conducted for various particle density what allowed to investigate particle motion during fluid flow. CFD analysis allowed to investigate particles trajectory depending on their weight as well as obtain quantitative information like mass flow rate of solid particles on pump outlet. CFD simulation allowed also to obtain information about maximal particles velocity, which was found to be more than three times less that driven fluid velocity. Furthermore, it has been found that the particle velocity is not uniform within the jet pump cross section.

CFD methods with applied Lagrangian-Eulerian approach seems to be very efficient tool in simulation of transport mixtures of liquids and solid particles.

## References

- [1] Karassik I.J., Messina J.P., Cooper P., HealdCh.C., *Pump Handbook*, Third Edition, McGraw Hill, 2001.
- [2] Xue-Guan Song, Joon-Hong Park, Seung-Gyu Kim, Young-Chul Park, *Performance comparison and erosion prediction of jet pumps by using a numerical method*, Mathematical and Computer Modelling, Volume 57, Issues 1–2, January 2013, 245-253.
- [3] Ansys CFX Theory Guide.
- [5] Domagala M., *Simulation of cavitation in jet pumps*, Technical Transactions. Mechanics, Kraków 2013, 51-58.
- [6] Momeni H., *CFD modelling of two stages liquid jet liquid pump*, Rozprawa doktorska, Politechnika Krakowska, Kraków 2011.





YUKA NOBUTA, FUMITO MASUI, MICHAL PTASZYNSKI\*

## MODELING LEARNING MOTIVATION OF STUDENTS BASED ON ANALYSIS OF CLASS EVALUATION QUESTIONNAIRE

### MODELOWANIE MOTYWACJI DO NAUKI U STUDENTÓW NA PODSTAWIE ANALIZY KWESTIONARIUSZA OCENY ZAJĘĆ

#### Abstract

In this paper, we present our research on modeling learning motivation of students by analyzing class evaluation questionnaires, carried out with students as respondents at the end of each term to improve the courses in future semesters. We firstly defined three elements influencing learning motivation: (1) interest, (2) usefulness in the future and (3) satisfaction. Original questionnaire enquiring about those three elements was designed and conducted in multiple classes across different school years. Next, we conducted an experiment to classify students' motivation for learning using the provided answers. The results of the experiment showed that students' learning motivation can be estimated using the three elements defined in this study.

*Keywords: Information engineering, Learner model, Class analysis, Educational technology*

#### Streszczenie

W niniejszym artykule przedstawiono badania dotyczące modelowania motywacji do nauki u studentów poprzez analizę kwestionariuszy oceny zajęć przeprowadzanych w celu poprawy jakości zajęć w następnych semestrach. Najpierw zdefiniowano trzy elementy wpływające na motywację do nauki: (1) zainteresowanie przedmiotem, (2) jego przydatność w przyszłości i (3) zadowolenie z udziału w zajęciach. Oryginalny kwestionariusz zaprojektowany w celu indukcji powyższych elementów został przeprowadzony na słuchaczach różnych kursów na przestrzeni kilku lat. Zabrane odpowiedzi posłużyły do automatycznej klasyfikacji motywacji u studentów. Wyniki pokazały, że motywacja do nauki może być oszacowana za pomocą trzech elementów określonych w niniejszym artykule.

*Słowa kluczowe: kluczowe: inżynieria informacji, model studenta, analiza zajęć, technologie edukacyjne*

\* Ph.D. Yuka Nobuta, Ph.D. Fumito Masui, Ph.D. Michal Ptaszynski, Department of Computer Science Kitami Institute of Technology, Japan.

## 1. Introduction

On the authors' university, similarly to many other universities and educational institutions, one of the elements of class evaluation is conducting a questionnaire at the end of each term with students as respondents. The main goal of such questionnaires is to utilize its results to improve classes in the future. Unfortunately, often in such questionnaires the learner's perspective and learning motivation has not been sufficiently considered.

For example, by dividing students into "learners with low motivation", and "learners with high motivation", the views over the evaluated classes differ greatly. Therefore, the expectations and the satisfaction (or dissatisfaction) of the classes differ depending on the students. Although these differences between students should be considered in the questionnaires, in most cases they are not identified at all, which makes "a student" to be considered as a constant value. If in such typical questionnaires the evaluations and opinions by students of different learning motivations are mixed, it could make the results of the questionnaire less reliable and not optimally useful for further course improvement.

To solve this problem, we developed a learner's model which focuses on differences in learning motivation. In this paper, we firstly define what motivation for learning is, and indicate that it can be perceived as the will to learn the contents to be learned in the classroom. Next, we present the learner's motivation model using a combination of three specific elements that in our assumption make up the learning motivation.

The outline of the paper is as follows. Firstly, we describe other research on class evaluation questionnaires in Section 2. Next, we describe Quantitative Learner's Motivation Model (QLMM) in Section 3. Furthermore, in Section 4 we describe the questionnaire design based on QLMM and describe the learning motivation prediction procedure Using QLMM. We present the evaluation experiments of the proposed model in Section 5. The results are discussed and explained in detail in Section 6. Finally, in Section 7 we conclude the paper and propose some of the ideas for future improvement of the method.

## 2. Related Research

There has been a number of research on class evaluation questionnaires. For example, Abe et al. [1] examined relations between questionnaire results and respondents' grades, and analyzed which questionnaire items are most important to obtain sufficient results. They used the multiple regression analysis and factor criteria for selection to evaluate the questionnaires' result and the respondent's grades. As for the results of the analysis, they found out that three items of the questionnaire had the most significant impact on performance, namely, "Interest in the course", "Understanding of the syllabus" and "Enthusiasm of teachers."

In other research Inayoshi and Shibata [2] performed principal component analysis using questionnaire results and attempted to extract a learner's characteristics. They discussed the problems occurring with class evaluation when the characteristics of learners is not considered in the evaluation.

In other research Itabashi [3] has analyzed a learner's learning time outside the class. He revealed that students spent more time on language classes and studying specialized subject

classes than they did other classes. On the other hand, Itabashi pointed out the limitations of analyzing the aggregated results of the questionnaire.

Keller [4, 5] proposed the ARCS model designed to stimulate the motivation of learners. The model describes the motivation of learners by applying four perspectives: “attention”, “relevance”, “confidence”, and “satisfaction.” However, since the ARCS model is a qualitative learner model, it is difficult to quantify the degree and the change in motivation.

In this study, we propose a new model to quantify learning motivation. In the proposed model, motivation is assumed to consist of three elements, which we quantify to represent the motivation of learners. Each element is quantified by carrying out the questionnaire and analyzing the overall result. Moreover, we conduct the questionnaire at the beginning and at the end of the course based on the idea that learning motivation changes with the progress of the class material and we considered the transition by comparing the quantified motivation at each time point.

### 3. Quantitative Learner’s Motivation Model (QLMM)

We developed a Quantitative Lerner’s Motivation Model (QLMM). It is composed of three basic elements representing the attitude of students towards the attended courses. Furthermore, quantification of these elements represents the general level of learning motivation in students.

In QLMM, learning motivation is regarded as “the will to learn the contents provided in the class”. To calculate it we consider the following three elements: (1) interest, (2) usefulness in the future, and (3) satisfaction. We represent learning motivation with a combination of these three elements. Each element corresponds to the points of view included in the ARCS model. Figure 1 shows the relationship between the QLMM and ARCS models.

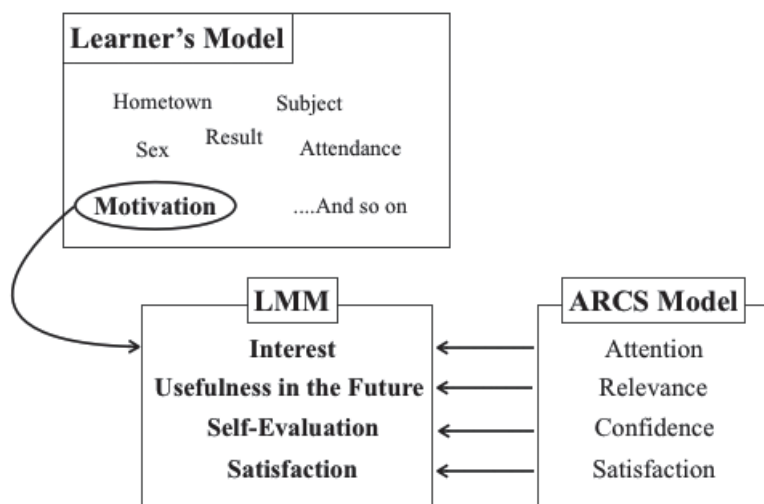


Fig. 1. Relationship of QLMM and ARCS Model

Below we describe in detail each of the three basic elements.

1. **Interest** contains elements reflecting the generally perceived interest and attention paid by the learners to the contents of the course and corresponds to the “attention” in ARCS model;
2. **Usefulness in the future** represents the elements reflecting the potential to contribute to the improvement of the skills and knowledge possessed by the learners themselves and corresponds to the “relevance” in the ARCS model;
3. **Satisfaction** contains the elements reflecting the expectations toward the class at the beginning of the course or the satisfaction of the course at the end of the school year and corresponds to the “satisfaction” in the ARCS model.

#### 4. Questionnaire Design Based on QLMM

We designed an original questionnaire for the purpose of estimation of learning motivation in students. The designed questionnaire consists of ten questions, including both choice-, and free answer-questions. All questions inquire about four elements: (1) interest, (2) usefulness in the future, (3) satisfaction, and (4) self-evaluation on the basis of the ARCS model, as described in the previous section. Figure 2 shows several questions from the questionnaire carried out at the end of the school year. Furthermore, the answers in the questionnaire designed as choice fields (with a 5-point scale), were designed to help us deal with quantification of each of the elements forming in our assumption the concept of learning motivation.

- (1) Did you have an interest in this course?
- (2) Do you think participating in this course will help in the future (further college life or job hunting)?
- (3) Were you satisfied with this course?
- (4) Did you attend this course with a desire to learn?

Fig. 2. Questionnaire examples from the questionnaire

Next, to verify the accuracy of the estimation results we applied the term of “Self-confidence” (or shortly “Confidence”) from the ARCS model. Confidence gives the learner the opportunity to self-evaluate himself or herself and is calculated on the basis of the reply to the question (4) which inquires about the learner’s self-evaluation and motivation for learning.

In addition, we conducted similar questionnaires at the beginning and at the end of the course based on the assumption that learning motivation changes with the progress of class material and consider the transition by comparing the quantified motivation at each time point.

Next, we performed an experiment to predict the motivation of learners by using the answers to the four questions shown in Figure 2. The prediction was made for the answers collected from the questionnaire performed at the end of the school year. The

experiment was performed according the following procedure. Assume that questionnaire  $Q = \{q_1, q_2, q_3, \dots, q_m\}$  consists of  $m$  questions. The  $Q$  is then applied to a learner group  $X = \{x_1, x_2, \dots, x_j, \dots, x_n\}$  containing  $n$  number of persons.

**Step 1.** Firstly, the values of evaluation  $r_{i,j}$  from the answers of learners  $x_j$  for the questionnaire  $q_i$  are collected and for each question mean average  $\mu_i$  and standard deviation  $\sigma_i$  of the respondents are calculated. In this case,  $\mu_i$  is calculated according to equation (1), and  $\sigma_i$  is calculated according to equation (2).

$$\mu_i = \frac{1}{n} \sum_{j=1}^n r_{i,j} \quad (1)$$

$$\sigma_i^2 = \frac{1}{n-1} \sum_{i=1}^n r_{i,j} - \mu_i \quad (2)$$

**Step 2.** Next, classify  $r_{i,j}$  for each of the three evaluated items using as threshold  $\sigma_i$ , as in equation (3) and produce scores for all elements  $s_{i,j}$ . Next, calculate the scores  $s_{i,j}$  of each learner  $x_i$  for each question  $i$  times. Finally, sum the  $s_{i,j}$  for each learner and predict the learner's motivation  $M_j$  according to equation (4).

$$s_{i,j} = \begin{cases} 1 & \text{if } r_{i,j} \geq \mu_i \pm \sigma_i \\ -1 & \text{if } r_{i,j} \leq \mu_i \pm \sigma_i \\ 0 & \text{otherwise} \end{cases} \quad (3)$$

$$M_j = \sum_{i=1}^m s_{i,j} \quad (4)$$

**Step 3.**  $M_j$  obtained in Step 2 has the following properties:  $\{M_j | M_j \leq |m|, M_j \in \mathbb{Z}\}$ . Therefore, we classify the learning motivation  $M_j$  into three classes according to equation (5).

$$\text{Learner's motivation is } \begin{cases} \text{high} & \text{if } M_j \geq 1 \\ \text{low} & \text{if } M_j \leq -1 \\ \text{neither high nor low} & \text{otherwise} \end{cases} \quad (5)$$

### Calculation Example

If we predict learner's motivation when the number of questions is three ( $m = 3$ ) for five learners ( $i = 5$ ),  $Q$  is represented as  $Q = \{q_1, q_2, q_3\}$  and  $X$  is represented as  $X = \{x_1, x_2, x_3, x_4, x_5\}$ . Next, if we obtain the values for evaluated items for each learner  $\{r_{1,j}, r_{2,j}, r_{3,j}\} = \{(5, 1, 4, 3, 4), (5, 1, 4, 2, 3), (4, 2, 3, 1, 2)\}$ , the mean average  $\{\mu_1, \mu_2, \mu_3\} = \{3.4, 3.0, 2.4\}$ , and  $\{\sigma_1, \sigma_2, \sigma_3\} = \{1.52, 1.58, 1.14\}$ . In this case, learner  $x_1$  obtains  $\{s_{1,1}, s_{1,2}, s_{1,3}\} = \{1, 1, 1\}$  according to equation (3) and  $M_1 = 3$ . This prediction indicates that the learning motivation in this learner is "high".

## 5. Evaluation of Proposed Model

To evaluate the proposed model we carried out a questionnaire according to the design described in Section 4, using as input attendees of multiple courses available on the authors' university. In particular, we conducted the questionnaire for nine courses, which included both the compulsory and elective courses offered to undergraduates of 1st to 3rd year. We broadened the span of undergraduates' school years (not limiting the study to only one year), and analyzed them separately on purpose – to investigate whether or not there is a difference of learning motivation in learners depending on the stage of their university career (school year) and the level of importance of the course (whether the course is elective or compulsory). In addition, we conducted the questionnaire at the beginning and at the end of the course to test the assumption that learning motivation changes with the progress of class material, and investigated the transition of learning motivation by comparing its quantified results at each time point. As a result, we obtained a total of 5,040 answers including those performed at the beginning and at the end of the school year.

Next, we performed automated prediction of learners' motivation according to the procedure described in Section 4. Finally we performed the evaluation in order to verify the validity of the predicted learners' motivation. In the experiment, we verified the validity of the predicted results using the scores of question (4) from the questionnaire (see Fig. 2), which inquires about the learner's self-evaluation regarding the learning motivation.

As evaluation criteria we used standard Precision (P), Recall (R) and balanced F-measure (F) calculated according to the equations (6), (7) and (8).

The Precision is the percentage which matches self-evaluation and the result of prediction with the three elements. The Recall is the percentage which matches self-evaluation and the result of prediction with the three elements. F-measure is a harmonic average of Precision and Recall, and is an index which represents the performance of the evaluated item.

$$P = \frac{n}{A} \quad (6)$$

*n*: Number of predictions based on three elements matching self-evaluation

*A*: Number of all responses predicted using three elements

$$R = \frac{n}{B} \quad (7)$$

*n*: Number of predictions based on three elements matching self-evaluation

*B*: Number of all responses inferred by self-evaluation of learners

$$F = \frac{2 * P * R}{P + R} \quad (8)$$

Table 1 shows the results of evaluation.

Table 1

### Evaluation results

Learner's Motivation	Precision	Recall	F-measure
Low Motivation	0.45±0.22 S.D	0.88±0.12 S.D	0.57±0.20 S.D
Neither	0.96±0.05 S.D.	0.58±0.20 S.D	0.70±0.16 S.D
High Motivation	0.44±0.16	0.89±0.15 S.D	0.57±0.17 S.D
Average	0.62	0.78	0.61

As a result of the evaluation, Precision of prediction was 0.62. Recall was 0.78. F-measure was 0.61. Therefore, we can say that the obtained results were promising. Next, we performed Fisher's exact test to verify statistical significance of the validity of the prediction results and self-evaluations, by creating a 3\*3 contingency table. As a result, the statistical significance value was  $p = 3.61e-57$ , which by standard criteria means that the results were extremely significant ( $p < 0.001$ ). This indicates that the classification based on the proposed definition of learner's motivation (QLMM) and the self-evaluation are significantly correlated.

## 6. Discussion

As the results of evaluation experiment, F-measure for the prediction of learner's motivation as "neither high nor low" was 0.70, while F-measure for the prediction of learner's motivation as either "high" or "low" was 0.57. Therefore, it was easier to accurately predict "Neither high nor low" comparing to other classes. However, performance of the prediction that "the learner has high motivation" was slightly better than the performance of predicting that "the learner has low motivation". We examined in detail the responses classified as "Neither high nor low". The comparison of quantified results with free answers revealed that in some cases although the number selected by a learner indicated to "neither high nor low" motivation, the free answer contained expressions suggesting that the learner is in fact biased to one of the sides. This confusion in the self-evaluation questions indicates that in some of the learners perception of numerical values is subjective.

To solve this problem we need to perform a similar experiment to subdivide the classes primarily set for prediction. In particular, we consider adding two classes which would refer to the cases where "the learner has slightly high motivation" and "the learner has slightly low motivation", and conduct the experiments for five classes.

Next, when we add the score of each question and predict a learner's motivation, we need to further re-examine the combination of scores for each classified item. The probable combinations of scores for each classification is represented in Figure 3. By the combination of the five categories the possible score is triplicated. For example, in the case of Combination 1 when the score is from the span  $\{-3, -2\}$ , we can predict that "the learner has low motivation". Similarly, when the score is  $\{-1\}$ , we can predict that "the learner has slightly low motivation". Take score equal to  $\{0\}$ , allows predicting that "the learner has



neither high nor low learning motivation”. The score of {1}, would indicate that “the learner has slightly high motivation”. Finally when the score is from the span {2, 3}, we can predict that “the learner has high motivation”.

After obtaining applicable results we will verify experimentally the optimal combination.

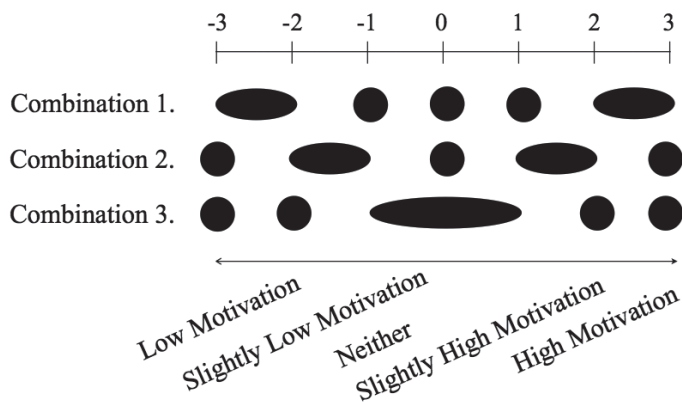


Fig. 3. Possible combinations of scores applicable for different classes

## 7. Conclusions

In this study we proposed an original Quantitative Lerner’s Motivation Model (QLMM) based on the ARCS model (Keller 1987, 1988). Next, we designed an original questionnaire to investigate the learning motivation of students. We conducted the designed questionnaire in multiple classes across different school years, and repeated the study for several years. To classify students’ learning motivation we used the answers obtained from the questionnaire and applied Fisher’s exact test as the evaluation measure. The results of the experiment showed that students’ learning motivation can be estimated using the three elements defined in this study, namely “interest”, “usefulness in the future”, and “satisfaction”.

In the future, we plan to increase the number of classes applied in the classification from the present three to five in order to further improve the classification performance. We will also re-examine the scores depending on different combinations of classes applied in the classification process.

## References

- [1] Takehiko Abe, Takuya Tajima, Kimura Haruhiko, *Ta henryō bunseki ni yoru jugyō ankē to bunseki to jugyō kaizen ni kansuru kōsatsu* (Analysis of Questionnaire using Multivariate Analysis for Improving Lectures) [In Japanese], In *Kōgaku kōgyō kyōiku kenkyō kōen-kai kōenronbunshō* (Collection of Lectures on Education Engineering and Education Industry), Japanese Society for Engineering Education, 2006, 136-140.

- [2] Masami Inayoshi, Ken Shibata, *Jugyō hyōka ankēto no dēta kaiseki* (Data analysis of a questionnaire on the evaluation of lectures) [In Japanese], College of Nagoya Bunri University Bulletin No. 23, 1998, 105-110.
- [3] Takayuki Itabashi, '*Jugyō ankēto*' no katsuyō ni okeru genjō to kadai (The Present Situation and Challenges concerning The Utilization of 'Course Evaluation for Students') [In Japanese], Center for Research and Development of Education Fukushima University Bulletin, 2010, 25-32.
- [4] Keller J.M., Kopp T., *Application of the ARCS model of motivational design*. In C.M. Reigluth (Ed.), *Instructional theories in action: Lessons illustrating selected theories and models*. Lawrence Erlbaum Associates, USA 1987.
- [5] Keller J.M., Suzuki K., *Use of the ARCS motivation model in courseware design (Chapter 16)*. In D. H. Jonnasen (Ed.), *Instructional designs for microcomputer courseware*. Lawrence Erlbaum Associates, USA 1988.



ANDRZEJ OPALIŃSKI, MIROSŁAW GŁOWACKI,  
IZABELA OLEJARCZYK-WOŹEŃSKA, BARBARA MRZYGLÓD\*

## PREDICTION OF TECHNOLOGICAL PROCESS PARAMETERS BASED ON EXPERIMENTAL DATA

### PRZEWIDYWANIE PARAMETRÓW PROCESU TECHNOLOGICZNEGO W OPARCIU O DANE EKSPERYMENTALNE

#### Abstract

In studies of new materials or products, it is necessary to carry out a series of tests to determine the physical properties of the product as a function of the manufacturing process parameters. The technological process of making successive samples for both experimental and research purposes is a mechanism which is time-consuming and which usually requires considerable financial outlays. At the same time, scientific literature offers a large number of experimental results carried out for a similar range of problems. The idea conceived in this study is to create a model that, based on the results of experiments collected from the scientific literature, will reduce the number of necessary physical tests by replacing them with an effective mechanism estimating some of the technological process parameters. Consequently, the concept of an algorithm has been presented to estimate the parameters of the manufacturing process of ADI (Austempered Ductile Iron). It can operate as a fundamental part of a larger expert system, supporting the design and configuration of production processes in various industries. This article describes the results of tests showing the efficiency of the proposed solution and outlines plans for further development of the system to increase its effectiveness and usefulness.

*Keywords: decision support systems, information extraction, process parameter estimation*

#### Streszczenie

Podczas fazy badań nowych materiałów lub produktów zachodzi konieczność przeprowadzenia serii testów w celu określenia właściwości fizycznych wytwarzanych produktów w zależności od zastosowanych parametrów procesu produkcyjnego. Proces technologiczny wytwarzania kolejnych próbek w celach eksperymentalnych i badawczych jest mechanizmem czasochłonnym, wymagającym zwykle sporych nakładów finansowych. Jednocześnie w literaturze naukowej dostępna jest często duża liczba wyników eksperymentów, przeprowadzanych w podobnym zakresie. Ideą prezentowaną w niniejszej pracy jest utworzenie modelu, który w oparciu o wyniki eksperymentów, zebrane z dostępnej literatury naukowej, pozwoli ograniczyć liczbę niezbędnych fizycznych testów, przez zastąpienie ich skutecznym mechanizmem szacowania części parametrów procesu technologicznego. Artykuł przedstawia koncepcję algorytmu umożliwiającego szacowanie parametrów procesu wytwarzania żeliwa ADI (Austempered Ductile Iron) mogącego być bazą większego systemu ekspertowego, wspomagającego proces projektowania i konfiguracji procesów produkcji w różnych dziedzinach przemysłu. W artykule opisano rezultaty testów prezentujące skuteczność proponowanego rozwiązania oraz przedstawiono plany dalszego rozwoju systemu, w kierunku zwiększenia jego skuteczności i przydatności.

*Słowa kluczowe: systemy wspomagania decyzji, ekstrakcja informacji, szacowanie parametrów procesu*

\* Ph.D. Eng. Andrzej Opaliński, Prof. D.Sc. Eng. Mirosław Głowacki, M.Sc. Eng. Izabela Olejarczyk-Woźeńska, Ph.D. Eng. Barbara Mrzyglód, Faculty of Metals Engineering and Industrial Computer Science, AGH University of Science and Technology.

## 1. Introduction

The subject discussed in this study is a practical use of the results of experiments contained in the technical literature as a source of knowledge in expert systems to support the configuration and modelling of the manufacturing process. Regardless of the science or industry sector under consideration, the introduction of a new product invariably requires carrying out a series of tests to prove that the product has the desired properties. This type of testing, often performed with the use of specialised equipment and advanced technologies, is time-consuming and cost-intensive.

A good example of this situation is the production of ADI, which due to its properties – a favourable combination of high abrasive wear resistance with fracture toughness and fatigue strength – is an interesting alternative for materials commonly used to date in the industry, to mention the instance of selected steel grades. Continuous and dynamic development of research in this area has resulted in a significant number of experimental results describing this material. To back up the development in this particular area of studies, further research and experiments are required but, quite obviously, a substantial amount of work and financial input are needed to carry them out.

The idea conceived in this work is to use the available literature data describing the manufacturing process of ADI and, based on this data, develop the tools (methods) which will allow for the determination of the technological process parameters suitable for making products with specific properties. Another issue described in this study is testing the efficiency of such a model, especially as regards the determination of specific parameters covered by the range of its applicability.

The second chapter of the work describes the data sources used in the implementation of the presented concepts, the methods for their filtering and their final selection. The third section presents the estimation algorithm for the examined parameters, while chapter four discusses the results obtained with this algorithm. The last chapter provides a summary of the results obtained and identifies directions for further work on this concept.

## 2. The model of the process and characteristics of source data

The industrial process, which is the subject of the present study, is related with the production of ADI. ADI is the casting material formed by appropriate heat treatment (OC) conducted on ductile iron, which is the starting product for the ADI production. The heat treatment consists of two stages, i.e. austenitising and austempering. The parameters of the heat treatment, including the temperature –  $T_a$  and time –  $t_a$ , of austenitising, and the temperature –  $T_{ii}$  and time –  $t_{ii}$  of austempering, are selected in accordance with the attributes the manufactured product is expected to have, e.g. high ductility and moderate strength and hardness, or vice-versa, low ductility but high hardness and strength. The combination of the desired properties must be optimal for subsequent operating conditions of the cast item.

To obtain data on the ADI manufacturing process, a number of reference literature items describing the subject and incorporating the results of experiments have been reviewed

[1–9]. Based on the data collected, a general model of the manufacturing process was proposed using the following base process parameters:

- chemical composition of cast iron – the percent content of the following elements: C, Si, Mn, Mg, Cu, Ni, Mo, S, P, B, V, Cr, Ti, Sn, Nb, Al;
- the size of the samples;
- the time and temperature parameters of the manufacturing process:
  - $T_a$  – temperature of austenitising [ $^{\circ}\text{C}$ ],
  - $t_a$  – time of austenitising [s],
  - $T_{it}$  – temperature of austempering [ $^{\circ}\text{C}$ ],
  - $t_{it}$  – time of austempering [s].

The outcome of the manufacturing process described by the above mentioned parameters is a material tested after the manufacturing for its mechanical properties. The basic characteristics that are available in most of the literature reference data include:

- tensile strength (Rm),
- elongation (A5),
- hardness (HRC).

Based on the literature review, 192 variants of the ADI manufacturing process were selected and characterised with the aforementioned parameters of the manufacturing process, including the mechanical properties of the products obtained by the described processes of manufacturing. To eliminate the discrepancies that might occur due to large differences in the chemical composition of the base cast iron, the source data was filtered. Subsequently, a group of 70 products with similar chemical composition and temperature ( $T_a$ ) and time ( $t_a$ ) of the austenitising process was selected.

The difference between the manufacturing process parameters occurred only in the data on the temperature ( $T_{it}$ ) and time ( $t_{it}$ ) of austempering. Examples of the experimental data (17 out of 70) are provided in Table 1.

Table 1

Fragment of the experimental results (17 out of 70) on which the tests were based

LP	C	Si	Mn	Mg	Cu	Ni	Mo	S	P	Cr	$T_{aus}[^{\circ}\text{C}]$	$t_{aus}[\text{s}]$	$T_{wyg}[^{\circ}\text{C}]$	$t_{wyg}[\text{s}]$	Rm	A5	HRC
1	3,59	2,52	0,31	0,03	0,03	1,53	0,32	0,01	0,02	0,04	900	7200	230	1800	896	0,8	54
2	3,59	2,52	0,31	0,03	0,03	1,53	0,32	0,01	0,02	0,04	900	7200	230	3600	1120	1	51
3	3,59	2,52	0,31	0,03	0,03	1,53	0,32	0,01	0,02	0,04	900	7200	230	4500	1320	1,8	48
4	3,59	2,52	0,31	0,03	0,03	1,53	0,32	0,01	0,02	0,04	900	7200	230	5400	1560	2,9	47
5	3,59	2,52	0,31	0,03	0,03	1,53	0,32	0,01	0,02	0,04	900	7200	230	7200	1450	1,9	46
6	3,59	2,52	0,31	0,03	0,03	1,53	0,32	0,01	0,02	0,04	900	7200	230	14400	1600	2,4	47
7	3,59	2,52	0,31	0,03	0,03	1,53	0,32	0,01	0,02	0,04	900	7200	230	21600	1590	2,6	46
8	3,59	2,52	0,31	0,03	0,03	1,53	0,32	0,01	0,02	0,04	900	7200	230	28800	1580	2,8	46
9	3,59	2,52	0,31	0,03	0,03	1,53	0,32	0,01	0,02	0,04	900	7200	260	1800	1160	1,4	48
10	3,59	2,52	0,31	0,03	0,03	1,53	0,32	0,01	0,02	0,04	900	7200	260	3600	1490	3,8	44
11	3,59	2,52	0,31	0,03	0,03	1,53	0,32	0,01	0,02	0,04	900	7200	260	4500	1420	2,6	43
12	3,59	2,52	0,31	0,03	0,03	1,53	0,32	0,01	0,02	0,04	900	7200	260	5400	1450	4	43
13	3,59	2,52	0,31	0,03	0,03	1,53	0,32	0,01	0,02	0,04	900	7200	260	7200	1480	3	44
14	3,59	2,52	0,31	0,03	0,03	1,53	0,32	0,01	0,02	0,04	900	7200	260	10800	1500	3,6	44
15	3,59	2,52	0,31	0,03	0,03	1,53	0,32	0,01	0,02	0,04	900	7200	260	14400	1520	4	44
16	3,59	2,52	0,31	0,03	0,03	1,53	0,32	0,01	0,02	0,04	900	7200	260	21600	1500	4,2	43
17	3,59	2,52	0,31	0,03	0,03	1,53	0,32	0,01	0,02	0,04	900	7200	260	28800	1470	4,8	43

A model of the manufacturing process based on the data selected for testing and the elements for final estimation are presented in Figure 1. In the adopted version of the model, the input data was product properties ( $R_m$ ,  $A_5$ , HRC) and the parameters that the model was expected to determine were the temperature ( $T_{it}$ ) and time ( $t_{it}$ ) of austempering. The selected model of parameter estimation allows subsequent determination of the efficiency of the proposed solution, mainly by comparing the obtained results with those set in the literature.

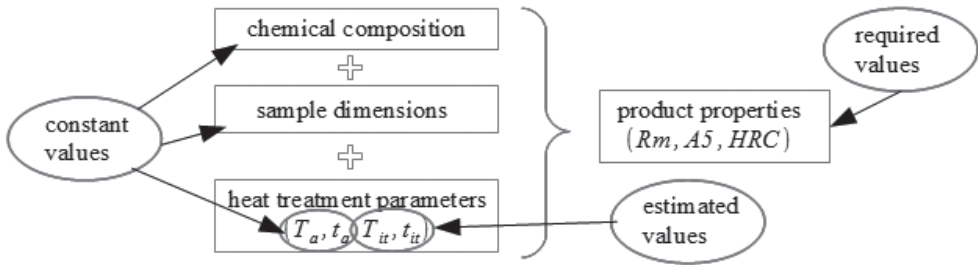


Fig. 1. Model and parameters of the manufacturing process

### 3. The concept of a model for parameter prediction

The concept of a model to predict the technological process parameters is based on an idea of the approximation of process parameters using the data on other technological processes but with input parameters similar to the process to be estimated. This model is a relatively simple solution, but it has to show the validity of the presented approach and pre-determine which process parameters can be measured in that way.

Detailed prediction algorithm for the model used in this study is shown in Figure 2. The idea of the algorithm operation is to select an  $N$  number of samples (experimental results) with properties most similar to the expected input parameters. Since 3 types of properties ( $R_m$ ,  $A_5$ , HRC) were considered, a total of 30 samples were selected. The estimation of the parameters  $T_{it}$  and  $t_{it}$  consisted in the calculation of these values based on the values of the same parameters used for similar products, taking into account the degree of similarity with respect to input parameters.

### 4. The results of a model operation for parameter prediction

To verify the model's efficiency, a series of tests based on 70 samples were carried out. Partial results of those tests are shown in Table 1. To eliminate the effect of the parameter type and value, before the estimation process, standardisation of all the data was done. The results determined by the algorithm were also returned in a standardised form, easy for back conversion.

The results of algorithm operation for the estimation of the standardised values of parameters  $T_{it}$  and  $t_{it}$  are presented in Table 2.

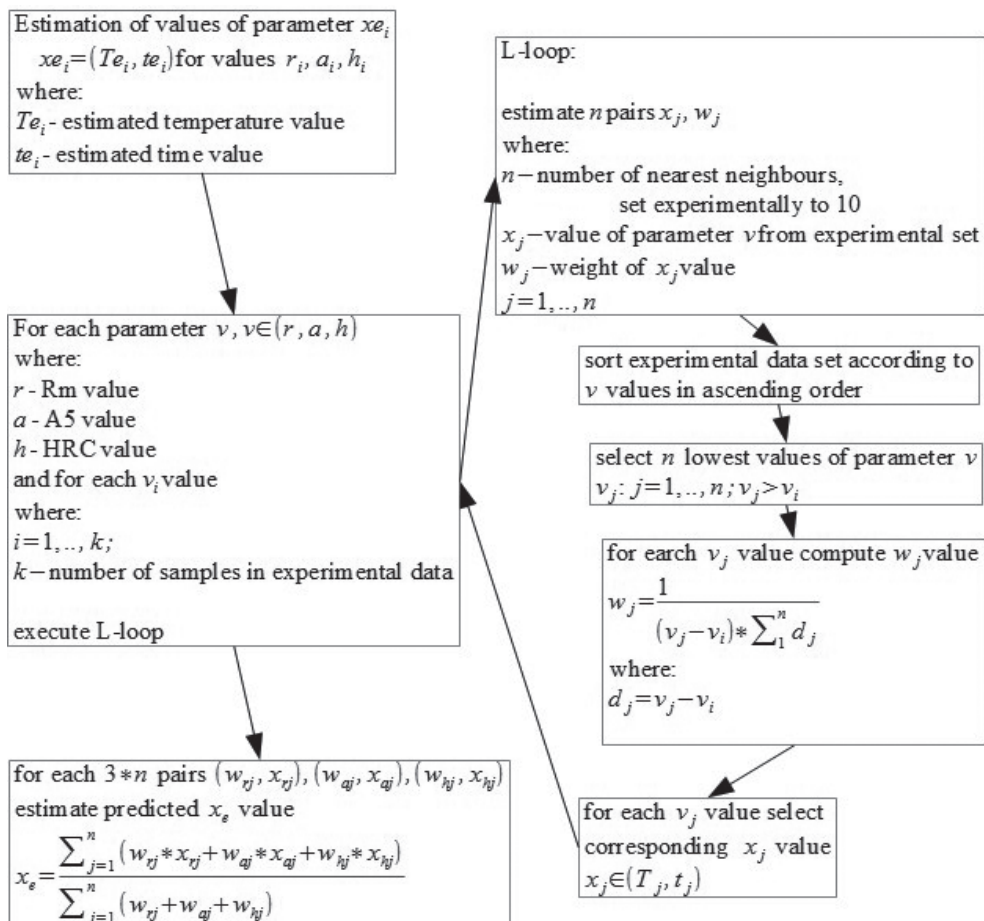


Fig. 2. An algorithm of a model for parameter prediction

For each of the samples, a mean square error was calculated based on the value estimated and value given in the literature. The estimation efficiency was based on the dependence of the mean square error and standardised range of parameter values according to Equation 1:

$$Eff = \frac{range(x) - \sqrt{mse}}{range(x)} \quad (1)$$

$$range(x) = \max(x) - \min(x)$$

The values of the estimation efficiency for time ( $t_{it}$ ) and temperature ( $T_{it}$ ) are shown in the graph in Fig. 3.

Based on the data compared in Table 2 and using the graph in Fig. 3 representing all the tests conducted, the following conclusions have been drawn:



Fragment of a set of standardised experimental data (17 out of 70)  
with predicted values

LP	Real		Estimated		Rm	A5	HRC
	Temp	Time	Temp.	Time			
1	-1,892	-0,875	-1,418	0,254	896	0,8	54
2	-1,892	-0,769	-1,276	-0,043	1120	1	51
3	-1,892	-0,663	-1,252	0,158	1320	1,8	48
4	-1,892	-0,452	-1,222	-0,010	1560	2,9	47
5	-1,892	0,395	-1,428	0,155	1450	1,9	46
6	-1,892	1,241	-1,358	0,046	1600	2,4	47
7	-1,279	-0,875	-1,023	0,058	1590	2,6	46
8	-1,279	-0,769	-0,849	-0,107	1580	2,8	46
9	-1,279	-0,663	-0,797	-0,076	1160	1,4	48
10	-1,279	-0,452	-0,866	0,081	1490	3,8	44
11	-1,279	-0,028	-1,049	0,087	1420	2,6	43
12	-1,279	0,395	-0,987	0,091	1450	4	43
13	-1,279	1,241	-0,883	-0,091	1480	3	44
14	-1,279	2,088	-0,556	-0,107	1500	3,6	44
15	-0,666	-1,087	-0,703	-0,242	1520	4	44
16	-0,666	-0,875	-0,682	-0,090	1500	4,2	43
17	-0,666	-0,769	-0,668	0,004	1470	4,8	43

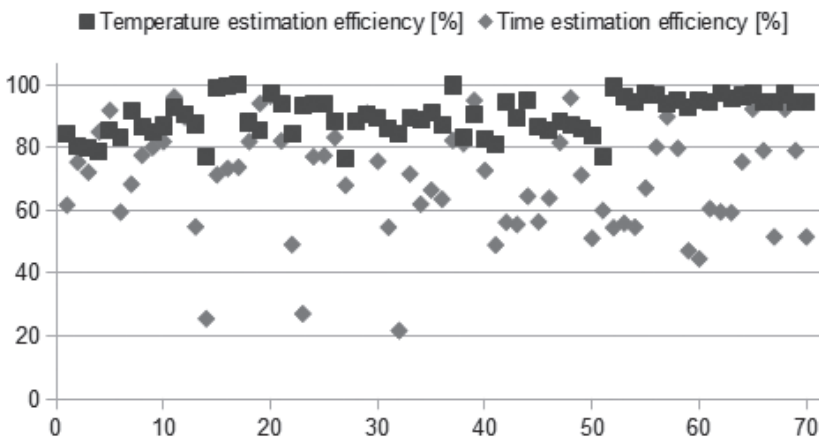


Fig. 3. Efficiency of estimation of the process time and temperature

- the presented model for the process parameter estimation is very efficient in the estimation of the austempering temperature ( $T_{it}$ ). The average estimation efficiency obtained on 70 samples was 90.06%,
- the efficiency of estimation of the austempering time ( $t_{it}$ ) at an average level of 69.74% allows only to indicate the order of magnitude of this parameter,

- after a more detailed analysis of the austempering time – product properties relationship and calculation of the values of this correlation it can be concluded that the effect of the austempering time on product properties is much less pronounced than that of the austempering temperature ( $T_{it}$ ) – thus confirming once again the lower efficiency of estimation done with the help of the developed model.

## 5. Conclusions and further work

The results of the study indicate that the approach using the literature data jointly with the developed algorithm for the process parameter estimation is applicable in the estimation of selected process parameters. The results show high efficiency of estimation obtained for austempering temperature ( $T_{it}$ ) and average efficiency for austempering time ( $t_{it}$ ). However, the mere fact that these results could be derived from a relatively small number of data and using a simple estimation algorithm proves the validity of the conducted research. It seems advisable to continue studies on the development of models estimating the parameters of the production process based on the data in the literature. The next stage in the development of the presented approach will relate to the extension of the range of data on which the applicant model is based, and to the use of a more advanced applicant models and algorithms. Examples of solutions that can be used as estimation models are neural networks and fuzzy logic elements.

Summing up, it can be stated that the results presented in this paper confirm the validity of the adopted concept of studies and the implemented system is a promising solution for further development and research work in this field.

*The work has been supported by the Polish Ministry of Science and Higher Education – AGH University of Science and Technology Funds No. 11.11.110.300.*

## References

- [1] Kochański A., Kozłowski J., Kłębczyk M., Perzyński P., *Modelowanie własności żeliwa sferoidalnego ADI za pomocą danych literaturowych opracowanych z wykorzystaniem metodyki przygotowania danych*, Polska metalurgia w latach 2006–2010, WN Akapit, Kraków 2010.
- [2] Zahiri S.H., Davies C.H.J., *Simultaneous prediction of austemperability and processing window for austempered ductile iron*, Pereloma E.V., Materials Science and Technology, Vol. 19, 2003, 1761-1770.
- [3] Dymski S., *Kształtowanie struktury i własności mechanicznych żeliwa sferoidalnego podczas izotermicznej przemiany bainitycznej*, praca habilitacyjna, Bydgoszcz 1999.
- [4] Susil K. Putatunda, *Development of austempered ductile iron (ADI) with simultaneous high yield strength and fracture toughness by a novel two-step austempering process*, Materials Science and Engineering A315, 2001, 70-80.

- [5] Susil K. Putatunda, *Influence of austempering temperature toughness of low manganese austempered ductile iron (ADI)*, Materials and Manufacturing Processes, 16(2), 2001.
- [6] Lin C.K., Lai P.K., Shih T.S., *Influence of microstructure on the fatigue properties of austempered ductile irons – I High-cycle fatigue*, Int. J. Fatigue, Vol. 18, 1996, 297-307.
- [7] Janowak J.F., Morton P.A., *A guide to mechanical properties possible by austempering 1,5% Ni – 0,3% Mo ductile iron*, AFS Transaction, V 92 Paper 84-120, 1984, 489-498.
- [8] Biel-Gołaska M., Kowalski A., *Charakterystyki wytrzymałościowe żeliwa typu ADI przeznaczonego na elementy nośne w podajnikach stosowanych w górnictwie*, Prace IO 4, XLVI, 1996, 333-344.
- [9] Kowalski A., Tybulczuk J., Jackowski J., *Manufacture and properties of the bainitic – austenitic ductile iron with additions of Ni and Cu*, The Japan Foundrymen's Society Ginza 8-12-13, Tokyo, Osaka 1990.

PAWEŁ PIĄTEK\*

## ACQUIRING ROAD PROFILES USING WALKING-PROFILER AND COMPUTER MODELLING PLANOGRAPH'S MEASUREMENT

### POZYSKANIE PROFILU DROGI Z UŻYCIEM *WALKING-PROFILERA*, A NASTĘPNIIE KOMPUTEROWE ZAMODELOWANIE RZECZYWISTEGO POMIARU PLANOGRAFEM

#### Abstract

The assessment of road pavements in terms of their properties and surface features is both complex and difficult. The indicators which describe the surface quality are eg. a longitudinal and transverse profile, a coefficient of friction, the International Roughness Index (IRI) and surface cracks. The article presents a method of using the data describing a real longitudinal profile of pavements, which was obtained by way of a self-constructed device named Walking-Profiler. It also proposes a way of calculating it with the use of numerical modelling of a Planograph, and also (simultaneously) the collected data can be used to calculate the International Roughness Index.

*Keywords: IRI, Walking-Profiler, Planograph, Planograph Simulator*

#### Streszczenie

Analiza nawierzchni drogowych pod względem ich parametrów i cech powierzchniowych jest złożona i kłopotliwa. Czynniki, które charakteryzują jej jakość powierzchniową, są m.in. równość podłużna i poprzeczna, stan spękań, wsp. tarcia, IRI. Artykuł prezentuje propozycję wykorzystania danych opisujących rzeczywisty profil podłużny nawierzchni jezdni, zebrany przy zastosowaniu własnej konstrukcji urządzenia profilometrycznego oraz przeliczenia ich przy użyciu numerycznego zamodelowania planografu, a także (niejako przy okazji) zebrane dane mogą posłużyć do kalkulacji wskaźnika IRI.

*Słowa kluczowe: Wskaźnik IRI, Walking-Profiler, Planograf, Symulator Planografu*

\* M.Sc. Eng. Paweł Piątek, Institute of Applied Informatics, Faculty of Mechanical Engineering, Cracow University of Technology.

## 1. Introduction

Road surface profile measurement is a compulsory stage during the construction of roads and highways; they are the final stage. Without receiving the optimum measurement results, the road may not be approved for use. If the test results do not meet the requirements of the profile referred to in RMTiGM Dz.U. 1999.43.430 [1] or RMTiGM Dz.U. 2002.12.116 [2], the commissioning of road surface by the customer may be impossible or financial penalties will be imposed on the Contractor for failure to comply with the desired quality of the construction work. Longitudinal and transverse profile measurements are also performed periodically on networks of roads administered by different levels of road administration, i.e. the General Directorate for National Roads and Motorways (*Generalna Dyrekcja Dróg Krajowych i Autostrad – GDDKiA*), Voivodship Road Authorities (*Zarządy Dróg Wojewódzkich – ZDW*) or Local Road Authorities (*Zarządy Dróg Powiatowych – ZDP*), in order to determine the degree of road consumption and, if necessary, to make structural corrections or surface treatments in homogeneous road sections, for which test results do not meet the requirements contained in the relevant reference documents (The Pavement Condition Evaluation System – *System Oceny Stanu Nawierzchni – SOSN*). In Poland, since 1969, that is since the time of the introduction of the standard BN-68/8931-04 [3], the methods of measurement described in this norm have been applied and measuring equipment is still developed on the basis of schemas described in the standard. Longitudinal profile measurements with the use of the so called: method of ‘patches and wedge’ are quite rare, but measurements with the use of a planograph are very often applied in a measurements procedure. However, the use of the planograph is problematic because of its design, size and weight and also the way of carrying out the measurements. It was, therefore, necessary to develop a better method, which, as far as possible, would completely displace a planograph, at the same time obtaining identical measurements results.

This article describes the project, whose goal was to build our own profilometric device, hereinafter referred to as ‘Walking-Profiler’, which allows for registering the real pavement longitudinal profile. The next step was to design and create software using numerical methods, the aim of which was to correctly model (visualize in a computer program) and calculate the reaction of a planograph moving on a precisely registered longitudinal profile of the test section of the road. Having the data of the real road profile, the International Roughness Index (IRI) can also be determined, which is one of the indicators that describe the quality of the pavement.

## 2. International Roughness Index (IRI)

IRI – the International Roughness Index is a parameter describing the work of the vehicle suspension in the ‘top-down’ axis for a hypothetically perfect car vehicle, the so-called ‘golden car’ [6], moving at a constant speed of 80 km/h along a registered road pavement profile on the specified road section. This coefficient is expressed in mm/m (for short road sections) or in m/km (for long road sections). In accordance with the Polish classification system of roads – the so called SOSN (The Pavement Condition Evaluation System – Polish: System Oceny Stanu Nawierzchni – SOSN) the tested road section needs to be divided into

50- or 100-meter-long sections (50-meter-long road sections are required at the stage of road pavement commissioning, 100-meter-long sections are required for periodic road check-ups) and IRI indices are determined for each of the sections.

For new roads, the obtained results need to be arranged in the increasing sequence, and it is necessary to determine values congruent with quantiles: 0.5; 0.8 and the maximum value, and then make a comparison of the obtained profile parameters with the extreme values (requirements) determined in appropriate documents [1, 2]. If the index exceeds the permitted norm, it must be stated that the whole tested section does not meet the requirements, and thus cannot be accepted for use. In some situations, such a section may be accepted for use, on the condition that structural defects do not pose a danger for users, and these defects do not have a significant impact on the deterioration of the technical condition of the road. A customer may reach an agreement with the contractor by forcing them to extend the warranty period or reduce the contract price.

As far as conditions permit, the road pavement needs to be repaired (IRI values for individual sections of 50 or 100 meters indicate the points which must be repaired). For older regularly used roads on which periodic tests are carried out, it is necessary to mark the places which require an immediate general repair (IRI outside the norm) on the basis of the table of results, the short-term repairs (IRI around the norm extreme) by e.g. milling surfaces, and places of an increased demand for restoration works (IRI in the B class).

There are spreadsheets, programming libraries and even ready-to-use calculation programs (e.g. ProVal) containing the implemented method of IRI calculation on the basis of input data of the road profile. In the case of this project, having the surface profile data obtained by the use of the Walking Profiler, there is no reason why the data should not be analyzed by the use of one of the above methods and IRI determined for individual sections of the tested area.

### **3. Walking-Profiler**

A Walking-Profiler is a measuring device for measuring the longitudinal profile of the road surface. Its main element is a high-quality inclination recorder that defines the real angular position of the device relative to the vertical axis of the globe (that is, the inclination from the vertical gravity). The second element is the rotary encoder mounted on one of the wheels. Its task is to count revolutions of the wheel, and thus the measurement of the distance covered by the device. The encoder used in the device allows for the registration of up to 40,000 steps per revolution, significantly reducing measurement uncertainty. For example, the distance measurement on the test section of 1 kilometer deviated from the real distance by 12 centimeters, so a measurement error was 0.012%.

These elements allow to obtain information about the distance of any measuring point from the beginning of the test section and also the device inclination at this point. By taking the data at specified distance intervals, measuring the value of consecutive inclinations, making transformation of inclination (with respect to distance) to a height and summing up the received heights, a function describing the exact shape of the covered testing section can be created.

In order to do this, the following assumptions must be met:

- The values of the measured heights have a relative nature; this means that the starting point of the tested section equals zero, the rest of the points are counted in relation to it;
- A measuring step should be as small as possible. The smaller the value of the step, the more measurement points – the data describing inclination (heights); it entails a more accurate profile function. The standard measuring step is 1 mm-long, but this value can be modified if needed;
- The values measured by the inclination sensor brought together give a quite shapeless, and acute function. The results in this form are not suitable for further analysis and require a correction;
- The construction of the device with a track of wheels equaling 500 mm introduces automatic averaging (filtration) of the collected data. It works like a low-pass filter.

Various factors have an influence on the deformations described in point 3. The construction of the device and installation of the sensor are burdened with a technological error. The measurement performed by the sensor is also burdened with a measuring error. The device itself works in dynamic conditions, that is, it does not stop at a specified distance and it does not stabilize in order to take a sample. Additionally, the measurement is taken only in the course of movement, which also disturbs the measurement. Therefore, the initially received inclination function must be subjected to rectification. There are a lot of methods and algorithms for analysing distorted signals. Probably the best and also the most commonly used one is the Kalman filter [5, 6]. The rectified inclination function may be finally regarded as an optimum and in such a form it can be used to determine the correct function of the profile.

#### **4. Planograph**

A Planograph is a measuring device used to measure the height of local vertical deformations of the pavement relative to the plane determined by the wheels of the device. The official design guidelines can be found in standard BN-68/8931-04 [3]. Since the time when the standards were introduced, technology has been constantly changing, and thus some construction changes are permitted, for example, in terms of the shape of the frame, structural materials, and the use of electronic systems (measurement with digital registration data). However, elements such as a diameter and a track of wheels must be maintained in accordance with the guidelines.

The mechanical design of the planograph contains 4 main parts:

- The Trolley Frame (1) on the skeleton of which the other items are mounted. The standard allows for freedom in this regard, provided that it does not affect the correctness of the other points. The weight of the device should be evenly distributed so that the center of gravity is exactly in the axis of the sensor. It is necessary to use construction weights when this condition is not met;
- Wheels (2), with a diameter of 200 mm. The device has 14 wheels, 7 on each side (front, rear). The specific wheels are paired with each other. The paired wheels are arranged symmetrically in equal distances relative to the axis of the sensor. The distance between other wheels and the axis of the sensor is deliberately uneven. It is aimed at catching the

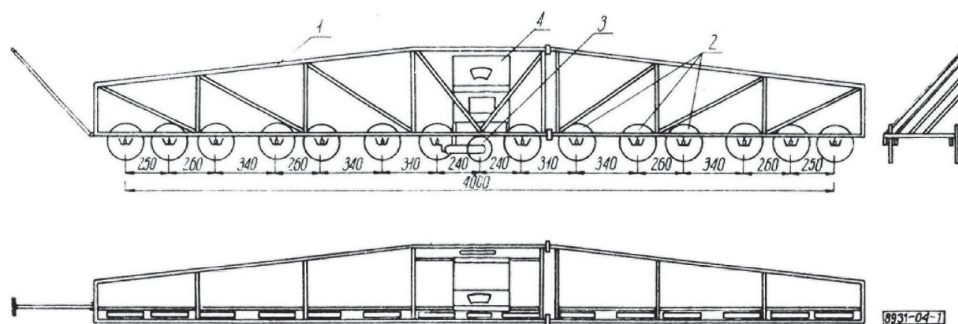


Fig. 1. Technical diagram of a Planograph

maximum range of the waves [6] of unevenness that may be found on the roadway. The device also has one additional wheel, placed on its side. Its only function is to maintain the device in a vertical position, so that it did not fall out. This wheel is not important in the procedure of measurement and has no influence on the results obtained;

- Measuring Wheel (3), with a diameter of 150 mm. It is mounted centrally in the axis of the device, on the resistanceless rail or a similar element that allows free ‘top-down’ movement of the wheel in relation to the device. The sensor wheel, when passing through a rut or a bump, rises or falls, which enables to register the profile of the pavement;
- The Measurement Table (4). It can be any mechanical design, an electric or electronic one, that enables to record the changes in the position of the measuring wheel for the entire duration of the test. In the first versions of the device there were recorders mounted on the tape, which drew graphs on graph paper (like a seismograph). Now electronic sensors and microprocessor systems are applied. They allow to make accurate measurements and record data on a digital medium.

Additionally, according to the norm the following requirements must be met. The measurement accuracy cannot be worse than 0,1 mm. Secondly, the test must be carried out in a continuous mode, i.e. it must register the sensor’s values in the continuous movement of the device.

## 5. The Planograph Simulator

The Planograph Simulator is a software for numerical calculations that can be used to model the response of a planograph, mainly to determine the exact position of the sensor on the basis of the data of the profile of the road covered by the device. The road profile data can be obtained in any way. As mentioned in an earlier chapter, to generate data of the road profile, the Walking-Profiler was used.

### 5.1. The physical model of the planograph-analysis

The centroid and the axis of symmetry in relation to the vertical axis of the device. In this axis the measuring sensor is placed in the form of a circle of a certain diameter. It was



assumed that the starting point of the sensor is located at the intersection of the axis of symmetry and the axis of the wheels. This point is a point of reference for all calculations. The distribution of wheels is symmetrical on each side. The measuring base is the so called 'zero line'. This is a straight line designated by a tangent line to all wheels at the point where the wheels and the test surface meet. The sensor wheel moves always in a line perpendicular to the zero line. Due to the symmetry of shape and weight, the device will always be based on the tested profile at least by one of the 'front' wheels and at least one of the 'rear' wheels. The wheels on which, at a given moment, the device is supported are called the supported wheels. This assumption is referred to as the assumption of minimum supporting. It has been used in all calculation methods.

## 5.2. Calculation of the planograph's position on the profile

**Method No. 1** entails the maximum simplification of the model without taking into account its real inclination. The support point of the wheel is treated as a material point, the highest point under the circumference of the wheel. The zero line is always horizontal to the profile. The left supported wheel is the one which stands on the highest profile point. The same goes for the right wheel.

A simultaneous assumption that the zero line is always horizontal and an assumption of a minimum support, causes an interesting effect. Because there is at least one support point on each side, theoretically there is a 'break' in the middle of the device.

The base point of the sensor (the zero point), from which the height is determined, should be therefore determined either by the average value of the difference in height (inaccurate), or by an average difference in height taking into consideration the weights-distances of the supported wheels from the middle.

The method is very fast and easy to implement, but causes a lot of errors when the difference in height between the supported wheels is significant (there are inclinations present which are not taken into account). What is more, this method does not provide for a situation that may occur in reality, when as a result of the inclination (which is not taken into account), the most external wheels on one side are below the presupposed height and thus possibly supporting at some point, which as a consequence may lead to raising one side of the device, interfering with the indication of the sensor.

**Method No. 2** assumes the average simplification of the model, taking into account the real inclination. The support point of the wheel is treated as a material point, the highest point under the circumference of the wheel. The weights of the height for the supported points for wheels are counted as the quotient of the height (the vertical distance of the possible supporting point of wheels in relation to the level of a temporary zero line) and the width (horizontal distance of the supporting point of the wheel from the axis of the sensor).

The method is fairly simple to calculate with greater calculation complication from the previous method. It is accurate, but only if the wheels are supported exactly in the middle point of the wheel's circumference. When in reality the wheels are supported slightly further than this point, there are errors. The greater the difference between the theoretical support point and the real one, the greater error may occur.

**Method No. 3** assumes no application of any simplification. The method takes into account the real inclination angle. The supporting point for the wheel is treated as a real point

profile, on which the wheel is supported. The zero line is determined by the real supported wheels.

The method assumes calculation of the real supporting point for each of the wheels. Assuming that the measurement step is taken every 1 mm, when a wheel diameter is 200 mm, this gives 200 checks for one wheel, giving 2,800 checks for all wheels at each step in the test profile. The method of calculation of weights is the same as in the previous method.

The method is complicated and of high calculation complexity, due to repeated calculation and checking supporting points at each measurement step. However, the method is the most accurate one.

Determination of the appropriate supported wheels (in methods 2 and 3) consists in picking the wheels of extreme weight results on each side. For example, if the device is located on a perfectly flat profile, the weights will equal zero, because all the supporting points of the wheels will be on the same height. Otherwise, the device will be leaned to one of the sides, thus all height values on this side must always have negative values. Depending on the direction of inclination, a pair of weights must be taken into account – ‘the smallest left one, the largest right one’ or ‘the largest left one, the smallest right one’.

This is an iterative method. When determining the height of each of the wheels and the appropriated supported wheels, it is necessary to check if the remaining wheels meet the requirements (the wheels are mounted on a rigid frame, and they all must lie in one line). If some of the wheels ‘fell under the profile’, it would be necessary to ‘raise them’ to the profile height, to raise the other wheels proportionally and repeat the procedure of counting the inclination. If in the next iteration the numbers of the supported wheels repeat, it will mean that the appropriate supported wheels have been determined correctly. When having the supported wheels determined, it is possible to mark the inclination, the real location of the base point of the sensor, and then make a calculation for the sensor’s measurement.

### 5.3. Calculation of the sensor’s wheel’s position

Having the knowledge of the ‘zero’ point of the sensor (the intersection of the axis of the wheels with the axis of the sensor), calculated with the use of the above methods, it is possible to calculate the sensor’s wheel’s position. In order to do this, in theory, it is necessary to lower the sensor perpendicularly to the calculated inclination line until the sensor stops on the road profile. In practice, this requires more precise calculations, so an iterative method is applied.

The first step is to lower the sensor in the Y-coordinate until an obstacle is encountered in the form of the profile and to specify its height. Then, it is necessary to compare the X-coordinate of the sensor to the X-coordinate of the point (for the same height as the sensor) of the line perpendicular to the line of inclination going through the ‘zero’ point of the sensor. If this value is higher than the allowable measurement error, the sensor needs to be moved in the X-coordinate so that the middle point of the sensor temporarily lies on the perpendicular line. Temporarily, because the calculation of the sensor height needs to be repeated (the profile points under the wheel sensor must be checked) for a new location, it may turn out that the sensor in the new location will change its height, and thus it will be required to once again move the sensor in the X-coordinate in the direction of the perpendicular line. The process should be repeated until the values fall within the limits of the permitted error.

It is also necessary to mention that the sensor, due to its construction, measures the height in a determined way. A sensor in the form of a circle of a certain diameter will not be able

to measure a small rut, because its diameter will prevent it from 'falling into' them. With a small measuring step, the sensor will detect all, even the smallest bumps. Therefore, it is recommended to use small measuring steps in order to avoid a situation where during the tests big bumps are skipped, which, during the actual trip will be felt, and which will not be seen during the tests. Such a situation can be found for example in the literature [4] where it is described in detail.

## 6. Conclusions

The project described in the article consists of two parts. Walking-Profiler was built in accordance with previous assumptions. Thanks to this device, it is easy to obtain the actual longitudinal profile, the so called 'true profiles' [6], covered by the device. This data can be used later to establish the International Roughness Index for the test section with the use of one of the methods described in Section 2. IRI.

The second stage of the project was the creation of numerical software, which would model the behavior of the actual device – a planograph moving along this profile, and the behaviour of its measuring sensor. In the previous section the analysis of this problem was presented and several possible algorithms for dealing with specific situations were shown. It was stated that the most appropriate method to calculate the device's position will be method No. 3. Although in comparison to other described methods method 3 is most complex in terms of the numerical method, it has the largest calculation complexity and is the most difficult one to implement, it provides the most accurate results and generates the fewest errors. Then, the method was used for determining the supported wheels on the basis of the value of the extreme weights on each side. Having the exact location and inclination of the device, the values calculated by the measuring sensor can be obtained.

By repeating this procedure for all points of the test section, a very accurate print of the values can be obtained as they were indicated by the sensor of the actual planograph if it covered a given profile. The method proposed in the article, however, allows to get exactly the same results as if the planograph was used in the tests, but without the use of a physical device and testing only using a simulator. The proposed method is less troublesome and, above all, disproportionately more accurate, because the measurement takes place in somewhat quasi-static conditions, the applied electronic components have a significantly better measuring capacity, there is a lack of moving components and the problems with technical support issues of the planography operation are completely eliminated.

## References

- [1] Rozporządzenie MTiGM w sprawie warunków technicznych dla dróg publicznych i ich usytuowania, Dz. U. Nr 43, poz. 430, 2 marca 1999.
- [2] Rozporządzenie MTiGM w sprawie przepisów techniczno-budowlanych dotyczących autostrad, Dz. U. Nr 12, poz. 116, 16 stycznia 2002.
- [3] BN-68/8931-04, *Pomiar równości nawierzchni planografem i latą.*

- [4] Chabowski E., Osysko A., *Badanie równości podłużnej planografem – przypadkowość czy dokładność*, Opracowanie Techniczne, 06-2012.
- [5] “Filtr Kalmana”, [in:] Wikipedia, Free Encyclopedia.
- [6] Sayers M.W., Karamihas S.M., *The Little Book of Profiling*, University of Michigan, September 1998.



JANUSZ POBOŻNIAK\*

## USING CONCAVITY INDEX FOR MANUFACTURING FEATURE RECOGNITION

---

### ZASTOSOWANIE INDEKSU WKŁĘSŁOŚCI W ROZPOZNAWANIU CECH TECHNOLOGICZNYCH

#### Abstract

The paper presents the usage of the concavity index for the effective recognition of the concave, open manufacturing features like open pockets, through slots and steps. The determination of this index using B-Rep representation is presented in detail. This is a fragment of an algorithm for the recognition of manufacturing features defined in the STEP-NC standard.

*Keywords: manufacturing feature recognition, STEP-NC, CAD/CAM integration*

#### Streszczenie

W artykule przedstawiono zastosowanie indeksu wklęsłości do efektywnego rozpoznawania wklęsłych cech technologicznych typu otwartego, jak kieszenie otwarte, rowki przelotowe czy uskoki powierzchni. Szczegółowo omówiono procedurę wyznaczania tego indeksu w oparciu o reprezentację B-Rep. Jest to fragment algorytmu rozpoznawania cech technologicznych zdefiniowanych w standardzie STEP-NC.

*Słowa kluczowe: rozpoznawanie cech technologicznych, STEP-NC, integracja CAD/CAM*

---

\* Ph.D. Janusz Pobożniak, Production Engineering Institute, Faculty of Mechanical Engineering, Cracow University of Technology.

## 1. Introduction

CNC machine tools are now basic manufacturing machines. One of the key tasks to automate the CNC machine tool programming is the manufacturing feature recognition. Manufacturing feature recognition groups geometrical elements into the information units significant from the point of view of the manufacturing process planning, i.e. manufacturing features. So, it groups faces, edges, points, etc. into the manufacturing features like pockets, slots, holes etc.

Three commonly used recognition methods for the B-Rep format are graph-based algorithms [4], volumetric decomposition techniques [1] and hint based geometric reasoning [9]. There is no doubt that the up-to date functionality of the feature recognition, both in commercial software as well as in the research works, still requires further development. The main problems are the recognition of interacting manufacturing features and the use of the manufacturing knowledge during the recognition process [5, 8].

The paper presents the concavity index developed by the author of this paper. This index allows for the efficient recognition of the open, concave manufacturing features like open pockets or through slots. In contrast to the graphs approaches [4], it allows for the recognition of the manufacturing features regardless of the number of the faces constituting the features. This index allows also for the automatic determination of the feature orientation, which is necessary to determine the machining set-up or to select the suitable machining tool. This index is also used in the STEP-NC manufacturing feature recognition algorithm [7, 8]. The input data is the part model in the STEP standard [2, 3]. After processing this input data, the algorithm generates the set of STEP-NC manufacturing features, which can be directly used by the system for automatic CNC machine tool programming in the STEP-NC standard.

## 2. Algorithm for manufacturing feature recognition in STEP-NC standard

### 2.1. B-Rep data structure

The input data is the B-rep structure encoded in ISO-10303-21 standard [3]. This data can be output using most of commercially available CAD systems.

In the B-Rep representation, the faces creating the shape are stored (faces  $f_1 \dots f_{11}$  in Fig. 1b). These can be plane, cylindrical, conical, b-spline faces, etc. Each face has one external loop defining its boundary. The faces can have optionally the internal loops. The face has internal loops when it is the base for the concave (for example pockets) or convex features (for example boss) (Fig. 1b). The direction of each loop, both external as well as internal is so, that during the movement along the loop, the material remains on the left side. Each loop has an edge list. For each edge, the start point, end point and the edge type are stored. The edge types are lines, arcs, `b_spline_curve`, `b_spline_curve_with_knots`, etc. Each edge is shared by exactly two faces. Fig. 1b shows the edges shared by  $f_1/f_3$  and  $f_1/f_8$  faces.

If the two neighboring faces form a convex angle (as the angle between faces  $f_1$  and  $f_3$ ), the edge between these faces is called a convex edge (Fig. 1c). If the two neighboring faces form a concave angle (as the angle between faces  $f_1$  and  $f_8$ ), the edge between these faces is called a concave edge.

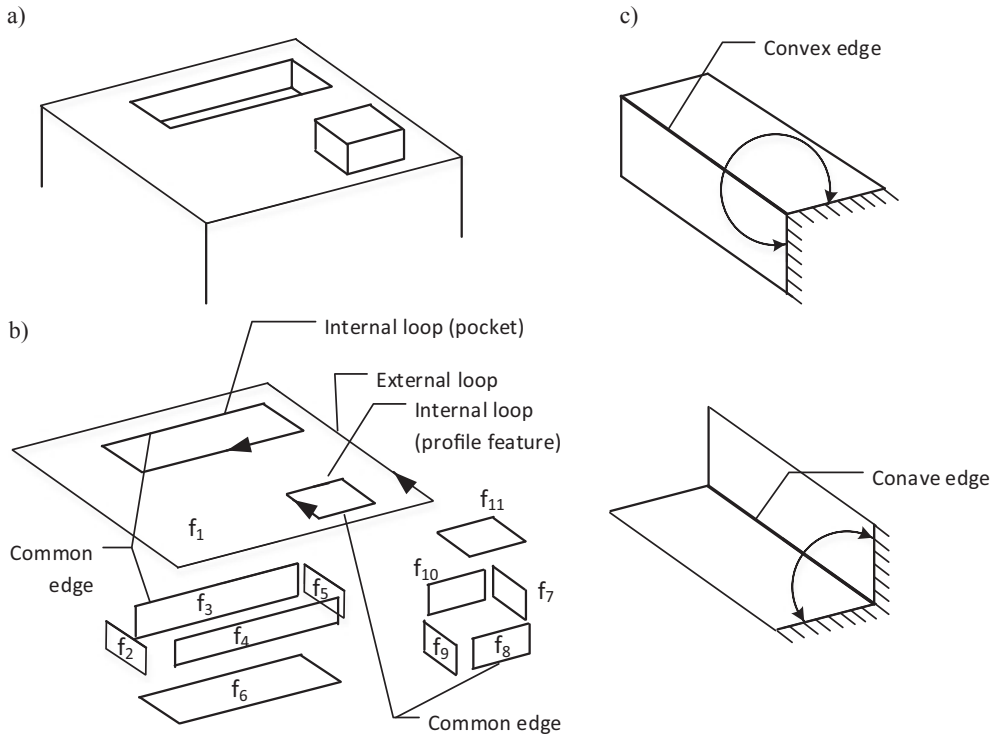


Fig. 1. B-Rep representation: a) Part, b) B-Rep representation, c) Convex/concave edges

## 2.2. Determination of the type of edges (convex/concave)

As already mentioned, the classification of the edges (concave or convex) (Fig. 1c) depends on the angle between the faces sharing the given edge. Let  $e$  be the edge between  $f_1$  and  $f_2$  faces (Fig. 2). To determine the angle between these faces, first the vector product  $c$  using  $n_1$  and  $n_2$  perpendicular to the faces  $f_1$  and  $f_2$  is calculated.

$$c = n_1 \times n_2 \quad (1)$$

If the coordinates of  $n_1$  vector are  $[n_{1x}, n_{1y}, n_{1z}]$ , and the coordinates of  $n_2$  vector are  $[n_{2x}, n_{2y}, n_{2z}]$ , the resultant  $c$  vector has the coordinates:

$$\begin{aligned} c_x &= n_{1y}n_{2z} - n_{1z}n_{2y} \\ c_y &= n_{1z}n_{2x} - n_{1x}n_{2z} \\ c_z &= n_{1x}n_{2y} - n_{1y}n_{2x} \end{aligned} \quad (2)$$

The resultant  $c$  vector is perpendicular to the face created by the vectors normal to the  $f_1$  and  $f_2$  faces, so it is parallel to the  $e$  edge. The direction of this  $c$  vector can be determined



using the right-hand rule. If the directions of the  $c$  and  $e$  vectors are the same, the angle between the  $f_1$  and  $f_2$  faces is concave so we have the concave edge. In the other case, if the direction of  $c$  and  $e$  vector are different, we have the convex edge. The order of the faces in the equation (1) should be noted. The direction of  $e$  edge determines that order (from right to left).

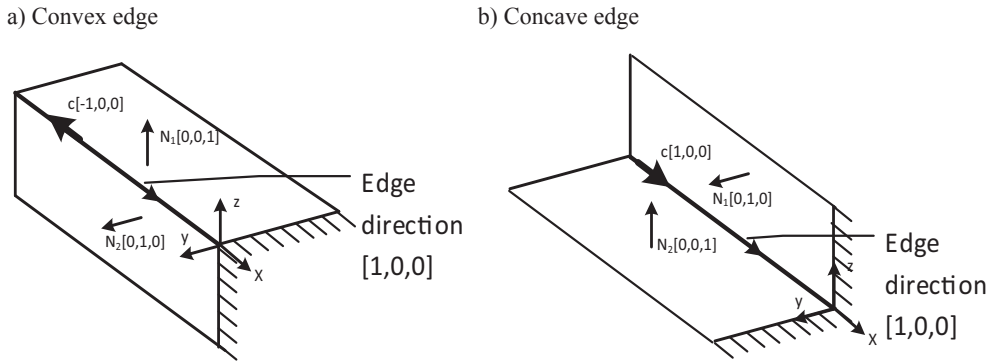


Fig. 2. Vector product of the vectors normal to faces

To determine if the  $e$  and  $c$  vectors have the same direction, the scalar product  $d$  between  $e$  and  $c$  vectors is calculated.

$$d = c \cdot e \quad (3)$$

If the coordinates of  $c$  vector are  $[c_x, c_y, c_z]$ , and the coordinates of  $e$  vectors are  $[e_x, e_y, e_z]$ , then:

$$d = c_x e_x + c_y e_y + c_z e_z \quad (4)$$

Taking into account that the scalar product between  $c$  and  $e$  vectors is:

$$d = c \cdot e = |c| |e| \cos(\alpha) \quad (5)$$

A negative value of this scalar product means that the angle between these vectors is  $180^\circ$ , so the vectors have opposite directions. If the directions are the same, the angle is  $0^\circ$ ,  $\cos(0^\circ)$  is equal 1, so the scalar product has the positive value and the two faces share the concave edge.

Using the above formulas, the type of edge is determined.

### 2.3. Manufacturing feature recognition algorithm

The manufacturing features recognition algorithm includes the following steps [6–8] (Fig. 3):

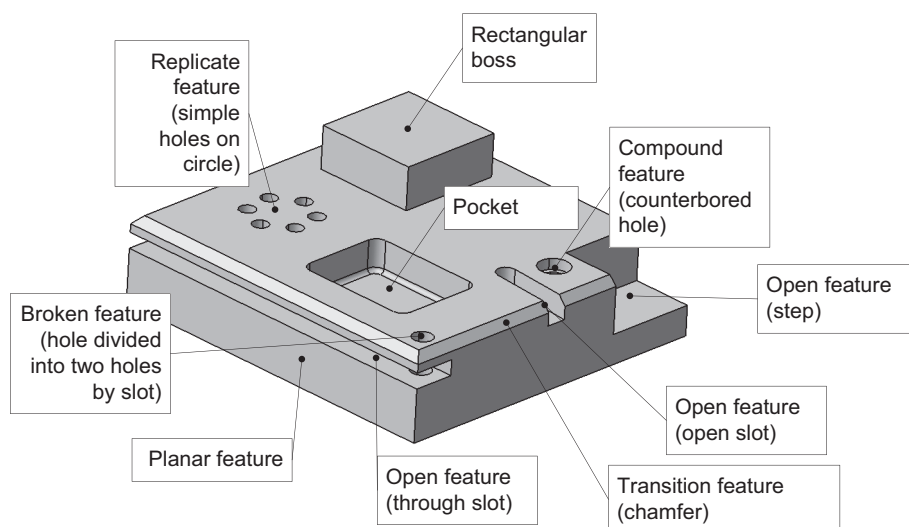


Fig. 3. Different types of manufacturing features

- Preparatory calculations including the reading of ISO 10303-21 file, creation of the internal B-Rep structure and the adjacency matrix;
- Recognition of convex features by analysis of internal bounds with concave edges only. If the face has the loop containing only concave edges, there is the convex feature on this face, like, for example, boss;
- Recognition of concave features by analysis of internal bounds with convex edges only. If the face has the loop containing only convex edges, there is the concave feature on this face, like, for example, close pocket or hole;
- Recognition of concave, open-type features using concavity index. If there are still convex edges, not belonging to the features recognized up to now, there is at least one open, concave feature. This could be open pocket, step, through slot, etc.;
- Recognition of the plane features and transitions features (phases and rounding);
- Combining the broken features, i.e. combining the features divided into more than one feature because of the intersection with other features;
- Grouping features into compound features and replicate features (number of similar features, e.g. a circle of holes or a mesh of holes).

### 3. Concavity index

One of the steps of the above algorithm is the recognition of the open, concave features. These features are recognized using the unique rule, developed by the author. First, the concavity index is calculated. This index for the given face is the number of concave edges in the external loop of that face. For example, the value of concavity index of the bottom face of open pocket is 7 (Fig. 4). The side cylindrical face of this pocket, pointed to in the figure

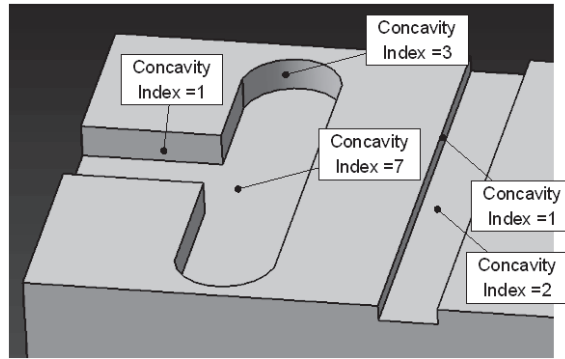


Fig. 4. Concavity index

has the index of 3, because the face has three concave edges (edges shared with the two side faces and one edge shared with the bottom face). In case of the through slot (Fig. 4), the concavity index is 2, because this face has two concave edges (these are the edges between the slot bottom and the two side faces). Of course, index is calculated only for the features not marked as recognized. So, the index is not calculated for the faces of the closed pockets, as such features were recognized in the previous step of the algorithm. All faces with the concavity index are sorted by the decreasing value of this index. In case of the presented example (Fig. 4), the highest value of the index is 7. The face with that index value is selected as the bottom face of the new feature (pocket or slot, the classification takes place later). Knowing the bottom, we can determine the feature orientation and the possible tool access directions (TAD). The faces connected with the bottom face will be included as the side faces. The side face with the greatest dimension in the direction of the vector normal to the bottom is used to select the pocket depth. Bottom and side faces are marked as recognized. This also removes these faces from the list of faces with concavity index. Because of this, during the recognition of the next feature, the greatest index has the bottom face of the through slot. This face will be selected as the bottom face of the new feature.

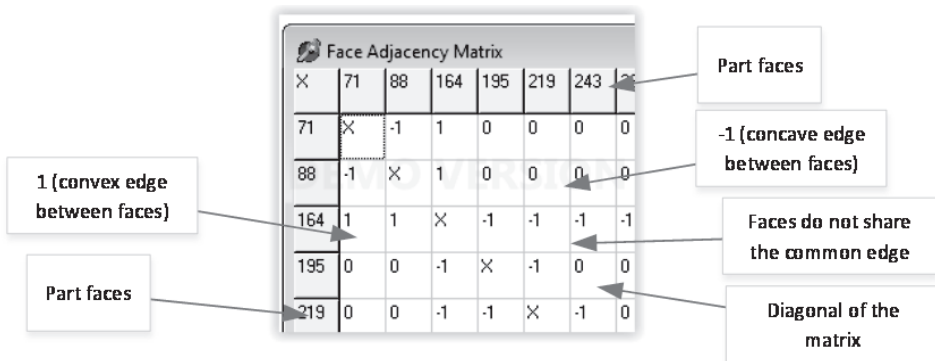


Fig. 5. Adjacency matrix

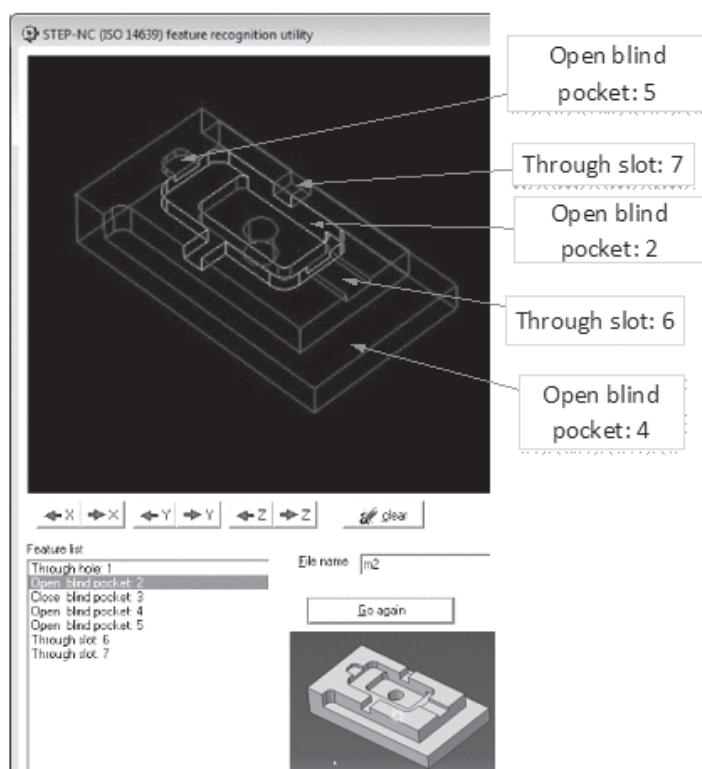


Fig. 6. The screenshot of the developed software showing the recognition results

To calculate this index, the adjacency matrix created during the preparatory calculations is used. It is the square matrix and its dimension is equal to the number of faces. The elements  $a_{ij}$  of this matrix describe the type of the edge between faces:

- 0 : face i and j does not share the edge
- $a_{ij} = x$  : elements on the diagonal of the matrix
- 1 : faces i and j share the convex edge
- 1 : faces i and j share the concave edge

The procedure for the determination of the type of edges is described in point 2.2. The creation of this matrix speeds up the calculations because the algorithm checks these relations very often. Also the list of all edges is created. Each edge on the list is assigned two faces sharing this edge. Also this list is created to speed up the calculation. Fig. 5 shows the fragment of the matrix created for the test part.

#### 4. Conclusions

The paper presents an algorithm for the recognition of manufacturing features, with special emphasis put on the use of the concavity index for the recognition of open, concave features.

The algorithm was verified through the developed software (Fig. 6). The presented algorithm is part of the works to develop the automatic CNC machine tool programming system in the STEP-NC standard. The presented algorithm does not consider many intersecting manufacturing features. This system uses the back growing approach, i.e. the program is created starting from the finished part and ending on the raw material. The recognition process is called after each transformation on condition that the transformed features interact with other manufacturing features [8]. Such approach allows to eliminate the need for the recognition of the intersecting manufacturing features.

### References

- [1] Babic B., Nesic N., Miljkovic Z., *A review of automated feature recognition with rule-based pattern recognition*, Computers in Industry, Volume 59, Issue 4, 2008.
- [2] ISO 10303-1:1994 Industrial automation systems and integration – Product data representation and exchange – Part 1: Overview and fundamental principles.
- [3] ISO 10303-21:2002, Industrial automation systems and integration – Product data representation and exchange – Part 21: Implementation methods: Clear text encoding of the exchange structure.
- [4] Joshi S., Chang T.C., *Graph based heuristics for recognition of machined features from 3D solid model*, Computer Aided Design 20 (2), 1998.
- [5] Mokhtar A., Xu X., Lazcanotegui I., *Dealing with feature interactions for prismatic parts in STEP-NC*, Journal of Intelligent Manufacturing, 04/2012.
- [6] Pobożniak J., *Algorithm for ISO 14649 (STEP-NC) feature recognition*, Management and Production Engineering Review, Vol. 4, No. 4, December 2013.
- [7] Pobożniak J., *Automation of CNC Machine Tool Programming Using STEP-NC (ISO 14649)*, Applied Mechanics and Materials Vol. 656, 2014.
- [8] Pobożniak J., *The approach for the recognition of interacting manufacturing features*, The Ninth International Conference on Engineering Computational Technology, 2–5 September, Naples, Italy, 2014.
- [9] Vandenbrande J.H., Requicha Aristides A.G., *Spatial reasoning for the automatic recognition of machinable features in solid models*, IEEE Pattern Analysis and Machine Intelligence. 01/1993.

MICHAŁ PTASZYŃSKI\*, PAWEŁ LEMPA\*\*, FUMITO MASUI\*

## A MODULAR SYSTEM FOR SUPPORT OF EXPERIMENTS IN TEXT CLASSIFICATION

## MODULARNY SYSTEM WSPOMAGANIA DOŚWIADCZEŃ Z DZIEDZINY KLASYFIKACJI TEKSTU

### Abstract

This paper presents a modular system for the support of experiments and research in text classification. Usually the research process requires two general kinds of abilities. Firstly, to laboriously analyse the provided data, perform experiments and from the experiment results create materials for preparing a scientific paper such as tables or graphs. The second kind of task includes, for example, providing a creative discussion of the results. To help researchers and allow them to focus more on creative tasks, we provide a system which helps performing the laborious part of research. The system prepares datasets for experiments, automatically performs the experiments and from the results calculates the scores of Precision, Recall, F-score, Accuracy, Specificity and phi-coefficient. It also creates tables in the LaTeX format containing all the results and it draws graphs depicting and informatively comparing each group of results.

*Keywords: Experiment support, Pattern extraction, Graph generation*

### Streszczenie

W niniejszym artykule przedstawiono modularny system wspomaganie eksperymentów i badań z dziedziny klasyfikacji tekstu. Zazwyczaj proces badawczy wymaga dwóch typów umiejętności. Do pierwszego typu można zaliczyć wykonanie mozolnej analizy dostępnych danych, przeprowadzenie eksperymentu, a z wyników eksperymentu – stworzenie materiałów do umieszczenia w pracy naukowej, takich jak tabele lub wykresy. Drugi typ umiejętności obejmuje na przykład przeprowadzenie twórczej dyskusji na temat otrzymanych wyników. Aby pomóc naukowcom skupić się na zadaniach twórczych, w niniejszej pracy prezentujemy system, który ułatwia wykonywanie żmudnej części badań. System przygotowuje zestawy danych do eksperymentów, automatycznie przeprowadza eksperymenty, a z wyników oblicza wyniki w formie Precyzji, Zwrotu, F-miary, Dokładności, Swoistości i współczynnika phi. System tworzy również tabele w formacie LaTeX zawierające wyniki eksperymentów i rysuje wykresy porównujące każdą grupę wyników.

*Słowa kluczowe: Wspomaganie eksperymentów, ekstrakcja wzorców, rysowanie grafów*

\* Ph.D. Michał Ptaszyński, Ph.D. Fumito Masui, Department of Computer Science, Kitami Institute of Technology.

\*\* M.Sc. Paweł Lempa, Institute of Applied Informatics, Faculty of Mechanical Engineering, Cracow University of Technology.

## 1. Introduction

It is often said ironically about economists: “If you are so smart, why aren’t you rich?” A similar remark can be said about researchers involved in natural language processing (NLP), or computational linguistics (CL): “If you have so many language analysis and generation techniques, why don’t you use them to perform the research for you and generate a paper and presentation slides in the end?” Unfortunately, there has been astonishingly little research on scientific paper generation, presentation slides generation or even on support of the research process. One of the reasons for this is the fact that many stages of the research process require creativity, for which effective computational models still do not exist. Parts of the research which require such creative skills include for example, preparing descriptions of research background, literature review, and especially, discussion and detailed analysis of the results of experiments.

However, apart from these creative parts of research, a wide range of activities involved in the process is of a different, non-creative nature. Preparing data for experiments, conducting the experiments, step-by-step manual changing of feature sets to train and test machine learning classifiers are only some of the examples. Moreover, a thorough calculation of final scores of the evaluated tools, generating tables for the description of experiment results in technical reports and scientific papers, generating graphs from those results, and finally, description and analysis of the results – all those tasks do not require creative thinking. On the contrary, they are the non-creative part of everyday research drill. However, despite being non-creative, such activities are laborious since they require most of the researcher’s focus and precision. This could influence the motivation towards research and in practice consumes time, which could be used more efficiently for creative tasks, such as writing a detailed and convincing discussion of the results.

To help the researchers perform their research in a more convenient and efficient way we developed a system for the support of research activities and writing technical reports and scientific papers. The system is released as an Open Source set of libraries. After being initialized by one short command, the whole process including preparation of data for the experiment, conducting the experiment and generating materials helpful in writing a scientific paper is conducted automatically.

The paper’s outline is as follows. Firstly, we describe the background of our research in which we introduce a number of research studies similar to ours. Secondly, we describe the whole system. We present in detail each of the parts responsible for data preparation, experiment conduction and generation of supporting materials. Next, we present the evaluation process, which verifies the practical usability of the system. Finally, we conclude the paper and propose other features we plan to implement in the near future.

## 2. Related Research

The research on supporting the process of research itself is rare. The authors found only a few pieces of literature that could be considered as related to the presented system.

One of the most usable and helpful environments developed so far is the WEKA environment<sup>1</sup>. WEKA provides a wide range of machine learning algorithms useful in data mining tasks. It can be used as a stand-alone software, or can be called from a custom Java code to analyse data on the fly. WEKA allows data pre-processing, classification or clustering. It also provides simple visualizations of results. WEKA is widely used in the research society, especially in natural language processing (NLP) and computational linguistics (CL) fields. Unfortunately, WEKA needs especially prepared files with measurements in appropriate columns and cannot deal with plain unprocessed data (unprocessed collections of sentences, etc.). It also does not provide graphs in the format easily applicable in a research paper, nor does it provide natural language descriptions of the analysis of results.

Another tool with well-established renown is the Natural Language Toolkit (NLTK)<sup>2</sup>. NLTK is a Python-based platform allowing various experiments with human language data. It provides a number of tools for text classification, tokenization, stemming, and tagging, parsing, and semantic reasoning. A worth mentioning feature of NLTK is that it provides not only tools for text processing, but also a number of natural language corpora and lexical resources. A disadvantage of NLTK is that all the tools need to be launched separately. This requires at least minimal knowledge of programming languages, preferably Python, in which the toolkit was created. Thus NLTK is a very powerful and useful tool for researchers with at least minimal knowledge of programming. Another disadvantage is that not all tools included in NLTK are compatible with languages of non-alphabetic transcription (Japanese, Chinese, Korean, etc.).

In a different kind of research, Nanba et al. [1] focus on automatic generation of literature review. They assumed that in research papers researchers include short passages which can be considered as a kind of summary describing the essence of a paper and the differences between the current and previous research. Their research was very promising, as Nanba et al. [1] dealt with the creative part of research. Unfortunately, after the initial paper which presents interesting preliminary results, the method has not been developed any further. This could suggest that the creative part of the research they attempted to support, namely description of background and previous research, could still be too difficult to perform fully automatically.

Shibata and Kurohashi [2] focused on a different task, namely, on automatically generating summary slides from texts. This is not exactly the same task as creating presentation slides from a scientific paper, which we consider as one of our future tasks. However, the method they proposed, after several modifications, could be applied in our research as well. They generated slides by itemizing topic and non-topic parts extracted from syntactically analysed text. In our method the parts created by the system are grouped automatically, which could help in the itemization process.

Apart from the research described above, an interesting, although not quite scientific experiment was done by anonymous researchers involved in a campaign against dubious conferences<sup>3</sup>. In their attempt they generated scientific papers by picking random parts of actual papers and submitted those fake-papers to specific conferences to verify the review process of those questionable conferences. They succeeded in their task and were accepted to the conferences, which in general proved that the process of review of some conferences

---

<sup>1</sup> <http://www.cs.waikato.ac.nz/ml/weka/>

<sup>2</sup> <http://www.nltk.org/>

<sup>3</sup> <https://sites.google.com/site/dumpconf/>



is not of the highest quality. Therefore, if there is a similar attempt in the future, although desirably more ambitious (non-random scientific paper generation), it should submit the artificially created papers to conferences or journals of proved and well known reputation.

### 3. System Description

**SPASS**, or **Scientific Paper Writing Support System** performs three tasks. Firstly, it prepares the data for the experiment, secondly, it conducts the experiment under the conditions selected by the user, and thirdly, it summarizes the results and prepares the materials for a technical report or a scientific paper. We describe each part of the process in the sections below. The general overview of the system is represented in Figure 1.

#### 3.1. User Input

The system performs the laborious and non-creative tasks from the process of research automatically “with one click”. It is developed to help in text classification and analysis tasks. At present the system handles up to two datasets (binary classification), preferably of opposite features, such as “positive” and “negative” in sentiment analysis (SA), although the applicability of the system is not limited to SA. The user needs to prepare two separate files containing the sentences from the two corpora to be compared. The contents of these files are contrasted with each other in the process of automatic evaluation. If the input consists of only one corpus the system will simply produce the most frequent patterns (In this paper we use the words “pattern” and “n-gram” interchangeably) for the corpus.

**Dataset Pre-processing.** The provided sentences can be in an unprocessed form. In such a situation processed elements will consist of words (sentence tokens). However, SPASS allows any pre-processing of the sentence contents, thus making possible any kind of generalization the user might wish to apply. The experiments can be repeated with different kinds of pre-processing to check how the pre-processing influences the results. The examples of pre-processing are represented in Table 1.

Table 1

**Three examples of pre-processing of a sentence in Japanese; N = noun, TOP = topic marker, ADV = adverbial particle, ADJ = adjective, COP = copula, INT = interjection, EXCL = exclamative mark**

Sentence:	今日はなんて気持ちいい日なんだ！
Transliteration:	<i>Kyōwanantekimochiihinanda!</i>
Meaning:	Today TOP what pleasant day COP EXCL
Translation:	What a pleasant day it is today!
Preprocessing examples	
1. Words:	<i>Kyō wa nante kimochi ii hi nanda !</i>
2. POS:	N TOP ADV N ADJ N COP EXCL
3. Words+POS:	<i>Kyō[N] wa[TOP] nante[ADV] kimochi[N] ii[ADJ] hi[N] nanda[COP] ![EXCL]</i>

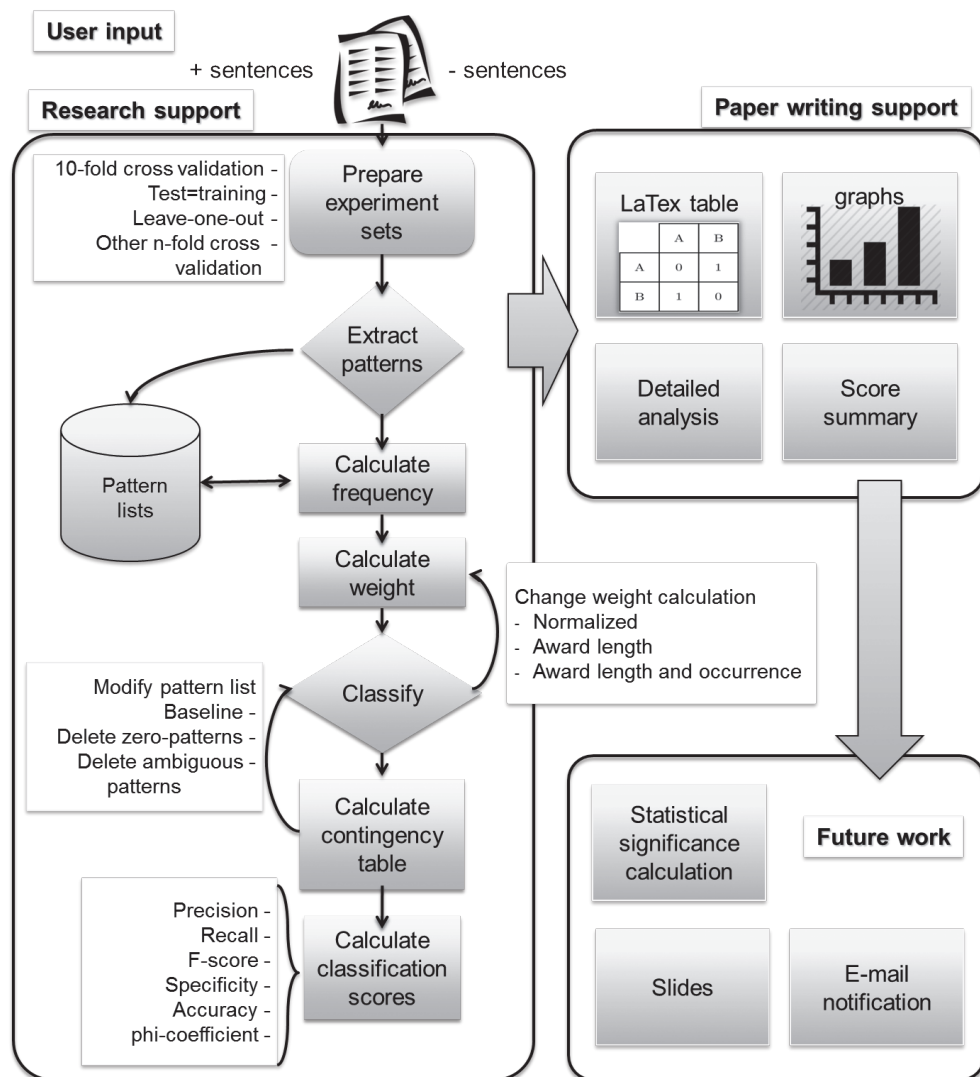


Fig. 1. General overview of SPASS divided into research support and paper writing support parts

- In those examples a sentence in Japanese is pre-processed in the three following ways:
- **Tokenization:** All words, punctuation marks, etc. are separated by spaces;
  - **Parts of speech (POS):** Words are replaced with their representative parts of speech;
  - **Tokens with POS:** Both words and POS information is included in one element.

In theory, the more generalized a sentence is, the less unique patterns (n-grams) it will produce, but the produced patterns will be more frequent. This can be explained by comparing tokenized sentence with its POS representation. For example, in the sentence from Table 1 we can see that a simple phrase *kimochi ii* (“feeling good/pleasant”) can be represented by

a POS pattern  $N_{ADJ}$ . We can easily assume that there will be more  $N_{ADJ}$  patterns than *kimochi ii*, since many word combinations can be represented by this morphological pattern. In other terms, there are more words in the dictionary than POS labels. Therefore, POS patterns will come in less variety but with a higher occurrence frequency. By comparing the result of classification using different pre-processing methods we can find out whether it is more effective to represent sentences as more generalized or as more specific.

### 3.2. Experiment Preparation Module

The initial phase in the system consists of preparation of data for the experiments. In this phase the datasets are prepared for an n-fold cross-validation test. This setting assumes that the provided data sets are first divided into n parts. Next, n-1 parts are used for training and the remaining one for testing. This procedure is performed n times so every part is used in both training and testing. The number of folds in n-fold cross-validation can be selected by the user with one simple parameter. For example, assuming the system is launched as

```
$ bash main.sh
```

The user can perform a 5-fold cross validation by adding a parameter 5, like below.

```
$ bash main.sh 5
```

The default experiment setup is 10-fold cross-validation. Setting the parameter to 1 will perform a test in which test data is the same as training data. A special additional parameter is `-100` in which the test is performed under the “leave-one-out” (LOO) condition. In this setting all instances except one are used for training. The one left is used as a test data. The test is performed as many times as the number of all instances in the data set. For example, LOO cross validation test on a set of 35 sentences will perform the test 35 times. To speed up the process of validation, all tests are performed in parallel.

### 3.3. Pattern List Generation Module

The next step consists of generation of all patterns from both provided corpora. It is possible to extract patterns of all lengths. However, an informal maximum length of n-grams used in the literature is either 5-grams (applied in Google N-gram Corpus English version<sup>4</sup>), or 7-grams (applied in Google N-gram Corpus Japanese version<sup>5</sup>). This length limit was set experimentally with an assumption that longer n-grams do not yield sufficiently high frequencies. The difference between English and Japanese comes from the fact that Japanese sentences contain more grammatical particles, which means that extracting an n-gram of the same length for both languages will come with less amount of meaning for Japanese. In our system we set the default as 6-grams, although the setting can be modified freely by the users.

<sup>4</sup> <http://catalog.ldc.upenn.edu/LDC2006T13>

<sup>5</sup> <http://googlejapan.blogspot.jp/2007/11/n-gram.html>

Based on the above assumptions the system automatically extracts frequent sentence patterns distinguishable for a corpus. Firstly, all possible n-grams are generated from all elements of a sentence. From all the generated patterns only those which appear in each corpus more than once are retained as frequent patterns appearing in a given corpus. Those appearing only once are considered as not useful and rejected as pseudo-patterns. The occurrences of patterns  $O$  are used to calculate pattern weight  $w_j$ . The normalized weight  $w_j$  is calculated, according to equation 1, as a ratio of all occurrences from one corpus  $O_{pos}$  to the sum of all occurrences in both corpora  $O_{pos} + O_{neg}$ . The weight of each pattern is also normalized to fit in range from +1 (representing purely positive patterns) to -1 (representing purely negative patterns). The normalization is achieved by subtracting 0.5 from the initial score and multiplying this intermediate product by 2.

$$w_j = \left( \frac{O_{pos}}{O_{pos} + O_{neg}} - 0.5 \right) * 2 \quad (1)$$

The weight is further modified in several ways. Two features are important in weight calculation. A pattern is more representative for a corpus when, firstly, the longer the pattern is (length  $k$ ), and the more often it appears in the corpus (occurrence  $O$ ). Thus, the weight can be modified by

- awarding length,
- awarding length and occurrence.

The formulas for modified pattern weight are represented for the “length awarded” weight  $w_l$  modification in equation 2, and for the “length and occurrence awarded” weight  $w_{lo}$  modification in equation 3

$$w_l = w_j * k \quad (2)$$

$$w_{lo} = w_j * k * O \quad (3)$$

The list of frequent patterns created in the process of pattern generation and extraction can be also further modified. When two collections of sentences of opposite features (such as “positive vs. negative”) are compared, a generated list of patterns will contain patterns that appear uniquely in only one of the sides (e.g. uniquely positive patterns and uniquely negative patterns) or in both (ambiguous patterns). Therefore the pattern list can be further modified by erasing:

- all ambiguous patterns,
- only those ambiguous patterns which appear in the same number on both sides<sup>6</sup>.

All of the above situations represent separate conditions automatically verified in the process of evaluation in the text classification task using the generated pattern lists. With these settings there is over a dozen of conditions for each of which the n-fold cross validation test is performed.

---

<sup>6</sup> Further called “zero patterns” as their normalized weight is equal to 0.

### 3.4. Text Classification Module

In the text classification experiment each analysed item (a sentence) is given a score. The score is calculated using the pattern list generated in the Experiment Preparation Module. There is a wide variety of algorithms applicable in text classification with which the calculation of scores can be performed. However, in the initial version of SPASS we used simple settings, which will be upgraded along the development of the system. Specifically, the score of a sentence is calculated as a sum of weights of all patterns matched for a certain sentence, like in equation 4.

$$\text{score} = \sum w_j, \quad (1 \geq w_j \geq -1) \quad (4)$$

In the future we will increase the number of applied classification algorithms, including all of the standard algorithms such as Neural Networks and Support Vector Machines. The use of a simple algorithm in the initial version allowed us to thoroughly test other parts of the system.

The score, calculated for each sentence, is automatically evaluated using sliding of the threshold window. For example, under the condition that above threshold 0 all sentences are considered positive, a sentence which got a score of 0.5 will be classified as positive. However, if the initial collection of sentences was biased toward one of the sides (e.g., more sentences of one kind, or the sentences were longer, etc.), there will be more patterns of a certain sort. Thus, to avoid bias in the results, instead of applying a rule of thumb, threshold is automatically optimized and all settings are automatically verified to choose the best model.

### 3.5. Contingency Table Generation Module

After the scores are calculated for all sentences the system calculates the contingency table. Depending on whether the sentence actually was positive or negative (all test sentences represent Gold Standard) the score becomes either True Positive (TP), False Positive (FP), True Negative (TN) or False Negative (FN). By calculating this for all sentences we get the contingency table for one test set (one threshold). The calculation is performed automatically for all thresholds, by sliding the threshold window by 0.1. From the contingency tables we calculate final scores using five measures. These are Precision, Recall, balanced F-score, Accuracy, Specificity and phi-coefficient. Finally, the scores are averaged for all folds from the n-fold cross validation. The average scores are a basis for further post processing.

### 3.6. LaTeX Table Generation Module

From all the scores we generate a table in the LaTeX format using a custom Perl script. The table is provided in a form already usable in a scientific paper. It contains all scores for all five measures within the whole threshold span, for experiments performed under all possible conditions (pattern list modifications and weight calculations). The table containing

all information is a product of one whole single experiment and usually covers one page of an A4 or Letter type document in the LaTeX format. An example of such table is represented in an Appendix at the end of the paper, and it represents the results obtained in one of the experiments in which the described system was used.

### 3.7. Graph Generation Module

All scores are stored in `.dat` files readable by Gnuplot<sup>7</sup>, a standard tool for generation of high quality graphs available under most operating systems. We applied a custom Perl script to automatically generate graphs in Gnuplot for visualization of comparisons of different groups of results. One graph is generated for one kind of measure (Precision, Recall, F-score, etc.) for one compared group of results. Below we explain the compared groups of results. The graph for comparison of different weight calculations (normalized weight, length awarding, length and occurrence awarding) is drawn for:

- basic settings (with the following results compared in one graph: all patterns, length awarded all patterns, length and occurrence awarded all patterns),
- zero deleted (zero deleted, length awarded zero deleted),
- ambiguous deleted (ambiguous deleted, length awarded ambiguous deleted).

The graph for comparison of different pattern modification lists (all patterns, zero-patterns deleted, ambiguous patterns deleted) is drawn for:

- basic settings (all patterns, zero deleted, ambiguous deleted),
- length awarded (length awarded all patterns, length awarded zero deleted, length awarded ambiguous deleted).

Additionally, for all the above conditions separately, the script draws graphs containing both Precision and Recall together in one graph. This allows comparison of Break-Even Points (BEP) for all results. Also, a graph containing all results together for one measure is drawn to compare the results in a wider context. Examples of such graphs are represented in an Appendix at the end of the paper, which represents the results obtained in one of the experiments in which SPASS was used.

### 3.8. Result Analysis and Sentence Template Generation Module

The calculated scores are automatically analysed according to simple instructions. This module looks at the scores and compares them across the whole threshold span. It verifies the following items:

- Which modification of the algorithm was better for most of the threshold span (for all five scores);
- Which version obtained the highest BEP (in case of more than one BEP the highest one is used; calculated for Precision and Recall);
- Which version achieved the highest possible score (for all scores);
- Which version was more balanced (an algorithm which achieved high score only for one threshold is considered as generally worse than an algorithm which achieved slightly worse scores, but generally high on the whole threshold span).

---

<sup>7</sup> <http://www.gnuplot.info/>

Next, the results of this verification are imported into simple sentence templates, such as

“The highest [Precision / Recall / F-score] of all was achieved by the [zero deleted / ambiguous deleted / ...] version of the algorithm”,

or

“When it comes to [weight calculations / pattern list modifications / ...], the highest [BEP / balanced F-score / Accuracy / ...] was achieved by [zero deleted / ambiguous deleted / ...]”.

### 3.9. Most Useful Pattern Extraction Module

One of the disadvantages of using standard classification algorithms, such as SVM, or Neural Networks, and making them inapplicable in traditional linguistic and corpus linguistic studies, is the fact that the analysed sentences are converted into a set of vectors. This hinders detailed analysis of the linguistic data. Therefore, we added a module allowing extraction of the most useful patterns for further linguistic analysis. During each fold in each cross validation experiment most useful patterns are extracted in the pattern matching and sentence scoring procedure. All patterns from all experiments are collected together and the patterns which appeared more than once are retained. This provides a general filtered list of patterns which were most useful during all experiments. This function has already proved to be useful by Ptaszynski et al. [3]. In their research on extracting emotive patterns from sentences they showed that patterns included in such list contained many items from their previously hand-crafted lexicon of exclamations and interjections. This suggests that it could be possible to automatically bootstrap generation of lexicons with this module. Moreover, [6] showed that such most often used pattern lists reveal not only known but also new linguistic knowledge. In their work on statistical analysis of conversations, they compared most frequent patterns from different groups of conversations between people of different age, gender, social distance and status. They found out that apart from known expressions typical for male or female interlocutors, the lists contained previously unknown patterns revealing social distance. Such patterns were not bound by any previously known linguistic rules, but in practice were used only by one group in specific conditions (e.g., only in conversations between friends, or only between people who first met).

## 4. Evaluation

Due to the lack of literature on research closely related to ours, no standards have been previously proposed regarding the means of evaluation of systems like the one described here. Therefore, we needed to propose our own evaluation means. One of the popular evaluation means usable in many research is a usability questionnaire. Since the system is launched

by one command in a command line and the whole computation process takes place in the background, we could not ask our users questions about features such as “usability” (whether the system is easy to use), or GUI intelligibility. Instead we asked about other features or functions that might be useful to implement in the system. In the second means of evaluation we were guided by similar words to the ones opening the Introduction to this paper. Namely, “If the system is so helpful, what would be the acceptance rate for papers written with the use of it?” We understand that it is not the most objective way to evaluate the system due to many factors being involved, such as writing skills of the authors, acceptance rate of the conference etc. However, we decided to apply it as this is the most practical and an ultimate way of evaluation.

As for the first evaluation means, we performed free conversations with the present users of the system (twelve people, students and researchers of different age and career stage). From those conversations we extracted the following remarks. Having so many experiment results produced by the system it is laborious to perform statistical significance tests. One of the reasons we did not implement this feature in the initial version of the system is that there is a large number of different significance tests, depending on the type of data applied in the research. Therefore, in the future we plan to either allow users to choose their test, or, which would be more desirable, find a method for automatic selection of a statistical significance test depending on the data. Another useful function would be to generate presentation slides, at least partially. This could be easily implemented as the system generates all materials in a LaTeX template. The third function worth implementation would be email notification when the whole process is finished. Depending on the amount of data, the whole process could take a few seconds, an hour, or even a day or more, especially, when the user tries to analyse BigData. It could be tiresome to sit and wait for the results. Therefore an email notification would be a useful feature. However, this would mean the necessity of additional settings (ensuring the server has appropriate generic software to send a simple email message), while initially we meant the system to work “out of the box”.

As for the second means of evaluation, at the time of writing, there have been several papers accepted to different conferences written with the use of SPASS. First three of them analyse emotional and non-emotional sentences [3–5]. In this research our system helped confirm that completely automatic approach to extraction of emotional patterns from sentences can give similarly good results to tools developed manually. In the second set of publications [6, 7], the system was applied in a conversation analysis task to find similarities in conversations between interlocutors of different age, gender, social distance and status. Interestingly, the system extracted several linguistic rules (confirmed statistically) which were previously unknown. Finally, in the last set of publications [8, 9] the system was applied in the analysis of future related expressions for the task of future prediction from trend information. The experiments performed by the system helped prove that sentences referring to the future contain frequent patterns, while patterns in other sentences (non-future related, such as present, past or not time related) are sparse and scattered. This proved that “future-referring sentences” can be treated and analysed as one separate kind of sentences. This discovery helped Nakajima et. al [8] choose appropriate methods for further analysis of their data (e.g., grounded in linguistics rather than in information extraction, or data mining).



## 5. Conclusions

Research is a process requiring two kinds of abilities – creativity and precision. The tasks requiring creativity include preparing detailed analysis of experiment results or writing a convincing discussion. The tasks which are not creative, but requiring focus and precision include laborious preparation of data for experiments, performing the experiments and preparing materials for writing a scientific paper, such as tables or graphs. Computers are poor at creative tasks, but good at laborious non-creative tasks. People on the other hand are experts when it comes to creativity, but the passion for research could be severely impaired by the laborious tasks included in the everyday research drill. Therefore to ease the researchers, and allow them focus on the creative part of the research process, we developed SPASS – a system which helps performing the laborious part of the research. SPASS is a system for the support of research and writing of scientific papers. The system prepares the data for the experiments, automatically performs the experiments and from the results calculates the scores according to five different kinds of measures (Precision, Recall, etc.). It also creates tables in the LaTeX format containing all the results, draws graphs depicting and informatively comparing each groups of results and generates descriptions of those results using sentence templates. And what is most important, it does all that with one single command.

## 6. Future work

In the near future we plan to upgrade the system further and implement additional functions. First of all, we plan to add various classification algorithms for more thorough evaluation. We also plan to include automatic calculation of statistical significance of results. We also plan to perform the n-fold cross validation multiple times to further improve the objectivity of the results. A useful function would be an e-mail notification about the finalization of the whole experiment process so the researchers did not have to wait for the results. When it comes to the descriptions of experiment results, at this point they are generated as generic sentences containing certain knowledge. In the near future we plan to perform automatic summarization of sentence templates to increase the readability and informativeness of the descriptions. This would move the research from paper writing support one step toward an actual automatic paper generation. We also plan to implement a script for generation of presentation slides in the LaTeX template from the results description, similarly to Shitaba and Kurohashi [2]. At present the system handles only two classes of labels, or two corpora differing in a certain feature (positive/negative). In the future we plan to perform different kinds of data as well, especially multi-label classification, with classes either related to each other, or unrelated. This could help deal with not only binary classification-like corpora comparison (such as sentiment analysis), but also wider scale analysis, such as extracting expressions specific for certain emotion types (fear, sadness, joy etc.), or gradual sentiment (for example product reviews on Amazon<sup>8</sup>). This would help extract pragmatic generalizations from corpora, similarly to Potts and Schwarz [10], and could contribute greatly to the emerging field of computational pragmatics.

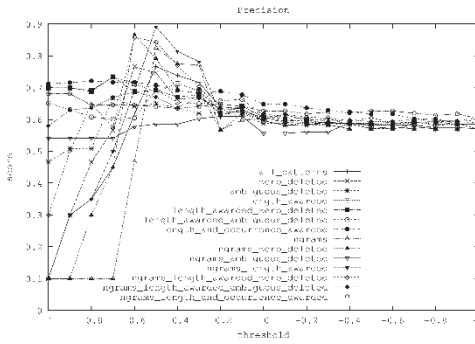
---

<sup>8</sup> <http://www.amazon.com/>

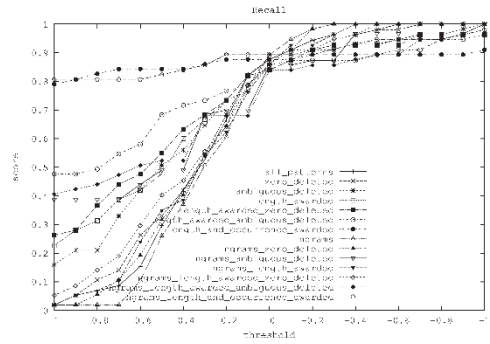
## References

- [1] Hidetsugu Nanba, Noriko Kando, Manabu Okumura, *Classification of research papers using citation links and citation types: Towards automatic review article generation*, [in:] Proceedings of 11th ASIS SIG/CR Classification Research Workshop, 2000, 117-134.
- [2] Tomohide Shibata, Sadao Kurohashi, *Automatic slide generation based on discourse structure analysis*, [in:] Proceedings of IJCNLP, Springer Berlin Heidelberg, 2005, 754-766.
- [3] Ptaszynski M., Fumito Masui, Rzepka R., Kenji Araki, *Automatic Extraction of Emotive and Non-emotive Sentence Patterns*, [In:] Proceedings of The Twentieth Annual Meeting of The Association for Natural Language Processing (NLP2014), Sapporo, Japan, 2014, 868-871.
- [4] Ptaszynski M., Fumito Masui, Rzepka R., Kenji Araki, *Emotive or Non-emotive: That is The Question*, [in:] Proceedings of 5th Workshp on Computational Approaches to Subjectivity, Sentiment & Social Media Analysis (WASSA 2014), Baltimore, USA, 2014, 59-65, held in conjunction with The 52nd Annual Meeting of the Association for Computational Linguistics (ACL 2014), June 22–27.
- [5] Ptaszynski M., Fumito Masui, Rzepka R., Kenji Araki, *Detecting emotive sentences with pattern-based language modelling*, [in:] Proceedings of the 18th International Conference on Knowledge-Based and Intelligent Information & Engineering Systems – KES2014, 484-493, Gdynia, Poland 2014.
- [6] Ptaszynski M., Dai Hasegawa, Fumito Masui, Hiroshi Sakuta, Eijiro Adachi, *How Differently Do We Talk? A Study of Sentence Patterns in Groups of Different Age, Gender and Social Status*, [in:] Proceedings of The Twentieth Annual Meeting of The Association for Natural Language Processing (NLP2014), Sapporo, Japan 2014, 3-6.
- [7] Ptaszynski M., Dai Hasegawa, Fumito Masui, *Women Like Backchannel, But Men Finish Earlier: Pattern Based Language Modeling of Conversations Reveals Gender and Social Distance Differences*, [in:] Samsung HLT Young Researchers Symposium, 9th International Conference on Natural Language Processing (PoITAL 2014), paper ID: 02, Warszawa, Poland 2014.
- [8] Yoko Nakajima, Ptaszynski M., Hirotohi Honma, Fumito Masui, *Investigation of Future Reference Expressions in Trend Information*, [in:] Proceedings of the 2014 AAAI Spring Symposium Series, “Big data becomes personal: knowledge into meaning For better health, wellness and well-being”, Stanford, USA 2014, 31-38.
- [9] Yoko Nakajima, Ptaszynski M., Hirotohi Honma, Fumito Masui, *Extraction of Future Reference Expressions in Trend Information*, [in:] The Proceedings of 24th Intelligent System Symposium (FAN2014), Kitami, Japan 2014.
- [10] Potts Ch., Schwarz F., *Exclamatives and heightened emotion: Extracting pragmatic generalizations from large corpora*, Ms., UMass Amherst, 2008.

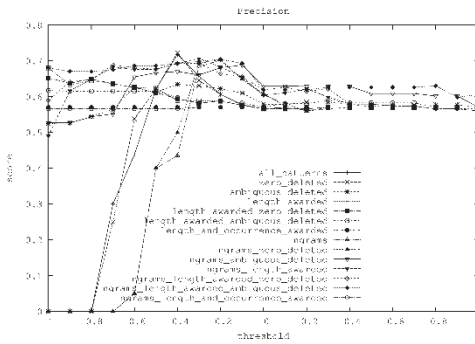
Appendix 1: Graphs representing experiment results from Ptaszynski et al. [4]



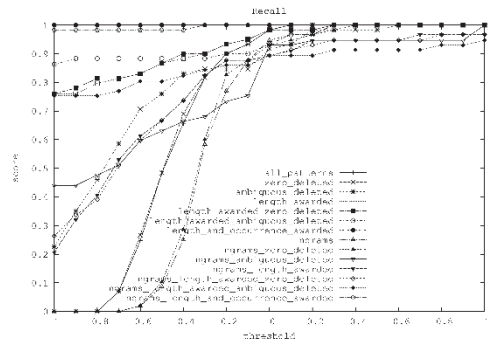
(a) Precision comparison for tokenized dataset.



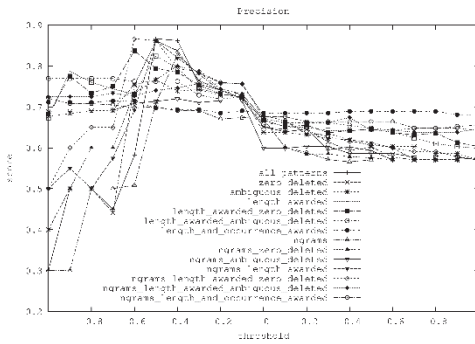
(b) Recall comparison for tokenized dataset.



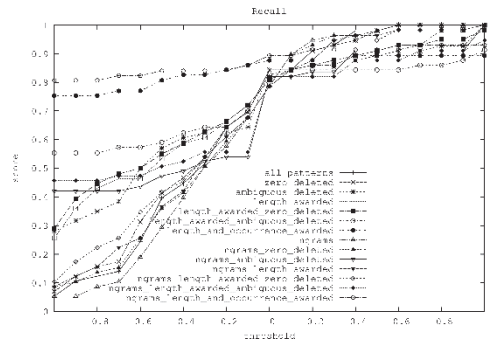
(c) Precision comparison for POS-tagged dataset.



(d) Recall comparison for POS-tagged dataset.



(e) Precision comparison for tokenized dataset with POS tags.



(f) Recall comparison for tokenized dataset with POS tags.

**Appendix 2:** Experiment results from Ptaszynski et al. [4],  
corresponding to graphs in Appendix 1

ngrams																						
Threshold	1.00	0.90	0.80	0.70	0.60	0.50	0.40	0.30	0.20	0.10	0.00	-0.10	-0.20	-0.30	-0.40	-0.50	-0.60	-0.70	-0.80	-0.90	-1.00	
Precision	0.10	0.10	0.10	0.47	0.82	0.77	0.77	0.57	0.60	0.60	0.59	0.59	0.58	0.57	0.57	0.57	0.57	0.57	0.57	0.57	0.57	0.57
Recall	0.02	0.02	0.02	0.02	0.10	0.26	0.37	0.51	0.61	0.78	0.89	0.95	0.98	1.00	1.00	1.00	1.00	1.00	1.00	1.00	1.00	1.00
F-score	0.03	0.03	0.03	0.03	0.17	0.40	0.50	0.61	0.59	0.68	0.72	0.73	0.73	0.74	0.73	0.73	0.73	0.73	0.73	0.73	0.73	0.73
ngrams zero deleted																						
Threshold	1.00	0.90	0.80	0.70	0.60	0.50	0.40	0.30	0.20	0.10	0.00	-0.10	-0.20	-0.30	-0.40	-0.50	-0.60	-0.70	-0.80	-0.90	-1.00	
Precision	0.10	0.10	0.30	0.45	0.87	0.79	0.70	0.57	0.62	0.60	0.58	0.59	0.58	0.57	0.57	0.57	0.57	0.57	0.57	0.57	0.57	0.57
Recall	0.02	0.02	0.06	0.11	0.19	0.32	0.40	0.54	0.64	0.82	0.88	0.91	0.98	1.00	1.00	1.00	1.00	1.00	1.00	1.00	1.00	1.00
F-score	0.03	0.03	0.10	0.17	0.32	0.45	0.51	0.61	0.60	0.71	0.71	0.71	0.74	0.74	0.73	0.73	0.73	0.73	0.73	0.73	0.73	0.73
ngrams ambiguous deleted																						
Threshold	1.00	0.90	0.80	0.70	0.60	0.50	0.40	0.30	0.20	0.10	0.00	-0.10	-0.20	-0.30	-0.40	-0.50	-0.60	-0.70	-0.80	-0.90	-1.00	
Precision	0.54	0.54	0.54	0.54	0.58	0.59	0.59	0.60	0.61	0.61	0.56	0.56	0.56	0.56	0.56	0.58	0.58	0.58	0.58	0.57	0.57	0.57
Recall	0.39	0.39	0.39	0.39	0.44	0.49	0.49	0.49	0.68	0.70	0.70	0.86	0.86	0.87	0.87	0.97	0.97	0.97	0.97	0.97	0.97	1.00
F-score	0.45	0.45	0.45	0.45	0.50	0.53	0.53	0.64	0.65	0.65	0.67	0.67	0.68	0.68	0.73	0.73	0.73	0.73	0.73	0.72	0.72	0.73
ngrams length awarded																						
Threshold	1.00	0.90	0.80	0.70	0.60	0.50	0.40	0.30	0.20	0.10	0.00	-0.10	-0.20	-0.30	-0.40	-0.50	-0.60	-0.70	-0.80	-0.90	-1.00	
Precision	0.10	0.30	0.35	0.50	0.69	0.89	0.81	0.78	0.61	0.63	0.60	0.62	0.60	0.60	0.58	0.58	0.58	0.58	0.57	0.57	0.57	0.57
Recall	0.02	0.05	0.07	0.10	0.24	0.35	0.39	0.54	0.62	0.76	0.86	0.93	0.93	0.96	1.00	1.00	1.00	1.00	1.00	1.00	1.00	1.00
F-score	0.03	0.09	0.12	0.17	0.36	0.50	0.52	0.64	0.62	0.69	0.71	0.74	0.73	0.74	0.74	0.74	0.74	0.74	0.73	0.73	0.73	0.73
ngrams length awarded zero deleted																						
Threshold	1.00	0.90	0.80	0.70	0.60	0.50	0.40	0.30	0.20	0.10	0.00	-0.10	-0.20	-0.30	-0.40	-0.50	-0.60	-0.70	-0.80	-0.90	-1.00	
Precision	0.30	0.50	0.65	0.57	0.86	0.84	0.77	0.70	0.62	0.62	0.61	0.62	0.61	0.61	0.60	0.61	0.59	0.58	0.57	0.57	0.57	0.57
Recall	0.05	0.09	0.14	0.19	0.30	0.40	0.45	0.56	0.64	0.79	0.86	0.91	0.91	0.95	0.96	1.00	1.00	1.00	1.00	1.00	1.00	1.00
F-score	0.09	0.15	0.23	0.29	0.44	0.55	0.57	0.62	0.63	0.70	0.71	0.73	0.73	0.74	0.74	0.75	0.74	0.74	0.73	0.73	0.73	0.73
ngrams length awarded ambiguous deleted																						
Threshold	1.00	0.90	0.80	0.70	0.60	0.50	0.40	0.30	0.20	0.10	0.00	-0.10	-0.20	-0.30	-0.40	-0.50	-0.60	-0.70	-0.80	-0.90	-1.00	
Precision	0.58	0.63	0.64	0.67	0.69	0.67	0.64	0.67	0.64	0.63	0.62	0.61	0.60	0.59	0.60	0.59	0.59	0.60	0.60	0.60	0.60	0.60
Recall	0.41	0.42	0.44	0.47	0.51	0.52	0.52	0.68	0.68	0.68	0.84	0.84	0.86	0.86	0.88	0.89	0.89	0.95	0.95	0.97	1.00	1.00
F-score	0.48	0.51	0.52	0.55	0.58	0.59	0.57	0.67	0.66	0.65	0.71	0.70	0.71	0.70	0.71	0.71	0.71	0.71	0.74	0.73	0.74	0.75



DITTAPON SANITIN, HIROSHI MASUI\*

## INTEGRATION OF THE RURAL ROADS DATABASE IN THAILAND WITH THE PARALLEL COMPUTING ENVIRONMENT

---

## INTEGRACJA BAZY DANYCH DRÓG WIEJSKICH ZE ŚRODOWISKIEM OBLICZEŃ RÓWNOLEGŁYCH

### Abstract

We present a solution to integrate the database of the Department of Rural Roads (DRR) in Thailand and to utilize the data on the environment of the parallel computing. We define and classify the usage of the data according to the level of the collaboration for different sources. For the user interface of the integration, we provide a web-based environment with the technique of the HTML5.

*Keywords: roads database, HTML5, parallel computing*

### Streszczenie

Prezentujemy rozwiązania dotyczące integracji bazy danych Departamentu Dróg Wiejskich (DRR) w Tajlandii oraz wykorzystywania danych w środowisku obliczeń równoległych. Definiujemy i klasyfikujemy wykorzystanie danych zgodnie z poziomem współpracy dla różnych źródeł. Dla interfejsu użytkownika tej integracji zapewniamy środowisko webowe z technologią HTML5.

*Słowa kluczowe: drogowe bazy danych, HTML5, obliczenia równoległe*

---

\* M.Sc. Dittapon Sanitin, Prof. Hiroshi Masui, Kitami Institute of Technology, Japan.

## 1. Introduction

Transport developments directly contribute to an improvement in standards of living. Roads provide access to schools and hospitals and connect communities. Urban mass transits, which are public transportations in cities, save time and expense. Inter-city passenger transport, which is provided by highways, makes it more convenient for people to travel either for pleasure or business. In addition, transport development can help to facilitate economic development, for example, by reducing the costs of doing business.

Among them, land transport is the most important mode of transport in Thailand accounting for 99% of total domestic passenger movement and 88% of domestic freight transport in 2006. Currently road is the most dominant mode of transport for both passengers and freight with the modal share of 85% and 86%, respectively, see Fig. 1. About 98.5% of the main roads and collector road in Thailand are paved. The quality is considered moderate, with the International Roughness Index (IRI) of around 3.5-4.5. However, the average IRI has decreased over the years [1]. Passenger transport in Thailand are dominated by personal vehicles (primarily cars and pickup trucks) and motorcycles. National personal vehicle ownership (expressed as in-use vehicles per thousand population) has been growing at an average of 8%–10% per year, and this trend is expected to continue. With the continuing per capita income growth, it has been expected that ownership of four-wheel vehicles will grow faster than motorcycle ownership [2]. Since the size of the four-wheel vehicle is much bigger than that of a motorcycle, it is necessary to plan an appropriate strategy to maintain the roads and to extend them.

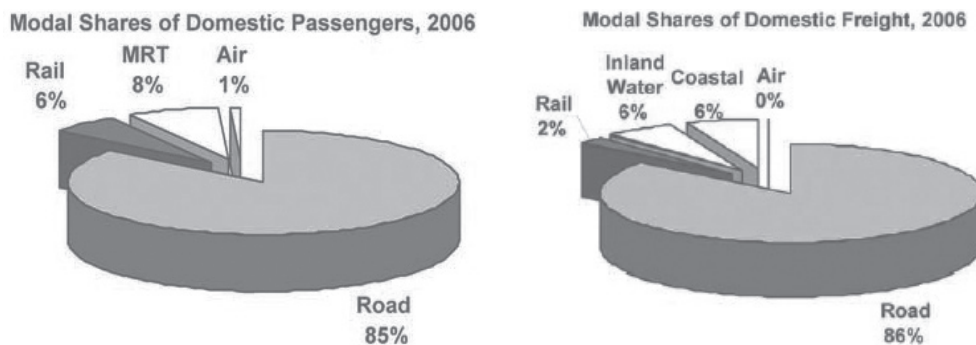


Fig. 1. Models shares of domestic passenger and domestic freight in Thailand 2006, Ministry of transport

The total road network in Thailand is estimated to be 400,000 kilometers (km) long. That can be classified into 3 types, namely, 1) Highways 2) Rural Roads and 3) Local Roads. Highways are arterial roads that connect regions in Thailand passing through several provinces providing high mobility with limited access, and the department of highways (DOH) oversees the Highways. Local roads, in contrast, provide access to all residences with compromised mobility and are overseen by the local administrative organization. Rural

Roads are classed in-between Highways and Local Roads and are overseen by the Department of Rural Roads (DRR). More precisely, Rural Roads connect local roads to highways and provide smooth traffic from and to those roads. Also, the function of the Rural Roads is that the road users need not get onto a highway to access the destination nearby the origin. They can use the rural roads, which are systematically organized as local regional networks so as to reach their destinations. DOH and DRR are managed by the Ministry of Transport, which is the department designated to formulate the policies for development, construction and regulation of the domain of Thailand. The Ministry of Transport oversees the land, marine, and air transportation systems on the basis of adequate services and decides the direction of the accessibility, efficiency, cost-effectiveness and fairness. On the other hand, the local administrative organization is managed by the Ministry of Interior, which has a different mission from the Ministry of Transport. Since the department of Local Roads lack of expert staff and budgets for construction and maintaining compared to Highways or Rural Roads, the main mission of DRR is being a technical mentor for local governments.

## 2. Overview of the integration of roads data

Thailand is faced with specific limitations in road-transportation on top of other major problems such as high traffic volume, the geometry of roadways, lack of parking space for large vehicles, noise from the vehicles, pollution and heavy fuel consumption due to the heavy traffic. Under these circumstances, we have to consider the following points:

- (1) A truck may not pass between two states, and goods must be transferred to other trucks that belong to a neighboring country. This generates extra costs in addition to a time-consuming issue with a high risk that products may be damaged;
- (2) Overloading trucks may result a high road-maintenances cost;
- (3) Laws and regulations relating to logistics and the transportation sector have not been enforced strictly up to international standards [3].

DRR has a main mission in order to plan for managing the rural roads around the country, that spanned for 40,000 km long, with a design and construction of the rural roads. In addition, DRR has to be a technical mentor for local governments who have to take care of the other 300,000 km of local roads nationwide. In order to develop rural roads effectively, the department applies both road engineering and a social science knowledge. Local Roads are always allowed to participate in all processes of the rural roads development. With the help of the participant of the Local Roads, DRR can understand the real needs of people and can carefully balance engineering with social requirements.

However, due to human resource constraints, DRR decided to introduce the information technologies to facilitate works as integrated. Information technologies we would like to apply to the work of DRR is divided into two categories; (I) Database System and (II) Geographic Information System. By using these solutions for the problems we faced in handling dramatically increasing data, which is sometimes inconsistent and inaccurate in the process of registration and duplication. The main reason for these problems is that DRR does not have sufficient collaboration from other bureaus who collect data and the format to collect data. Furthermore, data recorded into the road database systems is not so well organized. Therefore, it is difficult to analyse and convert this data into information for decision making.



Hence, the data integration is expected to be able to solve the problems concerned with moving, transforming, and consolidating information from various parts. The project's elements, i.e. systems, databases, applications, files, and web services, are going to be applied for the purpose of regulating and integrating sources of the road data. For the integration effort to be successful, it is important to use a formal sequence of steps:

- (i) Identifying data elements shared with bureaus. Other difficulties such as the redundancy and inconsistency of the data and modelling conflicts are examined at the same time;
- (ii) Fixing the above problems in terms of data consistency;
- (ii) Constructing metadata with the integration effort by accumulating and normalizing the database;
- (iv) Based on the metadata and related database, an interface to utilize this data should be constructed.

The purpose of work is to learn the difference and the common part of the roads data and to find a solution for the data integration. Further, with the help of the integrated data, we will proceed to consider the optimization of the road management of DRR in Thailand under the parallel computing facility.

For the implementation of the system, we use MySQL for the database and an HTML5 technique for the web interface. In most organizations today, data and other information is managed in isolated databases by independent teams using various data management tools. This is also true for DRR. In DRR, each bureau has created a database for use in their own projects. For example, the bureau of maintenance has created Central Rural roads Database management system (CRD) and Flood Management System (FMS), and the bureau of local roads development have created Central Local roads management Database system (CLD). The information and technology center also has created Geographic Information System (GIS). By surveying these circumstances, the integrated database in DRR can be classified into 3 types, 1) database for the main project, 2) database for various asset and resources management, 3) database for budget management.

Here, as the first step solution for integration of the databases, we will unify only road databases such as GIS, CRD and CLD, since these are used for supporting the main project in DRR as shown in Fig. 2.

To integrate road databases for the purpose of finding the relation between conditions of roads and traveling of masses of people, we examine the consistency in the duplication and how the data is collected. For example, the primary key is assigned to the ID number of the road. In that case, a difference may occur in the format of the ID number, i.e. numeric or alphanumeric. Further, even if the same format is used, the same road may have different numbers in different databases. Also, we need to check whether the data format of the road length and definition of the starting and end point is the same or not. A point in this examination is that we focus on the name of the roads, the unit of length (meter or kilometer) and the ID number to identify the road. After that, we have to create a master database constructed on MySQL.

In Fig. 3, we show an example of a unified road table in the master database by collecting the road's ID, "road code" and "road name" from the databases; GIS, CRD and CLD. Here, the "road code" is used as the name of the road, and "road name" shows the starting and end points of the road. As for the primary key of the unified table, we defined a new ID number in the format of "r#####", since the ID numbers in three databases are different numbers and the format.

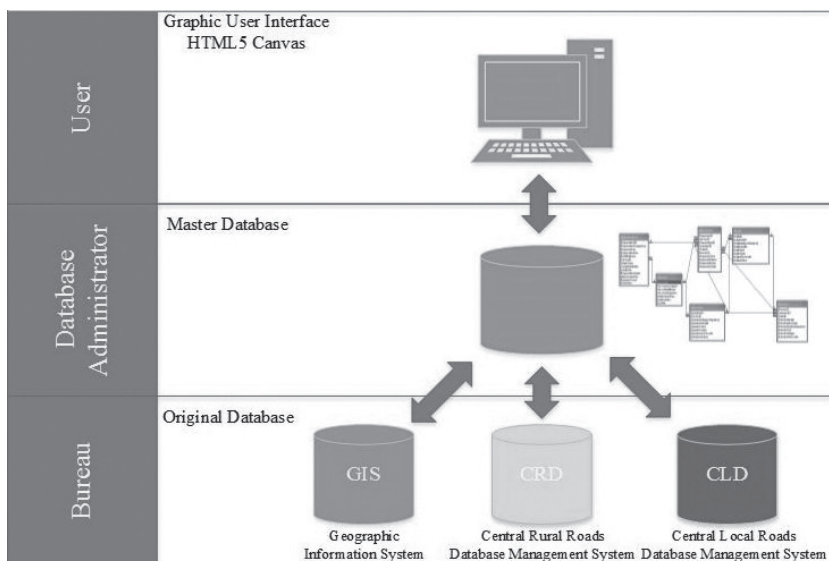


Fig. 2. (Color online) Concept of Integration Database in Department of Rural Roads

### Master Database (Table. "road")

No.	Mroad_id	link_id	gid	way_id	Road_code	Road_name
1	r140001	10023	10023	-	กจ.3086	แยกทางหลวงหมายเลข 323 (กม.ที่ 1+400) - บ้านหนองขาว
2	r140002	10028	10028	-	กจ.3095	แยกทางหลวงหมายเลข 323 (กม.ที่ 114+400) - บ้านดอนกระเพรา
3	r140003	10029	10029	-	กจ.3096	แยกทางหลวงหมายเลข 323 (กม.ที่ 98+650) - บ้านองค์รักษ์
4	r140004	10030	10030	-	กจ.3097	แยกทางหลวงหมายเลข 323 (กม.ที่ 79+166) - บ้านหนองรี
5	r140005	10031	10031	-	กจ.4002	แยกทางหลวงหมายเลข 3492 (กม.ที่ 51+100) - บ้านหนองบัว
6	r140016	-	-	34374	กจ.ถ1-0001	บ.ลุ่มดงกระเบา - บ.ถ้ำ
7	r140017	-	-	34341	กจ.ถ1-0002	สายบ้านพลเสียบ - บ้านจันลุย
8	r140018	-	-	34595	กจ.ถ1-0003	บ.ดอนเจดีย์ - หนองขาว
9	r140019	-	-	34423	กจ.ถ16-001	พนมทวน - บ้านม้อหว้า
10	r140020	-	-	34323	กจ.ถ1-0015	บ.พังซีว - อ้อกระทุง

No.	link_id	road_id	road_name
1	10023	กจ.3086	แยกทางหลวงหมายเลข 323 (กม.ที่ 1+400) - บ้านหนองขาว
2	10028	กจ.3095	แยกทางหลวงหมายเลข 323 (กม.ที่ 114+400) - บ้านดอนกระเพรา
3	10029	กจ.3096	แยกทางหลวงหมายเลข 323 (กม.ที่ 98+650) - บ้านองค์รักษ์
4	10030	กจ.3097	แยกทางหลวงหมายเลข 323 (กม.ที่ 79+166) - บ้านหนองรี
5	10031	กจ.4002	แยกทางหลวงหมายเลข 3492 (กม.ที่ 51+100) - บ้านหนองบัว
6	10047	กจ.ถ16-001	แยกทางหลวงหมายเลข 3220 (กม.ที่ 17+000) - บ้านหนอง

GIS (Table. "public.road")

No.	gid	road_code	road_name
1	10023	กจ.3086	แยกทางหลวงหมายเลข 323 (กม.ที่ 1+400) - บ้านหนองขาว
2	10028	กจ.3095	แยกทางหลวงหมายเลข 323 (กม.ที่ 114+400) - บ้านดอนกระเพรา
3	10029	กจ.3096	แยกทางหลวงหมายเลข 323 (กม.ที่ 98+650) - บ้านองค์รักษ์
4	10030	กจ.3097	แยกทางหลวงหมายเลข 323 (กม.ที่ 79+166) - บ้านหนองรี
5	10031	กจ.4002	แยกทางหลวงหมายเลข 3492 (กม.ที่ 51+100) - บ้านหนองบัว
6	10047	กจ.ถ16-001	แยกทางหลวงหมายเลข 3220 (กม.ที่ 17+000) - บ้านหนอง

CRD (Table. "Link")

No.	way_id	way_code	way_name
1	34374	กจ.ถ1-0001	บ.ลุ่มดงกระเบา - บ.ถ้ำ
2	34341	กจ.ถ1-0002	สายบ้านพลเสียบ - บ้านจันลุย
3	34595	กจ.ถ1-0003	บ.ดอนเจดีย์ - หนองขาว
4	34423	กจ.ถ16-001	พนมทวน - บ้านม้อหว้า
5	34323	กจ.ถ1-0015	บ.พังซีว - อ้อกระทุง
6	34565	กจ.ถ1-0018	บ.หนองหว้า - บ้านหนอง

CLD (Table. "way")

Fig. 3. (color online) Example of a unified road table as the master database

In the process of integration, we need to collect various road data such as road name, code, connection point with other road, structure and condition of roads and so on from the original database. In order to remain the same scheme to accumulate road data from the accrual of road conditions, we will not change or modify anything in the original database. Therefore, the metadata is necessary to be defined so as to unify the road conditions and capacities of all road databases (GIS, CRD and CLD).

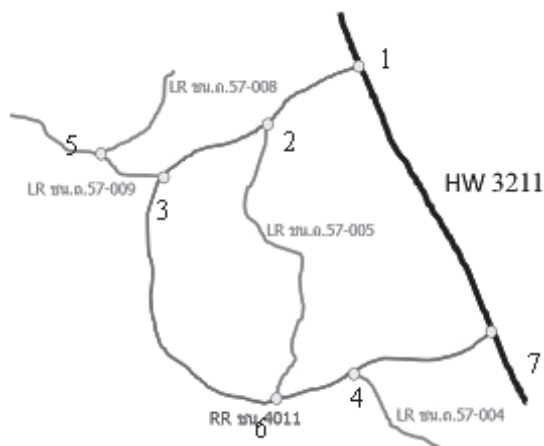


Fig. 4. (color online) Roads network and connection point

In Fig. 4 we show an example of the structure of the road network in Thailand. Thick black line (color online) shows the highway “HW3211”. A Rural Road, “No. 4011” connects to the highway HW3211 at the connecting point No. 1. Three Local Roads; “No. 57-005”, “No. 57-009” and “No. 57-004” connect to the Rural Road No. 4011 at points No. 2, 3 and 4, respectively. Also, a Local Road “No. 57-008” connects to the Local Road No. 57-009 at point No. 5. In the original databases; GIS, CRD and GLD, the attribute “road name” corresponds to the connection of the roads. However, the format of the road name is not appropriate to express the connection. Because, the road name is defined as the form as “starting point (point of the edge of the road + distance from the edge) – end point (name of the province)”. Hence, while the starting point is clearly defined, the end point is unclear, and we can only know the name of the province (village or town) of the end point.

By considering the situation of the road name, we construct a connection point table as shown in Table 1. This table has the attributes of the “connecting point ID”, “road 1” (the ID of the road) and “road 2” (the ID of the road: connected to road 1). Using this table, we can store the topological structure of the road connection to the unified database.

There is one thing we have to be more careful: it is whether the RDB (relational database) is appropriate to express the road connection. Usually, the connection of elements, such as CAD data, is treated in the object database. In our case, the elements are the roads themselves, and the structure of the table with the RDB scheme may become more complicated. Therefore, we define the connection as the point of two roads, which are identified by the road ID.

The relation from the unified table to each original database is constructed with road IDs, which have different names and numbers in GIS, CRD and CLD, in terms of the foreign key. The connection point is also a sub-table of the unified table through the road ID. So far, we only consider the integration of the three databases; GIS, CRD, and CLD. This procedure goes on to include other databases, such as Highway and Local Roads.

Information of the road connection provides us with a useful knowledge and a way to utilize the road data. On the table of the connection point, we define the connecting points using the two crossing roads. The roads contain information for the traffic, properties of

the road for instance, lengths of lane and its shape, surface type, condition. We express the connection of roads in terms of the “nodes” and “links”. Here, connecting points correspond to the nodes, which contain the population of the city around the connecting point, and roads are links.

Table 1

Example of connection point table

No.	Connection point ID	Road 1	Road 2
1	P14000001	HW3211	RR 4011
2	P14000002	RR 4011	LR 57-005
3	P14000003	RR 4011	LR 57-009
4	P14000004	RR 4011	LR 57-004
5	P14000005	LR 57-009	LR 57-008

Under this correspondence, we can simplify the topology of roads into the nodes and links as shown in Fig. 5. In this example, the thickness of the links shows the traffic. Other properties of the roads can be added to the link values. Similarly, the values of the nodes can be treated as the node values. Hence, the topological connection of nodes with links can simulate the situation of the data of DRR.

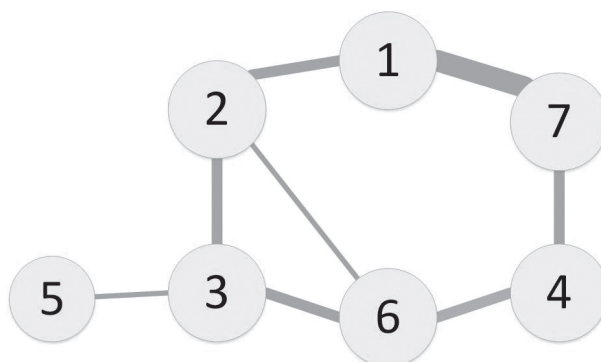


Fig. 5. Schematic figure of the road network

The remaining part of the development of the system is to design and construct the interface for making the connection of the nodes. For the interface part of the system, we implement the system on the web-interface using the HTML Canvas. Using the Canvas, the connection of links between the nodes can be easily done by an intuitive click-and-drag operation on the web browser. In the case for planning the re-construction or optimizing the road geometry and/or topological structure, we can change them with interactive operations.

As an advantage of Canvas, we can retrieve the structure value for the topological shape of the connection of the links and nodes. Once we obtain the structure value, we can estimate and optimize the topological shape of the road connection by putting it to a computational facility. To sum up and calculate the structure value, the process can be parallelized within the processes of calculation for the link and node values, since the attributes of these values are independent from each other. If the computational time is considerably short, we can examine the re-construction and its efficiency through the interface of the web-browser. We consider this process will be a useful tool for solving the problem on DRR in Thailand.

### 3. Summary and discussion

Data integration is a process in which heterogeneous data is retrieved and combined as an incorporated form and structure. Data integration allows different data types (such as data sets, documents and tables) to be merged by organizations for usages as personal or business processes and functions. In this work, we apply the data integration for the road data of DRR. It can solve problems on duplication and inconsistency of road databases. With the help of the integrated data, DRR will have more precise road data for a good decision or planning to construct and maintain the roads. It is expected that this solution can be applied for other types databases in DRR such as human resources databases, other asset management databases.

### References

- [1] Thailand infrastructure annual report, the National Economic and Social Development Board of Thailand (NESDB) and the World Bank, 2008.
- [2] Asian Development Bank, Publication Stock No. RPS113935.
- [3] Pomlaktong, N., Ongkittikul S., *Infrastructure Development in Thailand*, [in:] *International Infrastructure Development in East Asia – Towards Balanced Regional Development and Integration*, ed. N. Kumar, ERIA Research Project Report 2007-2, Chiba: IDE-JETRO, 2008, 263-291.

ANDRZEJ SKOWRONEK\*

## REDUCING THE NUMBER OF RUNS IN EXPERIMENTAL RESEARCH USING SMART DESIGNS OF EXPERIMENT

---

## ZMNIEJSZANIE ILOŚCI BADAŃ EKSPERYMENTALNYCH Z ZASTOSOWANIEM INTELIGENTNYCH PLANÓW EKSPERYMENTU

### Abstract

This paper presents the results of a computer simulation, performed to check how the number of smart designs of experiment units affects the quality of information to be obtained in experimental research conducted on the basis of the analyzed designs. In the simulation, a real research object was replaced by a special testing function whose values were compared to the values predicted by the neural networks trained with the use of data sets based on smart designs of experiments containing various numbers of units.

*Keywords: smart design of experiment, experimental research, neural approximation*

### Streszczenie

W artykule przedstawiono wyniki symulacji komputerowej do oceny wpływu liczby układów elastycznych planów doświadczeń na jakość informacji, którą można uzyskać, wykonując badania eksperymentalne na podstawie analizowanych planów. W symulacji rzeczywisty obiekt badań został zastąpiony specjalną funkcją testową, której znane wartości były porównywane z aproksymowanymi wartościami zwracanymi przez sieć neuronową trenowaną z użyciem zbiorów danych opartych na analizowanych planach doświadczeń o różnych wielkościach.

*Słowa kluczowe: elastyczny plan eksperymentu, badania eksperymentalne, aproksymacja neuronowa*

---

\* Ph.D. Andrzej Skowronek, Faculty of Mechanical Engineering, Cracow University of Technology.

## 1. Introduction

In many areas of science, experimental research serves as the main source of obtaining knowledge and information. If it is necessary to limit the cost or time of an experiment, one can use special techniques offered by the theory of experiment, also known as the design of experiment methodology (DoE). Depending on the goal of research, various types of experimental designs can be used [1–3]. The application of the experimental designs with special techniques for the analysis of experiment’s results can often facilitate reducing the size of the experiment (number of runs, observations, etc.) and obtaining relevant information from the research, without reducing its quality [4–5].

However, in the traditional designs of experiments, the researcher cannot change the number of design’s units, the number of inputs’ levels and has to carry out the experiment strictly according to the design which is used. Quite a different approach to the concept of experiment planning is applied in smart designs of experiments [6] which allow the researcher to set the number of design’s units and the number of inputs’ levels.

## 2. The idea of smart designs of experiments

Smart designs of experiment are generated in a dedicated computer application, based on three important principles: adaptation, randomness and equipartition [6–7]. The first principle means the possibility of adjusting the design’s characteristics to the conditions of the experiment and characteristics of the analyzed object. The researcher is able, for example, to set the number of design’s units and the number its levels for each input. The second principle means that smart designs are created in a non-deterministic manner: both the generation of input’s levels and the selection of design’s units are conducted with using pseudo-random numbers. However, there are some limitations put on the random way of generation of design’s units:

- using a parameter called “important difference” ( $\Delta x$ ), a minimal permissible distance between the currently generated value and the existing values of each input factor levels (Fig. 1),
- a parameter called “minimal Euclid’s distance” ( $esmin$ ) – it is Euclid’s distance to the nearest “neighbour-unit” in the input’s space, calculated for each design’s unit, each unit must fulfill the condition:  $es \geq esmin$  (Fig. 2)

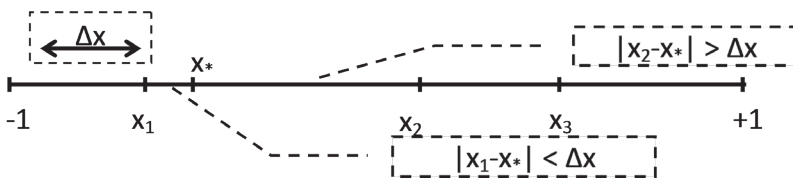


Fig. 1. Value  $x^*$  fails the important difference condition test and will be removed

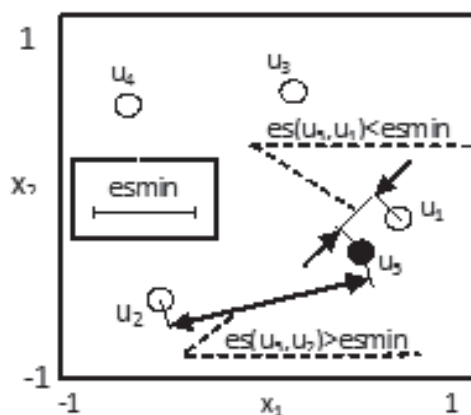


Fig. 2.  $es(u_3, u_1) < esmin$ , unit  $u_3$  fails the  $es \geq esmin$  condition test and will be removed

The conceptions of both parameters described above are based on the conception of Euclid's distance and they use the fact that a set of experimental design units in the space of inputs is equivalent to the set of points in the orthogonal coordinate system as well as the combinations of inputs' levels (which make up the units of designs) are equivalent to the points' coordinates. The  $\Delta x$  and  $esmin$  parameters support equipartition of the design's units in the inputs' space. If there are no other assumptions, design's units should cover regularly the whole inputs' space (the third rule). To estimate the regularity of the distribution of the design's units, the method of equipartitional analysis (EPA, [6]) is used. The analyzed (created) experimental design is compared with the master-design of the units which are distributed perfectly regularly in the inputs' space ([6–7], Fig. 3). The master-designs have the same numbers of inputs as the

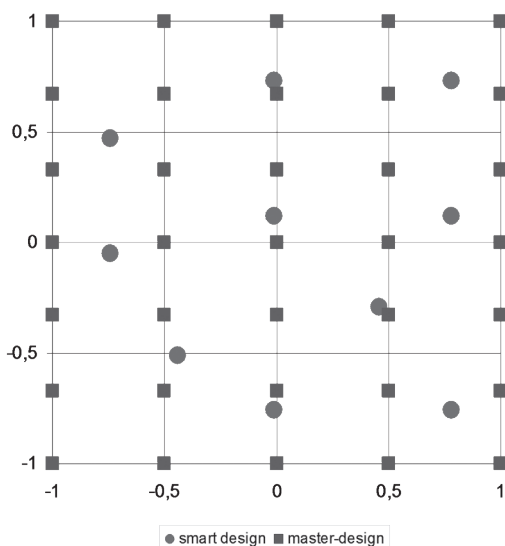


Fig. 3. 2-inputs master-design and smart design



analyzed designs and the same number of various inputs levels, but the number of design's units is often significantly higher and equal to the product of numbers of all input's levels. However, the levels of the master-design are calculated for each input by dividing the length of input range by the number of input's levels (Fig. 3). For each unit of the master-design, one can evaluate Euclid's distance to the nearest unit of the analyzed design. For such a collection (called an equipartitional set), one can evaluate a lot of statistical parameters (e.g. descriptive statistics [8]) or make one of the statistical tests [9]. Each of them could be an equipartition criterion in this analysis. Two parameters have been used: the maximal (*elmax*) and mean (*elmean*) value of an equipartitional set. The *elmean* parameter describes the central tendency of an equipartitional set and the *elmax* parameter gives the information whether there are some huge empty areas in the inputs' space (without design's units), which is important when taking into consideration the assumption that the design's units should cover the whole inputs' space. The dependence between both parameters and the design's quality (quality means equipartition, perfect regularity of the design's units in the inputs' space) was verified and described in [7]. The conclusion was: the smaller value of the equipartitional parameter, the more regular distribution of the design's units in inputs' space.

There are three ways to generate inputs' levels [10]. In the first method ("Z" method), inputs' levels are generated as pseudo-random values from the normalized range  $[-1, 1]$  and checked if they pass the important difference condition test (see Fig. 1). If a value fails the test, it is removed and the next one is generated to reach the right amount. In the "R" method, the levels of inputs are calculated by dividing the input's ranges by the demanded numbers of input's levels. The smallest level is calculated as the minimum of the input's range, whereas the biggest level is calculated as the maximum of the input's range. In the R2-method, the idea of levels calculation is that each level should be the center point of equal areas of influence. The first and the last levels are not equal to the minimum or maximum of the input's range (Table 1).

Table 1

Examples of levels in R and R2 methods

Method	Values used in the case of 5 levels				
R	-1	-0.5	0	0.5	1
R2	-0.8	-0.4	0	0.4	0.8

The generating of the smart designs of experiment consists of the following steps [7]:

- defining characteristics of the design: the number of inputs (factors), the number of designs units, the number of inputs' levels;
- generating the inputs' levels according to the method chosen;
- generating the sets of levels of inputs' factors;
- generating the set of all possible design's units by permuting all inputs' levels;
- completing the design by selecting from the set of all possible design's units only the ones which fulfill the *esmin* condition;
- equipartitional analysis to evaluate the quality of the design (quality means regular and equipartitional distribution of design's units in inputs' space).

The smart design's generator in the current version has implemented the functionalities which support the selection of the optimal values of important generation parameters – the important difference ( $\Delta x$ , used in Z-method of levels' generating) and the minimal Euclid's distance (*esmin*, used to ensure high regularity and equipartition of design's units in the inputs' space) [7]. Using previous versions of the generator, a researcher must set it by himself. If he does not know well the principles of how the smart designs generator functions, or he does not have some intuition or experience in the designs' generating process, it is likely that the generated design will not be optimal – designs' units will not cover equally the whole inputs' space. In the case of setting too small values of generation parameters, equipartition decreases or it is not possible to get the experimental design with the assumed number of units otherwise. To increase the probability of obtaining high-quality designs, they are generated in series and each design has to fulfill the *esmin* condition. If at least one design can be created, the *esmin* value is automatically increased and new designs are generated again. If any design is created, the *esmin* value is automatically decreased and designs are generated again. In the case of an increasing *esmin* value, if the newly generated design has a better quality than the previous one, the *esmin* value increases again and new designs are generated once again. If the new generated design is of worse quality than the previous one, the new design is not generated again and the previous design is saved. In the case of decreasing the *esmin* value, if at least one new design can be generated, new designs are not generated again. If any new design can be generated, the *esmin* value is automatically decreased again and new designs are generated once again. The design of better quality is selected on the basis of equipartitional parameters: *e1max* and *e1mean*.

The smart designs of experiment are multiple-generated [11]. The reason is the application of pseudo-random numbers in the algorithm of designs generating. Designs generated with the same seed of a pseudo-random number generator, the same parameters of generation ( $\Delta x$ , method of input's levels generating, *esmin*) and the same design's characteristic (the number of inputs, the number of input's levels, the number of design's units) will be identical. But if the seed value is changed or just if one tries to generate it next time even with the same generation parameters, they could be different and the difference of the design's quality could be sometimes significant. To avoid such problems, it seems necessary to generate several designs and choose one, based on EPA-parameters (*e1max* and *e1mean*). That is the idea of multi-generated smart designs of an experiment. The researcher can set a pseudo-random number generator seed value by oneself or can generate it, based on the real-time clock. To generate the identical design again, only its seed value must be known. The researcher can select the EPA-parameter with which he prefers to choose the best design. Each design generating is repeated up to 20 times to get 10 designs.

### 3. Computer Simulation

To study how the number of the smart designs of experiment units affects the quality of information to be obtained in experimental research which is conducted on the basis of the analyzed designs, a computer simulation was performed, where a real research object was simulated by a special testing function – Rosenbrock's Function [12]:

$$f(x) = \sum_{i=1}^{N-1} \left( (1-x_i)^2 + 100 \cdot (x_{i+1} - x_i^2)^2 \right) \quad (1)$$

The idea of using the testing function simulating the real object is easy to evaluate its values for each point in the input's space and compare them to the values predicted by neural networks trained with the use of data sets based on the smart designs of an experiment. It was assumed that the values predicted by the neural network will be significantly influenced by a training set which was built on the basis of the analyzed smart design. The comparison of the values predicted by the neural network with the values of the testing function calculated for a special testing set allow indirectly evaluate the quality of information gain in a computer simulation of an experiment conducted according to the smart design. By comparing the results obtained for the designs consisting of various numbers of units, one can study the impact of their size (number of units) on the simulation errors. It is very likely that the same effect could be observed in the real scientific experiment carried out with the use of smart designs.

Although many methods of approximation are known in the simulation, the neural approximation method was applied due to the easiness of implementation and the lack of additional assumptions, which is important especially when the function of a real object being the subject of experimental research is poorly known, or not known at all. The neural networks were created in the Statistica Automated Neural Networks module. For all the neural networks, the same methods of learning were applied, so the same influence on the results is assumed. The Automated Network Search tool was used which enabled the automated evaluation and the selection of multiple network architectures. The random selection of learning cases and the default settings were used: 70% cases as a learning set, 15% cases as a testing set and 15% cases as a validation set. The multi-layer perceptron type of nets, with between 3 and 10 hidden neurons, was used. The automated learning tool used the BFGS algorithm. While searching for the best net, various activation functions were checked: linear, logistic, hyperbolic tangent and exponential. 20 nets with various settings (the number of hidden neurons, activation functions) were trained and the best 5 were saved. Finally, the best nets were selected on the basis of nets quality parameters (sum of squares errors) which were calculated for learning, testing and validation sets.

In the simulation the author studied 3-inputs designs with 5 (first input), 7 (second input), 9 (third input) levels generated according to R and R2 methods. The numbers of design's units were set as 10% (32), 25% (79), 50% (158), 75% (237) of the full design units' number (315). The full design consists of units which are all possible combinations of all inputs' levels. In the case of 5, 7 and 9 levels for 3 inputs there are 315 combinations. The real and approximated values were calculated with the use of a special testing set, consisting of 1331 units and built as all combinations for 11 levels of 3 inputs. The levels were calculated by dividing regularly the input range  $[-1, 1]$  into 10 subranges:  $-1, -0.8, -0.6 \dots 1$ . For each error set (a collection of differences between real and approximated values), statistical parameters were calculated: the maximal and average error, standard deviation, the number of errors' values higher than 0.1 (10% of output range  $[0, 1]$ ).

#### 4. Results of Simulation

For each error set (the collection of differences between testing function values and approximated values) statistical parameters were calculated: the maximal error, the average error, standard deviation, the number of absolute errors in values higher than 0.1 (10% of the length of the standardized output range 0..1). Additionally, the nonparametric two-samples Kolmogorov-Smirnov test ( $\alpha = 0.05$ ) [9] was conducted to compare approximated values sets and testing function sets. The test, which is very popular to determine whether distributions of two random samples differ significantly, is sensitive to any kind of distributional difference and there is no need to make an assumption about, for example, normality or homogeneity of sample variance. The simulation errors, obtained for the errors sets consisting of values calculated for a special testing set as absolute differences between testing function values and neural approximated values, are shown in Table 2.

Table 2

**Simulation errors obtained for the R- and R2-method of smart designs generating**

units	errors for R-method					errors for R2-method				
	max	average	err > 0.1	std. dev.	p-value (K-S test)	max	average	err > 0.1	std. dev.	p-value (K-S test)
32	0.45	0.04	100	0.05	< 0.001	0.46	0.05	117	0.05	< 0.001
	0.70	0.11	700	0.09	< 0.001	0.57	0.04	117	0.06	< 0.001
79	0.13	0.01	1	0.01	< 0.01	0.30	0.03	54	0.03	< 0.1
	0.06	0.01	0	0.01	< 0.005	0.38	0.03	53	0.04	> 0.1
158	0.18	0.01	4	0.01	> 0.1	0.12	0.02	7	0.02	> 0.1
	0.05	0.01	0	0.01	> 0.1	0.07	0.01	0	0.01	> 0.1
237	0.04	0.01	0	0.01	> 0.1	0.18	0.02	23	0.02	> 0.1
	0.19	0.02	5	0.02	< 0.025	0.14	0.02	4	0.02	> 0.1
315	0.02	0.01	0	0.01	> 0.1	0.13	0.01	3	0.01	> 0.1
	0.07	0.02	0	0.02	< 0.05	0.10	0.01	1	0.02	> 0.1

Taking into consideration the maximal error, the values evaluated for both generating methods (R and R2) in the case of 32 design's units are definitely too high. The output range for the testing function was normalized to the 0..1 range. The maximal error, for example 0.70, means therefore the difference between the testing function value and the approximated value is on the level of 70% of the length of the output range and it disqualifies the design to be used instead of, for example, a full-design. Furthermore, other errors (e.g. the number of cases where the absolute error is higher than 0.1) calculated for 32-unit designs are high and significantly worse than in the case of other unit numbers. However, it must be noted that 32 units are only 10% of full-design units' number, so the increase of approximation errors (which means a possible loss of information gain in a real experiment conducted according to the analyzed smart design) is very likely. Comparing the errors obtained for the cases of 79, 158 and 237 units, the errors in the case of the R2 generating method are a little bit higher. But the fact is that error values are less varied

when comparing two results obtained for the neural approximation made twice in each case of unit number. Taking into consideration average errors, their low values and low variety are noticed. Additionally, by analyzing the number of cases where absolute errors are higher than 0.1, it can be concluded that the cases of really high absolute errors are not too frequent, which could be important, especially if the average error is preferred instead of the maximal error in order to evaluate a smart design.

Let us focus now on p-values obtained in the two-samples Kolmogorov-Smirnov (K-S) test, conducted using  $\alpha = 0.05$  significance level. While comparing the distributions of testing function values sets and approximated values sets, a lot of cases where the difference is significant can be noticed for the R-method. In the case of the R2-method of design generation, the situation seems to be clear – for designs with 79 or more units there are no significant differences between testing function values samples and approximated values samples.

## 5. Conclusions

The simulation shows that it is possible to reduce the number of experiments (observations, runs) performed in the experimental research. The application of smart designs of experiment could facilitate their reduction, even to 25–50% of the number of full design's units. It could sometimes mean reducing the time or the cost of research significantly. The simulation was conducted for 3-input smart designs. However, the procedures of generating and analyzing smart designs are universal for all designs' characteristics, so the conclusions should also be true for cases of other numbers of inputs, levels or design's units, and could be used in a broad area of engineering.

Having compared the two analyzed methods of generating design's units, the R2-method appears to be more recommended, especially because of the Kolmogorov-Smirnov test results and a smaller variation of errors. The same conclusions might be drawn by analyzing the results of the simulation in which the influence of generation methods on the quality of smart designs of an experiment was studied [13].

## References

- [1] Polański Z., *Design of experiment in technology*, PWN, Warsaw 1984 (in Polish).
- [2] Montgomery D.C., *Design and Analysis of Experiments*, John Wiley & Sons, 2012.
- [3] Hinkelmann K., Kempthorne O., *Design and Analysis of Experiments. Volume 1. Introduction to Experimental Design*, John Wiley & Sons, Hoboken 2008.
- [4] Hinkelmann K., Kempthorne O., *Design and Analysis of Experiments. Volume 2. Advanced Experimental Design*, John Wiley & Sons, Hoboken 2005.
- [5] Goos P., Jones B., *Optimal Design of Experiments: A Case Study Approach*, John Wiley & Sons, Hoboken 2011.
- [6] Polański Z., *Empirical research – methodology and computer aiding*, [in:] *Modern metrology*, ed. J. Barzykowski, WNT, Warsaw 2004 (in Polish).
- [7] Skowronek A., *A method of self-adaptation calculating the value of the smart designs of experiment generation's parameter*, Pol. J. Environ. Stud. 18 (3B), 2009, 327-331.

- [8] Johnson R.A., Bhattacharyya G.K., *Statistics: Principles and Methods*, John Wiley & Sons, Hoboken 2010.
- [9] Sheskin D.J., *Handbook of parametric and nonparametric statistical procedures*, 3rd ed., Chapman&Hall/CRC, 2004.
- [10] Skowronek A., *The smart designs of experiment generated with circular input's ranges*, [in:] *Problems of Modern Techniques in Engineering and Education*, ed. P. Kurtyka, P. Malczewski, K. Mroczka, K. Ziewiec, Pedagogical University of Cracow, Kraków, 2009, 123-129.
- [11] Skowronek A., *A conception of multi-generated smart designs of experiment*, [in:] *Computer Methods in Mechanics CMM-2009: short papers*, ed. M. Kuczma [et al.], Zielona Góra, Univ. Ziel. Góra Press, 2009, 419-420.
- [12] [http://www-optima.amp.i.kyoto-u.ac.jp/member/student/hedar/Hedar\\_files/TestGO\\_files/Page364.htm](http://www-optima.amp.i.kyoto-u.ac.jp/member/student/hedar/Hedar_files/TestGO_files/Page364.htm), retrieved November 2013
- [13] Skowronek A., *Evaluating the influence of generation methods on the quantity of the smart design of experiment*, *Technical Transactions*, 1-M/2013, 357-364.



ANDRZEJ SKOWRONEK\*

## COMPARING THE EFFECTS OF APPLICATION OF THE SMART AND TRADITIONAL DESIGNS OF EXPERIMENT

---

### PORÓWNANIE EFEKTÓW ZASTOSOWANIA ELASTYCZNYCH I TRADYCYJNYCH PLANÓW EKSPERYMENTU

#### Abstract

This paper presents an analysis of comparing the effects of the application of the smart and traditional designs of experiment. The smart designs of experiment generated according to two various methods were compared to the central composite designs for two and three inputs. To check how the use of selected designs will affect the results of the experiment a computer simulation was performed, where a real research object was replaced by two special testing functions whose values were compared to the values predicted by the neural networks trained with the use of data sets based on compared smart and traditional designs of the experiment.

*Keywords: smart design of experiment, central composite design, experimental research*

#### Streszczenie

W artykule przedstawiono wyniki porównania efektów zastosowania elastycznych i tradycyjnych planów eksperymentu. Plany elastyczne były generowane z użyciem dwóch różnych metod i porównane z planem centralnym kompozycyjnym. W celu zbadania wpływu zastosowanego planu eksperymentu została wykonana symulacja komputerowa, w której rzeczywisty obiekt badań został zastąpiony dwoma funkcjami testowymi, których wartości były porównywane z wartościami aproksymowanymi za pomocą sieci neuronowych, uczonych na zbiorach opartych o porównywane plany.

*Słowa kluczowe: elastyczny plan eksperymentu, plan centralny kompozycyjny, badania eksperymentalne*

---

\* Ph.D. Andrzej Skowronek, Faculty of Mechanical Engineering, Cracow University of Technology.



## 1. Introduction

Scientific experiment seems nowadays to be a very important source of obtaining information. It is caused by the need of experimental validation of various devices, systems and processes, and on the other hand, planning and execution of an experiment is strongly supported by the use of the various techniques of conducting and analyzing the experiment. These techniques known as the design of experiment methodology (DoE) are particularly useful when the researcher seeks for a way to limit the cost or time of the planned experiment without reducing its quality [1–2]. The goal of research determines using various types of experimental designs. One can mention, for example, full factorial designs, fractional designs, dedicated for mixtures or based on the response surface analysis. Choosing the traditional designs of experiments determines the number of the design's units and the number of inputs' levels. The other approach to the planning of an experiment is the main idea of the smart designs of the experiment which allows the researcher to set a number of design's units and the number of inputs' levels.

## 2. The Idea of Smart Designs of Experiments

Smart designs of an experiment are generated in a dedicated computer application, based on three important principles: adaptation, randomness and equipartition [3]. The first principle means the possibility of adjusting the design's characteristics to the conditions of the experiment and characteristics of the object under research. The researcher is able, for example, to set a number of design's units and levels for each input. The second principle means that smart designs are created in a non-deterministic manner: both the generation of input's levels and the selection of design's units are conducted with the using of pseudo-random numbers. However, there are some limitations put on the random way of generating design's units [3–4]:

- a parameter called "important difference" ( $\Delta x$ ), a minimal permissible distance between the currently generated value and the existing values of each input factor levels,
- a parameter called the "minimal Euclid's distance" ( $esmin$ ) – it is the Euclid's distance to the nearest "neighbour-unit" in the input's space, calculated for each design's unit, where each unit must fulfill the condition:  $es \geq esmin$ .

Both parameters described above are based on the conception of the Euclid's distance and use the fact that a set of design units in the space of inputs is equivalent to the set of points in the orthogonal coordinate system as well as the combinations of inputs' levels (which make up the units of designs) are equivalent to the point coordinates. The  $\Delta x$  and  $esmin$  parameters support equipartition of the design's units in the inputs' space.

There are three ways to generate the inputs' levels [4]. In the first method (Z-method), inputs' levels are generated as pseudo-random values from the normalized range  $[-1, 1]$  and checked if they pass the important difference condition test. If a value fails the test, it is removed and the next one is generated to reach the demanded amount of input's levels. In the R-method, the levels of inputs are calculated by dividing the inputs' ranges by the demanded numbers of input's levels. The smallest level is calculated as the minimum of the input's range, whereas the biggest level is calculated as the maximum of the input's range. For

example, in case of 5 levels the set of values consists of the following values:  $\{-1.0, -0.5, 0, 0.5, 1.0\}$  (see Fig. 1). In the R2-method, the idea of level calculation is that each level should be the center point of equal areas of influence. The first and the last levels are not equal to the minimum or maximum of the input's range. In case where 5 levels are assumed, the set of inputs' levels consists of the following values:  $\{-0.8, -0.4, 0.0, 0.4, 0.8\}$  (see Fig. 1).

The third rule fulfilled by the smart design is equipartition of their units. If there are no other assumptions, design's units should cover regularly the whole inputs' space. To estimate the regularity of the distribution of the design's units, the method of the equipartitional analysis (EPA, [3]) is used. The analyzed (created) experimental design is compared to the master-design, the units of which are distributed perfectly regularly in the inputs' space ([5], Fig. 2).

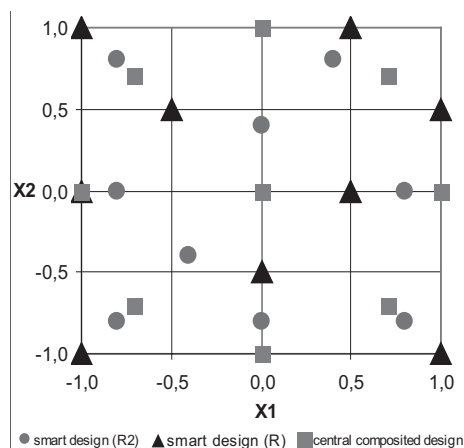


Fig. 1. 2-inputs smart designs (R and R2-method) and central composited design

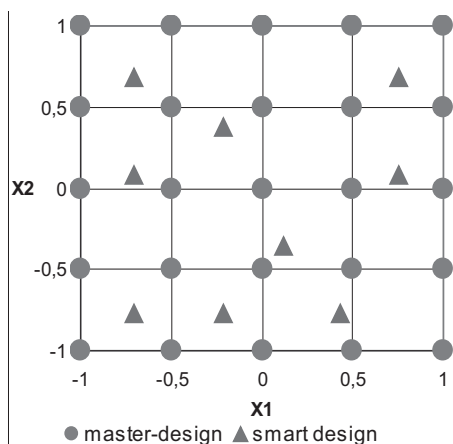


Fig. 2. 2-inputs master-design and smart design

The master-designs have the same number of inputs as the analyzed designs and the same number of various input's levels, but the number of design's units is often significantly higher and equal to the product of numbers of all input's levels. However, the levels of the master-design are calculated for each input by dividing the length of the input range by the number of input's levels. For each unit of the master-design, one can evaluate the Euclid's distance to the nearest unit of the analyzed design. For such a collection (called equipartitional set), one can evaluate a lot of statistical parameters (e.g. descriptive statistics [6]) or make one of the statistical tests [7]. Each of them could be an equipartition criterion in this analysis. Two parameters have been used: the maximal (*elmax*) and mean (*elmean*) value of an equipartitional set. The *elmean* parameter describes the central tendency of an equipartitional set and the *elmax* parameter gives the information whether there are some huge empty areas in the inputs' space (without design's units), which is important when taking into consideration the assumption that the design's units should cover the whole inputs' space.

The following steps are performed while generating the smart designs of an experiment [5]:

- defining characteristics of the design: the number of inputs (factors), the number of designs' units, the number of inputs' levels;
- generating the inputs' levels according to the chosen method;
- generating the sets of levels of inputs' factors;
- generating the set of all possible design's units by permuting all inputs' levels;
- completing the design by selecting from the set of all possible design's units only the ones which fulfill the *esmin* condition;
- equipartitional analysis to evaluate the quality of the design (quality means regular and equipartitional distribution of design's units in inputs' space).

The smart design's generator in the current version has implemented the functionalities which support an automatic selection of the optimal values of important generation's parameters – the important difference ( $\Delta x$ , used in Z-method of levels' generating) and the minimal Euclid's distance (*esmin*, used to ensure high regularity and equipartition of design's units in the inputs' space) [5]. Using previous versions of the generator, a researcher had to set it himself.

To increase the probability of obtaining high-quality designs, they are generated in the series and each design has to fulfill the *esmin* condition. If at least one design can be created, the *esmin* value is automatically increased and new designs are generated again. If any design is created, the *esmin* value is automatically decreased and designs are generated again [5]. The design of better quality is selected on the basis of the described above equipartitional parameters: *eImax* and *elmean*.

The smart designs of an experiment are multiple-generated [8]. The reason is the application of pseudo-random numbers in the algorithm of designs generating. The designs generated with the same seed of a pseudo-random number generator, the same parameters of generation ( $\Delta x$ , method of input's levels generating) and the same design's characteristic (the number of inputs, the number of input's levels, the number of design's units) will be identical. But if the seed value is changed or just if one tries to generate it next time even with the same generation parameters, they could be different and the difference of the design's quality could be sometimes significant. To avoid such a problem, it seems to be necessary to generate several designs and choose one, based on the EPA-parameters (*eImax* and *elmean*). Each design generating is repeated up to 20 times to get 10 designs.

### 3. Computer Simulation

The main aim of this study was to compare the effects of use the traditional and smart designs in an experiment conducted according to these designs. The central composited designs and smart designs were analyzed for two (Fig. 1) and three inputs. The smart designs were designed with the same numbers of units (9 for 2 inputs and 15 for 3 inputs) and the same numbers of each levels (5) as compared to central composited designs. The smart designs were generated with the application of the R-method and R2-method of generation the inputs' levels. In the previous studies [9] both methods allow for the best results of experiments as the Z-method.

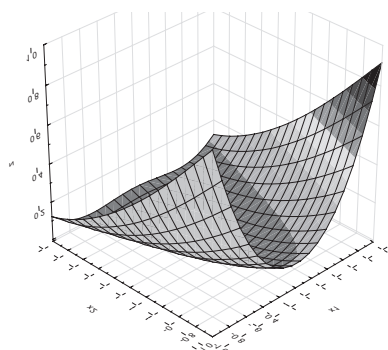


Fig. 3. Rosenbrock's function

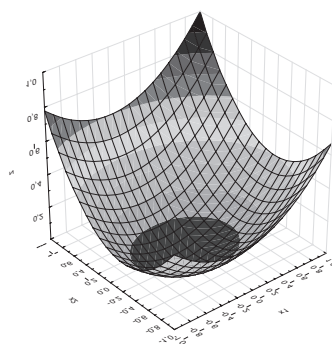


Fig. 4. SumOfSquare function

The research was carried out as a computer simulation where a real research object was simulated by two special testing functions – Rosenbrock's (1) and SumOfSquare (2) known very well as testing functions in optimization [10].

$$f(x) = \sum_{i=1}^{N-1} \left( (1 - x_i)^2 + 100 \cdot (x_{i+1} - x_i^2)^2 \right) \quad (1)$$

$$f(x) = \sum_{i=1}^N \left( (i+1) \cdot x_i^2 \right) \quad (2)$$

For the testing functions simulating the real research object one can evaluate easily its values for each point in the input's space and compare them to the values predicted by neural networks trained with the use of data sets based on the studied designs of the experiment. It was assumed that the values predicted by the neural network will be significantly influenced by a training set which was built on the basis of the analyzed design. The comparison of the values predicted by the neural network with the values of the testing function calculated as absolute differences for a special testing sets (simulation errors) allows indirectly evaluate the quality of information gain in computer simulation of an experiment conducted according to the designs, and at the same time evaluate the influence of the design on the quality of information gained in the conducted experiment.

Neural approximation is one of the popular methods of approximation. The advantages of this method are an easy implementation and a lack of additional assumptions, which is important especially when the function of a real object being the subject of experimental research is poorly known, or not known at all. The neural networks were created in the Statistica Automated Neural Networks module. For all the neural networks, the same methods of learning were applied, so the same influence on the results are assumed. The Automated Network Search tool enabled the automated evaluation and selection of multiple network architectures. The learning cases were selected randomly. 70% cases was assigned to a training set and 30% to a testing set. However, the small size of the learning set should be noted, as they were 9-elements for 2-inputs designs and 15-elements for 3-inputs designs.

The multi-layer perceptron type of nets consist of between 3 and 10 hidden neurons and learns with application of the BFGS algorithm. Various activation functions were checked while searching for the best net: linear, logistic, hyperbolic tangent and exponential. The Automated Network Search tool trains 20 nets with various settings (the number of hidden neurons, activation functions) and saves the best five. On the basis of nets' quality parameters (sum of squares with errors) which were calculated for learning and testing sets, the best was selected and applied to the prediction of the data.

The compared neural approximated and real values were calculated for special testing sets, consisting of 121 (for two inputs designs) and 1331 (for three inputs designs) units. The sets were built as combinations of 11 levels for each input. The levels were calculated by dividing regularly the input range  $[-1, 1]$  into 10 subranges:  $-1, -0.8, -0.6 \dots 1$ . For each error set (a collection of the absolute differences between real and approximated values), statistical parameters were calculated: the maximal and average error, the percent of testing cases where error values were higher than 0.1 (10% of output range  $[0, 1]$ ) and standard deviation. To check whether the approximated values sets and testing function sets differ significantly, the nonparametric two-samples Kolmogorov-Smirnov test [7] was conducted. This test does not require any assumption about normality or homogeneity of sample variance and is known to be sensitive to any kind of distributional difference.

#### 4. Results of Simulation

The results of simulation are shown in Table 1. There are the following symbols used in the table: Ros means Rosenbrock's function, SoS means SumOfSquare function, CC means central composited design, R2 means smart design generated according to the R2-method and R means smart design generated according to the R-method. Errors means a set of absolute differences between testing function values and the values predicted by neural nets calculated for special testing sets consisting of 121 cases for 2 inputs and 1331 cases for 3 inputs.

The average values of the error parameters calculated for all three compared designs' types are shown in Table 2.

Taking into consideration the average values of errors, the best results were obtained for smart designs generated according to the R2-method. The error average values for all types of designs seem to be relatively low for the output range  $[0, 1]$ . However, the maximal values of absolute differences are in the same time definitely to high, especially in the case of a central composited design. It should be noted that the maximal value as a descriptive statistic parameter means only one value calculated sometimes for a huge set and not always describes adequately the analyzed data. As in the case of the average error, also the lowest value of maximal error was obtained for the R2-design but the difference compared to the other two designs was significant (about 30%). The question is which type of statistical parameters is more important for the researcher. Taking into consideration the percentage of cases where the absolute difference between the real (obtained for testing functions) and the approximated (predicted by neural net) values were higher than 0.1 (10% of  $[0, 1]$  output range length), you can notice a similar trend as in the case of an average error. The best result was obtained for 2 and 3-inputs designs generated according to the R2-method. Standard deviation indicates whether the cases tend to be very close to the mean value (low value)

or rather are spread out over a large range of values (high value). The calculated values are quite similar, however the lowest value was obtained for designs generated with application of the R2-method.

Table 1

### Simulation errors

number of inputs	testing function	type of design	maximal error	average error	errors > 0.1 [%]	standard deviation	K-S test
2	Ros	CC	0.87	0.10	40	0.12	$p > .10$
2	Ros	R2	0.59	0.09	31	0.10	$p > .10$
2	Ros	R	0.60	0.13	41	0.14	$p < .10$
2	SoS	CC	0.56	0.17	63	0.13	$p < .001$
2	SoS	R2	0.57	0.19	72	0.13	$p < .001$
2	SoS	R	0.83	0.18	64	0.16	$p < .10$
3	Ros	CC	0.71	0.10	36	0.10	$p < .001$
3	Ros	R2	0.83	0.11	30	0.12	$p < .001$
3	Ros	R	0.60	0.10	34	0.10	$p < .001$
3	SoS	CC	1.44	0.26	69	0.29	$p < .001$
3	SoS	R2	0.48	0.12	51	0.08	$p < .001$
3	SoS	R	0.86	0.18	68	0.13	$p < .001$

Table 2

### Average values of simulation errors

type of designs	maximal error	average error	errors > 0.1 [%]	standard deviation
CC	0.90	0.16	52	0.16
R	0.73	0.15	52	0.13
R2	0.62	0.12	46	0.11

The last statistical parameter calculated to evaluate the effects of the application both types of designs was *p-value* parameter for the Kolmogorov-Smirnov test. The assumed significant level of the test ( $\alpha$ ) was equal to 0.05. If the *p-value* is smaller than the  $\alpha$ -value, it suggests rejecting the null hypothesis (that two compared samples come from the same distribution) and accepting the alternative hypothesis. Unfortunately, the results (Table 1) are not very optimistic. In most cases the obtained p-values are smaller than the ones used in test  $\alpha = 0.05$ . But you should remember that the learning sets were extremely small and it was probably not enough to learn the neural nets successfully.

## 5. Conclusions

The study of the simulation results leads to two main conclusions. The first conclusion is that the errors obtained in the simulation of an experiment conducted according to smart designs of an experiment are less than in the cases of using two- and three-input central composited designs. The difference is especially significant for maximal error statistic. The best results were obtained for the smart designs generated according to the R2-method. The second conclusion is that the researcher must consider the problem of the minimal number of design's units, because setting the number which is too low may cause a decrease of the amount of information gain in an experimental research. The idea of smart designs of an experiment is that the researcher can define the number of design's units and the only limitation is the ability to carry out the experiment according to the design generated with the assumed number of units. Generally speaking, the problem is that the purpose of experimental research is often searching for unknown dependences like for example research object function which determines the output depending on the inputs.

## References

- [1] Polański Z., *Design of experiment in technology*, PWN, Warsaw 1984 (in Polish).
- [2] Montgomery D.C., *Design and Analysis of Experiments*, John Wiley & Sons, 2012.
- [3] Polański Z., *Empirical research – methodology and computer aiding*, [in:] *Modern metrology*, ed. J. Barzykowski, WNT, Warsaw 2004 (in Polish).
- [4] Skowronek A., *The influence of method of generating the levels of input factors on the quality of the smart designs of experiment*, Technical Transactions, 4-M/2011/B, 481-488 (in Polish).
- [5] Skowronek A., *A method of self-adaptation calculating the value of the smart designs of experiment generation's parameter*, Pol. J. Environ. Stud. 18 (3B), 2009, 327-331.
- [6] Johnson R.A., Bhattacharyya G.K., *Statistics: Principles and Methods*, John Wiley & Sons, Hoboken 2010.
- [7] Sheskin D.J., *Handbook of parametric and nonparametric statistical procedures*, 3rd ed., Chapman&Hall/CRC, 2004.
- [8] Skowronek A., *A conception of multi-generated smart designs of experiment*, [in:] *Computer Methods in Mechanics CMM-2009: short papers*, ed. M. Kuczma [et al.], Zielona Góra, Univ. Ziel. Góra Press, 2009, 419-420.
- [9] Skowronek A., *Evaluating the influence of generation methods on the quantity of the smart design of experiment*, Technical Transactions, 1-M/2013, 357-364.
- [10] [http://www-optima.amp.i.kyoto-u.ac.jp/member/student/hedar/Hedar\\_files/TestGO\\_files/Page364.htm](http://www-optima.amp.i.kyoto-u.ac.jp/member/student/hedar/Hedar_files/TestGO_files/Page364.htm), retrieved November 2013.

TOMASZ SPOTOWSKI, KAROL OSOWSKI, ZBIGNIEW KĘSY\*

## CONTROL SYSTEM OF LABORATORY STAND FOR GEARBOX AND COUPLING TESTING

---

### SYSTEM STEROWANIA STANOWISKA LABORATORYJNEGO DO BADAŃ PRZEKŁADNI I SPRZĘGIEŁ

#### Abstract

The scheme control system of a laboratory stand for gearbox and coupling testing, capable of fulfilling many miscellaneous requirements has been described in the paper. The innovative solution, as well as the benefits of the application, based on the Program Logic Controller, connected with electrical motor drives and a computer measurement system, have been described and depicted. Special features of the suggested solution, such as flexibility and ability to develop or adjust for another application, have been characterized.

*Keywords: control system, laboratory stand, gearboxes and coupling testing*

#### Streszczenie

Artykuł przedstawia system sterowania laboratoryjnego stanowiska do badania przekładni i sprzęgieł, który ze względu na swoją programowalność pozwala symulować różne warunki pracy. Opisano i przedyskutowano innowacyjne rozwiązanie oraz korzyści płynące z połączenia układu sterowania PLC z komputerowym układem pomiarowym. Przedstawione rozwiązanie sterowania stanowiska cechują takie właściwości jak: wysoka programowalność, możliwość opomiarowania dowolnej wartości procesu, otwartość na dalszą rozbudowę oraz możliwość zastosowania do innych stanowisk badawczych.

*Słowa kluczowe: system sterowania, stanowisko badawcze, badania przekładni i sprzęgieł*

---

\* M.Sc. Eng. Tomasz Spotowski, M.Sc. Karol Osowski, Prof. PhD. Eng. Zbigniew Kęsy, Institute of Applied Mechanics and Energetics, Faculty of Mechanical Engineering, Kazimierz Pulaski University of Technology and Humanities in Radom.



## 1. Introduction

The development of modern engineering science based on electronics, computer measuring systems, and computing technologies gives many possibilities of machine design solutions. Plenty of programs offered on computer markets, measuring boards, control systems in general, can become an obstacle in developing a modern laboratory system for testing mechanical subassemblies, components or parts. The issue of an embedded control system of a laboratory stand for gearbox and coupling testing, that makes programmed tests possible to be performed, and also gives valid measurements for further engineering analysis, has been considered in the article.

Different designs of test rigs for testing subassemblies used in the machine power transmission system, have been presented in the papers [1–8].

Unlike in the commonly used solutions, the developed control system can also be programmed in order to change working parameters of the examined object, while taking measure values into account. In addition, all calculations, measured values and working parameters can be read and stored by the computer measuring system. In an innovative assumption, the control system is electrically separated from the computer measuring system and it is connected with it only via an industrial network that gives the possibility to get all the desired data, using only the computer software tool.

## 2. Requirements

Designing the solution control system, questions like what should be controlled and why as well as which physical values need to be measured, have to be considered. When the object of the study is a gearbox or a coupling, at least one input shaft and one output shaft have to be attached to the analyzed subassembly. At this point, the stand already requires some control and measurements of the input and output shaft.

When the speed of the input shaft and the load given by the output shaft is determined, some features concerning the analyzed object can be expressed. Performing tests of adjustable gearboxes or couplings requires also a possibility of parameter dynamic changes of the tested object. According to mathematical control rules, a dynamic change of control system output parameters is a function of inputs. If so, some output values based on the examined subassembly measured values have to be calculated and carried out. It is necessary, that the object measurements have to be connected to one embedded control system. The input shaft speed and output shaft load characteristics as well as all calculations have to be performed at the same time by one embedded control system. As all process data is calculated and stored in one memory of the control system (one device), and this memory has to be accessible by some reading software of a personal computer (PC) via some industrial network. All that should be done subsequently is to read and store the desired process parameters on the PC's hard disk at the same timeline for further analysis.

### 3. Solution draft

The stand for gearboxes and coupling testing has an input and output shaft connected mechanically with the examined subassembly. In most tests the speed of the input shaft with the load on the output shaft are compared. In the described solution the input shaft is powered by the electrical motor alternating current (AC Motor), and the load on the output shaft is provided by the electrical motor direct current (DC motor) (Fig. 1).

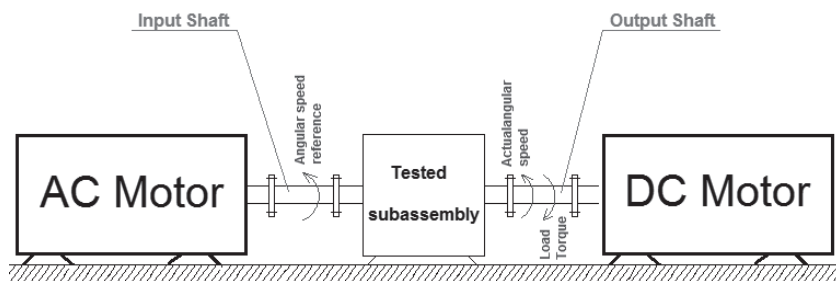


Fig. 1. Motors and examined subassembly connection scheme

As the input shaft angular speed reference and the output load shaft reference characteristics have to be followed by two electrical motors, both of them are powered by drives. As it is shown in Fig. 2 both motors are powered by variable speed drives (VSD): the AC motor is

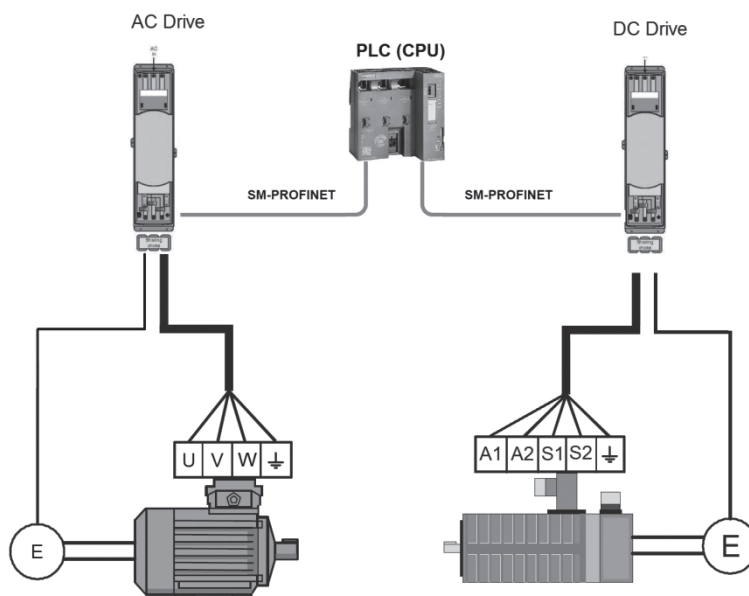


Fig. 2. Electric motors with corresponding drives and encoders [9]

powered by the AC Drive, the DC motor is powered by the DC Drive. Both drives receive the speed feedback from encoders attached to corresponding electrical motors in order to provide a precise speed and load control (Fig. 2).

As motor drives, two Variable Speed Drives from the Emerson company have been chosen. Table 1 contains detailed information about the parts used.

Table 1

**Technical data of Variable Speed drives, electrical motors and PLC**

Part	Company	Type	Remarks
PLC	Siemens	Simatic DP 6ES7151-8AB01-0AB0	—
AC Drive	Emerson	Unidrive SP 1406	connected with PLC via Profinet Network
DC Drive	Emerson	Mentor MP 25A4R	connected with PLC via Profinet Network
AC Motor	Tamel	3Skg 132S-4	PN =5,5KW Un = 400V In=15,4A
DC Motor	Tamel	G11.05	PN =5,5KW Un = 400V In=15,4A

As both drives have to follow some speed and torque programmed reference characteristics, a master control for both drives has to be established. Taking into consideration the fact that the master control has to:

- exchange data between the master control and both drives in order to perform reference speed of the input shaft and the load torque of the output shaft,
- measure values from the examined subassembly,
- calculate output values,
- be able to communicate with other additional devices, using standard industrial electric signals (output cards) and standard industrial network (Profinet, Profibus)
- be able to extend a new input and output card and be able to communicate with new devices via industrial networks.

Programmable Logic Controller (PLC) has been used [10]. PLC communicates and exchanges data between both drives using the industrial Profinet network [11, 12], see Fig. 2 and Fig. 3. Generally, the solution with variable speed drives controlled by a PLC is based on industrial control systems that are widely used around the world.

In the described control system, the PLC controls both drives by exchanging data with them via the industrial Network Profinet [11]. Electronic input and output cards have been added to the PLC. Chosen parameters of the examined subassembly (temperature, pressure), using industrial standards, are measured by input cards 4 .. 20 mA or 0 – 10 V. Based on the measurements and the loaded program, the PLC provides feedback to the tested subassembly, using output cards with industrial standards (4 .. 20 mA, 0 – 10 V) or by means of the industrial network. In Fig. 3 the connection with the Controllable Power Supply via the

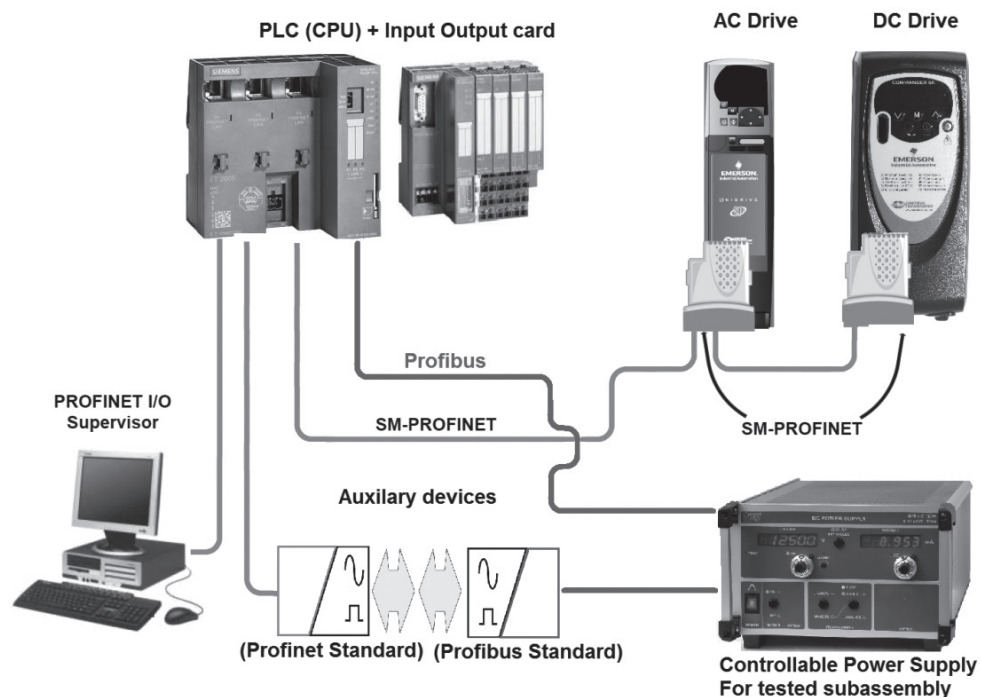


Fig. 3. Scheme of industrial network device connection: Profinet I/O Supervisor – computer used for reading data; PLC (CPU) with input-output cards; SM-Profinet – industrial network used to connect PLC to Drives; Controllable Power Supply used to power tested subassembly if necessary; Potential extensions (Profibus or Profinet standard)

industrial network Profibus has been shown. Due to the fact that the chosen PLC can “communicate” using Profinet and/or Profibus network, it is possible to connect it with other auxiliary devices which makes the described control system very flexible for any modification during the laboratory stand extension. When the “communication” between PLC, motor drives and input-output cards has been established, the PLC is ready to carry out the loaded program. When all the systems are connected together and configured, the program loaded to the PLC can be very easily and quickly modified, which gives the possibility to perform various tests. This feature is especially important at the beginning of the subassembly test when sophisticated knowledge concerning its features is limited. In order to program a PLC, a personal computer with a dedicated program has to be used.

Due to the fact that a PC is connected to the PLC via an industrial network (in this case – Profinet), it can be used both for programming tasks and for measuring purposes. Based on the fact that all the input data (measured speeds, currents, torques from drives, real measurement on input cards), calculated values, and references for devices and output cards) are stored in the PLC’s memory, all that remains to be done is to use the computer to read and save the chosen data on a time plot, directly from the PLC. In order to do this, no measuring cards are required. What is needed, is the special software that is programmed to read and store data from the PLC’s memory. As it has been mentioned, the connection between the PC and PLC

via an industrial network for programming purposes, allows also to carry out measurement tasks, which means reading data from the PLC's working memory to the PC's memory. The PC has to be programmed for this activity. Because preparing software is not an issue in this case, the program IBA-PDA by IBA AG company has been chosen to read and save data from the PLC's memory to the PC's memory. This software provides real time plots (Fig. 4) and saves data for further off line analysis (Fig. 5). This method is not direct because, for example, shaft speeds are measured by drives via encoders and then are sent to the PLC via an industrial network.

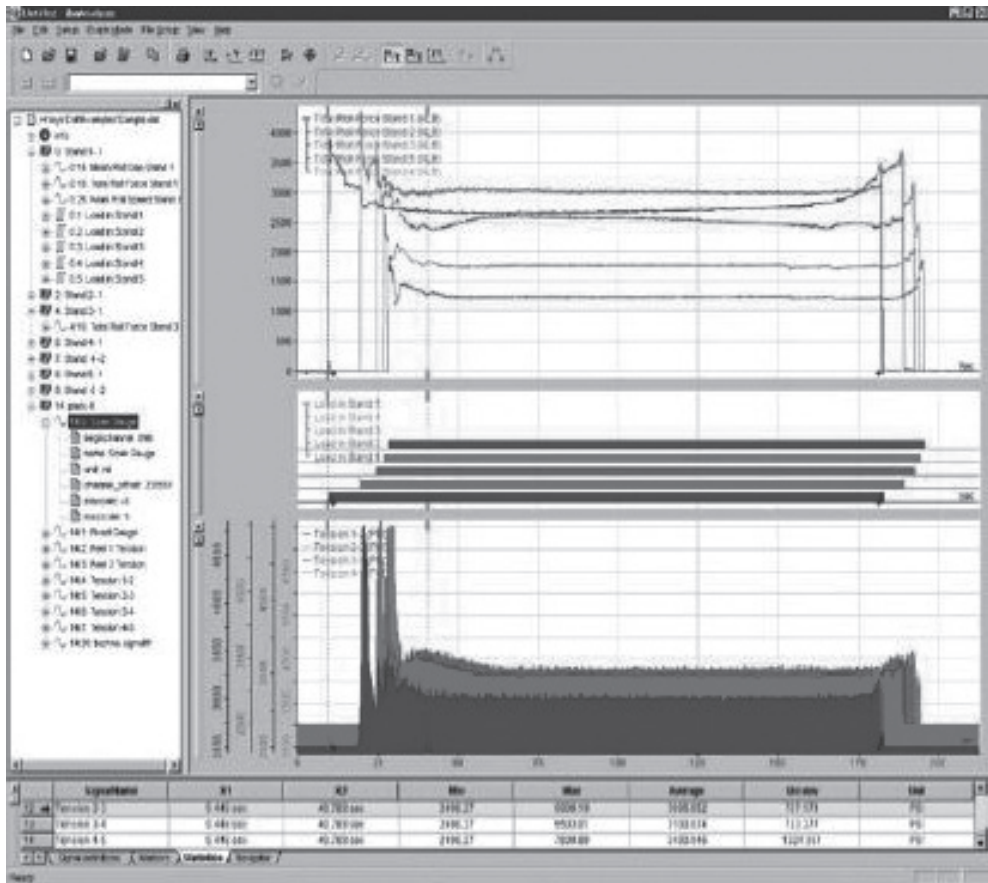


Fig. 4. Example of real time recording and plotting carried out by IBA PDA software

The sampling time is a significant limitation of indirect measurements (reading data from the PLC). Sampling time of measurements is the maximum value from the PLC program loop time and PC software reading time, and can be expressed as follows:

$$T_{smp} = \max(T_{plc}, T_p) \quad (1)$$

where:

- $T_{\text{samp}}$  – sampling time,
- $T_{\text{lt}}$  – PLC program execution loop time,
- $T_r$  – PC reading time.

Substituting the PLC program execution loop time  $T_{\text{lt}} = 12$  ms and PC reading time  $T_r = 20$  ms to equation (1) the sampling time of measurements can be calculated as  $T_{\text{samp}} = 20$  ms.

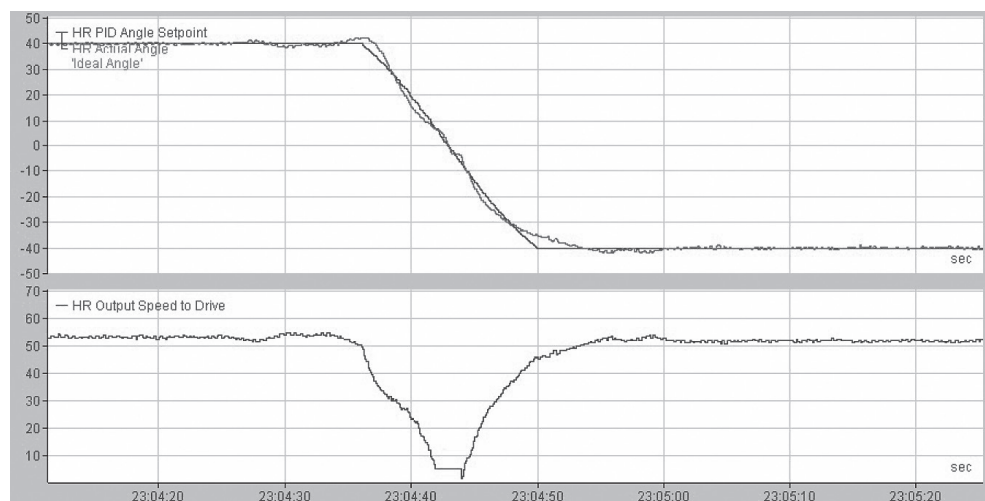


Fig. 5. Example of off line analysis made with IBA Analyzer software tool

In order to assign a certain time moment for each sample, it is necessary to program the real timer inside a PLC. Reading this timer together with other desired data (speeds, torque etc.) gives certain information when the data sample has been collected. This feature needs to be applied only when general features of the examined subassembly are discovered and next steps in the examination are necessary to be done, such as Fourier analyses of signals or statistical calculations.

Because of sampling time, the limitation of measurements should always be taken into consideration during the experiment preparation.

Although sampling time can be an obstacle, flexibility of the recorded data is remarkable. In the described solution, up to sixty values can be read simultaneously. This limitation is only the limitation of the IBA reading software license. Nevertheless, sixty signals are enough to examine a gearbox or a coupling. In order to measure the values, no electrical connection or measuring boards are necessary. All the working parameters and input values from the stand are read and stored in the PLC's memory. The PC "reads" the chosen values from the PLC's memory, using the IBA software. The values from the PLC that have to be stored, are chosen in the IBA software. It is also worth mentioning that the control system based on a PLC (widely used in most modern industrial applications) is able to be connected to any auxiliary systems with industrial standard features. This makes the described control system solution open for any further extension.

#### 4. Conclusions

The control system of the laboratory stand for gearbox and coupling testing has been described in this paper. Basic schemes of the stand mechanical part and the idea of gearbox and coupling test performance have been shown.

On the basis of the undertaken analysis of the stand control system the following conclusions can be formulated:

1. The control method based on a PLC and measurements performed by the IBA-PDA software is suitable to set out requirements such as flexibility for modification and extension;
2. The capability of recording many parameters at the same time base plot and free and the speed of choosing them from the control system is a remarkable advantage;
3. Sampling time can be a limitation of the proposed solution but methods of dealing with it have been described;
4. It must also be underlined that the control system is able to 'communicate' with all devices via standard industrial protocols;
5. The collected experience and knowledge during setting up this kind of control systems can also be useful and desired in commercial engineering.

#### References

- [1] Ishihara T., *A Study of Hydraulic Torque Converter*, II Report of University of Tokyo, Vol. 5, No. 7, Tokyo 1955.
- [2] Herbertz R., *Untersuchung des dynamischen Verhaltens von Fttinger – Getrieben*, Dissertation, Technischen Universitt Hannover, Hannover 1973.
- [3] Pawelski Z., *Badanie charakterystyk przekładni hydrokinetycznej przy wybranych nieustalonych stanach obciążeń*, Praca doktorska, Politechnika Łódzka, Łódź 1980.
- [3] Behrens H., *Nichtlineare Modellierung und Identifikation hydrodynamischer Kupplungen mit allgemeinen diskreten Modellansätzen*, Dissertation. Ruhr Universität Bochum, Bochum 1977.
- [4] Kęsy Z., *Sterowanie przekładni hydrokinetycznej cieczą roboczą*, Monografia, Wydawnictwo Politechniki Radomskiej, Radom 2003.
- [5] Behrens H., Jaschke P., Steinhausen J., Waller H., *Modelling of Technical Systems: Application to Hydrodynamic Torque Converters and Couplings*, Mathematical and Computer Modeling of Dynamical Systems, No. 3/2006.
- [6] Woźniak M., *Badania stanowiskowe i symulacyjne własności dynamicznych przekładni hydrokinetycznej*, Praca doktorska, Politechnika Łódzka, Łódź 2010.
- [7] Kęsy A., Olszak A., Sarnik P., *Przekładnia hydrokinetyczna o małej mocy*, *Hydraulika i Pneumatyka*, nr 4/2010.
- [8] Kęsy A., De La Fuente P., Migus M., *Wywoływanie obciążeń dynamicznych w badaniach stanowiskowych podzespołów hydrokinetycznych*, *Napędy i Sterowanie*, nr 7/8 Lipiec–Sierpień 2011.
- [9] *Podręcznik Użytkownika Wersja podstawowa Unidrive SP*, Numer katalogowy: 0471-0033-02, Wydanie: 2.

- [10] Siemens Simatic, *ET 200S distributed I/OIM 151-8 PN/DP CPU interface module* System manual A5E02049034-02, 6/2010,  
[http://cache.automation.siemens.com/dnl/TA/TA1NzY3MwAA\\_47409312\\_HB/et200s\\_im151\\_8\\_pn\\_dp\\_cpu\\_operating\\_instructions\\_en-US\\_en-US.pdf](http://cache.automation.siemens.com/dnl/TA/TA1NzY3MwAA_47409312_HB/et200s_im151_8_pn_dp_cpu_operating_instructions_en-US_en-US.pdf).
- [11] *User Guide SM-PROFINET Solutions Module for:* Unidrive SP, Commander SK, Digitax ST, Mentor MP, Affinity Part Number: 0471-0163-03 Issue Number: 3.
- [12] Siemens Simatic, *PROFINET System Description*, System manual A5E00298288-04, 06/2008, [http://www.siemens.fi/pool/products/industry/iadt\\_is/tuotteet/automaatiotekniikka/teollinen\\_tiedonsiirto/profinet/man\\_pnsystem\\_description.pdf](http://www.siemens.fi/pool/products/industry/iadt_is/tuotteet/automaatiotekniikka/teollinen_tiedonsiirto/profinet/man_pnsystem_description.pdf).





JOLANTA STACHARSKA-TARGOSZ, KONRAD NERING\*

## INFLUENCE OF DISCHARGE RESISTANCE ON INTERNAL FLOW STRUCTURE AND PERFORMANCES OF THE CROSS FLOW FAN AND THE UNIT INCORPORATING HEAT EXCHANGER

### WPLYW OPORU W STREFIE TŁOCZENIA NA WEWNĘTRZĄ STRUKURĘ PRZEPŁYWU I CHARAKTERYSTYKI PRACY WENTYLATORA POPRZECZNEGO ORAZ UKŁADU ZAWIERAJĄCEGO WYMIENNIK CIEPŁA

#### Abstract

In this paper some selected problems dealing with an influence of different throttling conditions on the flow structure inside a cross flow fan working in a unit incorporating a heat exchanger as well as on aerodynamic performances of a cross flow fan and unit have been studied. Different experimental and numerical methods have been used to verify and confirm selected flow phenomena. The local pressure loss as an effect of a heat exchanger resistance has been estimated taking into consideration some experimental results confirmed by the Finite Volume Method computation.

*Keywords: cross flow fan, heat exchanger, performances, flow structure*

#### Streszczenie

W artykule przedstawiono wybrane problemy związane z wpływem zróżnicowanych warunków dławienia na strukturę przepływu w wentylatorze poprzecznym pracującym w układzie z wymiennikiem ciepła. Użyto eksperymentalnych i numerycznych metod w celu weryfikacji występujących zjawisk przepływowych. Analizując wybrane wyniki doświadczalne potwierdzone obliczeniami numerycznymi, podjęto próbę oszacowania lokalnej straty ciśnienia jako efektu oporu stawianego przez wymiennik ciepła w strefie tłoczenia wentylatora poprzecznego.

*Słowa kluczowe: wentylator poprzeczny, wymiennik ciepła, charakterystyki pracy, struktura przepływu*

\* Prof. Ph.D. D.Sc. Eng. Jolanta Stacharska-Targosz, Ph.D. Konrad Nering, Institute of Thermal and Process Engineering, Faculty of Mechanical Engineering, Carcov University of Technology.

## 1. Introduction

A relatively wide range of a cross flow fan application causes different requirements respecting the interior flow structure. Particularly such features as: generation of lower noise level in comparison to other kinds of fans and uniform velocity distribution at the outlet fan cross section are usually utilized in the ventilating and air conditional systems. The rectangular cross-sectional area of the fan inlet and outlet (Fig. 1) allows for a direct connection to the other device, for example, to a heat exchanger what significantly reduces or sometimes eliminates the loss of local pressure resulting in higher efficiency.

In a cross flow fan the fluid flows perpendicularly to the axis of rotation crossing twice the blading, generating two steps of compression and creating higher values of pressure coefficient  $\psi$  in comparison to other types of fans having the same diameter.

This two-stage flow machine characterizes a rather complex flow structure caused

by the constructional compromise of the blade passage shape fulfilling two different roles as an inlet and outlet part of blading. The velocity field inside the cross flow fan is usually divided into three different regions: the fan inlet, impeller interior with blading and fan outlet.

The flow structure inside the impeller is a function of several geometric parameters and flow conditions. Correlation between the selected elements of the casing and the impeller's geometry as well as their effect on the cross flow fan's performance has been studied and published earlier but in literature there is lack of experimental or theoretical results describing the relation between the flow structure or flow phenomena inside a cross flow fan and heat exchanger being a discharge resistance and creating one unit.

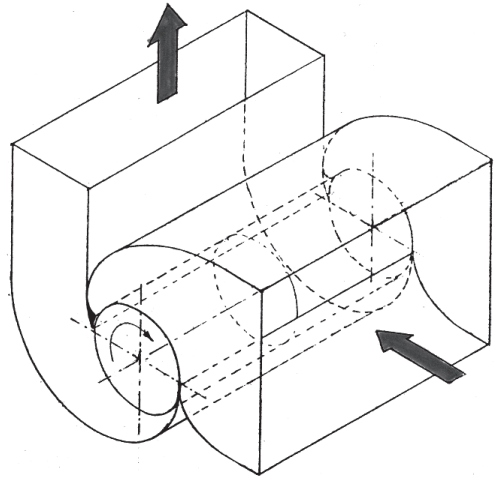


Fig. 1. Cross flow fan

## 2. Some selected experimental and numerical results of flow structure changes inside the cross flow fan as a result of throttling

Several applications of the cross flow fan have required some knowledge about the flow structure inside this flow machine which is changing as a result of varying flow conditions caused, for example, by throttling realized at the inlet or outlet fan cross section.

### 2.1. Flow visualization in water tank

Flow visualization is one of the effective methods allowing to identify and better understand some flow phenomena as well as to observe their arising and evolution in time.

This method gives quick and visible information with reference to casing and blading design parameters and it allows to analyze and find the relationship between the internal flow and performance curves. The selected results of water visualization with the use of polystyrene particles as tracers (the same density of polystyrene and water at the measurement temperature give an effect of suspension during the revolution of impeller) are presented in figures below. The visible influence on the flow structure has a change of flow conditions observed in Fig. 2 caused by varying resistance at the inlet part of the cross flow fan.

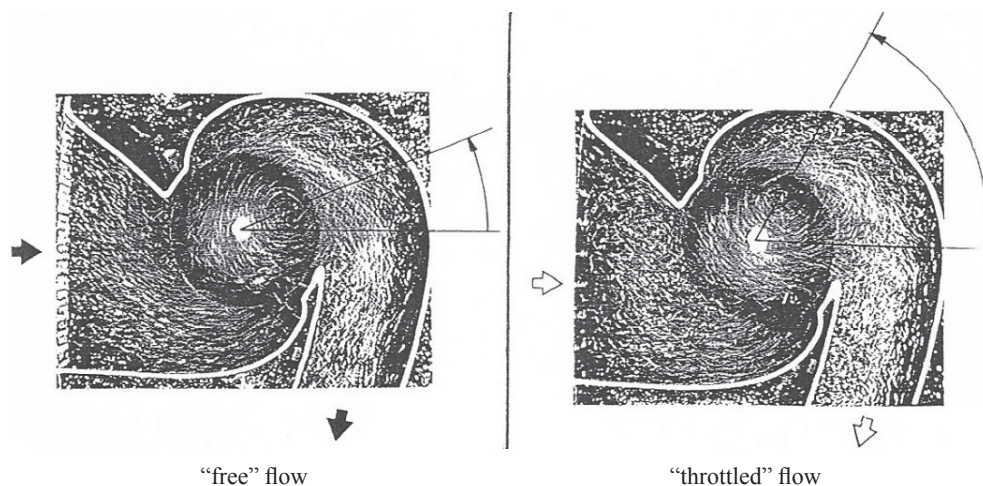


Fig. 2. Influence of throttling on flow structure and localization of eccentric vortex

As a consequence of throttling realized at the cross section of the fan inlet a movement of eccentric vortex in the direction of the rear wall as well as its magnitude increase are noticeable. In the “throttled flow” the reverse stream observed near the tongue (stabilizer) has crossed the blade ring and flowed into the impeller’s interior. This caused the main increase in the eccentric vortex’s size occupying, in this case, the greater part of blading. Recirculation and dead zones appearing as a result of very low volumetric flow rate as well as the eccentric vortex effected in the main reduction of a cross flow fan’s efficiency [1].

## 2.2. Measurements of velocity field in the air – effect of throttling

Analyzing the velocity distribution obtained in different throttling conditions of the air flow for the most interesting area – the impeller’s interior (Fig. 3) a similar flow structure is observed. The different regions of the interior flow determined by the vector velocity field: throughflow, eccentric vortex near the vortex stabilizer wall, the zone of the highest values of velocity at the outlet part of the impeller and recirculation zone at the inlet part of the impeller are visible. This recirculation region aroused from the stream crossing the blade passages under no adequate angles can be reduced by using different shape of the casing element at the inlet.

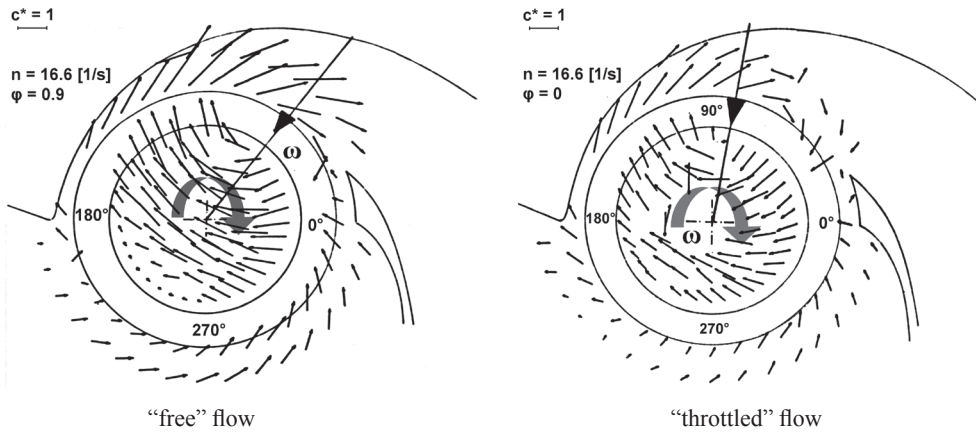


Fig 3. Absolute velocity distribution for “free” and “throttled” flows,  $n = 16.6 \text{ s}^{-1}$

The results of the vector velocity field measurements indicate the same tendency of the eccentric vortex movement towards the rear wall in the situation of throttling of a cross flow fan realized at suction as it was showed earlier in Fig. 2.

The analogy between flow parameters measured and calculated in two different media (air and water) allows to use a simple formula for local velocity estimations in the region where the direct measurements are impossible or complicated and require very special and expensive equipment, for example inside the rotating blade passages [1].

### 2.3. Numerical calculations

Qualitative results of flow visualization in water as well as quantitative measurements of the velocity field carried out in the air may be treated as an experimental verification of the numerical flow simulations. Most commercial computational fluid dynamics packages are based on the Finite Volume Method. This method implemented in the STAR-CD software has been used to compute two-dimensional incompressible flow of the viscous fluid with a standard Reynolds  $k-\epsilon$  turbulence model in the cross flow fan. The computational area was divided into eighteen casing blocks and one impeller block. The geometry of the tested cross flow fan was drawn in Microstation/J with a accuracy to a millionth part of the main unit. The tetrahedral volume elements (cells) with different density concentration have been used for building the grid. At the outlet area of the fan the blocks with the greatest number of cells were located because of the necessity of high accurate readability of the calculated values of pressure and velocity

Some selected results of numerical flow simulation in a cross flow fan indicating similarity to the results obtained experimentally are presented below. In Fig.4 the vector velocity fields obtained for two different flow conditions determined by variation of throttling realized at the outlet zone of the cross flow fan at a rotational speed of  $n = 24.17 \text{ s}^{-1}$  are presented [2].

Throttling has an important influence on the flow structure causing the displacement of recirculation zones as well as the eccentric vortex, which is visible analyzing the vector's velocity distribution.

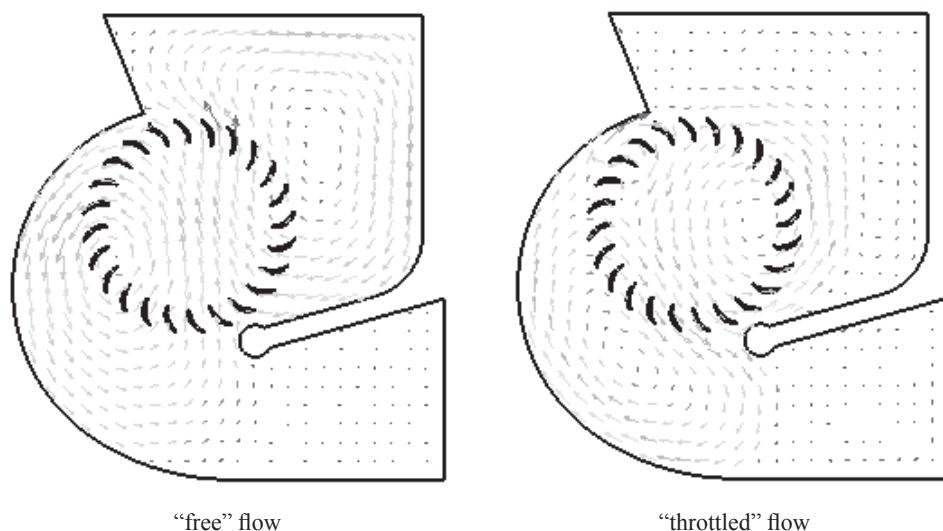


Fig. 4. Velocity vector distribution in two different flow conditions – numerical calculation

In numerical simulations the throttling was realized at cross flow fan discharge, so the eccentric vortex center has been moved in the direction of the vortex's stabilizer wall. Numerical results confirmed the localization of the eccentric vortex near blading, an increase of its size and its center displacement during different flow conditions.

### 3. Cross flow fan performances at varied working conditions

The flow phenomena described above have to be taken into account considering the cooperation of the cross flow fan with the heat exchanger, treated as a discharge resistance. This kind of fan is very sensitive and even a small change of geometric parameters as well as the variation of flow conditions' effect on the flow structure. The results of the study carried out for the air room conditioner incorporating a cross flow fan indicating the factors that influenced the fan's performance of the unit were presented in [3].

The quantitative estimation of the flow structure's influence on the cross flow fan working is analyzed based on the aerodynamics and efficiency curves obtained for different flow conditions. The comparison has been made for the performances obtained for a cross flow fan working separately and for the same cross flow fan working as an element of the unit containing a heat exchanger [4].

The relation between the total pressure coefficient and the flow coefficient in the form of curves: for the cross flow fan working separately (it means that the air is discharged straight to the atmosphere so static pressure at the outlet is assumed zero)  $\psi_t = f(\varphi)$  and being an element of the unit containing a heat exchanger  $\psi_t^* = f(\varphi)$ , measured at two rotational speeds:  $n = 15 \text{ s}^{-1}$  and  $n = 20 \text{ s}^{-1}$  are shown in Fig. 5. The experimental results have confirmed the two expected phenomena: the higher values of the total pressure coefficient obtained at a higher

rotational speed and the lower values of the total pressure coefficient obtained for a cross flow fan working as an element of unit  $\psi_t^*$  for both rotational speeds. The difference of the

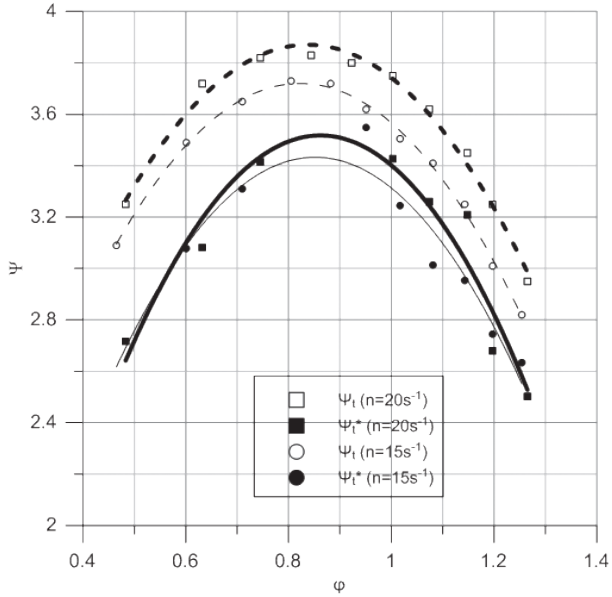


Fig. 5. Changes of total pressure coefficient for cross flow fan working separately  $\psi_t$  and asegment of unit  $\psi_t^*$  at different rotational speed:  $n = 20 \text{ s}^{-1}$  and  $n = 15 \text{ s}^{-1}$

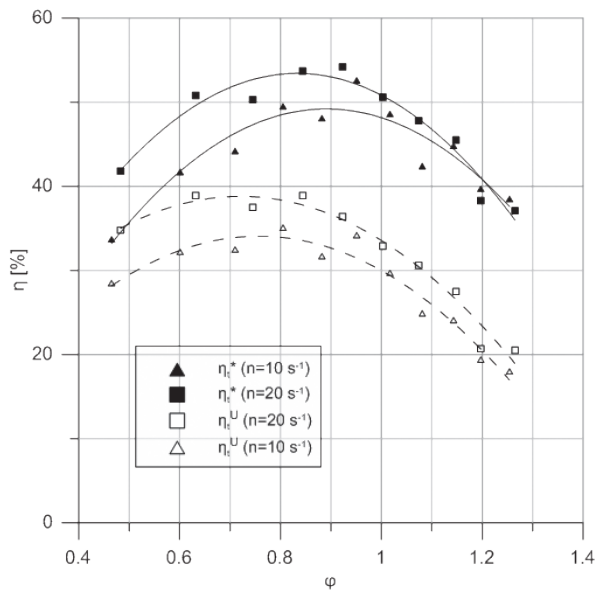


Fig. 6. Total efficiency vs. flow coefficient at rotational speed  $n = 20 \text{ s}^{-1}$  and  $n = 10 \text{ s}^{-1}$

total pressure coefficient varying in the range between 8% a 10% may be treated as the consequence of the heat exchanger resistance.

Graphs of total efficiency of the cross flow fan working as an element of unit  $\eta^*$  and efficiency of unit  $\eta^u$  (dotted lines) in the function of a flow coefficient for two rotational speeds:  $n = 20 \text{ s}^{-1}$  and  $n = 10 \text{ s}^{-1}$  are shown in Fig. 6. The difference between the efficiency of a cross flow fan in the unit and the total efficiency of the unit about 7% to 18% in the considered range of  $\phi$ , may be treated as “negative efficiency” of the heat exchanger located at the outlet section of the cross flow fan.

Resistance having an important influence on flow structure changes (see Fig. 4) especially in an increase of the eccentric vortex and exclusion of impeller blading from real work, causes a visible reduction in efficiency.

The reduction in efficiency is the consequence of resistance which has visible changes in the flow structure

#### 4. Effect of heat exchanger as discharge resistance

Quantitative estimation of the local pressure losses caused by the connection between the cross flow fan and heat exchanger has been performed for adifferent medium temperature: 20°C, 35°C, 40°C, 45°C and 50°C. The ratio of the experimental results of dynamic pressure as difference between the total and static pressure at the cross section before ( $A_1$ ) and behind ( $A_2$ ) heat exchanger obtained from measurements  $p_d^{h(m)}$  and calculated  $p_d^{h(c)}$  using the simplified formula:

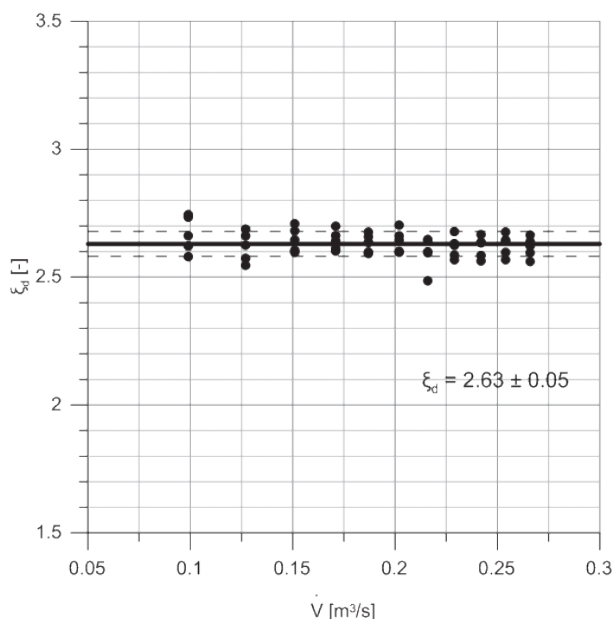


Fig. 7. Dimensionless coefficient  $\xi_d$  vs volumetric flow rate for different medium temperature



$$p_d^h = \frac{1}{2} \rho \left[ \frac{1}{\rho_3 A_3^2} - \frac{1}{\rho_2 A_2^2} \right] \quad (4)$$

is determined as “dimensionless coefficient of dynamic pressure”  $\xi_d$ . The graph  $\xi_d = f(\dot{V})$  is presented in Fig. 7.

Independence of  $\xi_d$  from the medium temperature in the range of 20°C÷50°C and an almost constant value 2.63 indicate a local dynamic pressure loss being the effect of the heat exchanger’s resistance located at the outlet’s cross section of the cross flow fan.

## 5. Conclusions

The investigations carried out in different media using different measurement methods: flow visualization in water and measurements of vector velocity fields in the air as well as the numerical flow simulation showed an important influence of throttling on the flow structure in a cross flow fan. Local pressure loss has been estimated in the form of a dimensionless coefficient of dynamic pressure  $\xi_d$ .

## Nomenclature

$D_2$	–	outer diameter of impeller, m
$L$	–	length of impeller, m
$u_2$	–	tangential velocity at outer diameter, m/s
$n$	–	rotational speed, 1/s
$p$	–	pressure, Pa
$\dot{V}$	–	volumetric flow rate, m <sup>3</sup> /s
$\rho$	–	fluid density, kg/m <sup>3</sup>
$\psi = \frac{2\Delta p}{\rho u_2^2}$	–	pressure coefficient
$\phi = \frac{\dot{V}}{D_2 L u_2}$	–	flow coefficient
$\eta = \frac{\Delta p \cdot \dot{V}}{P}$	–	efficiency

Subscripts:  $s$  – static,  $t$  – total,  $d$  – dynamic

## References

- [1] Stacharska-Targosz J., *Wentylatory poprzeczne*, Politechnika Krakowska, Kraków 2006.
- [2] Chmielowiec M., *Wyznaczanie charakterystyk aerodynamicznych wentylatorów poprzecznych za pomocą numerycznej symulacji przepływu*, Praca Doktorska, Politechnika Krakowska, Kraków 2008.
- [3] Matsuki K., Shinobu Y., Takushima A., Tanaka S., *Experimental study of internal flow of a room air conditioner incorporating a cross flow fan*, Conference Proceeding ASHRAE 3135, 1988.
- [4] Wojtuń S., *Analiza pracy układu wymiennik ciepła-wentylator poprzeczny*, Praca doktorska, Politechnika Krakowska, Kraków 2004.



SZYMON TENGLER, ANDRZEJ HARLECKI\*

## COMPUTER PROGRAM FOR DYNAMIC ANALYSIS OF SPECIAL VEHICLES WITH HIGH GRAVITY CENTRE

### PROGRAM KOMPUTEROWY DO ANALIZY DYNAMIKI SAMOCHODÓW SPECJALNYCH O WYSOKO POŁOŻONYM ŚRODKU CIĘŻKOŚCI

#### Abstract

The functionality of the authors' computer program which enables to analyze dynamics of special cars with a high gravity center, in particular, a technical rescue vehicle of fire service is presented in this article. The correctness of the analysis has been confirmed experimentally. The program consists of two essential parts: the calculation module and the animation module designed for three-dimensional visualization. Properly prepared input data in the XML format is processed by the calculation module which can solve the equations of motion including an uneven road surface. The results of this module are processed by the animation module performing a smooth computer animation. For mathematical modeling of road unevenness and presenting three-dimensional animated objects authors used an unconventional combination of the developed program with the Blender graphical environment.

*Keywords: computer modeling, dynamic analysis, special vehicles*

#### Streszczenie

W artykule przedstawiono funkcjonalność autorskiego programu komputerowego umożliwiającego analizę dynamiki samochodów specjalnych o wysoko położonym środku ciężkości, a w szczególności samochodów ratowniczo-gaśniczych straży pożarnej. Poprawność analizy potwierdzono doświadczalnie. Program zbudowano z dwóch zasadniczych części: modułu obliczeniowego i modułu animacji służącego do wizualizacji trójwymiarowej. Odpowiednio przygotowane dane wejściowe w formacie XML są przetwarzane przez moduł obliczeniowy rozwiązujący równania ruchu z uwzględnieniem nierównej nawierzchni drogi. Wyniki tego modułu są przetwarzane przez moduł animacyjny umożliwiający wykonanie płynnych animacji komputerowych. Do matematycznego modelowania nierówności nawierzchni drogi i prezentacji animowanych obiektów trójwymiarowych autorzy wykorzystali niekonwencjonalne połączenie opracowanego programu ze środowiskiem graficznym Blender.

*Słowa kluczowe: modelowanie komputerowe, analiza dynamiki, samochody specjalne*

\* Ph.D. Eng. Szymon Tengler; Ph.D. D.Sc. Eng. Andrzej Harlecki, prof. ATH; Faculty of Mechanical Engineering and Computer Science, University of Bielsko-Biala.

### 1. Introduction

Computer simulations of a motion of vehicles mentioned in the abstract, performed in the case of different variants of constraints, can predict a lot of potential threats, and the conclusions drawn from them can constitute important guidelines for vehicle designers. It is important for the prepared mathematical model of the vehicle to be a sufficiently accurate representation of the real system. According to the vehicle designers the computer simulations of an appropriately prepared mathematical model shorten the time of testing on a real prototype of the vehicle, and also reduce costs of the designing process.

Algorithms for generating the equations of motion have been formulated by homogenous transformations and Lagrange’s equations [3]. Generating these equations takes into account different types of experiments, e.g.: changing a lane plane, driving on a curved track, driving over uneven road surfaces, negotiating a circular track (driving on the track in the shape of a circle). Both the speed of the vehicle and its path can be controlled by a PID controller.

### 2. Computer program

The devised computer program was divided into two modules: a solver module and an animation module.

#### 2.1. Solver module

The developed solver module consists of mutually co-operating elements, which are specified in a diagram of the components (Fig. 1).

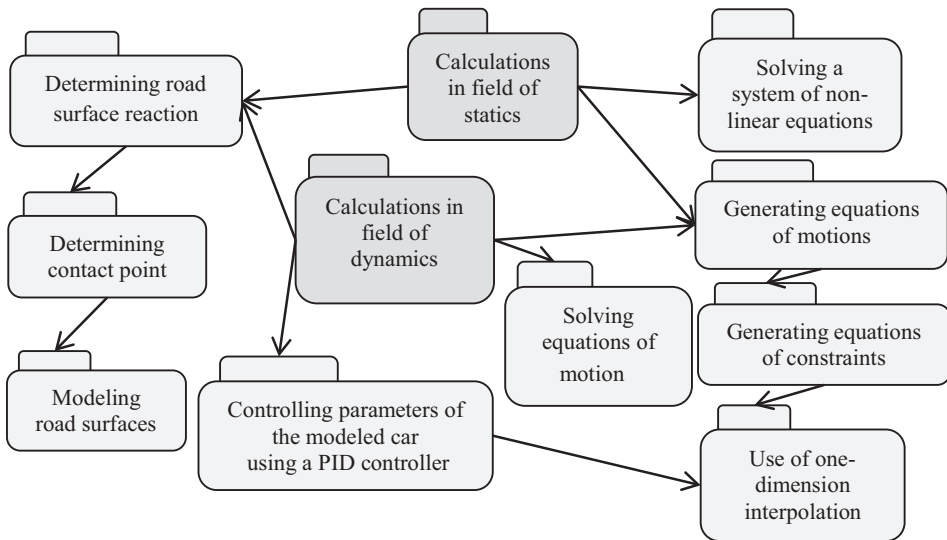


Fig. 1. A diagram of the components of the solver module

The main role is performed by the components used for making calculations from the field of statics and dynamics. The arrows guided appropriately symbolize their co-operation with other components of the solver module, which are characterized in Table 1.

Table 1

**Characteristics of the solver module components**

Name of component	Description
Solving system of non-linear equations	It serves to solve equations of statics [3] by the iterative Newton's method
Determining reaction of a road surface	It implements three models of tires: Fiala, Pacejka and Dugoff-Ufelmann [9]
Determining contact point	It implements algorithms which allow to determine the position of the point in which road surface reactions are applied to vehicle wheels
Modeling road surface	It implements a continuous and discrete model of the road surface described in the work [10]
Generating equations of motion	It generates equations of motion
Generating equations of constraints	It generates the so called equations of constraints described in the work [9]
Use of one-dimension interpolation	It implements functions of splines of the first and third order
Solving equations of motion	It implements methods of solving differential equations: fixed-step (Runge-Kutta IV order, Implicite Euler) and variable-step: (Runge-Kutta-Fehlberg, Bulirsha-Stoera-Daufhardta). Advantages and computing power of the methods mentioned are presented in the work [8]
Controlling parameters of modeled vehicle by use of PID controller	It implements the operation of a PID controller

The component which controls parameters of the modeled vehicle in accordance with the PID controller algorithm should be distinguished among the components presented in table 1. Its operation is used to provide the determined course of vehicle speed values or to maintain the trajectory of its motion in a shape of a circle. The initial value (controlling) of the PID controller depends on the reference value. In the first case the reference value is an assumed course of speed values of the modeled vehicle gravity centre (given e.g. in the form of a spline function), and the initial value is the course of values of driving torques applied to the rear wheels. In the second case the reference value is the assumed radius of a circular track, and the initial value is a turning angle of the front wheels. A method of manual adjustment in connection with the Ziegler-Nichols method was used to determine the PID controller amplification [12].

The solver performs calculations on the basis of property prepared input data obtained from the pre-processor. The input data contains all the necessary parameters needed for the proper operation of the solver module (Fig. 1). These parameters, among others, are:

- the type of analysis (statics and/or dynamics),
- simulation time and the type of a method solving equations of motion,
- parameters of bodies of a multibody system,
- parameters of equations of constraints,
- coordinates of mounting points of spring and damping elements,
- a stiffness coefficient of elastic and damping elements,
- parameters needed to control the vehicle speed value (PID),
- parameters needed to maintain the track of vehicle motion in the shape of a circle,
- parameters of particular tire models ,
- parameters of a road surface model,
- initial conditions (the vehicle parameters at the initial moment  $t = 0$ ).

The mentioned parameters' data is transferred to the solver module in format XML (eXtensible Markup Language) [7]. On the basis of the prepared data the solver module performs calculations.

## 2.2. Animation module

The second element of the program is the three dimensional animation module. Its main components are presented in Fig. 2.

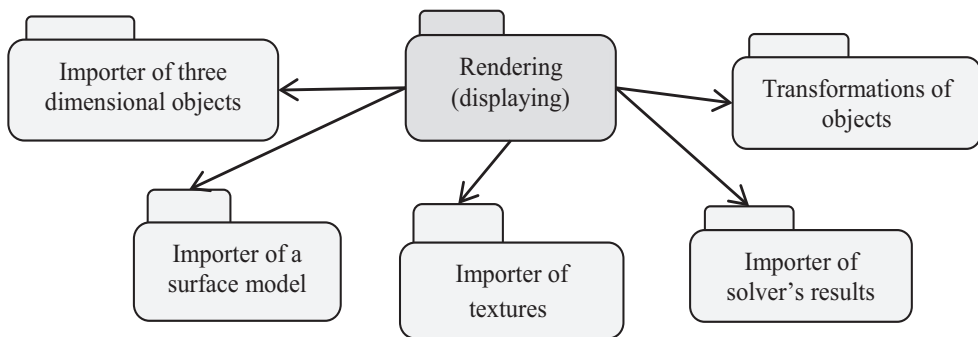


Fig. 2. A diagram of the components of the three dimension animation module

The components for importing three dimensional objects and textures are made in the form of libraries dll in language C++ [1]. The main joining element (the Rendering component) and other components co-operating with it are implemented in NET technology while using C# language [4] and OpenGL library [11].

The importer of objects enables to import any three dimensional objects written in the 3ds format. 3ds Max Autodesk company and Blender are popular environments for creating objects in this format on the information market. The first of the tools is commercial and the other is free of charge. However, for the needs of this work the Blender environment was selected because it can be used free of charge. Examples of the screen shots, presenting the selected model of the component (body building of a vehicle) made in the Blender environment, and then imported to the animation module, are presented in Fig. 3.

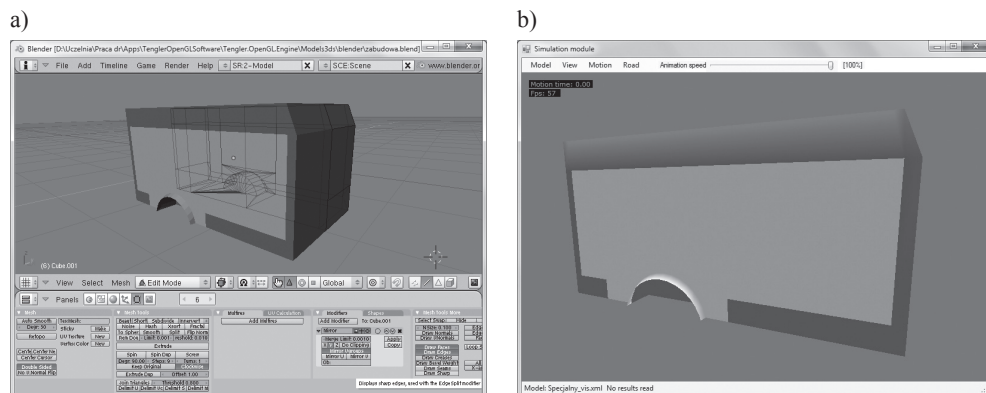


Fig. 3. Examples of screen shots showing operating of the component for importing 3ds objects: a) a 3ds object made by use of the Blender program, b) a 3ds object imported to the animation module

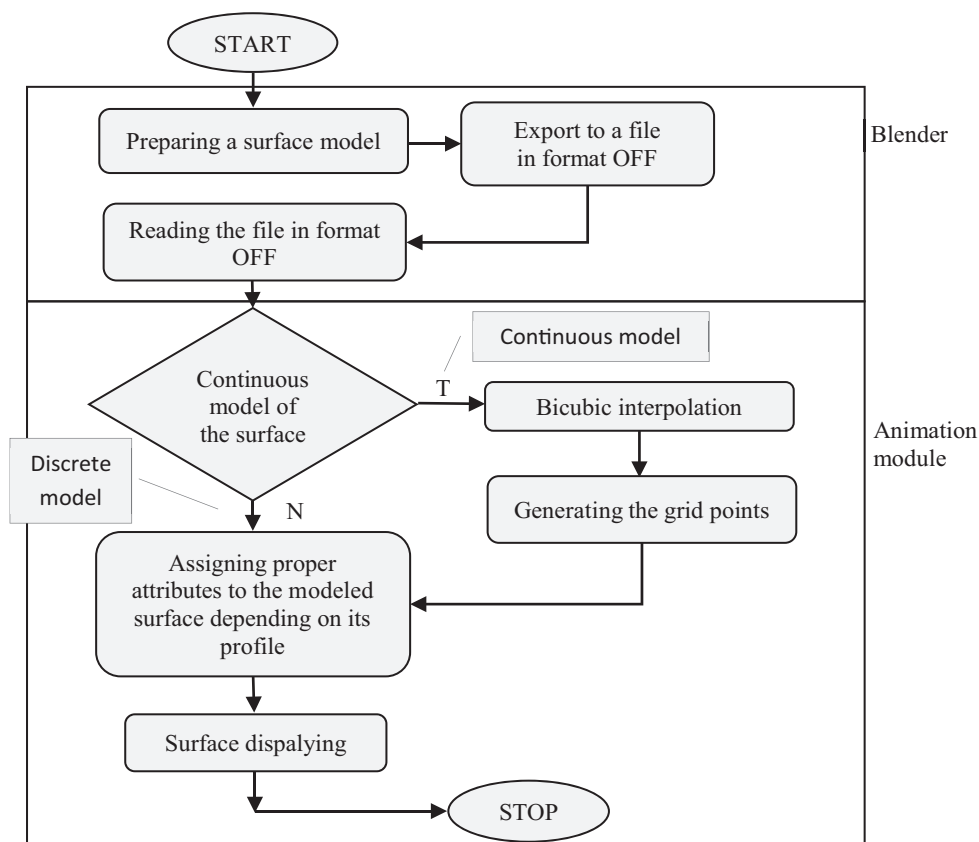


Fig. 4. A chart of operations concerning the rendering process of the road surface



The Blender program was also used for modeling different types of road surface. Import of the surface model from the Blender environment to the animation module is a slightly more complicated process than the import of the 3ds objects. It takes place according to the stages illustrated in Fig. 4.

A road surface model is prepared in the first step. Then, it is exported to a file in format OFF (Object File Format) [6]. Both of these operations are made in the Blender environment. The exported OFF file contains, among others, a set of coordinates of vertices (points) making a surface model. Depending on the selection of the surface model these points are used in the process of road surface rendering in an appropriate way. When computer simulations concern driving a vehicle over the modeled surface in a continuous way, then it is rendered by the use of the Bicubic interpolation method. An example of the model surface made by program Blender, and then imported to the animation module, is presented in Fig. 5.

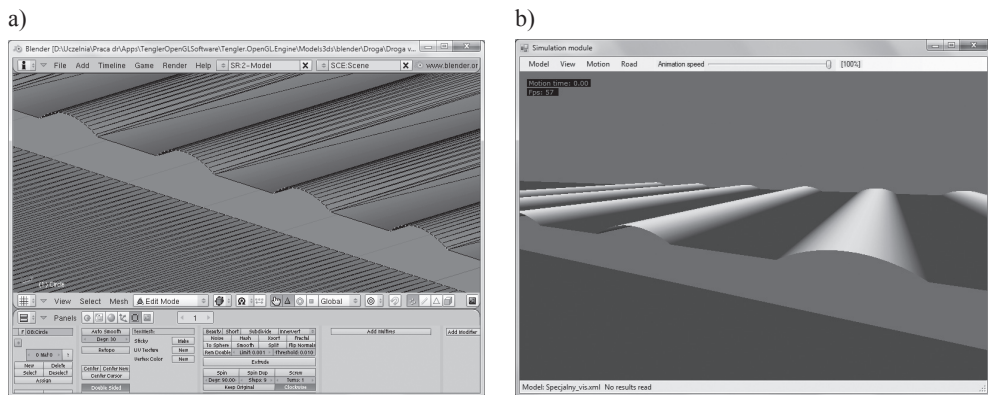


Fig. 5. An example of the surface model made in the Blender environment a) made by program Blender b) imported to the animation module

Other components of the animation module are characterized in Table 2.

Table 2

**Characteristics of the animation module components**

Name of a component	Description
Importer of textures	The component developed for importing graphic files in formats jpg, png, bmp and tiff, used in the process of imposing textures on the animated objects
Transformations of objects	The component developed for translations and rotations of the animated objects
Importer of the solver module results	The component importing the results generated by the solver module. The imported results are interpolated by a spline function of the first order to provide smoothness of animation

Particular components (Fig. 2) were programmed, using a technique of object-oriented programming with the application of design patterns [2]. A diagram of the classes of the Rendering component, presenting its main functionality, is shown Fig. 6.

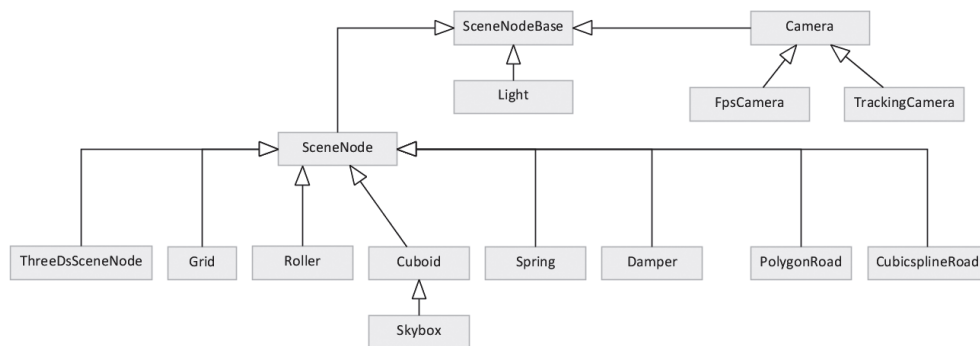


Fig. 6. The basic diagram of the rendering component classes

The base class for all objects is an abstract class – SceneNodeBase. From it the following classes inherit directly:

- Light – the class responsible for “scene” light,
- Camera – the class providing an appropriate view of objects on the scene; two independent cameras are available: FpsCamera (First Person Shooter) and TrackingCamera following the indicated object [5],
- SceneNode – the base class for the objects displayed on the “scene”.

Other classes illustrated in Fig. 6, inheriting from the SceneNode type, are the basic rendering elements of the characterized module.

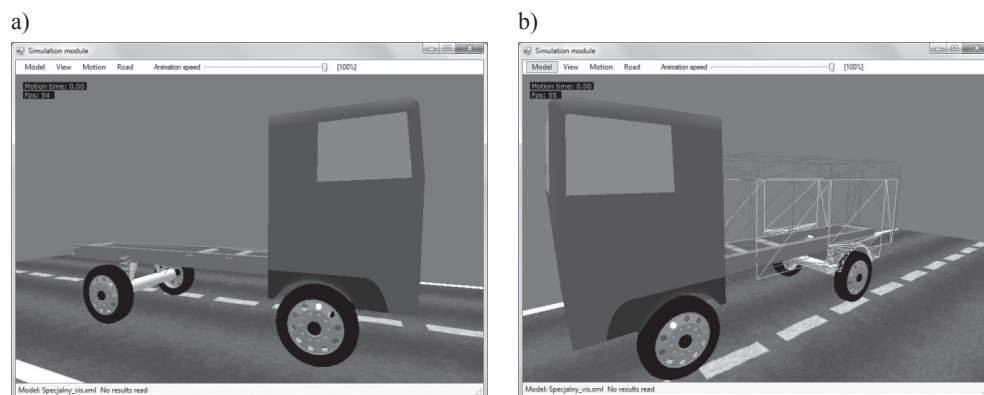


Fig. 7. The examples of the screen shots presenting: a) the hiding of modeled components, b) a “skeleton” view of the components

The presented structure of the prepared animation module has a universal character and enables to extrapolate it in a relatively easy way. With little effort it can be used e.g. for an animation of components, using the simulation results which come from other computing packages. Owing to the component for importing 3ds objects those can be animations of any complex shape.

The described animation module also offers a lot of useful functions connected with handling the animation process. A camera can be adjusted here in a lot of ways in order to follow “easily” the moving objects. Some objects can be also “hidden” to find out how particular modeled components of a vehicle move (Fig. 7).

### 3. Conclusions

A structure of two basic modules of the developed program to analyze dynamics of special vehicles with high gravity centre, that is the solver module and the animation module, is described in the article. A fact of a rarely met connection of authors’ computer program with the Blender environment should be emphasized. Owing to this, in this environment both road surface models and three dimension objects of any shapes, which then are imported in the authors’ program, can be built. Such a connection, according to the authors, shortens the time to prepare the final virtual model and allows to perform computer simulations in an effective way. The particular modules were made while using different programming languages and techniques of object-oriented programming combined with design patterns. An intuitive language of XML tags was selected as a format for transferring data between the modules. According to the authors the use of the object-oriented programming technique enables to expand the developed computer program with additional functionalities in a relatively easy way by other programmers. Additionally, the use of the XML language as “a bridge” between the developed modules, does not only allow to make separate programs co-operating with the solver module, but also to use the animation module for three dimension visualization of results, which come from other computing programs.

### References

- [1] Eckel B., *Thinking in C++*, Helion, Gliwice 2002.
- [2] Gamma E., *Wzorce projektowe – inżynieria oprogramowania*, Wydawnictwa Naukowo-Techniczne, Warszawa 2005.
- [3] Grzegózek W., Adamiec-Wójcik I., Wojciech S., *Komputerowe modelowanie dynamiki pojazdów samochodowych*, Wydawnictwo Politechniki Krakowskiej, Kraków 2003.
- [4] Jeffries J., *Programowanie ekstremalne w C#*, APN PROMISE, Warszawa 2005.
- [5] Pallister K., *Game programming Gems 5*, Charles River Media, Inc., Hingham, Massachusetts 2005.
- [6] Rost R.J., Bourke P., *OFF – A 3D Object File Format* (<http://paulbourke.net/dataformats/off>).
- [7] Rusty E., Scott W., *Means XML in a Nutshell*, O’Reilly, 2004.

- [8] Szczotka M., Tengler S., Wojciech S., *Numerical Effectiveness of Models and Methods of Integration of the Equations of Motion of a Car, Differential Equations and Nonlinear Mechanics*, Hindawi Publishing Corporation, Vol. 2007, Article ID 49157, 2006.
- [9] Tengler S., *Analiza dynamiki samochodów specjalnych o wysoko położonym środku ciężkości*, Praca doktorska, Wydział Budowy Maszyn i Informatyki, Akademia Techniczno-Humanistyczna, Bielsko-Biała 2012.
- [10] Tengler S., Harlecki A., *Ways of uneven road surface modeling used in the vehicle dynamics analysis*, Journal of KONES, Vol. 19, No. 1, 2012.
- [11] Wright R.S, Lipchak B., *OpenGL. Księga eksperta*, Helion, Gliwice 2005.
- [12] Ziegler J.G., Nichols N.B., *Optimum Settings for Automatic Controllers*, Transactions of the ASME, Vol. 64, 1942, 759-768.



## CONTENTS

P. Cykliš, R. Duda: Computer driven automatic control of the hybrid two stage refrigeration cycle.....	3
P. Cykliš, P. Młynarczyk: The role of the CFD modelling in the shape optimization of the pressure pulsations dampers.....	11
T. Czyżewski: Quaternions – alternative for Euler angles in kinematic analysis of machine mechanisms.....	19
W. Czyżycki: Modeling of heat flow through multilayer internal supports of cryogenic vessels....	27
T. Dębiniński, M. Hojny, D. Jędrzejczyk: Stereoscopic visualization for model of deformation of steels with mushy zone.....	35
M. Domagała: Modelling of direct acting relief valve using CFD-FSI simulation.....	43
P. Duda, R. Duda: Modeling of gas flow through valve (CRV).....	49
P. Duda, Ł. Felkowski: Modeling of stress state in thick walled pressure element based on European Standards and proposed creep equation.....	59
J. Fabiś-Domagała: FMEA analysis of a hydraulic cylinder using artificial neural network....	67
G. Filo: Asynchronous buffer read method in development of DAQ application for supporting research of hydraulic systems.....	77
G. Filo: The use of linear guides to move HEAVY loads.....	83
J. Habel: The idea of database for recording intermediate states of rotary parts for CAPP use.....	91
M. Hojny, J. Tarasiuk, S. Wroński: Development of the modeling strategy for the steel deformation in semi-solid state tomographic studies.....	101
M. Kluziewicz: Experimental verification of kinetostatic model of strut suspensio mechanism.....	111
W. Kwásny, T. Jung: The influence of deposition conditions on structure of PVD coatings obtained in the magnetron process.....	119
P. Lempa, E. Lisowski: Automated generation of 3D models of hydraulic components.....	125
E. Lisowski, J. Rajda: CFD analysis of flow forces acting on the spool of directional control valve type WE10J.....	133
F. Lisowski: Numerical computation of stresses and deformations in the planetary roller screw components.....	141
F. Lisowski: Optimization of a curvilinear thread profile in a planetary roller screw.....	149
J. Matlak, D. Słota: Solution of the Stefan problem by involving material shrinkage.....	157
M. Migus, K. Osowski, A. Olszak, A. Kęsy, Z. Kęsy: Computer-aided machine design with regard to new technologies and materials.....	165
P. Młynarczyk, G. Dziadkiewicz: Numerical modelling of the optical demultiplexer photonic structures.....	175
H. Momeni, M. Domagała: CFD simulation of transport solid particles by jet pumps.....	185
N. Yuka, M. Fumito, M. Ptaszynski: Modeling Learning motivation of students based on analysis of class evaluation questionnaire.....	193
A. Opaliński, M. Głowacki, I. Olejarczyk-Woźeńska, B. Mrzygłód: Prediction of technological process parameters based on experimental data.....	203
P. Piątek: Acquiring road profiles using Walking-Profler and computer modelling planograph's measurement.....	211
J. Pobożniak: Using concavity index for manufacturing feature recognition.....	221
M. Ptaszynski, P. Lempa, F. Masui: A modular system for support of experiments in text classification.....	229
S. Santitin, H. Masui: Integration of the Rural Roads database in Thailand with the parallel computing environment.....	245

A. Skowronek: Reducing the number of runs in experimental research using smart designs of experiment.....	253
A. Skowronek: Comparing the effects of application of the smart and traditional designs of experiment.....	263
T. Spotoski, K. Osowski, Z. Kęsy: Control system of laboratory stand for gearbox and coupling testing.....	271
J. Stacharsa-Targosz, K. Nering: Influence of discharge resistance on internal flow structure and performances of the cross flow fan and the unit incorporating heat exchanger.....	281
S. Tengler, A. Harlecki: Computer program for dynamic analysis of special vehicles with high gravity centre.....	291

## TREŚĆ

P. Cyklics, R. Duda: Wspierane komputerowo automatyczne sterowanie hybrydowego dwustopniowego układu chłodniczego.....	3
P. Cyklics, P. Młynarczyk: Rola modelowania CFD w optymalizacji kształtu tłumików pulsacji ciśnienia .....	11
T. Czyżewski: Kwaterniony – alternatywa dla kątów Eulera w analizie kinematycznej mechanizmów maszyn .....	19
W. Czyżycski: Modelowanie przepływu ciepła przez wielowarstwowe podpory międzyplaszczowe w zbiornikach kriogenicznych.....	27
T. Dębiniński, M. Hojny, D. Jędrzejczyk: Wizualizacja stereoskopowa modelu odkształcania stali w stanie półciekłym.....	35
M. Domażała: Modelowanie zaworów przelewowych bezpośredniego działania przy wykorzystaniu symulacji CFD-FSI .....	43
P. Duda, R. Duda: Modelowanie przepływu gazu przez zawór (RZR) .....	49
P. Duda, Ł. Felkowski: Modelowanie Stanu naprężenia w elemencie ciśnieniowym zgodnie z Europejskimi Normami i zaproponowanym równaniem pełzania.....	59
J. Fabiś - Domażała: Analiza FMEA siłownika hydraulicznego z zastosowaniem sztucznych sieci neuronowych .....	67
G. Fiło: Metoda asynchronicznego odczytu bufora w budowie aplikacji DAQ wspomagającej badania układów hydraulicznych.....	77
G. Fiło: Zastosowanie prowadnic liniowych do przemieszczania ciężkich ładunków .....	83
J. Habel: Koncepcja bazy danych do zapisu stanów pośrednich przedmiotów obrotowych dla potrzeb systemów CAPP .....	91
M. Hojny, J. Tarasiuk, S. Wróński: Opracowanie kompleksowego podejścia do modelowania odkształcania stali w stanie półciekłym – badania tomograficzne.....	101
M. Kluziewicz: Eksperymentalna weryfikacja kinetostatycznego modelu mechanizmu zawieszenia z kolumną prowadzącą .....	111
W. Kwaśny, T. Jung: Wpływ parametrów nanoszenia na strukturę powłok otrzymanych w magnetronowym procesie PVD .....	119
P. Lempa, E. Lisowski: Zautomatyzowane generowanie modeli 3D elementów hydraulicznych.....	125
E. Lisowski, J. Rajda: Analiza CFD sił hydraulicznych działających na suwak rozdzielacza typu WE10J .....	133
F. Lisowski: Obliczenia numeryczne naprężeń i odkształceń w elementach planetarnej przekładni śrubowej rolnkowej .....	141
F. Lisowski: Optymalizacja krzywoliniowego zarysu gwintu w planetarnej przekładni śrubowej rolnkowej .....	149
J. Matlak, D. Słota: Rozwiązanie zagadnienia Stefana z uwzględnieniem skurczu materiału....	157
M. Migus, K. Osowski, A. Olszak, A. Kęsy, Z. Kęsy: Komputerowe wspomaganie w budowie maszyn z uwzględnieniem nowych technologii i materiałów .....	165
P. Młynarczyk, G. Dziadkiewicz: Modelowanie numeryczne struktur fonicznych optycznego demultipleksera .....	175
H. Momeni, M. Domażała: Symulacja CFD transportu cząstek stałych w pompach strumieniowych.....	185
N. Yuka, M. Fumito, M. Ptaszynski: modelowanie motywacji do nauki u studentów na podstawie analizy kwestionariusza oceny zajęć .....	193
A. Opaliński, M. Głowacki, I. Olejarczyk - Woźnińska, B. Mrzygłód: Przewidywanie parametrów procesu technologicznego w oparciu o dane eksperymentalne .....	203



P. P i ą t e k: Pozyskanie profilu drogi z użyciem Walking-Profilera, a następnie komputerowe zamodelowanie rzeczywistego pomiaru planografem.....	211
J. P o b o ż n i a k: Zastosowanie indeksu wklęsłości w rozpoznawaniu cech technologicznych.....	221
M. P t a s z y n s k i, P. L e m p a, F. M a s u i: Modułarny system wspomagania doświadczeń z dziedziny klasyfikacji tekstu.....	229
S. S a n t i t i n, H. M a s u i: Integracja bazy danych dróg wiejskich ze środowiskiem obliczeń równoległych.....	245
A. S k o w r o n e k: Zmniejszanie ilości badań eksperymentalnych z zastosowaniem inteligentnych planów eksperymentu.....	253
A. S k o w r o n e k: Porównanie efektów zastosowania elastycznych i tradycyjnych planów eksperymentu.....	263
T. S p o t o w s k i, K. O s o w s k i, Z. K ę s y: System sterowania stanowiska laboratoryjnego do badań przekładni i sprzęgieł.....	271
J. S t a c h a r s a - T a r g o s z, K. N e r i n g: Wpływ oporu w strefie tłoczenia na wewnętrzną strukturę przepływu i charakterystyki pracy wentylatora poprzecznego oraz układu zawierającego wymiennik ciepła.....	281
S. T e n g l e r, A. H a r l e c k i: Program komputerowy do analizy dynamiki samochodów specjalnych o wysoko położonym środku ciężkości.....	291